



PHD

**Labelling of Small and Biomolecules for Tracking and Monitoring
(Alternative Format Thesis)**

Edelmann, Martin R.

Award date:
2023

Awarding institution:
University of Bath

[Link to publication](#)

Alternative formats

If you require this document in an alternative format, please contact:
openaccess@bath.ac.uk

Copyright of this thesis rests with the author. Access is subject to the above licence, if given. If no licence is specified above, original content in this thesis is licensed under the terms of the Creative Commons Attribution-NonCommercial 4.0 International (CC BY-NC-ND 4.0) Licence (<https://creativecommons.org/licenses/by-nc-nd/4.0/>). Any third-party copyright material present remains the property of its respective owner(s) and is licensed under its existing terms.

Take down policy

If you consider content within Bath's Research Portal to be in breach of UK law, please contact: openaccess@bath.ac.uk with the details. Your claim will be investigated and, where appropriate, the item will be removed from public view as soon as possible.



**Labelling of Small and Biomolecules
for Tracking and Monitoring**

Martin R. Edelman

A thesis submitted for the degree of Doctor of Philosophy

University of Bath

Department of Pharmacy and Pharmacology

October 2022

COPYRIGHT

Attention is drawn to the fact that copyright of this thesis rests with the author and copyright of any previously published materials included may rest with third parties. A copy of this thesis has been supplied on condition that anyone who consults it understands that they must not copy it or use material from it except as licenced, permitted by law or with the consent of the author or other copyright owners, as applicable.

Signed

Date

*This thesis is dedicated to my family,
especially my beloved mum, who could not wait
for this thesis to be finished and passed away
just a few weeks before submission*

Acknowledgements

It took more than 50 years to finish this thesis. I thought it would take longer. Now, I want to put science aside and thank the people who contributed to the success of this thesis. I have very fond memories of the first time I spoke to a lecturer from the University of Bath, which was the start of my PhD journey. A big thank you to my “Doktorvater” Dr Ian S. Blagbrough for his tireless support over the three years. Together with my second supervisor from the University of Bath, Prof Stephen M. Husbands, I was able to learn not only about science, but also about British culture, British humour, and the language (I will try to pronounce “tritium” correctly from now on). I am also very grateful to my two supervisors from Roche, Dr Michael B. Otteneder and Dr Filippo Sladojevich. In our countless joint meetings, I have had the privilege of learning so much from you. I always had the certainty that I will get support within a very short time whenever I was in despair. Many thanks, the four of you, for guiding me through this journey and for always standing by my side!

I am also very grateful to my line managers Thomas, Regina, Jean-Michel, Stefania, and Christopher from Roche for your trust, encouragement, and all your support. Also to the two former University of Bath students Hayley and Caitlin for the conversations about the university and the city of Bath. Many thanks to my colleagues in the isotope lab Thorsten, Fabian, Stephan, Mathias, Serana, and Dieter for your support, proof reading, and discussions about isotope chemistry. I also want to thank our Legal Department, especially Beat, who made the PhD journey possible through the agreements and together with my Head of Department Stefania had to do countless approvals. However, I cannot promise that there will be less approvals coming from me in the future.

I am grateful to my numerous co-authors in supporting the manuscripts and for the many scientific discussions. I want to especially thank my colleagues Eric, Arne, Markus, Wolfgang, who generated additional data in a short time to give the articles even more power. I really appreciate what you have done and know that it cannot be taken for granted.

Finally, I want to thank two very special people: Dr Helmut Ringsdorf (he prefers not to be called Prof anymore), who made science tasteful to me decades ago and significantly paved my career in the world of science. And I thank my little Leo for understanding that I have not always found the time to play with you in the last few years, but we will make up for it!

Abstract

This thesis opens with a critical review of the literature on radiolabelling small and biomolecules for tracking and monitoring. A novel concept of tritium labelling of antisense oligonucleotides *via* different conjugation agents was developed. It was demonstrated in *in vitro* and *in vivo* experiments that the conjugation of [³H]*N*-ethylmaleimide (NEM) to a thiol linker placed on an oligonucleotide has no impact on the pharmacokinetic (PK) behaviour compared to the unlabelled drug. A robust synthetic route was developed for a tritium-*O*-methylation of *N*-alkoxy maleimide derivatives that can be used as labelling reagents for biomolecules. In a 3-step synthesis, tritium-labelled maleimide derivatives were efficiently prepared that are significantly less volatile than NEM and therefore safer to handle in the laboratory with respect to radiation protection. Selective tritium labelling of neuromedin S (NMS) by derivatisation with [³H]*N*-succinimidylpropionate (NSP) was established. A functional ligand binding assay showed that labelling with NSP leads to a comparable result to unlabelled NMS, regardless of the degree of labelling and labelling position. With respect to antibody labelling, a functional *in vitro* assessment workflow for modified (fluorescently labelled or radiolabelled) antibodies was developed to predict the possible impact of labelling to protein properties or PK behaviour. Tritium-labelled therapeutic antibody was used in a biodistribution study of drug/anti-drug antibody (ADA) immune complexes (IC) to investigate the impact of IC formation on drug distribution. A high level of IC was found in the pancreas in female Wistar rats. Using multi-parameter optimisation, a morpholin-3-one derivative with an improved kinetic binding profile for imaging monoacylglycerol lipase (MAGL) in the central nervous system (CNS) was developed and successfully labelled with ¹¹C. The synthesis of eleven tetrazine (Tz) derivatives for CNS targeted imaging was described. Tzs were evaluated and classified for their properties as potential CNS radiotracers and click partners for bioorthogonal PET imaging based on several *in vitro* and *in vivo* experiments. These studies were predominantly performed with non-radioactive Tzs, but also included an *in vivo* biodistribution study with fluorine-18 labelled Tzs. Out of the eleven synthesised Tzs, two (Tz 1: 3-(4-methoxyphenyl)-6-methyl-1,2,4,5-tetrazine; Tz 2: *N*-[2-(2-fluoroethoxy)ethyl]-4-(6-methyl-1,2,4,5-tetrazin-3-yl)benzamide) were proposed for labelling as the most promising candidates that showed the best properties in terms of brain penetration and stability. Tz 1 was successfully tritium labelled and investigated for antibody-based *in vivo* CNS imaging. Although evaluation of a pretargeting approach using a TCO-conjugated BrainShuttle antibody and tritium-labelled Tz showed an *ex vivo* click response, *in vivo* conjugation has been unsuccessful. The isotopes ³H, ¹¹C, and ¹⁸F have been incorporated in biologically relevant ligands for tracking and monitoring.

Contents

Acknowledgements	III
Abstract	IV
Contents	V
Abbreviations	VI
Chapter One	1
Introduction and review of literature on the labelling of small and biomolecules for tracking and monitoring	
Chapter Two	32
Tritium labeling of antisense oligonucleotides <i>via</i> different conjugation agents	
Chapter Three	60
Tritium <i>O</i> -methylation of <i>N</i> -alkoxy maleimide derivatives as labeling reagents for biomolecules	
Chapter Four	74
Tritium-labelling of neuromedin S by conjugation with [³ H] <i>N</i> -succinimidyl propionate	
Chapter Five	96
Functional <i>in vitro</i> assessment of modified antibodies: Impact of label to protein properties	
Chapter Six	120
Biodistribution of drug/ADA complexes: the impact of immune complex formation on antibody distribution	
Chapter Seven	138
Multi-parameter optimization: development of a morpholin-3-one derivative with an improved kinetic profile for imaging monoacylglycerol lipase in the brain	
Chapter Eight	174
Synthesis of radiolabeled tetrazine derivatives for pretargeted imaging within the central nervous system	
Chapter Nine	212
Antibody-based <i>in vivo</i> imaging of central nervous system targets – Evaluation of a pretargeting approach utilizing a TCO-conjugated BrainShuttle antibody and radiolabeled tetrazines	
Chapter Ten	236
Conclusions	
APPENDIX	242
Abstracts of Invited Talks and Poster Presentations	

Abbreviations

%ID/g	Percentage of injected dose per gram tissue weight
°C	Celsius
µg	Microgramme
µL	Microliter
µm	Micrometre
µmol	Micromole
2-AG	2-Arachidonoyl-glycerol
3R	Replacement, reduction, and refinement
AAALAC	American Association for the Accreditation of Laboratory Animal Care
ABPP	Activity-based protein profiling
AD	Alzheimer's disease
ADA	Anti-drug antibody
ADME	Absorption, distribution, metabolism, and excretion
AIF	All-ion fragmentation
AMS	Accelerator mass spectrometry
ASAGPR	Asialoglycoprotein receptor
ASO	Antisense oligonucleotide
A _{xxx}	Absorbance at wavelength of xxx nm
Aβ	Amyloid beta
BBB	Blood-brain barrier
BEC	Brain-endothelial cell
BFC	Bifunctional chelating agent
Boc	<i>tert</i> -Butoxycarbonyl
BS	Brain Shuttle
BTC	Bis(trichloromethyl)carbonate (Triphosgene)
CDR	Complementary-determining region
Ci	Curie
CL	Clearance
CNS	Central nervous system
CPM	Counts per minutes
CRC	Concentration response curve
CT	Computed tomography
d	Day(s)
Da	Dalton
DCM	Dichloromethan
DIPEA	<i>N,N</i> -Diisopropylethylamine
DMSO	Dimethylsulfoxide
DNA	Deoxyribonucleic acid
DoL	Degree of label
DTT	Dithiothreitol
EC ₅₀	Half maximal effect concentration
EDTA	Ethylenediaminetetraacetic acid

ELISA	Enzyme-linked immunosorbent assay
EMA	European Medicines Agency
eq	Equivalent
ER	Efflux ratio
ESI	Electrospray ionisation
EtOH	Ethanol
FAAH	Fatty acid amide hydrolase
Fab	Fragment antigen-binding
FACS	Fluorescence-activated cell sorting
Fc	Fragment crystallisable
FcRn	Neonatal FC receptor
Fc- γ R	Fc-gamma receptor
FDA	Food and Drug Administration
FDG	Fluorodesoxyglucose
FLIPR	Fluorometric imaging plate reader
g	Gramme
GalNAc	<i>N</i> -Acetylgalactosamine
GCPR	G-Protein-coupled receptor
h	Hour(s)
HBD	Hydrogen bond donor
HEPES	4-(2-Hydroxyethyl)piperazine-1-ethanesulfonic acid
HFIP	Hexafluoro-2-propanol
HMW	High-molecular weight
HPLC	High-performance liquid chromatography
hr	Hour (only in chapter six)
HRMS	High-resolution mass spectrometry
HSCIE	High-temperature solid-state catalytic isotope exchange
HTE	Hydrogen/tritium exchange
Hz	Hertz
IC	Immune complexe
IC ₅₀	Half maximal inhibitory concentration
IEDDA	Inverse-electron-demand Diels-Alder
IgG	Immunoglobulin G
k _{bi}	Bimolecular reaction kinetic rate
K _d	Dissociation constant
keV	Kilo-electronvolt
kg	Kilogramme
K _i	Inhibition constant
KO	Knock out
k _{off}	Dissociation rate constant
k _{on}	Association rate constant
LC	Liquid chromatography
LDS	Lithium dodecyl sulfate
LGIC	Ligand-gated ion channel

LNA	Locked nucleic acid
LSC	Liquid scintillation counting
M	Molar
mAb	Monoclonal antibody
MAGL	Monoacylglycerol lipase
Malat1	Metastasis associated lung adenocarcinoma transcript 1
MAO-A, -B	Monoamine oxidase-A, -B
MBq	Megabecquerel
mCi	Millicurie
MDR1	Multidrug resistance protein 1
MeOH	Methanol
MES	2-(<i>N</i> -Morpholino)ethansulfonic acid
mg	Milligramme
MHC	Major histocompatibility complex
min	Minute(s)
mL	Milliliter
mM	Millimolar
mm	Millimeter
MPO	Multi parameter optimisation
MRI	Magnetic resonance imaging
mRNA	Messenger ribonucleic acid
MS	Mass spectrometry
MW	Molecular weight
MWCO	Molecular weight cut-off
NADP	Nicotinamide-adenine dinucleotide phosphate
NEM	<i>N</i> -Ethylmaleimide
ng	Nanogramme
NHP	Non-human primate
NHS	<i>N</i> -Hydroxysuccinimide ester
nm	Nanometre
nM	Nanomolar
NMM	<i>N</i> -Methylmaleimide
nmol	Nanomole
NMR	Nuclear magnetic resonance
NMS	Neuromedin S
NMU	Neuromedin U
NMUR ₂	Neuromedin U receptor 2
NSP	<i>N</i> -succinimidyl-3-propionate
PAMPA	Parallel artificial membrane permeability assay
PBS	Phosphate buffered saline
PD	Parkinson's disease
pEC ₅₀	Negative logarithm of EC ₅₀ value
PET	Positron emission tomography
PG	Prostaglandin

P-gp	P-glycoprotein
pH	Potential of hydrogen
pI	Isoelectric point
pIC ₅₀	Negative logarithm of pIC ₅₀ value
PK	Pharmacokinetic
pM	Picomolar
ppm	Parts per million
PSL	Photo-stimulated luminescence
QWBA	Quantitative whole-body autoradiography
RCP	Radiochemical purity
RIT	Radioimmunotherapy
RNA	Ribonucleic acid
rpm	Rounds per minutes
RT	Reaction time
SAX	Strong-anion exchange
SCN	Isothiocyanate; suprachiasmatic nucleus
SDS-PAGE	Sodium dodecyl sulfate–polyacrylamide gel electrophoresis
SEC	Size-exclusion chromatography
SPE	Solid-phase extraction
SPECT	Single-photon emission computed tomography
SPR	Surface plasmon resonance
SRM	Selected reaction monitoring
t _R	Relative retention time
t _{1/2}	Half-life
T _{1/2}	Terminal half-life
TAC	Time activity curve
TBq	Terabecquerel
TCEP	Tris(2-carboxyethyl) phosphine
TCO	<i>trans</i> -Cyclooctene
TEA	Triethylamine
TfR	Transferrin receptor
THF	Tetrahydrofuran
TIC	Total ion chromatogram
TLC	Thin-layer chromatography
TMS	Tetramethylsilane
TPSA	Topological polar surface area
Tris	Tris(hydroxymethyl)aminomethane
TSPO	Tryptophan-rich sensory protein
Tz	Tetrazine
UPLC	Ultra-performance liquid chromatography
UV	Ultraviolet
WT	Wild type
y	Year(s)

Chapter One


Introduction and review of literature on the labelling of small and biomolecules for tracking and monitoring

Aims and Objectives

The aims of this thesis are to develop and synthesise radiolabelling approaches of small and large molecules with a focus on novel therapeutic modalities, such as oligonucleotides, peptides, and proteins. In the ideal case, the label as well as the labelling process should have no influence on the biological properties compared to the native compounds. To verify this, the modified compounds are characterised in chemico-physical, subcellular, or cellular assays related to target affinity, physico-chemical properties, pharmacology, or pharmacokinetics. Finally, radiolabelled compound will be applied in animal experiments to gain insights in target binding, biotransformation, or biodistribution. The results will provide a valuable contribution in the development and application of new radiotracers and therefore enable a benefit for the patient, for example in the field of neurodegenerative diseases. The aims will be met through ten objectives, divided into Chapters:

- 1 Focused and critical review of the literature on radiolabelling of compounds from different modalities for tracking and monitoring.
- 2 Tritium-labelling of oligonucleotides and their assessment with respect to *in vivo* behaviour.
- 3 Synthesis of tritium-labelled maleimide derivatives for a general application of conjugations on biomolecules.
- 4 Tritium-labelling and characterisation of the peptide neuromedin S.
- 5 Labelling of proteins and its consequences with respect to their pharmacokinetic behaviour.
- 6 Monitoring of drug/anti-drug antibody immune complexes using tritium-labelled antibodies.
- 7 Development of brain-MAGL PET-tracers to monitoring new inhibitors from preclinical research.
- 8 Synthesis of radiolabelled tetrazine derivatives for bioorthogonal click reactions in the central nervous system.
- 9 Monitoring misfolded proteins in the central nervous system using radiolabelled tetrazines and a modified antibody.
- 10 Conclusions of the findings from the objectives, highlighting the successful achievement of the aims.

In this thesis, new radioactive labelling methods for small and biomolecules with beta emitters are described. Radiolabelling of small molecules has been the subject of intense research over the past few decades, and novel concepts for introducing radionuclides continue to be reported regularly. These established labelling approaches have limited applicability for nucleic acid-based drugs, therapeutic antibodies, or peptides, which are typical of the molecules now being investigated as novel therapeutic modalities. These target molecules are usually larger (significantly >1 kDa), mostly multiply charged, and often poorly soluble in organic solvents. However, in preclinical research they often require radiolabelling in order to track and monitor drug candidates in metabolism, biotransformation, or pharmacokinetic studies. Consequently, there is a need for new radiolabelling concepts for molecules of new modalities.

This declaration concerns the article entitled:			
Labelling small and biomolecules for tracking and monitoring			
Publication status (tick one)			
Draft manuscript	<input type="checkbox"/>	Submitted	<input type="checkbox"/>
In review	<input type="checkbox"/>	Accepted	<input type="checkbox"/>
		Published	<input checked="" type="checkbox"/>
Publication details (reference)	Edelmann MR. (2022) <i>RSC Adv.</i> 12 :32383-32400		
Copyright status (tick the appropriate statement)			
I hold the copyright for this material	<input checked="" type="checkbox"/>	Copyright is retained by the publisher, but I have been given permission to replicate the material here	<input type="checkbox"/>
Candidate's contribution to the paper (provide details, and also indicate as a percentage)	<p>The candidate contributed to / considerably contributed to / predominantly executed the...</p> <p>Formulation of ideas: 100%</p> <p>Design of methodology: 100%</p> <p>Experimental work: n/a</p> <p>Presentation of data in journal format: 100%</p>		
Statement from Candidate	This paper reports on original research I conducted during the period of my Higher Degree by Research candidature.		
Signed		Date	17.10.22

Introduction

When people hear of radioactivity, they immediately think of scientists like Marie Curie, Henri Becquerel, or Wilhelm Conrad Röntgen. Marie Curie's topic for her doctoral thesis¹ was inspired by new discoveries made by Becquerel and Röntgen. In December 1895, the German physicist Röntgen detected a type of rays that could penetrate solid wood or flesh and provide photographs of the bones of living people.² These mysterious rays were called X-ray by Röntgen, where X stands for unknown. Early in 1896, just a few months after Röntgen's detection, the French physicist Henri Becquerel had reported to the French Academy of Sciences that uranium compounds, even when kept in the dark, emitted rays that fogged a photographic plate.³ This was the beginning of radiographic imaging as we know it today from hospitals.⁴ These X-rays, together with gamma rays and electron beams, are also used in radiation therapy to treat cancer or kill malignant cells.⁵ This review is about radiolabelling molecules that are used for tracking and monitoring to study their biological and physicochemical behaviour.

Small molecules have been the dominant group of drugs since the early days of pharmaceutical development, but this is not a matter of course for the future. New therapeutic modalities are now filling the pipeline of the pharmaceutical industry. We need to expand the target space for targeting “undruggable” targets that are limited to reach with small molecules.⁶ New innovative biological modalities have emerged in the first two decades of the 21st century. Various formats of antibodies, bispecifics, antibody conjugates, peptides, modified RNA molecules such as antisense oligonucleotides (**Fig. 1**) are gaining popularity due to their potential to enter undruggable space.

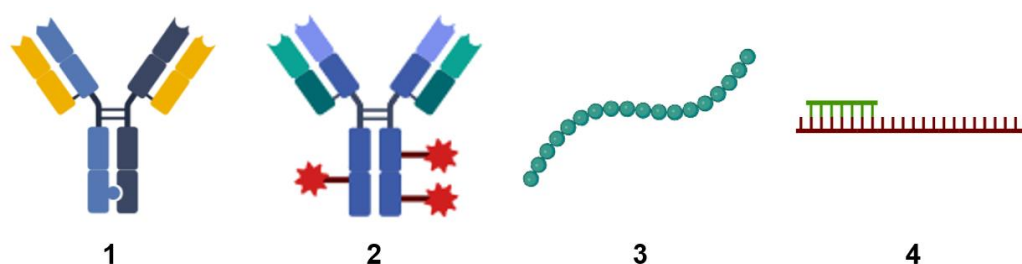


Fig. 1: Schematic sketches of **1:** bispecific antibody based on knobs-into-holes-technology;⁷ **2:** antibody conjugates. The red star symbolises payloads such as a small molecule, peptide, or oligonucleotide; **3:** peptide; **4:** antisense oligonucleotide in green with mRNA in red.

A major challenge with the novel modalities is the prediction of drug targeting, which together with solubility contributes to the ability of drugs and candidates to have overall exposure in the systemic circulation or tissue targeting like brain penetration.⁸ It is important to understand the fate of the potential drug candidate in humans and the relevance of the animal species used for preclinical toxicity and pharmacodynamic

studies. In preclinical research, biotransformation, metabolic identification, or binding studies are required in order to obtain information about the PK behaviour or the efficacy of the drug candidates. Although state-of-the-art high-resolution LC/MS techniques are commonly used for these studies, radiolabelled molecules are often required for quantification of metabolites, biodistribution, or to assess retention and excretion of all drug-related components. The classical approaches for radiolabelling small molecule drug candidates with long-lived radionuclide carbon-14 (^{14}C ; $t_{1/2}$: 5,730 y; molar activity: 2.3 GBq/mmol; 62.4 mCi/mmol) and tritium (^3H ; $t_{1/2}$: 12.3 y; molar activity: 984.2 MBq/mmol; 26.6 Ci/mmol) are limited for novel and complex modalities. ^{14}C -labelling is preferred for small molecule studies, but the molar activity is too low to be used for a corresponding study (in particular for imaging studies) with larger molecules (MW > 5,000 Da). In contrast, due to its more than 400-fold higher molar activity, tritium is better suited for radioactive labelling of large molecules in preclinical research.

In addition to the long-lived radionuclides, which are mainly used in the preclinical phase to characterise drug candidates, short-lived radionuclides such as ^{11}C ($t_{1/2}$: 20 min) and ^{18}F ($t_{1/2}$: 110 min), are widely used in diagnostic imaging studies. In this respect, functional imaging such as positron emission tomography (PET) or single-photon emission computed tomography (SPECT) has become essential for clinical decision-making in various areas of medicine.⁹⁻¹¹ Due to their short half-life, these molecules are not used to induce a therapeutic effect, but they bind to their target with fast kinetics for imaging or they can be tracked live in the body. While ^{11}C and ^{18}F are mainly important in research with small molecule, metallic radionuclides are found in novel modalities.

Of the commonly available radionuclides for PET imaging, ^{68}Ga ($t_{1/2}$: 68 min) is best suited for radiolabelling peptides, as the physical half-life is similar to the biological half-life of peptides, with a significant prevalence of ^{18}F and almost no ^{11}C -work reported in the literature.¹² An issue for these radionuclides is that they require the incorporation of synthetic functional groups into the native peptide. The two most common strategies for introducing the radionuclide into the peptide of choice use either bifunctional chelating agents (BFCs, **Fig. 2**) or prosthetic groups. Prosthetic groups are small, reactive entities that are first radiolabelled before being coupled to the peptide. BFCs are metal-binding chelators that are conjugated to the peptide of choice and subsequently complex a radioactive metal.

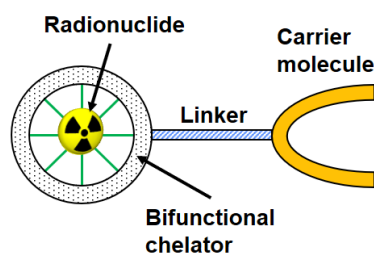


Fig. 2: Schematic illustration of a radionuclide complexing bifunctional chelator linked to a carrier molecule, e.g. oligonucleotide, peptide, antibody.

With regard to the radiolabelling of monoclonal antibodies (mAbs), ^{89}Zr ($t_{1/2}$: 78 h) and ^{64}Cu ($t_{1/2}$: 13 h) for PET or ^{111}In ($t_{1/2}$: 168 h) for SPECT are the most frequently mentioned radionuclides in the literature for diagnostic imaging of mAbs.^{13,14} Similar to peptide radiolabelling, synthetic modifications using chelating agents or by introduction of prosthetic groups are required.

Currently, $^{99\text{m}}\text{Tc}$ ($t_{1/2}$: 6 h) is used in most diagnostic SPECT-based imaging of nucleic acid-based medicines. In 2014, a direct labelling method with $^{99\text{m}}\text{Tc}$ was reported for the first time, in which the radionuclide was attached to the oligonucleotide without a chelator.¹⁵ Another method describes the indirect labelling of oligomers with $^{99\text{m}}\text{Tc}$, a labelling strategy similar to that for antibodies and peptides, by using BFCs conjugated *via* a linker to the oligonucleotide that binds the radiometal.¹⁶

Radionuclide Therapy

Another group of radiolabelled molecules are those that have a therapeutic effect. Of particular interest are radiotherapies using radionuclide-labelled peptides or antibodies, which make use of the therapeutic effect of ionising radiation in cancer therapy. Radioimmunotherapies (RIT) exploit an antibody as a carrier for radioactive isotopes to deliver a high radiation dose to a tumour.¹⁷⁻¹⁹ The choice of the optimal radionuclide for RIT depends both on its intended use and on practical considerations. From the plethora of existing radionuclides, the recently reported "Hopeful Eight" α -emitters²⁰ have aroused great interest in therapeutic applications: ^{225}Ac ($t_{1/2}$: 10 d), ^{211}At ($t_{1/2}$: 7 d), ^{212}Bi ($t_{1/2}$: 1 h), ^{213}Bi ($t_{1/2}$: 46 min), ^{212}Pb ($t_{1/2}$: 11 h), ^{223}Ra ($t_{1/2}$: 11 d), ^{146}Tb ($t_{1/2}$: 4 h), and ^{227}Th ($t_{1/2}$: 19 d). Each of these radionuclides has its own physical properties that hold promise for targeted alpha-therapy. Currently, ^{225}Ac appears to be the front-runner compared to other α -emitters. The interest in ^{225}Ac is also due to its half-life of 10 days which allows centralised production at the country level. ^{213}Bi was the first α -emitter to be clinically evaluated.^{21,22}

With respect to β -emitting radionuclides, ^{131}I ($t_{1/2}$: 8 d), ^{177}Lu ($t_{1/2}$: 7 d), and ^{90}Y ($t_{1/2}$: 3 d) are the most common in clinical RIT studies and represent the current standard in therapeutic beta-minus emitters.²³ ^{90}Y -Imbritumomab tiuxetan was the first radioimmunotherapy drug approved by the FDA in 2002 to treat B-cell non-Hodgkin lymphoma.²⁴ In 2018, Lutathera[®] was approved by the European Medicines Agency (EMA) as the first radiopharmaceutical peptide for radionuclide therapy.²⁵ Lutathera[®] uses the ionising radiation of ^{177}Lu for the treatment of gastroenteropancreatic neuroendocrine tumours.

Tritium-Labelled Oligonucleotides

Many disease targets are considered “undruggable” because they are located intracellularly or lack a specific binding pocket. Oligonucleotide therapeutics can precisely and efficiently modulate intracellular targets and they do not rely on the identification of a binding pocket, as is predominantly the case with small molecule-based therapeutics. The majority of oligonucleotide-based therapeutics address gene silencing,²⁶ although other strategies are also pursued, including splicing modulation and gene activation.²⁷ This expands the range of potential targets beyond what is typically accessible to traditional pharmaceutical modalities. As a result, an increasing number of nucleic acid-based therapeutics have been approved to treat or prevent diseases that previously could not be addressed.²⁸⁻³²

In preclinical research, radiolabelled drug candidates can provide a reliable quantitative tool for distribution, mass balance, metabolite profiling and identification studies. In the case of nucleic acid-based medicines, several aspects need to be considered for planning and execution of radiolabelling. Such considerations include the choice of radioisotope, the feasibility of the labelling methodology, and metabolic stability. However, to benefit from metabolite quantification by radiolabelling, the radiolabel must be confined to a specific position in the molecule. Random labelling in the oligonucleotide sequence, leading to multiple incorporation of radioisotopes, is a major disadvantage, as the molar activity of each metabolite is different depending on the number of radioisotopes remaining in its sequence, making structural analysis for quantification almost impossible.

Three isotopes (^3H , ^{14}C , ^{35}S) for radiolabelling of oligonucleotides are mainly discussed in the literature, and the most commonly used labelling positions with their isotopes are shown in **Fig. 3**.

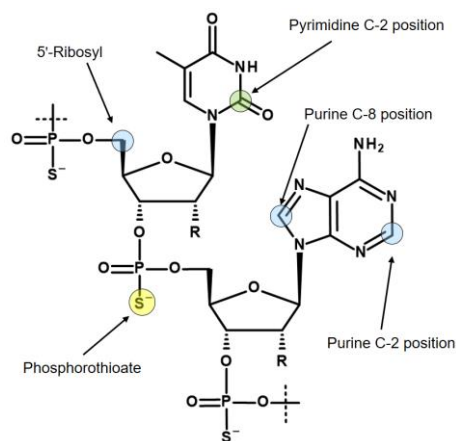


Fig. 3: Literature reported positions for radiolabelling of oligonucleotides in example of thymidine and adenosine. Colouring reflects the corresponding radioisotopes. Blue: ^3H ; green: ^{14}C ; yellow: ^{35}S .

Due to the relatively long terminal elimination half-life of oligonucleotides, in some cases 30–60 days or even longer,^{33,34} several properties of the most commonly used radioisotopes, ^3H , ^{14}C , and ^{35}S , need to be considered. The use of a ^{35}S label in the phosphorothioate backbone of drug candidates requires a timely study design due to the physical half-life of ^{35}S (87.5 d). Replication of a study with identical material is nearly impossible due to rapid isotopic decay.

As already mentioned, the molar activity of ^{14}C is the limiting factor for imaging of oligonucleotides. If a ^{14}C -based study requirement permits a low molar activity, for example using accelerator mass spectrometry or cavity-ring down spectroscopy for quantification,³⁵ then the ^{14}C -incorporation usually takes place in the C-2 position of pyrimidine bases.³⁶ However, in studies with ^{14}C -labelled oligonucleotides, it has been observed that pyrimidine bases account for a significant portion of metabolism, ultimately leading to loss of the label in the expired air as $^{14}\text{CO}_2$.³⁷

When a tritium atom is to be introduced into an oligonucleotide, the labelling position must be carefully considered. In the literature, three positions with different labelling methods are mainly described. Probably the easiest way to introduce a tritium atom into an oligonucleotide is a hydrogen/tritium exchange at the C-8 position of purine bases by using tritiated water without any catalyst.³⁸ Although the C-8 position of purines has long been known to pose a risk of tritium-hydrogen back-exchange by formation of tritiated water, particularly under alkaline conditions,³⁹ oligonucleotides are still tritiated using this approach.⁴⁰ Recently, a ruthenium nanoparticle catalyst was reported that allows hydrogen-tritium exchange at both the C-8 position of purines and the C-2 position.⁴¹ The C-2 position is significantly more stable to back-exchange. However, this labelling concept relies on randomised labelling, which, as mentioned earlier, makes a quantitative metabolic study almost impossible.

The most commonly used approach to tritium-labelled oligonucleotides, which consist of a phosphorothioate backbone, is based on a methodology that dates back to 1995 and is still state-of-the-art.⁴² The chemical approach requires a pre-synthesis of ³H-nucleoside phosphoramidite monomer by oxidation of the 5'-primary alcohol of ribose, followed by reduction with NaBT₄ to introduce a tritium atom at the 5'-carbon. Due to the instability of the ³H-nucleoside phosphoramidite caused by radiolysis, the monomer cannot be stored for the subsequent solid-phase synthesis, but has to be freshly prepared in a complex, multi-step synthesis. In addition, high molar activity cannot be achieved because the tritium-labelled nucleoside phosphoramidite must be diluted with non-radioactive monomer to avoid strong radiolysis. These issues lead to a high expenditure of time, a high level of radioactive waste, and thus to high costs. A different approach was reported by Ledoan and co-workers.⁴³ An amine-functionalised linker was placed terminally at the ASO-sequence for post-conjugation with [³H]succinimidyl propionate ([³H]NSP, **Fig. 4**).

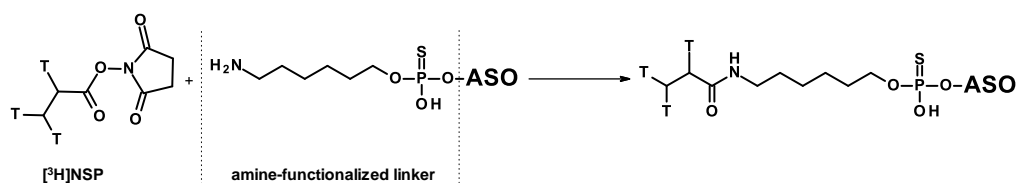


Fig. 4: General synthetic route to ASOs containing tritium labelled propionate functionalisation on C₆-amine linker.

Several aspects have to be taken into account: the stability of the label and, since the original chemical structure has been changed, the PK and pharmacodynamic behaviour should be compliant with that of the parent drug.

Synthesis of Tritium-labelled Maleimides for Bioconjugation

An alternative to NSP and amine linkers is a 1,4-Michael-type addition of a maleimide derivative, such as *N*-ethylmaleimide (NEM), to a thiol linker. However, bioconjugation with the corresponding [³H]NEM is challenging. Commercially available [³H]NEM is usually supplied in a pentane solution. For conjugations in aqueous buffer, a solvent exchange to a water-miscible solvent must be carried out beforehand. Due to the high volatility of NEM, solvent evaporation is not possible. This issue can be addressed using a silica gel-based cartridge. After removing the pentane, [³H]NEM can be eluted from the cartridge with e.g. DMSO. This solvent exchange process can lead to a loss of the radioactive NEM since syntheses with tritium-labelled compounds are usually on the microgram scale. A general disadvantage of NEM is that the tritium compound can only

be obtained in a complex, multi-stage synthesis in a molar activity range of 0.74 GBq/mmol-2.0 GBq/mmol (20-55 Ci/mmol). Tritium analogues with high molar activity (> 2.8 GBq/mmol; 75 Ci/mmol) are critical for accurate quantification in nanomolar ligand binding affinity studies as well as for imaging *in vivo* biodistribution by autoradiography. Thus, there is room for improvement in the development of tritiated maleimides for use in bioconjugation that exhibit low volatility and enable high molar activity.

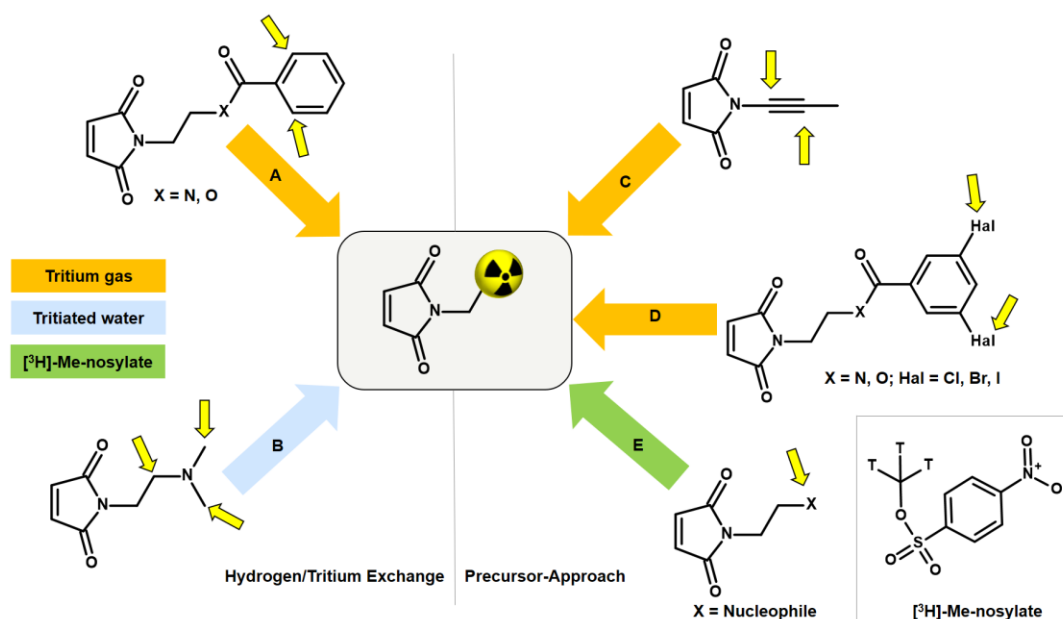


Fig. 5: Synthesis routes to tritium-labelled maleimide derivative. **A:** Metal-catalytic C-H activation followed by hydrogen/tritium exchange using tritium gas. **B:** Photoredox-mediated hydrogen/tritium exchange using tritiated water. **C:** Reduction of double/triple-bonds. **D:** Palladium-catalysed halogen/tritium exchange. **E:** Methylation on nucleophilic residue using [³H]methyl nosylate. Yellow arrows indicate possible labelling positions.

The incorporation of tritium into a maleimide derivative can be achieved by two general routes, namely by metal-catalysed hydrogen/tritium exchange (HTE) of the final compound or by the use of a precursor (**Fig. 5**). Metal-catalytic activation of aromatic C(sp²)-H for HTE using tritium gas requires directing groups such as ketones, sulfonic acids, carboxylic acids, or amides.⁴⁴⁻⁴⁷ The requirements for a successful HTE assume a "complex" molecular structure of the maleimide derivative. However, the modification of the tritium-labelled maleimide derivative should be minimal and the introduction of an additional catalyst-directing moiety containing functional groups that can form hydrogen bonds should be avoided in order to preserve the biological behaviour after conjugation with the oligonucleotide, and this limits the choice of a maleimide precursor. A recent method for HTE is based on photoredox-mediated hydrogen-atom transfer. Tritium can be installed in a single step using tritiated water as the source of ³H-targeting aliphatic-

amino C(sp³)-H bonds.⁴⁸ Studies have shown that maleimides containing amines in *N*-alkyl chains promote intramolecular base-catalysed hydrolysis, which results in ring opening.⁴⁹ Another approach to introduce tritium atoms into a molecule is based on the palladium-catalysed reduction of double/triple-bonds or halogen/tritium exchange using tritium gas. This is not possible with a maleimide derivative as the double bond of the maleimide core is also reduced and a subsequent conjugation to a thiol linker can no longer be carried out.⁵⁰ The introduction of a tritium-methyl group, for example using [³H]methyl nosylate, seems to be a successful approach as three tritium atoms are incorporated simultaneously into a maleimide derivative, resulting in a molar activity of > 2.8 GBq/mmol (75 Ci/mmol). Therefore, the maleimide precursor for tritium labelling has to meet the following properties: minimal modification at the *N*-moiety; few (better no) additional hydrogen bonds; no basic *N*-alkyl group; contain a target for S_N2-based methylation.

Peptide Labelling

Investigation of peptide receptors requires biologically active peptides containing fluorescent⁵¹ or radioactive labels. The radioactive labelling of peptides depends on the choice of isotope. In the case of ¹⁴C-labelling, ¹⁴C-containing amino acids are incorporated into the sequence *via* peptide synthesis.⁵² Due to the low molar activity of ¹⁴C-isotopes, this is a limitation for some studies, especially in imaging. Higher specific activities can be achieved by radioiodination. Depending on the physical and chemical properties of the different iodine isotopes, different synthetic routes are possible.⁵³ The most commonly used iodine isotopes with their half-life and applications are: ¹²³I (t_{1/2}: 13 h; SPECT), ¹²⁴I (t_{1/2}: 4 d; PET), ¹²⁵I (t_{1/2}: 59 d; SPECT, *in vitro* bioassays), ¹³¹I (t_{1/2}: 8 d; SPECT, radiotherapy). Radioiodination is generally performed on tyrosine (Tyr) or histidine (His) residues, in which an aromatic Tyr or His proton is replaced by the electrophilic radioiodine (I⁺). For this purpose, the radioiodide is generated from I⁻ *in situ* with an oxidising agent.^{54,55}

Peptides can also be labelled with metallic radionuclides in combination with bifunctional chelating agents. In the example of the approved peptide radiotherapeutic Lutathera[®], the same chelating agent was used to complex once with the diagnostic radionuclide ⁶⁸Ga and thereafter with the therapeutic ¹⁷⁷Lu. This has the advantage that with ⁶⁸Ga a tumour-imaging biomarker is available and in a further step with ¹⁷⁷Lu a therapeutic radiation dose can be delivered to the target tumour or metastasis.²⁵ These molecules, which have a close connection to diagnostics and also to related therapy, are sometimes termed theranostics. This personalised therapy could become a major

advantage in cancer treatment, and it is therefore to be expected that targeted radionuclide therapy will play a significant role in clinical nuclear medicine in the future.⁵⁶

Tritium-Labelled Peptides

Different synthetic routes are available for labelling peptides with tritium (**Fig. 6**). A novel labelling method based on photocatalytic HTE using T₂O as the tritium source was recently reported.⁵⁷ This is a promising approach to tritium labelling of peptides, as it allows fast access to radioactive peptides. However, so far only low molar activities (2-3 Ci/mmol) are achievable with this approach and there is still room for improvement. Significantly, higher specific activities can be achieved by solid-phase peptide synthesis using ³H-labelled amino acids from amino acid precursors. This is reported in the literature for smaller peptide sequences of only a few amino acids.⁵⁸ As an option for larger peptides, it is reported to incorporate the amino acid precursor into the sequence by solid phase synthesis. The most commonly used precursor amino acids are halogenated aromatic α -amino acids or synthetic- α -amino acids containing double or triple bonds. In the next step, the halogen is replaced by tritium by metal catalysis or the double/triple bond is reduced with tritium gas.⁵⁹

A stable precursor can also be obtained analogous to radioiodination with sodium iodide and an oxidising agent starting from the parent peptide, in which case the non-radioactive iodide (¹²⁷I) is used. The iodine on the Tyr residues can be catalytically exchanged in the presence of tritium gas to obtain the tritiated peptide.⁶⁰

Furthermore, radioactive labelling of a peptide by conjugating *N*-succinimidyl-[2,3-³H₃]-propionate ([³H]NSP) to accessible primary amines in the sequence is possible, which derivatises the peptide.^{61,62} These amines can be located at the *N*-terminus, at lysine residues, or they can be preceded by a lysine-like linker at the terminal guanidine nitrogen atom of arginine residues.⁶³ In this case, it must be taken into account that the chemical structure differs from the native peptide because of this derivatisation, which may result in changes in the biological and physicochemical properties, especially as Arg and Lys being basic and therefore protonated amino acid residues, may well play a significant role.

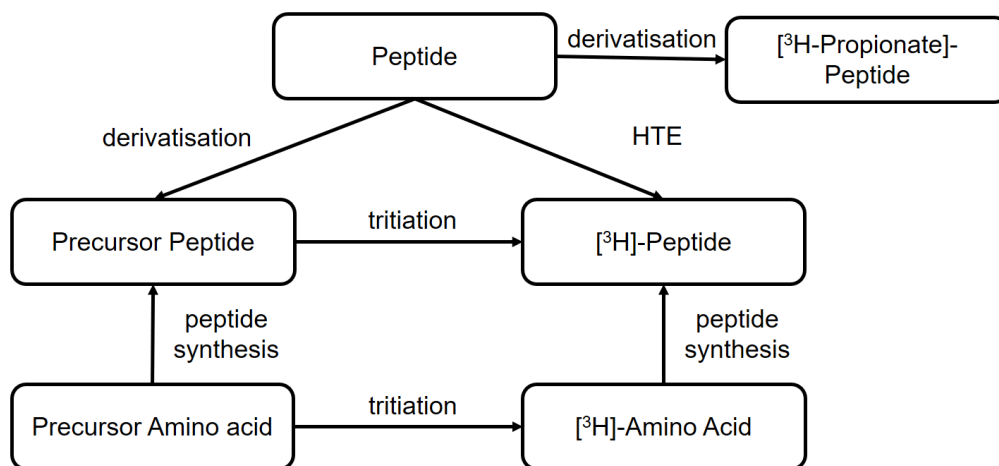


Fig. 6: Current synthetic routes to tritium-labelled peptides.

Labelling of Proteins and its consequences

Antibodies exhibit complex PK due to their large size, long circulating half-life, and immunogenic responses, making predictions about the distribution of monoclonal antibodies extremely difficult. Therefore, robust characterisation of the PK of novel next-generation antibodies, such as antibody-drug conjugates, bispecific antibodies, and other antibody constructs,⁶⁴⁻⁶⁶ in preclinical and clinical research can support the development of drug candidates. Conventional techniques for determining antibody PK include plasma clearance measurements using ELISA or LC-MS and tissue distribution using immunohistochemistry or immunofluorescence.⁶⁷ These bioanalytical methods, most of which require a labelled secondary antibody, are limited to ligand-binding assays. *In vivo* imaging or tracking of drug-related material at low concentrations is nearly impossible without a radioactive label.

Many different labelling concepts are reported in the literature. These include radiometals complexed with conjugated chelating agents,⁶⁸ labelling with radioactive iodine similar to peptide iodination,⁶⁹ or tritiation with an activated tritiated propionic acid.⁶¹ In addition, labelling with fluorescent dyes by post-modifying chemical syntheses on mAbs has been widely reported, as well as dual labelling of radionuclide and dye on antibodies.⁷⁰⁻⁷³

As with peptides, modifying a protein with a fluorescent or radioactive tag bears the risk of altering its biological behaviour. The degree of labelling, which corresponds to the number of labels per protein, can also change the biological properties of the antibody.⁷¹ It has also been shown that both the label as well as the labelling chemistry can influence binding to the neonatal Fc receptor (FcRn).⁷⁴ A lower affinity to FcRn results in a shorter half-life of the antibody. Modification of the framework with fluorescent dyes or chelators carrying carboxylic acid or sulfonic acid residues leads to a lower

isoelectric point (pI), mainly due to a more negative charge. Charge-mediated interactions may be associated with non-specific interactions with cell surfaces that trigger enhanced pinocytosis. Vascular endothelial cells are coated with highly negatively charged oligosaccharides such as heparan and heparin sulfates.⁷⁵ Excessive binding to these cell surface structures may increase the risk of pinocytotic uptake and consequently lead to more rapid proteolytic degradation. Non-specific binding to cell surfaces or extracellular matrix structures is considered to be one of the main factors for differences in the PK of antibodies.⁷⁶ Biodistribution experiments confirmed that the variant with a high pI was catabolised in the liver and spleen. These results indicate that antibody loading may have an effect on PK through changes in antibody catabolism independent of FcRn-mediated recycling.⁷⁷ There are only a few studies in the literature that compare different labelling methods with regard to their influence on PK or affinity properties.^{71,74,78-80} An *in vitro* assessment platform that allows predicting a change in biological behaviour after antibody modification using common labelling methods has not yet been reported. A chromatography-based platform should be able to detect changes in surface charges,⁸¹ affinity to FcRn, as well as high and low molecular weight impurities. A combination of size-exclusion chromatography (SEC), FcRn affinity, and heparin affinity chromatography can assess whether modification has affected protein properties. This would also avoid animal testing done with "damaged" labelled antibodies and thus corresponds to the 3R (replace, reduce, refine) principles. **Fig. 7** shows a proposed integrated quality assessment in a typical antibody labelling workflow.

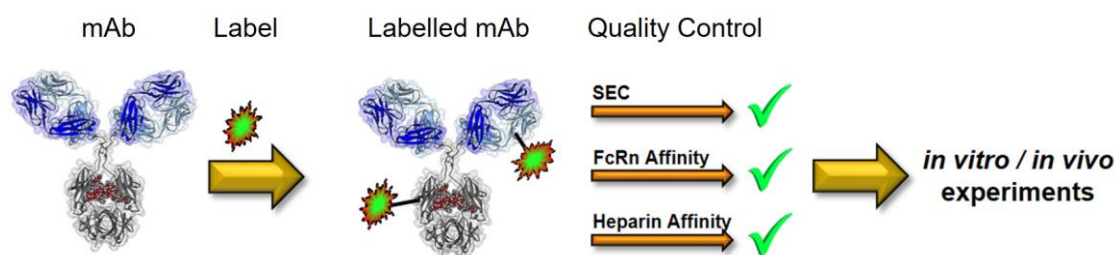


Fig. 7: Quality control has to be integrated into a typical labelling process for mAbs used in biological studies.

Monitoring of Drug/Anti-Drug Antibody Immune Complexes

The choice of radionuclides for labelling proteins depends on the research objective. In particular, for long-term investigations such as biodistribution, biotransformation⁸² or metabolite identification studies, short-lived radioisotopes are not suitable. In these cases, incorporation of the long-lived radionuclide tritium into the protein is preferred, as subsequent analyses can be carried out several times for quantification after the studies

without significant loss of radioactivity. In general, tritium labels offer excellent opportunities for monitoring PK behaviour of novel antibodies in preclinical research.

As previously mentioned, a critical aspect of antibody PK is the immunogenic response. It is known that all therapeutic antibodies, even those that are fully human, are immunogenic.⁸³ This means that they can trigger an immune response *via* an anti-drug antibody (ADA) and forming drug-ADA immune complexes (ICs). In this case, the therapeutic antibody can be considered as an antigen for the ADA. The ADA recognises the therapeutic mAb over a large area of its surface and binds to it through weak non-covalent interactions, such as electrostatic interactions, hydrogen bonds, van der Waals forces, and hydrophobic interactions. Depending on the mechanism of action as shown in **Fig. 8**, neutralising (binding to Fab region) or non-neutralising (binding to Fc domain), the presence of ICs can affect the concentration and function of the therapeutic antibody in the body, e.g. changing the biological effectiveness or even the safety profile.^{84,85} As a result, there may be reduced efficacy with neutralising ADAs or accelerated drug clearance with non-neutralising antibodies. Understanding the immunogenicity of biological therapies and how to manage them is important for the development of drug candidates.⁸⁶ Immunogenicity can be influenced by several factors, which can be clustered into three main categories: treatment-related, patient-related, and drug-property-related factors.⁸⁷ Many of these factors are not yet well understood. Furthermore, predicting an undesired immunogenicity of a therapeutic biomolecule is still difficult.

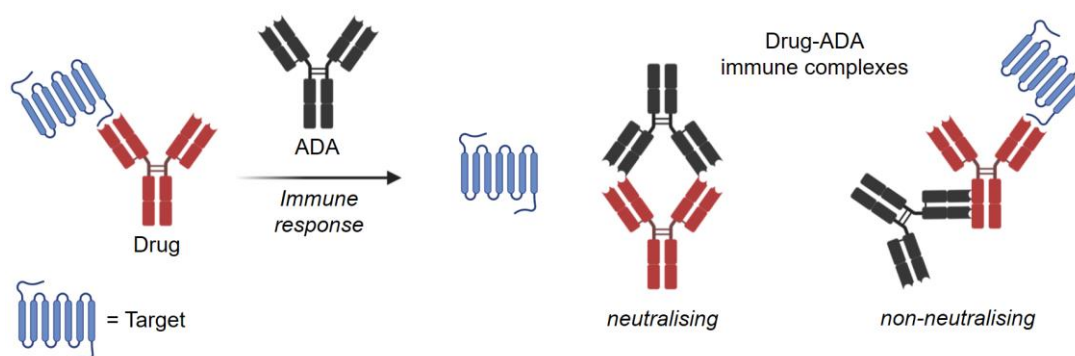


Fig. 8: Neutralising and non-neutralising Drug-ADA immune complexes.

Currently, several *in silico*, *in vitro*, and *in vivo* approaches have been reported to predict immunogenicity in the very early stages of drug development.⁸⁸⁻⁹⁰ However, it has not yet been possible to reconcile these predictions with the immunogenicity observed in clinical practice. In particular, no preclinical *in vivo* approach to predict immunogenicity has been able to correlate with the results of clinical therapy.^{91,92} Although the detailed interaction or formation between ADA and drug is understood⁹³ and according to the literature, large immune complexes degrade faster than smaller ICs,⁹⁴ quantitative

information on the exact size and structure of the immune complexes and their actual impact on drug PK is not yet available. Van Meer and co-workers accessed several market-registered mAbs to determine the relative immunogenicity of mAbs in non-human primates (NHPs) and humans. The results confirm that the ability to compare the relative immunogenicity of mAbs in NHPs and humans is low, with only 59% of cases.⁹⁵ Topp and co-workers have provided a comprehensive overview of the immunogenicity of therapeutic protein aggregates with a focus on immune mechanisms and their relationship to aggregate properties.⁹⁶ In conclusion, no preclinical *in vivo* approach to predict immunogenicity that correlates with outcomes of clinical therapy has been reported to date. This represents a gap to quantify the PK behaviour of immune complexes and consequently to be able to optimise the PK properties of therapeutic proteins that can influence the immune response. Therefore, the use of radiolabelled IC can provide a valuable contribution. In this way, the concentrations of ICs in different organs or tissues can be monitored, providing information about the biodistribution of the complexes by tracking or by imaging studies.

Positron Emission Tomography using Small Molecule Tracer

Standard imaging techniques such as X-ray, computed tomography (CT), and magnetic resonance imaging (MRI) allow healthy and diseased tissue to be visualised with great detail. However, certain diseases do not have structural anatomical abnormalities or only appear at later stages. Therefore, functional PET imaging can complement structural modalities to overcome some of the shortcomings. As an imaging technique based on positron-emitting molecules, PET is widely used in clinical diagnostics, quantification of pharmacological processes, and drug development.⁹⁷ A positron is the anti-particle of an electron and has all the properties of an electron except for the positive electric charge it possesses. Thus, a positron can be considered as an electron with a positive charge. A classical PET study uses small molecules in micromolar or nanomolar concentrations that have been labelled with short-lived positron-emitting isotopes such as ^{11}C ($t_{1/2}$: 20 min) and ^{18}F ($t_{1/2}$: 110 min). The development of molecular imaging approaches aimed at identifying pathologies in living patients is a very active area of research with the goal of distinguishing such disorders as early as possible and supporting the development of disease-modifying therapies. A PET tracer routinely used in the clinic represents the radiolabelled glucose analogue [^{18}F]fluorodeoxyglucose ([^{18}F]FDG), which has revolutionised the imaging assessment of a variety of diseases and cancer in particular. Almost all PET examinations are now carried out in combination with CT. PET-CT imaging with [^{18}F]FDG is now a common tool for diagnosis, initial

staging, assessment of response to therapy, radiotherapy planning, restaging, and prognosis for many cancer types.⁹⁸⁻¹⁰⁰

PET has also been able to provide unique and powerful insights into normal brain function as well as dysfunctions associated with various neurological disorders and diseases,¹⁰¹ focused on imaging six categories of brain proteins: G-protein coupled receptors (GPCR), membrane transporters, ligand-gated ion channels (LGIC), tryptophan-rich sensory proteins (TSPO), enzymes, and misfolded proteins.¹⁰² Small molecule-based positron-emitting inhibitors, which bind to the target molecule in the manner of receptor-ligand interaction, are often used as PET tracer for imaging and concentration assessment of brain-enzymes, such as monoamine oxidase A and B (MAO-A and MAO-B), acetylcholine esterase, fatty acid amide hydrolase (FAAH), or monoacylglycerol lipase (MAGL).

Monitoring of Brain-MAGL Inhibitors

MAGL is the major enzyme involved in the endocannabinoid 2-arachidonoylglycerol (2-AG) catabolism and has received significant attention as a therapeutic target for neurological disorders.^{103,104} The development of a PET radioligand with high target specificity for the preclinical and clinical characterisation of MAGL inhibitor drug candidates is therefore of great interest. However, a good drug candidate may not necessarily be a good candidate for CNS-PET imaging. While drug candidates with long target residence times and high metabolic stability foster therapeutic efficacy in treatment, PET tracer candidates with these properties can result in slow PK, which generally require longer scan times and this generates more variable outcome measurements.¹⁰⁵ The first set of five PET tracers for MAGL developed by Hicks *et al.* was published in 2014 and labelled with carbon-11.¹⁰⁶ These compounds have been reported to have moderate blood-brain barrier (BBB) penetration. The lack of MAGL-specific brain imaging led to the conclusion that none of the tracers was suitable for *in vivo* brain-MAGL quantification. The next generation of MAGL radioligands (**Fig. 9**) are mainly irreversible, like [¹¹C]SAR127303¹⁰⁷ as well as [¹¹C]PF-06809247¹⁰⁸ and [¹⁸F]PF-06795071¹⁰⁹ developed by Pfizer. However, irreversible PET tracers could hardly provide a comprehensive quantification of the drug-target interaction. Compared to irreversible MAGL radioligands,¹¹⁰ in which the formation of covalent bonds is a major contributor to binding, a reversible PET tracer probe requires additional moieties to interact non-covalently with residues of the binding site.¹¹¹ This usually leads to increased molecular weight and therefore adds several obstacles to crossing the BBB through active transport. To date, only a few radioligands have been described as reversible MAGL tracers. The reported examples [¹¹C]PAD and [¹⁸F]MAGL-4-11¹¹²

showed low brain uptake and were recognised by ATP-binding cassette (ABC) transporters expressed in the BBB. While their *in vivo* specificities were confirmed in peripheral MAGL-expressing organs, no specific interaction could be demonstrated in rat brain. [¹⁸F]T-401 and [¹⁸F]MAGL-2102 are recently reported reversible MAGL radioligands^{113,114} that showed specificity for CNS-MAGL *in vivo*. However, low to moderate brain uptake was observed for [¹⁸F]T-401 and a slow reversible binding mechanism was revealed for [¹⁸F]MAGL-2102. In summary, novel reversible MAGL-PET radioligands with improved brain uptake and suitable PK are highly desirable for clinical practice. These PET tracers would enable the development of new brain-MAGL inhibitors and monitor the effectiveness of the drugs.

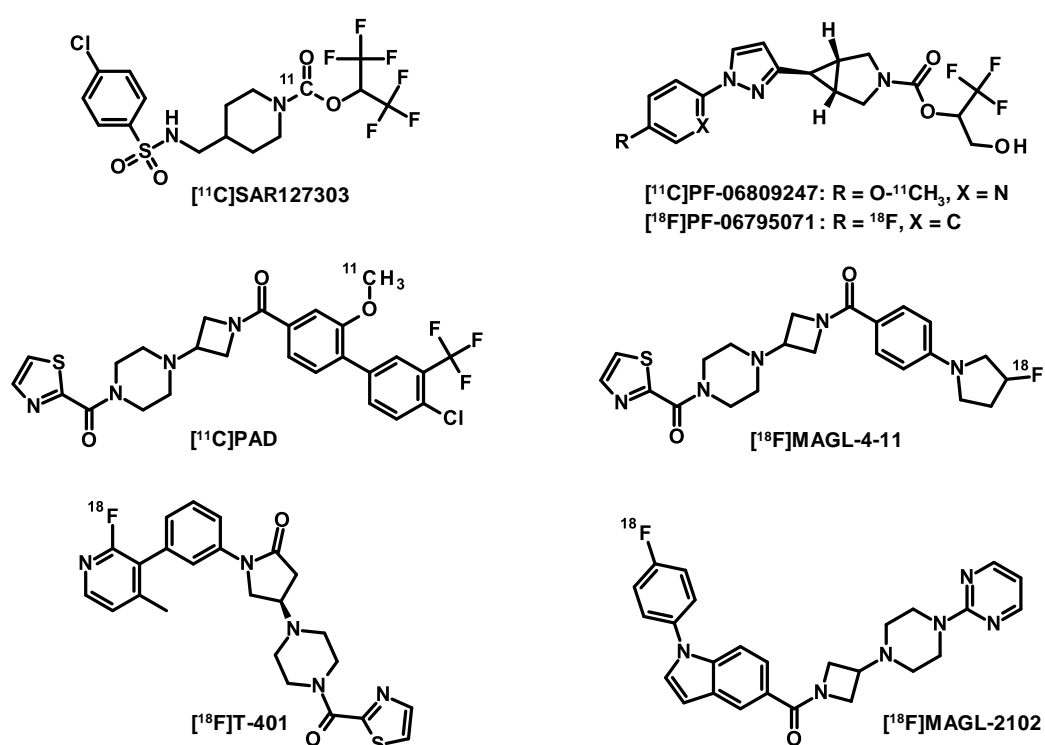


Fig. 9: Chemical structures of irreversible and reversible MAGL-PET tracers.

Synthesis of Tetrazines for Bioorthogonal Click-Reactions

Lang and Chin summarised in a paper the 20 most commonly reported bioorthogonal reactions, reactions that do not disrupt biological processes.¹¹⁵ The most attractive reaction for a bioorthogonal click reaction is currently the inverse electron-demand Diels-Alder (IEDDA) ligation between tetrazine (Tz) derivatives and *trans*-cyclooctene (TCO) functionalisations (**Fig. 10**).¹¹⁶

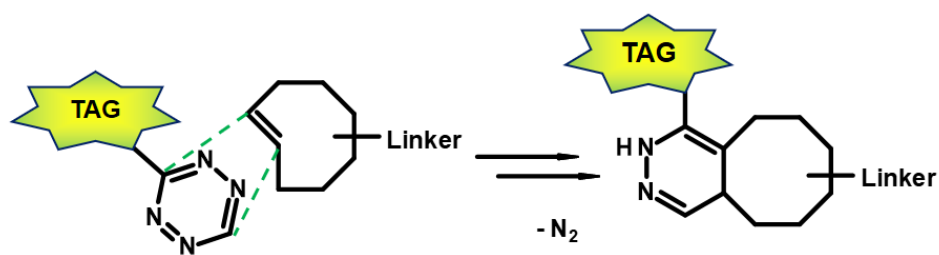


Fig. 10: Inverse electron-demand Diels-Alder ligation between a TCO linked to a carrier moiety and a tagged Tz derivative.

PET-nuclide labelled Tzs for the use of a bioorthogonal click reaction and pretargeted imaging can in principle be considered as small molecule PET tracers. In the case of Tzs, the target is not a receptor or enzyme, but a TCO-functionalised agent, such as antibodies,¹¹⁷ affibodies,¹¹⁸ or diabodies.¹¹⁹ A variety of Tzs have been developed for preclinical or diagnostic imaging. For this purpose, Tz derivatives were modified with fluorescent dyes¹²⁰ or chelators capable of complexing the corresponding PET radionuclides. ¹¹¹In and ⁶⁸Ga are given as common radionuclides for Tzs.¹²¹ A variant with ⁴⁴Sc ($t_{1/2}$: 4 h) was also developed to evaluate its application for pretargeting PET images.¹²² Currently, ¹¹C and ¹⁸F-labelled Tzs are predominantly reported, in which the PET nuclide is incorporated through a covalent bond rather than using a chelator.^{123,124} In a reverse approach, a TCO derivative is labelled with a PET nuclide and undergoes a click reaction with a Tz-modified counterpart.¹²⁵⁻¹²⁷ Although [¹⁸F]TCO can be considered a useful tracer for radiolabelling Tz-modified targeting molecules, studies indicate that its utility for *in vivo* chemistry and pretargeted imaging will be limited. [¹⁸F]TCO derivatives, while clearly reaching the brain, are rapidly metabolised with non-specific accumulation of radioactivity in brain and bone.¹²⁸

While a conventional PET tracer should bind to its target as quickly as possible, the challenge with the click-reaction approach is that the Tz should react with the TCO moiety as quickly as possible. A key factor in reaction rates is the chemical environment of the Tz. Fast IEDDA-reaction rates often come at the expense of probe stability.¹²⁹ In general, methyl-substituted Tzs showed the highest stability, but also had the lowest reaction kinetics. Electron-withdrawing substituents increase the click reactivity of Tzs with TCO, but these substituents also induce their decomposition. Electron-donating substituents show a higher stability, but also suffer from slow reaction kinetics (**Fig. 11**).¹³⁰

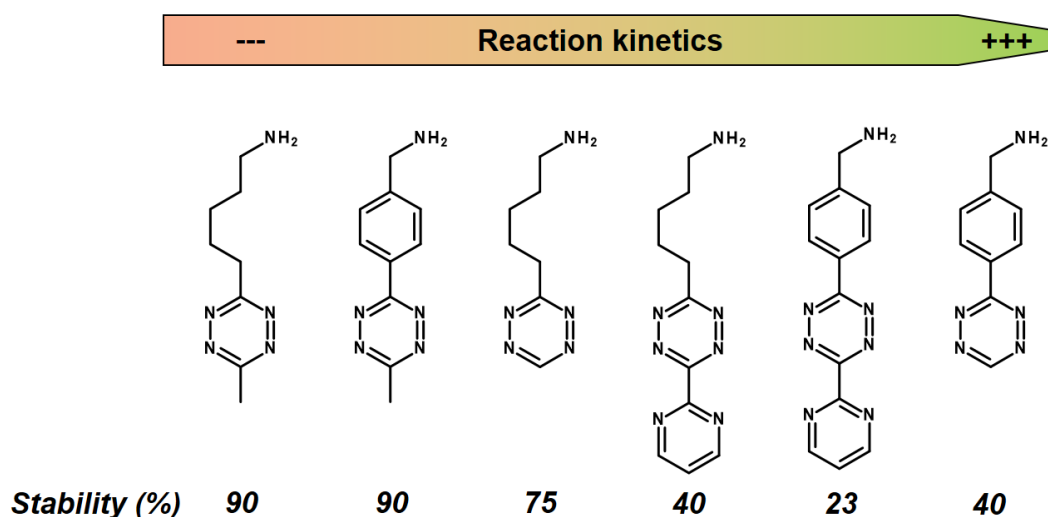


Fig. 11: Reaction kinetics from slow (left) to high (right) of selected Tzs with TCO in PBS at 37 °C and corresponding stability assessed in PBS at 37 °C for 10 h.

The challenge for effective labelling in *in vivo* systems is to achieve an optimal balance between reactivity and stability. It is of comparable complexity to deliver a radiolabelled Tz into the brain while maintaining its stability and reactivity. While there are many examples in the literature of an IEDDA click reaction in the periphery,^{122,131,132} there are only a few reports of Tzs penetrating the brain and serving as PET-nuclide carriers,¹²³ which represents a gap in nuclear medicine diagnostics of brain targets.

Monitoring of Misfolded Proteins

PET imaging of misfolded proteins, such as for amyloid- β ($A\beta$) plaques and tau fibrils in Alzheimer's disease (AD) or α -synuclein in Parkinson's disease (PD), is an extremely valuable neuroimaging tool and supports ongoing global efforts to better understand brain function.¹³³⁻¹³⁸ Although the use of small molecules as PET tracers for misfolded protein aggregates has been reported,^{134,139} the use of small molecules has some limitations. The pathological accumulation of misfolded proteins can vary in composition and isoform. In addition, the morphology of the protein construct changes between disease states.¹⁴⁰ Therefore, different binding sites can arise and the affinities of tracers can vary significantly between isoforms and morphologies of protein aggregates. Currently, no well-characterised, highly selective small molecule-based PET tracers are available for use in competitive binding studies that would allow the determination of $A\beta$, tau fibrils, or α -synuclein-specific signalling over the dynamic range of disease progression.

Instead of small molecules, monoclonal antibodies (mAbs) with their high specificity, high affinity, and serum stability can also be used for molecular imaging to

target radionuclides *in vivo* on protein aggregates of interest. Many studies have demonstrated the use of mAb-targeted imaging (Immuno-PET) for a variety of purposes, e.g., monitoring disease progressions and the effect on a therapeutic agent in pharmaceutical research and development.¹⁴¹⁻¹⁴⁴ Antibody-based radioligands have so far only been described for peripheral targets related to cancer diagnostics and theranostics, including some clinical applications.^{145,146} The main hurdle for an antibody-based radioligand to be delivered to the brain is the BBB. In 1994, it was demonstrated that only 0.1% of a peripherally administered immunoglobulin G (IgG) reaches the brain.¹⁴⁷ However, the BBB uses natural receptors expressed on brain endothelial cells (BECs) for active transport purposes. The transferrin receptor (TfR) has, due to its expression on the BBB, an interesting role as a BBB delivery receptor. A Brain Shuttle (BS) technology was developed to allow the delivery of mAbs with fully functional bivalent IgG antigen bindings, anti-brain target and anti-TfR.¹⁴⁸ This is achieved by fusing the BS module to the C-terminal part of the heavy chain (Fc) constant region. Therefore, these BS-antibodies could allow their use as PET radioligands within the CNS.¹⁴⁹

While antibodies allow prolonged circulation in the body due to their molecular size and structure, but even more due to their interaction with the neonatal Fc receptor, which protects IgGs from degradation,¹⁵⁰ this prolonged half-life is a limitation in molecular imaging due to higher background signals when using PET radionuclide-labelled mAbs. Compared to conventional imaging techniques in which a molecule is directly labelled with a radionuclide, the pretargeting approach offers an uncoupling of the PK half-life of the biological molecule of interest from the physical half-life of the radionuclide (**Fig. 12**).

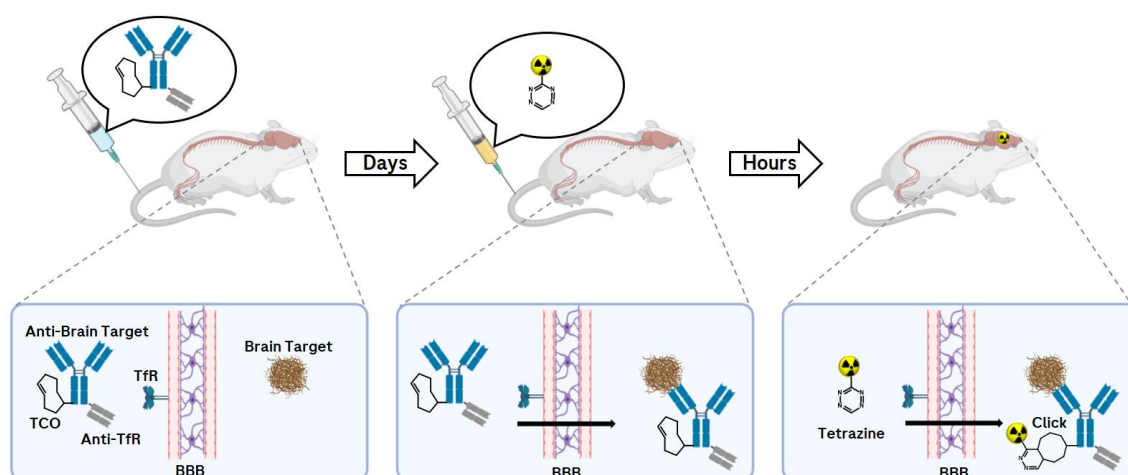


Fig. 12: Pretargeting workflow. In the first step, a BBB-penetrating TCO-modified antibody is injected. The mAb is actively transported across the BBB and binds to a target. In the second step, a PET nuclide-labelled Tz is injected and clicks with the TCO-mAb to generate PET-images of misfolded proteins.

The pretargeting approach allows an antibody to be prelocalised to a target before injecting after 1-3 days a small radiolabelled effector to recognise and specifically covalently bind to it *via* an *in vivo* click reaction.¹⁵¹ Applications are found, for example, in cancer imaging and targeted radionuclide therapy.¹⁵² So far, an *in vivo* bioorthogonal click reaction approach of a TCO-modified antibody with a PET nuclide-labelled Tz in the CNS has not been reported. The requirement for a successful click response is a brain-penetrating Tz that is stable and can react quickly with the pretargeted TCO-mAb. With this technique and the resulting imaging of misfolded proteins within the CNS, valuable information can be provided to accelerate drug development, monitor disease progression, and offer great benefit to patient care.

Conclusions

Radioactive labelling of molecules from novel modalities, such as oligonucleotides, peptides and antibodies, is often a major challenge. The established labelling methods used for small molecules have limited applicability for large, polar, highly charged molecules. The choice of radionuclide depends not only on the type of study, but also on molecular properties such as biological half-life, hydrodynamic radius, molecular surface charge, or target binding. This review provides an overview of current labelling methods for oligonucleotides, peptides and antibodies for use in tracking, monitoring, and imaging studies. In conclusion, there is an urgent need for new and efficient labelling concepts for molecules such as oligonucleotides, peptides, antibodies, and their characterisation in terms of a label impact on the molecular properties.

References

- (1) Wolke, R. L. (1988) Marie Curie's doctoral thesis: prelude to a Nobel Prize. *J. Chem. Educ.* 65, 561-573.
- (2) Röntgen, W. C. (1896) On a new kind of rays. *Science* 3, 227-231.
- (3) Becquerel, H. (1901) The radio-activity of matter. *Nature* 63, 396-398.
- (4) Carlton, R. R., Adler, A. M., and Balac, V. (2019) *Principles of radiographic imaging: an art and a science*, Cengage Learning.
- (5) Hendee, W. R., Ibbott, G. S., and Hendee, E. G. (2013) *Radiation therapy physics*, John Wiley & Sons.
- (6) Scannell, J. W., Blanckley, A., Boldon, H., and Warrington, B. (2012) Diagnosing the decline in pharmaceutical R&D efficiency. *Nat. Rev. Drug Discov.* 11, 191-200.
- (7) Klein, C., Schaefer, W., and Regula, J. T. (2016) The use of CrossMAb technology for the generation of bi- and multispecific antibodies. *MAbs* 8, 1010-1020.
- (8) Caron, G., and Ermondi, G. (2016) Molecular descriptors for polarity: the need for going beyond polar surface area. *Future Med. Chem.* 8, 2013-2016.

- (9) Wei, W., Ehlerding, E. B., Lan, X., Luo, Q., and Cai, W. (2018) PET and SPECT imaging of melanoma: the state of the art. *Eur. J. Nucl. Med. Mol. Imaging* 45, 132-150.
- (10) Valotassiou, V., Malamitsi, J., Papatriantafyllou, J., Dardiotis, E., Tsougos, I., Psimadas, D., Alexiou, S., Hadjigeorgiou, G., and Georgoulas, P. (2018) SPECT and PET imaging in Alzheimer's disease. *Ann. Nucl. Med.* 32, 583-593.
- (11) Vandenberghe, S., Moskal, P., and Karp, J. S. (2020) State of the art in total body PET. *EJNMMI Phys.* 7, 1-33.
- (12) Jackson, I. M., Scott, P. J., and Thompson, S. (2017) Clinical applications of radiolabeled peptides for PET. *Semin. Nucl. Med.* 47, 493-523.
- (13) Heskamp, S., Raavé, R., Boerman, O., Rijpkema, M., Goncalves, V., and Denat, F. (2017) ⁸⁹Zr-immuno-positron emission tomography in oncology: state-of-the-art ⁸⁹Zr radiochemistry. *Bioconjug. Chem.* 28, 2211-2223.
- (14) Mosley, M., Torres, J. B., Allen, D., and Cornelissen, B. (2020) Immuno-imaging of ICAM-1 in tumours by SPECT. *Nucl. Med. Biol.* 84, 73-79.
- (15) Correa, C. R., de Barros, A. L. B., de Aguiar Ferreira, C., de Goes, A. M., Cardoso, V. N., and de Andrade, A. S. R. (2014) Aptamers directly radiolabeled with technetium-99m as a potential agent capable of identifying carcinoembryonic antigen (CEA) in tumor cells T84. *Bioorg. Med. Chem. Lett.* 24, 1998-2001.
- (16) Liu, Y., Liu, G., and Hnatowich, D. J. (2010) A brief review of chelators for radiolabeling oligomers. *Materials* 3, 3204-3217.
- (17) Larson, S. M., Carrasquillo, J. A., Cheung, N.-K. V., and Press, O. W. (2015) Radioimmunotherapy of human tumours. *Nat. Rev. Cancer* 15, 347-360.
- (18) Vallabhajosula, S., Nikolopoulou, A., S Jhanwar, Y., Kaur, G., T Tagawa, S., M Nanus, D., H Bander, N., and J Goldsmith, S. (2016) Radioimmunotherapy of metastatic prostate cancer with; ¹⁷⁷Lu-DOTAhuJ591 anti prostate specific membrane antigen specific monoclonal antibody. *Curr. Radiopharm.* 9, 44-53.
- (19) Allen, K. J., Jiao, R., Malo, M. E., Frank, C., Fisher, D. R., Rickles, D., and Dadachova, E. (2019) Comparative radioimmunotherapy of experimental melanoma with novel humanized antibody to melanin labeled with ²¹³Bismuth and ¹⁷⁷Lutetium. *Pharmaceutics* 11, 348.
- (20) Eychenne, R., Chérel, M., Haddad, F., Guérard, F., and Gestin, J.-F. (2021) Overview of the most promising radionuclides for targeted alpha therapy: The "hopeful eight". *Pharmaceutics* 13, 906.
- (21) Poty, S., Francesconi, L. C., McDevitt, M. R., Morris, M. J., and Lewis, J. S. (2018) α -Emitters for radiotherapy: from basic radiochemistry to clinical studies—part 1. *J. Nucl. Med.* 59, 878-884.
- (22) Poty, S., Francesconi, L. C., McDevitt, M. R., Morris, M. J., and Lewis, J. S. (2018) α -emitters for radiotherapy: from basic radiochemistry to clinical studies—part 2. *J. Nucl. Med.* 59, 1020-1027.
- (23) Sgouros, G., Bodei, L., McDevitt, M. R., and Nedrow, J. R. (2020) Radiopharmaceutical therapy in cancer: clinical advances and challenges. *Nat. Rev. Drug. Discov.* 19, 589-608.
- (24) Witzig, T. E. (2004) Yttrium-90-ibritumomab tiuxetan radioimmunotherapy: a new treatment approach for B-cell non-Hodgkin's lymphoma. *Drugs Today* 40, 111-120.
- (25) Hennrich, U., and Kopka, K. (2019) Lutathera®: the first FDA-and EMA-approved radiopharmaceutical for peptide receptor radionuclide therapy. *Pharmaceutics* 12, 114.
- (26) Kay, C., Skotte, N., Southwell, A., and Hayden, M. (2014) Personalized gene silencing therapeutics for Huntington disease. *Clin. Genet.* 86, 29-36.
- (27) Rinaldi, C., and Wood, M. J. (2018) Antisense oligonucleotides: the next frontier for treatment of neurological disorders. *Nat. Rev. Neurol.* 14, 9-21.
- (28) Crooke, S. T., Witzum, J. L., Bennett, C. F., and Baker, B. F. (2018) RNA-targeted therapeutics. *Cell Metab.* 27, 714-739.

- (29) Khvorova, A., and Watts, J. K. (2017) The chemical evolution of oligonucleotide therapies of clinical utility. *Nat. Biotechnol.* **35**, 238-248.
- (30) Roberts, T. C., Langer, R., and Wood, M. J. (2020) Advances in oligonucleotide drug delivery. *Nat. Rev. Drug. Discov.* **19**, 673-694.
- (31) Blagbrough, I. S., and Zara, C. (2009) Animal models for target diseases in gene therapy-using DNA and siRNA delivery strategies. *Pharm. Res.* **26**, 1-18.
- (32) Blagbrough, I. S., and Metwally, A. A. (2013) Chapter 7: siRNA and Gene Formulation for Efficient Gene Therapy, in *Gene Therapy-Tools and Potential Applications* (Molina, F. M., Ed.) pp 135-173, IntechOpen.
- (33) Geary, R. S., Baker, B. F., and Crooke, S. T. (2015) Clinical and preclinical pharmacokinetics and pharmacodynamics of mipomersen (Kynamro®): a second-generation antisense oligonucleotide inhibitor of apolipoprotein B. *Clin Pharmacokinet* **54**, 133-146.
- (34) Kilanowska, A., and Studzińska, S. (2020) In vivo and in vitro studies of antisense oligonucleotides—a review. *RSC Adv.* **10**, 34501-34516.
- (35) Kratochwil, N. A., Dueker, S. R., Muri, D., Senn, C., Yoon, H., Yu, B.-Y., Lee, G.-H., Dong, F., and Otteneder, M. B. (2018) Nanotracing and cavity-ring down spectroscopy: A new ultrasensitive approach in large molecule drug disposition studies. *PLoS One* **13**, e0205435.
- (36) Crooke, S. T., Grillone, L. R., Tendolkar, A., Garrett, A., Fratkin, M. J., Leeds, J., and Barr, W. H. (1994) A pharmacokinetic evaluation of ¹⁴C-labeled afovirsen sodium in patients with genital warts. *Clin. Pharmacol. Ther.* **56**, 641-646.
- (37) Levin, A. A. (1999) A review of issues in the pharmacokinetics and toxicology of phosphorothioate antisense oligonucleotides. *Biochim. Biophys. Acta* **1489**, 69-84.
- (38) Liu, Y., Tseng, Y.-c., and Huang, L. (2012) Biodistribution studies of nanoparticles using fluorescence imaging: a qualitative or quantitative method? *Pharm. Res.* **29**, 3273-3277.
- (39) Shelton, K. R., and Clark Jr, J. M. (1967) A proton exchange between purines and water and its application to biochemistry. *Biochemistry* **6**, 2735-2739.
- (40) Wang, H., and Guo, P. (2021) Radiolabeled RNA nanoparticles for highly specific targeting and efficient tumor accumulation with favorable in vivo biodistribution. *Mol. Pharm.* **18**, 2924-2934.
- (41) Palazzolo, A., Feuillastre, S., Pfeifer, V., Garcia-Argote, S., Bouzouita, D., Tricard, S., Chollet, C., Marcon, E., Buisson, D. A., Cholet, S., Fenaille, F., Lippens, G., Chaudret, B., and Pieters, G. (2019) Efficient access to deuterated and tritiated nucleobase pharmaceuticals and oligonucleotides using hydrogen-isotope exchange. *Angew. Chem.* **131**, 4945-4949.
- (42) Tan, W., Iyer, R. P., Yu, D., and Agrawal, S. (1995) Site-specific synthesis of [³H] oligonucleotides in high specific activity through direct solid-phase redox chemistry. *Tetrahedron Lett.* **36**, 3631-3634.
- (43) Ledoan, T., Auger, R., Benjihad, A., and Tenu, J.-P. (1999) High specific radioactivity labeling of oligonucleotides with ³H-succinimidyl propionate. *Nucleosides Nucleotides Nucleic Acids* **18**, 277-289.
- (44) Atzrodt, J., Derdau, V., Kerr, W. J., and Reid, M. (2018) C– H functionalisation for hydrogen isotope exchange. *Angew. Chem. Int. Ed.* **57**, 3022-3047.
- (45) Valero, M., Becker, D., Jess, K., Weck, R., Atzrodt, J., Bannenberg, T., Derdau, V., and Tamm, M. (2019) Directed iridium-catalyzed hydrogen isotope exchange reactions of phenylacetic acid esters and amides. *Chem. Eur. J.* **25**, 6517-6522.
- (46) Valero, M., Weck, R., Güssregen, S., Atzrodt, J., and Derdau, V. (2018) Highly selective directed iridium-catalyzed hydrogen isotope exchange reactions of aliphatic amides. *Angew. Chem. Int. Ed.* **57**, 8159-8163.
- (47) Kerr, W. J., Mudd, R. J., Owens, P. K., Reid, M., Brown, J. A., and Campos, S. (2016) Hydrogen isotope exchange with highly active iridium (I) NHC/phosphine complexes: a comparative counterion study. *J. Label. Compds. Radiopharm.* **59**, 601-603.

- (48) Loh, Y. Y., Nagao, K., Hoover, A. J., Hesk, D., Rivera, N. R., Colletti, S. L., Davies, I. W., and MacMillan, D. W. (2017) Photoredox-catalyzed deuteration and tritiation of pharmaceutical compounds. *Science* 358, 1182-1187.
- (49) Ravasco, J. M., Faustino, H., Trindade, A., and Gois, P. M. (2019) Bioconjugation with maleimides: A useful tool for chemical biology. *Chem. Eur. J.* 25, 43-59.
- (50) Krivec, M., Gazvoda, M., Kranjc, K., Polanc, S., and Kocevar, M. (2012) A way to avoid using precious metals: the application of high-surface activated carbon for the synthesis of isoindoles via the Diels-Alder reaction of 2H-pyran-2-ones. *J. Org. Chem.* 77, 2857-64.
- (51) Ast, J., Arvaniti, A., Fine, N. H., Nasteska, D., Ashford, F. B., Stamataki, Z., Koszegi, Z., Bacon, A., Jones, B. J., and Lucey, M. A. (2020) Super-resolution microscopy compatible fluorescent probes reveal endogenous glucagon-like peptide-1 receptor distribution and dynamics. *Nat. Commun.* 11, 1-18.
- (52) Dell'isola, A., Brown, R. T., Jones, S., Kitson, S. L., Moody, T. S., Syvret, J., Upeandran, B., and Watters, W. H. (2019) Synthesis of carbon-14-labelled peptides. *J. Label. Compd. Radiopharm.* 62, 713-717.
- (53) Oliveira, M. C., and Correia, J. D. (2019) Biomedical applications of radioiodinated peptides. *Eur. J. Med. Chem.* 179, 56-77.
- (54) Doll, S., Woolum, K., and Kumar, K. (2016) Radiolabeling of a cyclic RGD (cyclo Arg-Gly-Asp-d-Tyr-Lys) peptide using sodium hypochlorite as an oxidizing agent. *J. Label. Compds. Radiopharm.* 59, 462-466.
- (55) Vaidyanathan, G., and Zalutsky, M. R. (2019) The Radiopharmaceutical Chemistry of the Radioisotopes of Iodine, in *Radiopharmaceutical chemistry* (Lewis, J., Windhorst, A., and Zeglis, B., Eds.) pp 391-408, Springer, Cham.
- (56) Langbein, T., Weber, W. A., and Eiber, M. (2019) Future of theranostics: an outlook on precision oncology in nuclear medicine. *J. Nucl. Med.* 60, 13S-19S.
- (57) Legros, F., Fernandez-Rodriguez, P., Mishra, A., Weck, R., Bauer, A., Sandvoss, M., Ruf, S., Méndez, M., Mora-Radó, H., and Rackelmann, N. (2020) Photoredox-mediated hydrogen isotope exchange reactions of amino-acids, peptides, and peptide-derived drugs. *Chem. Eur. J.* 26, 12738-12742.
- (58) Egan, J. A., and Filer, C. N. (2016) High specific activity tritium labelling of biologically active small peptides and a related analogue. *J. Radioanal. Nucl. Chem.* 307, 549-553.
- (59) Jazayeri, A., Rappas, M., Brown, A. J., Kean, J., Errey, J. C., Robertson, N. J., Fiez-Vandal, C., Andrews, S. P., Congreve, M., and Bortolato, A. (2017) Crystal structure of the GLP-1 receptor bound to a peptide agonist. *Nature* 546, 254-258.
- (60) De Prins, A., Martin, C., Van Wanseele, Y., Skov, L. J., Tömböly, C., Tourwé, D., Caveliers, V., Van Eeckhaut, A., Holst, B., and Rosenkilde, M. M. (2018) Development of potent and proteolytically stable human neuromedin U receptor agonists. *Eur. J. Med. Chem.* 144, 887-897.
- (61) Wang, M., Zhan, Y., O'Neil, S. P., Harris, S., Henson, C., McEwen, A., Webster, R., and O'Hara, D. M. (2018) Quantitative biodistribution of biotherapeutics at whole body, organ and cellular levels by autoradiography. *Bioanalysis* 10, 1487-1500.
- (62) Jacquot, G., Lecorché, P., Malcor, J.-D., Laurencin, M., Smirnova, M., Varini, K., Malicet, C., Gassiot, F., Abouzid, K., and Faucon, A. (2016) Optimization and in vivo validation of peptide vectors targeting the LDL receptor. *Mol. Pharm.* 13, 4094-4105.
- (63) Keller, M., Kuhn, K. K., Einsiedel, J., Hübner, H., Biselli, S., Mollereau, C., Wifling, D., Svobodova, J., Bernhardt, G., and Cabrele, C. (2016) Mimicking of arginine by functionalized N ω -carbamoylated arginine as a new broadly applicable approach to labeled bioactive peptides: high affinity angiotensin, neuropeptide Y, neuropeptide FF, and neurotensin receptor ligands as examples. *J. Med. Chem.* 59, 1925-1945.
- (64) Dickopf, S., Georges, G. J., and Brinkmann, U. (2020) Format and geometries matter: Structure-based design defines the functionality of bispecific antibodies. *Comput. Struct. Biotechnol. J.* 18, 1221-1227.

- (65) Georges, G. J., Dengl, S., Bujotzek, A., Hesse, F., Fischer, J. A., Gärtner, A., Benz, J., Lauer, M. E., Ringler, P., and Stahlberg, H. (2020) The Contorsbody, an antibody format for agonism: Design, structure, and function. *Comput. Struct. Biotechnol. J.* *18*, 1210-1220.
- (66) Dengl, S., Mayer, K., Bormann, F., Duerr, H., Hoffmann, E., Nussbaum, B., Tischler, M., Wagner, M., Kuglstatter, A., and Leibrock, L. (2020) Format chain exchange (FORCE) for high-throughput generation of bispecific antibodies in combinatorial binder-format matrices. *Nat. Commun.* *11*, 1-11.
- (67) Im, K., Mareninov, S., Diaz, M., and Yong, W. H. (2019) An introduction to performing immunofluorescence staining, in *Biobanking* (Yong, W. H., Ed.) pp 299-311, Humana Press, New York.
- (68) England, C. G., Jiang, D., Ehlerding, E. B., Rekoske, B. T., Ellison, P. A., Hernandez, R., Barnhart, T. E., McNeel, D. G., Huang, P., and Cai, W. (2018) ⁸⁹Zr-labeled nivolumab for imaging of T-cell infiltration in a humanized murine model of lung cancer. *Eur. J. Nucl. Med. Mol. Imaging* *45*, 110-120.
- (69) Chen, N., Wang, W., Fauty, S., Fang, Y., Hamuro, L., Hussain, A., and Prueksaritanont, T. (2014) The effect of the neonatal Fc receptor on human IgG biodistribution in mice. *MAbs* *6*, 502-508.
- (70) Saccomano, M., Dullin, C., Alves, F., and Napp, J. (2016) Preclinical evaluation of near-infrared (NIR) fluorescently labeled Cetuximab as a potential tool for fluorescence-guided surgery. *Int. J. Cancer* *139*, 2277-2289.
- (71) Cilliers, C., Nessler, I., Christodolu, N., and Thurber, G. M. (2017) Tracking antibody distribution with near-infrared fluorescent dyes: impact of dye structure and degree of labeling on plasma clearance. *Mol. Pharm.* *14*, 1623-1633.
- (72) Lütje, S., Rijpkema, M., Franssen, G. M., Fracasso, G., Helfrich, W., Eek, A., Oyen, W. J., Colombatti, M., and Boerman, O. C. (2014) Dual-modality image-guided surgery of prostate cancer with a radiolabeled fluorescent anti-PSMA monoclonal antibody. *J. Nucl. Med.* *55*, 995-1001.
- (73) Lee, H. J., Ehlerding, E. B., Jiang, D., Barnhart, T. E., Cao, T., Wei, W., Ferreira, C. A., Huang, P., Engle, J. W., and Cai, W. (2019) Dual-labeled pertuzumab for multimodality image-guided ovarian tumor resection. *Am. J. Cancer Res.* *9*, 1454.
- (74) Edelmann, M. R., Kettenberger, H., Knaupp, A., Schlothauer, T., and Otteneder, M. B. (2019) Radiolabeled IgG antibodies: Impact of various labels on neonatal Fc receptor binding. *J. Label. Compds. Radiopharm.* *62*, 751-757.
- (75) Bernfield, M., Götte, M., Park, P. W., Reizes, O., Fitzgerald, M. L., Lincecum, J., and Zako, M. (1999) Functions of cell surface heparan sulfate proteoglycans. *Annu. Rev. Biochem.* *68*, 729-777.
- (76) Datta-Mannan, A., Lu, J., Witcher, D. R., Leung, D., Tang, Y., and Wroblewski, V. J. (2015) The interplay of non-specific binding, target-mediated clearance and FcRn interactions on the pharmacokinetics of humanized antibodies. *MAbs* *7*, 1084-1093.
- (77) Li, B., Tesar, D., Boswell, C. A., Cahaya, H. S., Wong, A., Zhang, J., Meng, Y. G., Eigenbrot, C., Pantua, H., and Diao, J. (2014) Framework selection can influence pharmacokinetics of a humanized therapeutic antibody through differences in molecule charge. *MAbs* *6*, 1255-1264.
- (78) Chen, J., Wang, M., Joyce, A., DeFranco, D., Kavosi, M., Xu, X., and O'Hara, D. M. (2014) Comparison of succinimidyl [¹²⁵I] iodobenzoate with iodogen iodination methods to study pharmacokinetics and ADME of biotherapeutics. *Pharm. Res.* *31*, 2810-2821.
- (79) Szabó, Á., Szendi-Szatmári, T., Ujlaky-Nagy, L., Rádi, I., Vereb, G., Szöllösi, J., and Nagy, P. (2018) The effect of fluorophore conjugation on antibody affinity and the photophysical properties of dyes. *Biophys. J.* *114*, 688-700.
- (80) Vira, S., Mekhedov, E., Humphrey, G., and Blank, P. S. (2010) Fluorescent-labeled antibodies: Balancing functionality and degree of labeling. *Anal. Biochem.* *402*, 146-50.

- (81) Kraft, T. E., Richter, W. F., Emrich, T., Knaupp, A., Schuster, M., Wolfert, A., and Kettenberger, H. (2020) Heparin chromatography as an in vitro predictor for antibody clearance rate through pinocytosis. *MAbs* 12, # 1683432.
- (82) Schadt, S., Hauri, S., Lopes, F., Edelmann, M. R., Staack, R. F., Villaseñor, R., Kettenberger, H., Roth, A. B., Schuler, F., and Richter, W. F. (2019) Are biotransformation studies of therapeutic proteins needed? Scientific considerations and technical challenges. *Drug Metab. Dispos.* 47, 1443-1456.
- (83) Krishna, M., and Nadler, S. G. (2016) Immunogenicity to biotherapeutics—the role of anti-drug immune complexes. *Front. Immunol.* 7, 21.
- (84) Boehncke, W.-H., and Brembilla, N. C. (2018) Immunogenicity of biologic therapies: causes and consequences. *Expert Rev. Clin. Immunol.* 14, 513-523.
- (85) Pratt, K. P. (2018) Anti-drug antibodies: emerging approaches to predict, reduce or reverse biotherapeutic immunogenicity. *Antibodies* 7, 19.
- (86) Gunn, G. R., Sealey, D. C., Jamali, F., Meibohm, B., Ghosh, S., and Shankar, G. (2016) From the bench to clinical practice: understanding the challenges and uncertainties in immunogenicity testing for biopharmaceuticals. *Clin. Exp. Immunol.* 184, 137-146.
- (87) Pineda, C., Castañeda Hernández, G., Jacobs, I. A., Alvarez, D. F., and Carini, C. (2016) Assessing the immunogenicity of biopharmaceuticals. *BioDrugs* 30, 195-206.
- (88) Wadhwa, M., Knezevic, I., Kang, H.-N., and Thorpe, R. (2015) Immunogenicity assessment of biotherapeutic products: an overview of assays and their utility. *Biologicals* 43, 298-306.
- (89) Salazar-Fontana, L. I., Desai, D. D., Khan, T. A., Pillutla, R. C., Prior, S., Ramakrishnan, R., Schneider, J., and Joseph, A. (2017) Approaches to mitigate the unwanted immunogenicity of therapeutic proteins during drug development. *AAPS J* 19, 377-385.
- (90) Groell, F., Jordan, O., and Borchard, G. (2018) In vitro models for immunogenicity prediction of therapeutic proteins. *Eur. J. Pharm. Biopharm.* 130, 128-142.
- (91) Gokemeijer, J., Jawa, V., and Mitra-Kaushik, S. (2017) How close are we to profiling immunogenicity risk using in silico algorithms and in vitro methods?: an industry perspective. *AAPS J* 19, 1587-1592.
- (92) Shankar, G. (2019) Current challenges in assessing immunogenicity. *Bioanalysis* 11, 1543-1546.
- (93) Hoffmann, E., Jordan, G., Lauer, M., Ringler, P., Kuszniir, E. A., Rufer, A. C., Huber, S., Jochner, A., Winter, G., and Staack, R. F. (2019) Generation, characterization, and quantitative bioanalysis of drug/anti-drug antibody immune complexes to facilitate dedicated in vivo studies. *Pharm. Res.* 36, 1-15.
- (94) Rojko, J. L., Evans, M. G., Price, S. A., Han, B., Waine, G., DeWitte, M., Haynes, J., Freimark, B., Martin, P., and Raymond, J. T. (2014) Formation, clearance, deposition, pathogenicity, and identification of biopharmaceutical-related immune complexes: review and case studies. *Toxicol. Pathol.* 42, 725-764.
- (95) Van Meer, P. J., Kooijman, M., Brinks, V., Gispen-de Wied, C. C., Silva-Lima, B., Moors, E. H., and Schellekens, H. (2013) Immunogenicity of mAbs in non-human primates during nonclinical safety assessment. *MAbs* 5, 810-816.
- (96) Moussa, E. M., Panchal, J. P., Moorthy, B. S., Blum, J. S., Joubert, M. K., Narhi, L. O., and Topp, E. M. (2016) Immunogenicity of therapeutic protein aggregates. *J. Pharm. Sci.* 105, 417-430.
- (97) Luzi, F., Gee, A. D., and Bongarzone, S. (2021) Silicon compounds in carbon-11 radiochemistry: present use and future perspectives. *Org. Biomol. Chem.* 19, 6916-6925.
- (98) Groheux, D., Cochet, A., Humbert, O., Alberini, J.-L., Hindié, E., and Mankoff, D. (2016) ¹⁸F-FDG PET/CT for staging and restaging of breast cancer. *J. Nucl. Med.* 57, 17S-26S.
- (99) Kitajima, K., Nakajo, M., Kaida, H., Minamimoto, R., Hirata, K., Tsurusaki, M., Doi, H., Ueno, Y., Sofue, K., and Tamaki, Y. (2017) Present and future roles of

- FDG-PET/CT imaging in the management of gastrointestinal cancer: an update. *Nagoya J. Med. Sci.* 79, 527.
- (100) Sheikhabaei, S., Mena, E., Yanamadala, A., Reddy, S., Solnes, L. B., Wachsmann, J., and Subramaniam, R. M. (2017) The value of FDG PET/CT in treatment response assessment, follow-up, and surveillance of lung cancer. *Am. J. Roentgenol.* 208, 420-433.
 - (101) Montagne, A., Nation, D. A., Pa, J., Sweeney, M. D., Toga, A. W., and Zlokovic, B. V. (2016) Brain imaging of neurovascular dysfunction in Alzheimer's disease. *Acta Neuropathol.* 131, 687-707.
 - (102) Gunn, R. N., Slifstein, M., Searle, G. E., and Price, J. C. (2015) Quantitative imaging of protein targets in the human brain with PET. *Phys. Med. Biol.* 60, R363.
 - (103) Kinsey, S. G., and Lichtman, A. H. (2019) The Endogenous Cannabinoid System: A Cadre of Potential Therapeutic Targets, in *Cannabis Use Disorders* pp 21-29, Springer.
 - (104) Granchi, C., Caligiuri, I., Minutolo, F., Rizzolio, F., and Tuccinardi, T. (2017) A patent review of Monoacylglycerol Lipase (MAGL) inhibitors (2013-2017). *Expert Opin. Ther. Pat.* 27, 1341-1351.
 - (105) McCluskey, S. P., Plisson, C., Rabiner, E. A., and Howes, O. (2020) Advances in CNS PET: the state-of-the-art for new imaging targets for pathophysiology and drug development. *Eur. J. Nucl. Med. Mol. Imaging* 47, 451-489.
 - (106) Hicks, J. W., Parkes, J., Tong, J., Houle, S., Vasdev, N., and Wilson, A. A. (2014) Radiosynthesis and ex vivo evaluation of [¹¹C-carbonyl] carbamate-and urea-based monoacylglycerol lipase inhibitors. *Nucl. Med. Biol.* 41, 688-694.
 - (107) Wang, L., Mori, W., Cheng, R., Yui, J., Hatori, A., Ma, L., Zhang, Y., Rotstein, B. H., Fujinaga, M., and Shimoda, Y. (2016) Synthesis and preclinical evaluation of sulfonamido-based [¹¹C-carbonyl]-carbamates and ureas for imaging monoacylglycerol lipase. *Theranostics* 6, 1145.
 - (108) Zhang, L., Butler, C. R., Maresca, K. P., Takano, A., Nag, S., Jia, Z., Arakawa, R., Piro, J. R., Samad, T., and Smith, D. L. (2019) Identification and development of an irreversible monoacylglycerol lipase (MAGL) positron emission tomography (PET) radioligand with high specificity. *J. Med. Chem.* 62, 8532-8543.
 - (109) Chen, Z., Mori, W., Fu, H., Schafroth, M. A., Hatori, A., Shao, T., Zhang, G., Van, R. S., Zhang, Y., and Hu, K. (2019) Design, synthesis, and evaluation of ¹⁸F-labeled monoacylglycerol lipase inhibitors as novel positron emission tomography probes. *J. Med. Chem.* 62, 8866-8872.
 - (110) McAllister, L. A., Butler, C. R., Mente, S., O'Neil, S. V., Fonseca, K. R., Piro, J. R., Cianfrogna, J. A., Foley, T. L., Gilbert, A. M., and Harris, A. R. (2018) Discovery of trifluoromethyl glycol carbamates as potent and selective covalent monoacylglycerol lipase (MAGL) inhibitors for treatment of neuroinflammation. *J. Med. Chem.* 61, 3008-3026.
 - (111) Aida, J., Fushimi, M., Kusumoto, T., Sugiyama, H., Arimura, N., Ikeda, S., Sasaki, M., Sogabe, S., Aoyama, K., and Koike, T. (2018) Design, synthesis, and evaluation of piperazinyl pyrrolidin-2-ones as a novel series of reversible monoacylglycerol lipase inhibitors. *J. Med. Chem.* 61, 9205-9217.
 - (112) Chen, Z., Mori, W., Deng, X., Cheng, R., Ogasawara, D., Zhang, G., Schafroth, M. A., Dahl, K., Fu, H., Hatori, A., Shao, T., Zhang, Y., Yamasaki, T., Zhang, X., Rong, J., Yu, Q., Hu, K., Fujinaga, M., Xie, L., Kumata, K., Gou, Y., Chen, J., Gu, S., Bao, L., Wang, L., Collier, T. L., Vasdev, N., Shao, Y., Ma, J.-A., Cravatt, B. F., Fowler, C., and Josephson, L. (2019) Design, synthesis, and evaluation of reversible and irreversible monoacylglycerol lipase positron emission tomography (PET) tracers using a "tail switching" strategy on a piperazinyl azetidone skeleton. *J. Med. Chem.* 62, 3336-3353.
 - (113) Hattori, Y., Aoyama, K., Maeda, J., Arimura, N., Takahashi, Y., Sasaki, M., Fujinaga, M., Seki, C., Nagai, Y., and Kawamura, K. (2019) Design, synthesis, and evaluation of (4 R)-1-{3-[2-(¹⁸F) fluoro-4-methylpyridin-3-yl] phenyl}-4-[4-(1, 3-thiazol-2-ylcarbonyl) piperazin-1-yl] pyrrolidin-2-one ([¹⁸F] T-401) as a novel


- positron-emission tomography imaging agent for monoacylglycerol lipase. *J. Med. Chem.* **62**, 2362-2375.
- (114) Rong, J., Mori, W., Xia, X., Schafroth, M. A., Zhao, C., Van, R. S., Yamasaki, T., Chen, J., Xiao, Z., and Haider, A. (2021) Novel reversible-binding PET ligands for imaging monoacylglycerol lipase based on the piperaziny azetidine scaffold. *J. Med. Chem.* **64**, 14283-14298.
- (115) Lang, K., and Chin, J. W. (2014) Bioorthogonal reactions for labeling proteins. *ACS Chem. Biol.* **1**, 16-20.
- (116) Wu, H., and Devaraj, N. K. (2016) Inverse Electron-Demand Diels–Alder Bioorthogonal Reactions, in *Cycloadditions in Bioorthogonal Chemistry. Topics in Current Chemistry Collections*. (Vrabel, M., and Carell, T., Eds.) pp 109-130, Springer Nature, Switzerland.
- (117) Shah, M. A., Zhang, X., Rossin, R., Robillard, M. S., Fisher, D. R., Bueltmann, T., Hoeben, F. J., and Quinn, T. P. (2017) Metal-free cycloaddition chemistry driven pretargeted radioimmunotherapy using α -particle radiation. *Bioconjug. Chem.* **28**, 3007-3015.
- (118) Altai, M., Perols, A., Tsourma, M., Mitran, B., Honarvar, H., Robillard, M., Rossin, R., Ten Hoeve, W., Lubberink, M., and Orlova, A. (2016) Feasibility of affibody-based bioorthogonal chemistry-mediated radionuclide pretargeting. *J. Nucl. Med.* **57**, 431-436.
- (119) van Duijnhoven, S. M., Rossin, R., van den Bosch, S. M., Wheatcroft, M. P., Hudson, P. J., and Robillard, M. S. (2015) Diabody pretargeting with click chemistry in vivo. *J. Nucl. Med.* **56**, 1422-1428.
- (120) Beliu, G., Kurz, A. J., Kuhlemann, A. C., Behringer-Pliess, L., Meub, M., Wolf, N., Seibel, J., Shi, Z.-D., Schnermann, M., and Grimm, J. B. (2019) Bioorthogonal labeling with tetrazine-dyes for super-resolution microscopy. *Commun. Biol.* **2**, 1-13.
- (121) Edem, P. E., Jørgensen, J. T., Nørregaard, K., Rossin, R., Yazdani, A., Valliant, J. F., Robillard, M., Herth, M. M., and Kjaer, A. (2020) Evaluation of a ^{68}Ga -labeled DOTA-tetrazine as a PET alternative to ^{111}In -SPECT pretargeted imaging. *Molecules* **25**, 463.
- (122) Edem, P. E., Sinnes, J.-P., Pektor, S., Bausbacher, N., Rossin, R., Yazdani, A., Miederer, M., Kjær, A., Valliant, J. F., and Robillard, M. S. (2019) Evaluation of the inverse electron demand Diels-Alder reaction in rats using a scandium-44-labelled tetrazine for pretargeted PET imaging. *EJNMMI Res.* **9**, 1-8.
- (123) Stéen, E. J. L., Jørgensen, J. T., Petersen, I. N., Nørregaard, K., Lehel, S., Shalgunov, V., Birke, A., Edem, P. E., L'Estrade, E. T., and Hansen, H. D. (2019) Improved radiosynthesis and preliminary in vivo evaluation of the ^{11}C -labeled tetrazine [^{11}C] AE-1 for pretargeted PET imaging. *Bioorg. Med. Chem. Lett.* **29**, 986-990.
- (124) Keinänen, O., Fung, K., Pourat, J., Jallinoja, V., Vivier, D., Pillarsetty, N. K., Airaksinen, A. J., Lewis, J. S., Zeglis, B. M., and Sarparanta, M. (2017) Pretargeting of internalizing trastuzumab and cetuximab with a ^{18}F -tetrazine tracer in xenograft models. *EJNMMI Res.* **7**, 1-12.
- (125) Feng, H., Zhang, H., Wang, M., Vannam, R., Wang, H., Yan, X., Ouyang, W., Jia, X., Fox, J. M., and Li, Z. (2020) Improving tumor-to-background contrast through hydrophilic tetrazines: The construction of ^{18}F -labeled PET agents targeting nonsmall cell lung carcinoma. *Chem. Eur. J.* **26**, 4690-4694.
- (126) Ruivo, E., Adhikari, K., Elvas, F., Fissers, J., Vangestel, C., Staelens, S., Stroobants, S., Van der Veken, P., Wyffels, L., and Augustyns, K. (2019) Improved stability of a novel fluorine-18 labeled TCO analogue for pretargeted PET imaging. *Nucl. Med. Biol.* **76**, 36-42.
- (127) Rashidian, M., Keliher, E. J., Bilate, A. M., Duarte, J. N., Wojtkiewicz, G. R., Jacobsen, J. T., Cragolini, J., Swee, L. K., Victora, G. D., and Weissleder, R. (2015) Noninvasive imaging of immune responses. *Proc. Natl. Acad. Sci. (USA)* **112**, 6146-6151.

- (128) Thomae, D., Waldron, A.-M., Fissers, J., Dedeurwaerdere, S., Van der Veken, P., Joossens, J., Stroobants, S., Augustyns, K., and Staelens, S. (2014) In vivo evaluation of ^{18}F -labeled TCO for pre-targeted PET imaging in the brain. *Nucl. Med. Biol.* *41*, 513-523.
- (129) Nguyen, S. S., and Prescher, J. A. (2020) Developing bioorthogonal probes to span a spectrum of reactivities. *Nat. Rev. Chem.* *4*, 476-489.
- (130) Oliveira, B., Guo, Z., and Bernardes, G. (2017) Inverse electron demand Diels–Alder reactions in chemical biology. *Chem. Soc. Rev.* *46*, 4895-4950.
- (131) Meyer, J.-P., Kozłowski, P., Jackson, J., Cunanan, K. M., Adumeau, P., Dilling, T. R., Zeglis, B. M., and Lewis, J. S. (2017) Exploring structural parameters for pretargeting radioligand optimization. *J. Med. Chem.* *60*, 8201-8217.
- (132) García, M. F., Zhang, X., Shah, M., Newton-Northup, J., Cabral, P., Cerecetto, H., and Quinn, T. (2016) $^{99\text{m}}\text{Tc}$ -bioorthogonal click chemistry reagent for in vivo pretargeted imaging. *Bioorg. Med. Chem.* *24*, 1209-1215.
- (133) Vāvere, A. L., and Scott, P. J. (2017) Clinical applications of small-molecule PET radiotracers: current progress and future outlook. *Semin. Nucl. Med.* *47*, 429-453.
- (134) Gobbi, L. C., Knust, H., Körner, M., Honer, M., Czech, C., Belli, S., Muri, D., Edelmann, M. R., Hartung, T., and Erbsmehl, I. (2017) Identification of three novel radiotracers for imaging aggregated tau in Alzheimer's disease with positron emission tomography. *J. Med. Chem.* *60*, 7350-7370.
- (135) Quigley, H., Colloby, S. J., and O'Brien, J. T. (2011) PET imaging of brain amyloid in dementia: a review. *Int. J. Geriatr. Psychiatry* *26*, 991-999.
- (136) Verdurand, M., Levigoureux, E., Zeinyeh, W., Berthier, L., Mendjel-Herda, M., Cadarossanesaib, F., Bouillot, C., Iecker, T., Terreux, R. I., and Lancelot, S. (2018) In silico, in vitro, and in vivo evaluation of new candidates for α -synuclein PET imaging. *Mol. Pharm.* *15*, 3153-3166.
- (137) Maurer, A., Leonov, A., Ryazanov, S., Herfert, K., Kuebler, L., Buss, S., Schmidt, F., Weckbecker, D., Linder, R., and Bender, D. (2020) ^{11}C Radiolabeling of anle253b: a putative PET tracer for Parkinson's disease that binds to α -synuclein fibrils in vitro and crosses the blood-brain barrier. *ChemMedChem* *15*, 411-415.
- (138) Zhang, X., Jin, H., Padakanti, P. K., Li, J., Yang, H., Fan, J., Mach, R. H., Kotzbauer, P., and Tu, Z. (2014) Radiosynthesis and in vivo evaluation of two PET radioligands for imaging α -synuclein. *Appl. Sci.* *4*, 66-78.
- (139) W Miller, P., J deMello, A., and D Gee, A. (2010) Application of microfluidics to the ultra-rapid preparation of fluorine-18 labelled compounds. *Curr. Radiopharm.* *3*, 254-262.
- (140) Walker, L., McAleese, K. E., Thomas, A. J., Johnson, M., Martin-Ruiz, C., Parker, C., Colloby, S. J., Jellinger, K., and Attems, J. (2015) Neuropathologically mixed Alzheimer's and Lewy body disease: burden of pathological protein aggregates differs between clinical phenotypes. *Acta Neuropathol.* *129*, 729-748.
- (141) Garousi, J., Orlova, A., Frejd, F. Y., and Tolmachev, V. (2020) Imaging using radiolabelled targeted proteins: Radioimmunodetection and beyond. *EJNMMI Radiopharm. Chem.* *5*, 1-26.
- (142) Dammes, N., and Peer, D. (2020) Monoclonal antibody-based molecular imaging strategies and theranostic opportunities. *Theranostics* *10*, 938.
- (143) Carmon, K. S., and Azhdarinia, A. (2018) Application of immuno-PET in antibody–drug conjugate development. *Mol. Imaging* *17*, 1-10.
- (144) Colombo, I., Overchuk, M., Chen, J., Reilly, R. M., Zheng, G., and Lheureux, S. (2017) Molecular imaging in drug development: Update and challenges for radiolabeled antibodies and nanotechnology. *Methods* *130*, 23-35.
- (145) Jauw, Y. W., Menke-van der Houven van Oordt, C. W., Hoekstra, O. S., Hendrikse, N. H., Vugts, D. J., Zijlstra, J. M., Huisman, M. C., and van Dongen, G. A. (2016) Immuno-positron emission tomography with zirconium-89-labeled monoclonal antibodies in oncology: what can we learn from initial clinical trials? *Front. Pharmacol.* *7*, 131.
- (146) Niemeijer, A., Leung, D., Huisman, M., Bahce, I., Hoekstra, O., Van Dongen, G., Boellaard, R., Du, S., Hayes, W., and Smith, R. (2018) Whole body PD-1 and

- PD-L1 positron emission tomography in patients with non-small-cell lung cancer. *Nat. Commun.* **9**, 1-5.
- (147) Poduslo, J. F., Curran, G. L., and Berg, C. T. (1994) Macromolecular permeability across the blood-nerve and blood-brain barriers. *Proc. Natl. Acad. Sci. (USA)* **91**, 5705-5709.
- (148) Weber, F., Bohrmann, B., Niewoehner, J., Fischer, J. A., Rueger, P., Tiefenthaler, G., Moelleken, J., Bujotzek, A., Brady, K., and Singer, T. (2018) Brain shuttle antibody for Alzheimer's disease with attenuated peripheral effector function due to an inverted binding mode. *Cell Rep.* **22**, 149-162.
- (149) Sehlin, D., and Syvänen, S. (2019) Engineered antibodies: new possibilities for brain PET? *Eur. J. Nucl. Med. Mol. Imaging* **46**, 2848-2858.
- (150) Eigenmann, M. J., Fronton, L., Grimm, H. P., Otteneder, M. B., and Krippendorff, B.-F. (2017) Quantification of IgG monoclonal antibody clearance in tissues. *MAbs* **9**, 1007-1015.
- (151) Liu, G. (2018) A revisit to the pretargeting concept - A target conversion. *Front. Pharmacol.* **9**, Article 1476.
- (152) Rondon, A., and Degoul, F. (2019) Antibody pretargeting based on bioorthogonal click chemistry for cancer imaging and targeted radionuclide therapy. *Bioconjug. Chem.* **31**, 159-173.

Chapter Two

Tritium labeling of antisense oligonucleotides *via* different conjugation agents

This declaration concerns the article entitled:			
Tritium labeling of antisense oligonucleotides <i>via</i> different conjugation agents			
Publication status (tick one)			
Draft manuscript	<input type="checkbox"/>	Submitted	<input type="checkbox"/>
In review	<input type="checkbox"/>	Accepted	<input type="checkbox"/>
		Published	<input checked="" type="checkbox"/>
Publication details (reference)	Edelmann MR*, Husser C, Duschmalé MB, Fischer G, Senn C, Koller E, Brink A. (2021) <i>AAPS Open</i> 7:4		
Copyright status (tick the appropriate statement)			
I hold the copyright for this material	<input checked="" type="checkbox"/>	Copyright is retained by the publisher, but I have been given permission to replicate the material here	<input type="checkbox"/>
Candidate's contribution to the paper (provide details, and also indicate as a percentage)	<p>The candidate contributed to / considerably contributed to / predominantly executed the...</p> <p>Formulation of ideas: 100%</p> <p>Design of methodology: 50%</p> <p>Experimental work: 60%</p> <p>Presentation of data in journal format: 80%</p>		
Statement from Candidate	This paper reports on original research I conducted during the period of my Higher Degree by Research candidature.		
Signed		Date	17.10.22

Introduction

The transcription of DNA to RNA and subsequent translation to functional proteins is a central element in living cells. Using viral RNA, Stephenson and Zamecnik¹ demonstrated in 1978 that translation of proteins could be efficiently inhibited *in vitro* by competitive hybridization with antisense oligonucleotides (ASO). Today, there are several approved ASO-based therapies, such as Spinraza (Ionis/Biogen), Waylivra (Ionis/Akcea/PTC), Exondys (Sarepta Therapeutics), available on the market.² There is growing interest across the pharmaceutical industry to discover and develop new ASO-based therapies, employing various mechanisms to inhibit mRNA translation e.g., formation of ASO/RNA complexes that activate RNase H, which degrades the mRNA or prevents ribosome recruitment.³ ASOs are also used to modify splicing or to increase protein expression by targeting upstream open reading frames.^{4,5} As with small molecule drugs throughout the drug development process from preclinical to clinical studies, regulatory data packages for ASOs are required to demonstrate safety, efficacy, and tolerability of the new drug as well. The use of radiolabeled compounds allows a mechanistic and quantitative understanding of the fate of ASO in the body with the aim to characterize them and further optimize their absorption, distribution, metabolism, and excretion (ADME) properties. Often, carbon-14 is used to label small molecule drug candidates, since it can be introduced in a metabolically stable position. For larger molecules such as oligonucleotides, however, the resulting molar activity after carbon-14 (2.3 GBq/mmol; 62.4 mCi/mmol) labeling might be insufficient for a quantitative determination by liquid scintillation counting (LSC). Tracing of carbon-14 is possible by accelerated mass spectrometry (AMS), but this technology requires special equipment.

Therefore, tritium (molar activity: 984.2 MBq/mmol; 26.6 Ci/mmol; $t_{1/2}$: 12.3 y) was preferred over carbon-14 as a radioisotope for the ASO study, as the molar activity of tritium is about 430-times higher than that of carbon-14.

Various approaches have already been published to incorporate tritium into an oligonucleotide. In a biotransformation study described by Shemesh and colleagues,⁶ tritium was introduced into a linker that connects an ASO and a targeting moiety (GalNAc). These radiolabeled ASO constructs were compared to the corresponding cold (non-radioactive) ASOs and showed similar *in vivo* behavior.

Lesnik and co-workers⁷ described a hydrogen-tritium exchange in tritiated water at the C8 position in purines (**Figure 1: 1**). The rapid tritium exchange at the C8 position back to hydrogen does not allow for longer-term *in vivo* studies.

Another procedure for small interfering RNAs (siRNA) was based on inserting 5-bromouridine derivatives (**Figure 1: 2**) into the sequences followed by a halogen-tritium exchange by palladium-catalyzed hydrogenation with tritium gas.⁸ The transfer of

this approach to oligonucleotides containing phosphorothioate backbones was not successful, even with a high number of equivalents (> 100) of “catalyst”.

A different reported approach requires the oxidation of the 5'-terminal primary alcohol of nucleotide monomers, and, in a second step, reduction of the aldehydes with a tritium-labeled reducing agent such as NaBT₄.⁹ After multiple steps, involving 3'-phosphoramidite activation of the nucleotide, the tritium-labeled monomers can then be used for building up the desired oligonucleotide (**Figure 1: 3**). The key issue of this approach is the instability of the tritium-labeled nucleotide-phosphoramidite, which leads to low yields, high radioactive waste, and low specific activity of the final product.

Palazzolo, Pieters et al¹⁰ demonstrated a random hydrogen/tritium exchange on a 6-mer or 12-mer DNA-based oligonucleotide containing phosphate backbones under tritium gas and catalyzed with ruthenium nanoparticles. The reported exchange took place exclusively in purine rings at the C2 and C8 positions (**Figure 1: 1, 4**). As already mentioned, the risk of a re-exchange at C8 position to hydrogen is possible. To the best of our knowledge, a feasibility with a phosphorothioate-based oligonucleotide has not yet been reported. A general disadvantage of a random labeling technique is that the quantification of radioactively labeled oligonucleotides in metabolism studies is very difficult or even impossible, as the label is distributed evenly over the entire molecule.

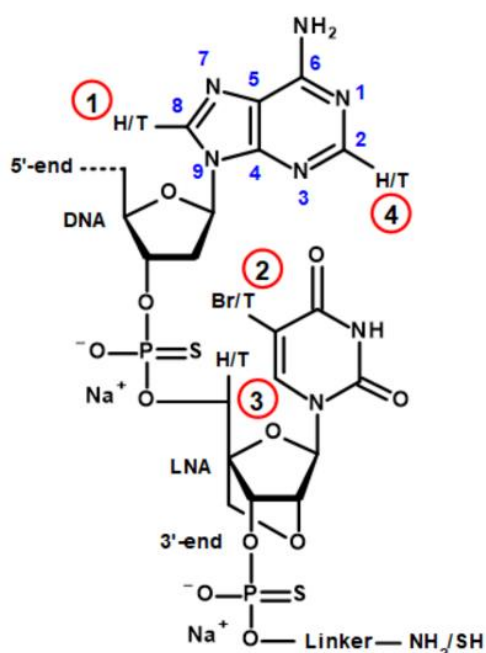


Figure 1: Schematic structure of two nucleotides linked together with a phosphorothioate bridge. Starting from the 5'-end: DNA-based adenosine and LNA-based uridine derivative. The standard numbering convention is shown on the purine ring in blue numbers from 1 through 9 on the aromatic base. Thiol or amine functionalized linker (**Figure 2**) is connected to phosphorothioate at 3'-end. The circled numbers represent the labeling approaches. **1**; hydrogen-tritium exchange by the use of tritiated water or tritium gas and ruthenium nanoparticles. **2**: palladium catalyzed bromo-tritium exchange. **3**: oxidation of 5'-alcohol and reduction with sodium borotritide. **4**: hydrogen-tritium exchange by the use of tritium gas and ruthenium nanoparticles.

Generally, radiolabeling of ASO molecules is not straightforward. Robust tritium-labeling techniques are not readily available, and thus often represent a bottleneck in pre-clinical ASO research. There is an urgent need for efficient approaches to increase the availability of radiolabeled ASOs for pre-clinical and clinical research.

To find new efficient ways to increase availability of tritium-labeled ASOs, a novel strategy was studied to conjugate pre-labeled tags *via* different linkers to the 3'-end using experimental oligonucleotides containing locked nucleic acids (LNAs).¹¹

First, we evaluated the feasibility of labeling concepts by conjugating different tags to functionalized linkers of oligonucleotides. Second, we investigated the metabolic stability and *in vitro* potency by target reduction of tagged tool-ASOs in human and mouse hepatocytes in comparison to their untagged analogs. Finally, to verify the *in vivo* applicability of our approach we conducted a PK study in mice using two tritium-labeled oligonucleotides to study ASO distribution into different tissues following subcutaneous administration.

The key questions of this study were whether whether bioconjugation from a tritiated building block to functionalized ASOs is feasible and whether this modification has an influence on stability, RNA-level reduction, or biodistribution compared to their congeners.

Materials and Methods

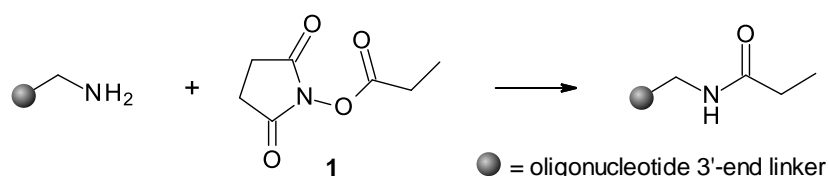
Chemicals & Equipment

All oligonucleotides, which were used as starting materials, were synthesized by Roche Pharma Research and Early Development using standard phosphoramidite chemistry. Modifiers were incorporated at the start of the synthesis by placing the amino or thiol-group at the 3'-end using 3'-Amino-Modifier TFA Amino C-6 Icaa CPG (Hauppauge, NY, USA) and 3'-Thiol-Modifier C₆ S-S (GLEN Research, Sterling, VA, USA). *N*-Succinimidyl propionate (Wako), *N*-methylmaleimide (Fluka), and *N*-ethylmaleimide (Fluka) are commercially available and have been used without further purification. Phosphate-buffered saline (PBS) was purchased from Thermo Fisher Scientific (Paisley, UK). PBS contained 1.54 mM potassium phosphate monobasic, 2.71 mM potassium phosphate dibasic, and 155.17 mM sodium chloride. Tritium-labeled [³H]*N*-ethylmaleimide (molar activity: 2 TBq/mmol = 55 Ci/mmol) was obtained from Pharmaron (Cardiff, Wales, UK) as a solution in pentane. LSC for tritium compounds was accomplished using a HIDEX 300 SL and ULTIMATE GOLD cocktail (PerkinElmer Inc., Waltham, MA, USA). Reaction monitoring and purity for NSP conjugations on amine-linkers were determined by HPLC Agilent 1210 at 260 nm wavelength, Waters XBridge RP18, 4.6 x 150 mm, 3.5 μm column at 60 °C ([A] = water/methanol/hexafluoro *i*-propanol/TEA : 950/25/21/2.3 mL;

[B] = water/methanol/hexafluoro *i*-propanol/TEA : 175/800/21/2.3 mL, at a flow rate of 1.0 mL/min with the following gradient: 10% [B] to 60% [B] in 12 min. Conjugations with maleimide derivatives were determined by UPLC Agilent 1290 at 260 nm wavelength, ACQUITY UPLC Oligonucleotide BEH C18, 2.1 x 50 mm, 1.7 μ m column at 80 °C with the same eluents and the following gradient: 10% [B] to 40% [B] in 6 min. Radiochemical purity was measured using the β -radioactivity HPLC detector RAMONA Quattro with an internal solid scintillator (Raytest, Straubenhardt, Germany). Mass spectrometry analysis was performed using a Thermo Fisher Scientific (Waltham, MA, USA) Vanquish UHPLC System, Orbitrap Fusion Lumos Tribrid, and a Waters ACQUITY Oligonucleotide BEH C18 (2.1 x 50 mm, 1.7 μ m) column in negative-ion mode. MS (*m/z*) was calculated from the multiply charged peak pattern. Preparative HPLC for NSP conjugation was performed using a Gilson PLC 2050 (Mettmenstetten, CH) with an XBridge C18 column, 5 μ m, 10 x 250 mm and using water (950 mL)/methanol (25 mL)/TEA (2.3 mL)/hexafluoro *i*-propanol (21 mL) as mobile phase [A] and water (175 mL)/methanol (800 mL)/TEA (2.3 mL)/hexafluoro *i*-propanol (21 mL) as mobile phase [B] in gradient elution with 10% [B] to 60% [B] in 15 min. Concentration was determined using a Eppendorf BioSpectrometer® basic (Hamburg, Germany) at 260 nm wavelength and the corresponding calculated molar extinction coefficient. In order to determine the specific activity of tagged ASOs, the activity concentration [MBq/mL] of oligonucleotide solution was determined by LSC and divided by the content concentration [mg/mL] to give the specific activity in MBq/mg. Based on the molecular weight, the molar activity in GBq/mmol was calculated for each tagged ASO.

Labeling Procedures

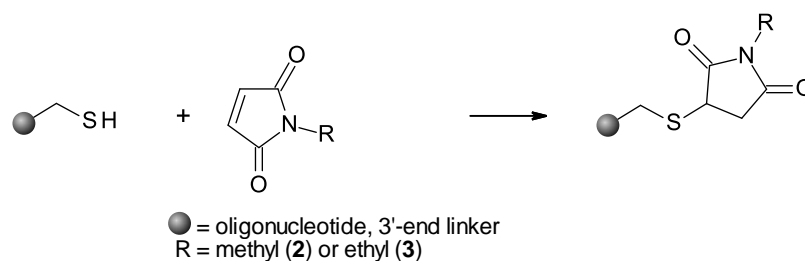
Labeling Procedure I: NSP conjugation on amino-linker



4.0 mg (0.73 μ mol) of ASO 2-precursor, containing 3'-end amino-linker, was dissolved in 0.5 mL *N,N*-dimethylformamide 5 μ L (29.06 μ mol) Hünig's base and 150 μ g (0.87 μ mol) *N*-succinimidyl propionate, dissolved in 60 μ L *N,N*-dimethylformamide, were added to give a colorless suspension. The mixture was stirred for 16 h at 22 °C to become a clear solution. The solvent was removed under high vacuum and the residue dissolved in PBS. Crude mixture was purified by preparative HPLC. The desired fractions were transferred into an Amicon® Pro purification system (MWCO: 3,000 Da) and

centrifuged at 4,000 rpm. Deionized water was added, and the process was repeated 4 more times to complete the exchange from HPLC eluent to water. The resulting aqueous solution was purified by preparative HPLC, and the collected fractions were lyophilized to isolate 3.0 mg (74%) of **ASO 2** as a colorless powder with a purity of 95%. MS (m/z): 5561.6 [M-(H)]⁻.

Labeling procedure II: maleimide derivatives conjugation on sulfhydryl-linker



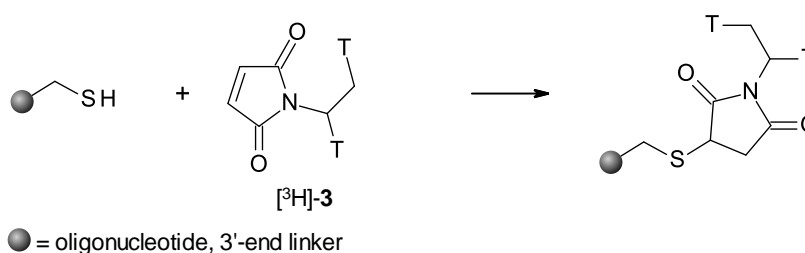
4.0 mg (0.73 μ mol) of ASO 3-precursor, containing 3'-end sulfhydryl linker, was dissolved in 1 mL PBS. (127 μ g, 1.14 μ mol) *N*-methyl maleimide, dissolved in 61 μ L dimethyl sulfoxide, was added to the aqueous solution and stirred at 22 °C for 16 h. UPLC analysis showed a complete addition of maleimide to the oligonucleotide. To exchange the buffer to water, the reaction mixture was transferred into an Amicon[®] Pro purification system (MWCO: 3,000 Da) and centrifuged at 4,000 rpm. Deionized water was added, and the process was repeated 4 more times to complete the exchange. The resulting aqueous solution was lyophilized to isolate 2.8 mg (69%) of the desired oligonucleotide as a colorless powder with purity of 97%. MS (m/z): 5602.2 [M-(H)]⁻.

ASOs 4 and 6 were prepared in a similar manner according to **Labeling Procedure II**:

ASO 4: Yield: 73%, purity: 96%, MS (m/z): 5616.2 [M-(H)]⁻;

ASO 6: Yield: 73%, purity: 99%, MS (m/z): 7833.4 [M-(H)]⁻.

Labeling procedure III: [³H]N-ethylmaleimide ([³H]3) conjugation on sulfhydryl-linker



1.1 GBq (30 mCi) of [³H]N-ethylmaleimide ([³H]3, 61.5 μ g, 0.477 μ mol) in 12 mL pentane was concentrated on a silica gel pre-packed column and eluted with 2x 0.5 mL

DMSO. A solution of 2.20 mg (0.401 μmol) ASO 7-precursor in 1 mL PBS was added and stirred for 1 h at 22 °C. UPLC analysis showed 40% of the desired product and 60% of unreacted starting material. Non-radioactive NEM (502 μg , 4.01 μmol) was added and stirred for 1 h at 22 °C. UPLC showed a complete addition to the desired product. The reaction solution was transferred into a 5 mL Float-A-Lyzer[®] tube (MWCO: 500-1,000 Da) and dialyzed against PBS pH 7.1 at 22 °C. The buffer was changed 4 times after 45 minutes and stored 16 h in the fridge. UPLC analysis showed a high polar radio impurity. The solution was filled into an Amicon[®] Pro purification system (MWCO: 3,000 Da) and centrifuged at 4,000 rpm. PBS was added and the process was repeated 4 more times to achieve a radiochemical purity of 99%. Isolated amount: 1.58 mg (yield: 70%), isolated radioactivity: 163 MBq (4.4 mCi), radiochemical yield: 15%, specific activity: 104 MBq/mg (2.8 mCi/mg) which is equal to 614 GBq (16.6 Ci/mmol).

ASO 8 was prepared in a similar manner according to *Labeling Procedure III*:

ASO 8: Yield: 92%, isolated radioactivity: 33.3 MBq (0.9 mCi), radiochemical yield: 9%, radiochemical purity: 93%, specific activity: 67 MBq/mg (1.8 mCi/mg), molar activity: 481 GBq/mmol (13.0 Ci/mmol).

Cell Culture, Oligonucleotide Treatment, mRNA Isolation and qPCR

Mouse hepatocytes were isolated from C57BL/6 mice by a two-step collagenase liver perfusion method as previously described.¹² Freshly isolated primary mouse hepatocytes were plated in collagen-I coated 96-well plates and treated in Williams Medium E containing 10% fetal bovine serum without antibiotics. Cells were treated with LNA solutions in the indicated concentrations in full cell culture medium about 1 hour after plating for an incubation time of 3 hours. Then the cells were washed 3 times with PBS containing Ca^{2+} and Mg^{2+} and incubated in fresh cell culture medium without the oligonucleotide compound. After 21 or 69 hours, hepatocytes were washed 3 times with PBS containing Ca^{2+} and Mg^{2+} and lysed with 135 μL PureLink Pro lysis buffer. 5, 10, and 20 μL were sampled for hybridization based ELISA assay as described earlier¹³ and 100 μL were used for mRNA purification using the PureLink Pro 96 RNA Kit from Thermo Fisher Scientific. One Step RT-qPCR for Malat1 mRNA levels was performed, respectively. mRNA levels were normalized to the total RNA amount quantified with Ribogreen QuantIT (Thermo Fisher Scientific). Total RNA was isolated using the PureLink Pro 96 RNA Kit from Thermo Fisher Scientific according to the manufacturer's instructions and RT-qPCR was performed using the LightCycler Multiplex RNA Virus Master (Roche) with primer probe sets (all from Thermo Fisher Scientific) human Malat1 (Hs00273907_s1), mouse Malat1 (Mm01227912_s1). The obtained data was

normalized to total RNA amounts determined *via* Ribogreen quantification. All data points were performed in triplicate, and data are given as the average. IC₅₀ values were fitted with GraphPad Prism with a constrained HillSlope set to 1. Results are reported as IC₅₀ value ± standard deviation.

In vivo Mouse Study

The study was conducted with the approval of the local veterinary authority with strict adherence to the Swiss federal regulations on animal protection and to the rules of the Association for Assessment and Accreditation of Laboratory Animal Care International (AAALAC).

Animals and Housing Conditions

Male C57BL/6 J mice (n = 24, 8 to 12 weeks old) were purchased from Charles River Laboratories, France. The mice were group housed in open cages and maintained on a 12:12-h light:dark cycle, with constant temperature (21–24 °C) and humidity (40–80%). Each cage was provided with unrestricted access to municipal water and sterilized food (Provimi Kliba 3436). All cages (except metabolism cages) were supplied with autoclaved sawdust bedding and environmental enrichments, which were applied to best practice animals' welfare standards and rotated weekly. The mice were acclimated for at least 1 week before the start of the study.

Study Design

The mice were randomly allocated into 4 groups (n = 6 per group) according to the 4 different compounds. The compounds were formulated as a solution in Dulbecco's PBS (pH 7) and administered subcutaneously as a single dose of 1 mg/kg of body weight (dosing volume of 4 mL/kg). In a composite sampling design, blood (100 µL/time point/mouse) was collected sublingually from mice under deep anesthesia with 5% isoflurane in pure oxygen. Blood was collected at 15 min, 1 h, 4 h, 24 h, 48 h, and 72 h post dose into EDTA coated polypropylene tubes followed by plasma separation by centrifugation at 15,000 rpm for 5 min at 4 °C. Urine samples were collected post injection by thoroughly rinsing the collection surface with 3 mL distilled water. For excretion collections, mice were housed in pairs in metabolic cages during 0-24 h, 24-48 h and 48-72 h intervals post administration. Organs and plasma were collected at terminal time points of 1 d, 3 d, and 14 d after pentobarbital-induced anesthesia (40 mg/kg, i.p.). Plasma samples were stored at -20 °C for further processing

and analysis. Samples of liver, kidney, and spleen were collected into homogenization tubes (Precellys® CK28, Bertin Instruments, France).

Bioanalytics

Quantitative Exposure Assessment of Full-Length Compounds

Tissue samples were collected and weighed during necropsy and stored at -80 °C in homogenization tubes CK28 (Precellys®) for subsequent bioanalytical examination by LC coupled to tandem mass spectrometry (LC-MS/MS). Prior to extraction tissue homogenates were diluted 5-fold in mouse blank plasma. The quantification was performed against a mouse plasma calibration curve. Calibration ranges were 0.267-666 nM for ASO 1 and 0.380-950 nM for ASO 5, respectively.

Fifty µL of calibration standards, quality control samples (freshly prepared in mouse plasma) and tissue homogenate samples diluted in mouse blank plasma were treated for protein denaturation with 150 µL of 4 M guanidine thiocyanate after addition of the internal standard (2,000 ng/mL). A characterized 16-mer oligonucleotide (MW: 5460 Da), consisting of DNA nucleotides, LNA nucleotides, and a complete phosphorothioate backbone, was used as an internal standard in order to exclude possible variations during pipetting, solid-phase work-up, or LC-MS/MS sample injections. After vigorously mixing (20 min at 1,600 rpm), 200 µL of a H₂O/HFIP/DIPEA solution (100:4:0.2, v/v/v) were added, followed by mixing (15 min at 1,500 rpm). Then, a clean-up step was performed using solid-phase-extraction cartridges (Waters, OASIS HLB, 30 µm) after elution and evaporation to dryness (30–45 min at 40 °C) the samples were reconstituted in 200 µL of mobile phase (H₂O/MeOH/HFIP/DIPEA [95/5/1/0.2, v/v/v/v]). After vortex mixing (10 min at 1,500 rpm), an aliquot (20 µL) was injected into the analytical column (Waters, Acquity BEH C18, 1.7 µm, 50 x 2.1 mm kept at 60 °C). The analyte and internal standard were separated from matrix interferences using gradient elution from H₂O/MeOH/HFIP/DIPEA (95/5/1/0.2, v/v/v/v) to H₂O/MeOH/HFIP/DIPEA (10/90/1/0.2, v/v/v/v) within 4 min at a flow rate of 0.4 mL/min. Mass spectrometric detection was carried out on an AB-Sciex 6500+ mass spectrometer using selected reaction monitoring (SRM) in the negative-ion mode. The selected ion reactions (m/z) were 680.6/94.8 and 658.9/94.8 for ASO 1 and ASO 5 respectively and 596.1/94.8 for Internal Standard. Detection was accomplished utilizing ion spray MS/MS in negative ion SRM mode.

In the case of animals dosed with GalNAc-conjugated compounds (ASO 5 and ASO 8), total or partial cleavage of the GalNAc moiety was expected; therefore, both the intact compound (with GalNAc) and also the naked moiety (corresponding to ASO 1 and

ASO 7, respectively) were measured to quantify the amount of GalNAc-cleavage compounds.

Determination of Total Radioactivity by Liquid Scintillation Counting

Plasma, urine, and fecal extract were analyzed using liquid scintillation analysis. To enable scintillation analysis, aliquots of each sample (typically 20-200 μL) were mixed with Ultima Gold liquid scintillation cocktail (5 mL; PerkinElmer) in plastic scintillation vials (7 mL; PerkinElmer) and analyzed using a Radiomatic 150TR flow or Tri-Carb 3100 TR scintillation analyzer with automatic quench correction against an external standard (PerkinElmer, Waltham, MA, USA). Further manipulation of the raw data and conversion to concentrations were performed on spreadsheets running on Microsoft Excel 2010.

Metabolite Identification in vitro and in vivo

For *in vitro* studies of metabolism, hepatocyte cell pellets were collected from the hepatocytes incubations described above. For *in vivo* metabolism studies, liver, kidney, and spleen tissue samples were collected after necroscopy in the described *in vivo* study and were stored at $-80\text{ }^{\circ}\text{C}$ in homogenisation tubes CK28 (Precellys[®]). Tissue homogenates and hepatocyte lysates were prepared by adding 300 μL of H_2O to 100 mg of tissue or to hepatocyte samples, respectively, followed by mixing the CK28 tubes in the Precellys homogenizer. The analysis of biotransformation of the oligonucleotide compounds in the resulting tissue homogenates and cell lysates was performed as described previously.^{14,15} In brief, 50 μL of homogenate or cell lysate were mixed with 250 μL of guanidine thiocyanate 4 M in 0.1 M Tris buffer pH 7.5 for 15 min at $25\text{ }^{\circ}\text{C}$ in a Thermo mixer. Then, 700 μL $\text{H}_2\text{O}/\text{HFIP}/\text{DIPEA}$ 100/2/0.2 *v/v/v* were added and mixed for 1 h at $25\text{ }^{\circ}\text{C}$. 4-8 μL of internal standard (ISTD) 20-1000 μM in $\text{H}_2\text{O}/\text{MeOH}/\text{HFIP}/\text{DIPEA}$ 100/10/1/0.1 *v/v/v/v* were added, and the sample centrifuged for 5 min at 14,000 rpm. Subsequently, the supernatant was subjected to a solid phase extraction (SPE) OASIS HLB 1 cc 30 mg cartridge (Waters, Wexford, Ireland) followed by analysis with LC-HRMS. A Thermo Scientific Dionex UltiMate NCP-3200RS Binary Rapid Separation HPLC system was used in combination with a Pal autosampler (CTC Analytics AG, Zwingen, Switzerland), and a Thermo Scientific Orbitrap Fusion Tribrid Mass Spectrometer (Thermo Scientific, Bremen, Germany) equipped with an electrospray ionization (ESI) source. The oligonucleotide metabolites were analyzed in negative-ionization mode using a full scan MS experiment combined with two parallel MS^2 experiments, one data-dependent scan and an untargeted all-ion fragmentation (AIF) experiment applying high collision energy. In the AIF scan, a diagnostic fragment originating from the phosphorothioate backbone (O_2PS^- : m/z 94.936) was formed

efficiently upon collisional activation. Based on this fragment an accurate determination of metabolites of oligonucleotides was achieved, independent of their sequence in an untargeted but highly selective manner. MS data were analysed using XCalibur software (Thermo Scientific, Bremen Germany). MS intensities were recorded as the sum of the most intense charge states of the most intense isotopes of the respective analyte applying an m/z window of 5 ppm.

Results

Conjugation Methods

To develop radiolabeling strategies for ASOs, the feasibility of labeling on functionalized linkers that are attached to ASOs was investigated. In the study, we selected experimental-ASOs that contain LNA, DNA monomers, and phosphorothioate backbones. Standard LNA-incorporating ASOs are usually based on single-stranded 14 – 20-mers and contain three structural units: LNA nucleotides, DNA nucleotides, and a phosphorothioate backbone. A comparative study has shown that LNA-modified ASOs display a 10-fold higher human serum stability compared to unmodified DNA counterparts. Furthermore, LNAs manifested an improved nuclease resistance, which results in a higher metabolic stability *in vivo*.¹⁶

Two labeling routes (*Route A*, *Route B*), which highlight the two types of linkers for subsequent labeling conjugations are shown in **Figure 2**. The introduction of a propionyl residue using *N*-succinimidyl propionate (NSP) is described in **Labeling Procedure I** (*Route A*). In brief, NSP was introduced at the 3'-end of the ASO *via* an aminopropylglycerol-based linker in *N,N*-dimethylformamide and Hünig's base. The crude conjugate was purified by preparative HPLC in a yield of 74 % and purity of 95%. **Labeling Procedure II** (*Route B*) describes maleimide-based conjugation to the thiol-linker at the 3'-end. Conjugations with both, *N*-methylmaleimide (NMM) or alternatively *N*-ethylmaleimide (NEM) were achieved. Actual tritiated oligonucleotides used for this study were only prepared with [³H]NEM as described in **Labeling Procedure III** (*Route B*). Each maleimide-based conjugation was carried out in an aqueous phosphate buffer and worked-up using ultra-centrifugal filtration. Recovery yields up to 92% and purities of > 93% were achieved with molar activities in the range of 481 GBq/mmol to 629 GBq/mmol (13-17 Ci/mmol).

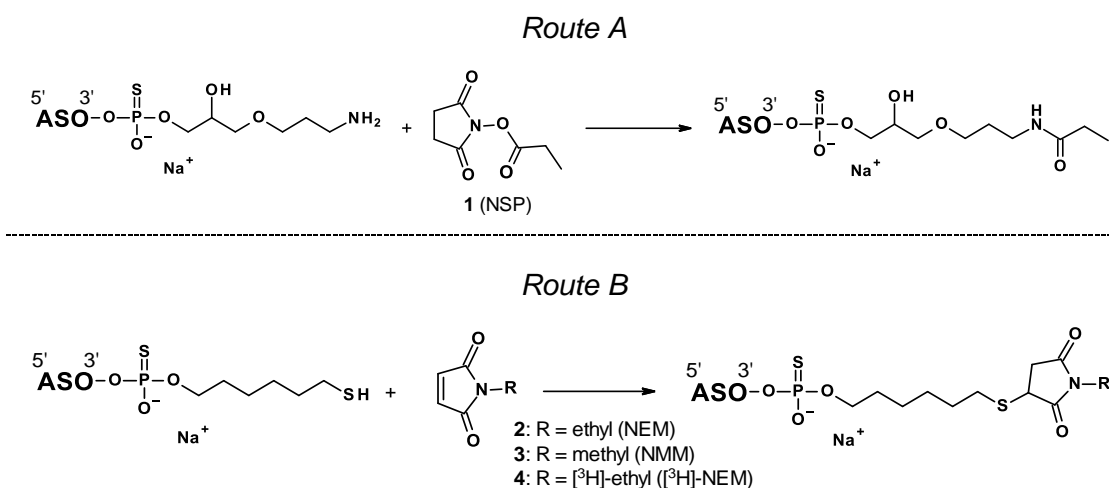


Figure 2: Overview of different approaches applied in this study to introduce tritium labels to oligonucleotides by conjugation. Introducing propionyl using *N*-succinimidyl propionate **1** (NSP) to the 3'-end *via* an aminopropylglycerol-based linker (*Route A*), and *via* Michael addition of *N*-ethylmaleimide **2** (NEM), *N*-methylmaleimide **3** (NMM), or *N*-[³H]ethylmaleimide **4** ([³H]NEM) to a C₆-thiol-linker at the 3'-end (*Route B*).

The labeling with [³H]NEM was a challenge when preparing for conjugations, as the radioactive tracer was supplied in a pentane solution. Evaporation of the solvent was not possible because NEM easily sublimates, and this led to a simultaneous loss of the radioactive maleimide derivative. This was addressed by a solvent exchange to a water-soluble solvent. The pentane solution was applied to a short silica-based column, the solvent was removed from the column using a stream of argon, and the remaining [³H]NEM was eluted with DMSO.

We hypothesize that the use of DMSO during the synthesis led to a partial sulfur/oxygen exchange in the phosphorothioate-backbone of the oligonucleotide. We observed side products in the synthesis product with mass shifts (-16 Da) that were consistent with the exchange of sulfur to oxygen. Based on MS signal intensity and semi-quantification by MS peak areas, a ratio of no exchange (38%) to 1x S/O exchange (-16 Da; 41%) to 2x S/O exchange (-32 Da; 21%) was observed for ASO 7. For ASO 8, the exchange was less pronounced: no exchange (62%), 1x S/O exchange (30%), 2x S/O exchange (8%). A similar exchange was not observed in the non-radioactive conjugations, possibly because significantly less DMSO was used in **Labeling Procedure II**. The conjugation to ASO 6 was therefore carried out under the same conditions as described in **Labeling procedure III**. In this case, a mass spectrometric analysis showed an S/O exchange in the ratio of no exchange (78%) to 1x S/O exchange (-16 Da, 19%) to 2x S/O exchange (-32 Da, 3%) which is similar to the mass pattern of the corresponding radiolabeled ASO 8. These findings support the hypothesis that there is a correlation between the use of DMSO and an S/O exchange. As a result of the S/O exchange that occurred, the molecular weight changed, and tissue concentrations of

tritium-labeled oligonucleotides could not be determined by LC-MS/MS using the reference compounds. Radioactivity measurements, however, were feasible so that ASO concentrations in tissues could be compared with untagged counterparts.

Table 1 provides an overview of synthesized oligonucleotide constructs used for *in vitro* and *in vivo* studies. Single-stranded ASO sequences of metastasis associated lung adenocarcinoma transcript 1 (Malat1; 16-mer) were conjugated with non-radioactive tags for assessing stability and target reduction *in vitro*. In addition, the Malat1 oligonucleotide was also tested as its *N*-acetylgalactosamine (GalNAc) conjugate. Conjugations of ASOs to GalNAc have been shown to shift their biodistribution from Kupffer cells towards hepatocytes in liver tissue *via* high-affinity binding to the asialoglycoprotein receptor (ASAGPR) expressed on the surface of hepatocytes.¹⁷

For a better clarification in this manuscript of individual ASO constructs, ASO-GalNAc conjugates, consisting of an *N*-acetylgalactosamine cluster with C₆-amine-linker, as well as two DNA nucleotides (cytosine, adenine, acting as “cleavable linker”) at the 5'-end of the ASO sequence is referred to as “GalNAc”. The identical sequence without a GalNAc construct is referred to as “naked”. The term “tagged” describes ASOs conjugated with NSP, NEM, or NMM on amine- or thiol-linkers. “Untagged” refers to the unmodified ASO, without linker and label.

For an *in vivo* proof-of-concept study, Malat1 ASOs (naked and GalNAc) were synthesized as tritium analogues to demonstrate the value and applicability of our labeling approach in preclinical studies.

Table 1: Overview of oligonucleotides used in different proof-of-concept studies. Capital letters in sequence describe LNA-modified nucleosides, small letters describe DNA nucleosides. GN: GalNAc, AmC₆: amino hexylene, GBB-Am: aminopropylglycerol-based bridge, C₆SH: hexylene sulfhydryl, NSP: *N*-succinimidyl propionate, NMM: *N*-methylmaleimide, NEM: *N*-ethylmaleimide. Column “Study” describes the use of oligonucleotides in different studies; *i*: *in vitro* target reduction and MetID; *ii*: *in vivo* mouse PK study.

ASO	Oligonucleotide sequence 5' → 3'	Linker	Adduct	Study
1	5'-GAGttacttgccaACT-3'	---	---	<i>i, ii</i>
2	5'-GAGttacttgccaACT-3'	3'-GBB-Am	NSP	<i>i</i>
3	5'-GAGttacttgccaACT-3'	3'-C ₆ SH	NMM	<i>i</i>
4	5'-GAGttacttgccaACT-3'	3'-C ₆ SH	NEM	<i>i</i>
5	5'-GN-AmC ₆ -caGAGttacttgccaACT-3'	---	---	<i>i, ii</i>
6	5'-GN-AmC ₆ -caGAGttacttgccaACT-3'	3'-C ₆ SH	NEM	<i>i</i>
7	5'-GAGttacttgccaACT-3'	3'-C ₆ SH	[³ H]NEM	<i>ii</i>
8	5'-GN-AmC ₆ -caGAGttacttgccaACT-3'	3'-C ₆ SH	[³ H]NEM	<i>ii</i>

In Vitro Studies

The introduction of a tritium tag *via* a short linker is, relative to the entire oligonucleotide construct, an overall small chemical modification at the 3'-end. In general, it is not expected that the hybridization of the modified ASOs with the target will be significantly altered. However, in order to verify that the tagging can be used for *in vivo* studies, two key features must be met: metabolic stability and maintenance of the target interaction resulting in a similar potency as its untagged counterpart. The following *in vitro* studies show which conjugation technique is suitable for an *in vivo* study in order to compare the modified tagged ASO with the untagged ASO.

Hepatocyte Incubations and RNA Measurements

The ability to decrease Malat1 RNA concentration levels was tested in primary mouse hepatocytes by adding the ASOs to the culture medium. After 3 h, the medium containing the ASOs was removed, the cells were washed, and then further incubated in fresh medium for 21 h and 69 h, respectively. Tagged naked ASOs 2 (NSP; $IC_{50} = 60.1 \pm 6.3$ nM), 3 (NMM; $IC_{50} = 70.0 \pm 6.3$ nM), and 4 (NEM; $IC_{50} = 77.6 \pm 3.6$ nM) reduced Malat1 RNA levels after 24 h (**Figure 3: A**) similar to the untagged ASO 1 ($IC_{50} = 74.3 \pm 9.1$ nM). After 72 h (**Figure 3: B**), the RNA level reduction was more pronounced than after 24 h. The untagged ASO 1 showed the highest Malat1 RNA reduction ($IC_{50} = 11.2 \pm 3.2$ nM), ASO 2 (NSP; $IC_{50} = 30.1 \pm 1.4$ nM) and 3 (NMM; $IC_{50} = 25.6 \pm 1.2$ nM) were in a similar range, while ASO 4 was slightly less potent (NEM; $IC_{50} = 54.3 \pm 2.9$ nM).

In addition to naked ASOs, GalNAc-conjugated ASO was also tagged with NEM on a 3'-end C₆ thiol-linker (ASO 6). As expected, the GalNAc-conjugation increased target RNA level reduction compared to the naked ASO 1, while a negative control ASO targeting ApoB mRNA¹⁸ did not show reduction in Malat1 RNA levels. The NEM-tagged ASO 6 ($IC_{50} = 1.40 \pm 0.10$ nM) showed a similar target reduction as the untagged ASO 5 ($IC_{50} = 1.24 \pm 0.17$ nM) after 24 h (**Figure 3: C**). As the uptake of GalNAc-conjugated ASOs was faster than with naked ASOs, the focus was on the early time point at 24 h and the measurement after 72 h was not carried out. The results, however, indicate that the chemical modifications did not change the uptake of ASO into hepatocytes, and that target reduction potential was similar for tagged ASOs compared to their untagged counterpart.

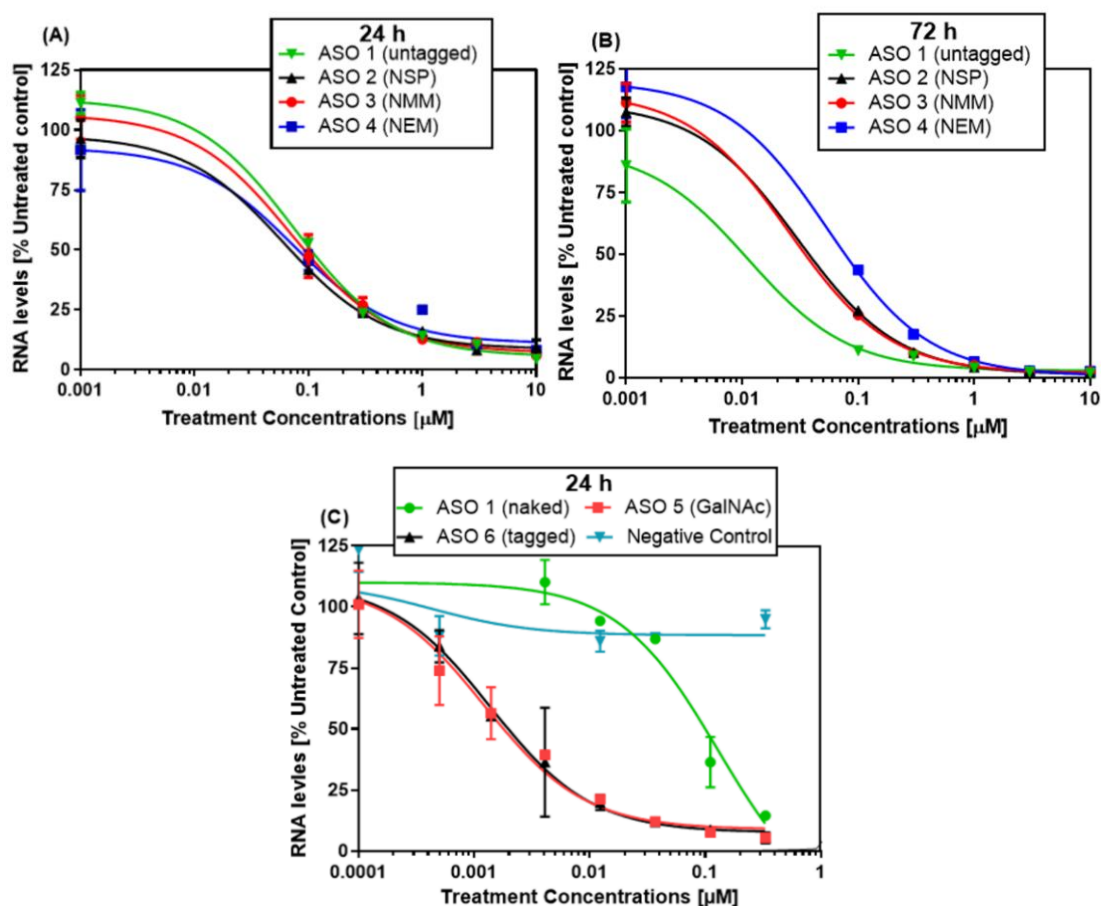


Figure 3: Concentration-dependent target reduction in mouse hepatocytes (*in vitro*) treated with NSP and maleimide-tagged naked ASOs and their untagged counterpart. Malat1 RNA levels were assessed after (A) 24 hours and (B) 72 hours. (C) Malat1 RNA levels of GalNAc-conjugated oligonucleotides compared with naked-Malat1 and negative-control ASO after 24 h. (Mean and SD, n=3)

Metabolite Identification

The stability towards degradation and metabolism was assessed for all ASOs after 3 h of incubation in primary mouse hepatocytes, followed by post-incubation periods of 21 h and 69 h, respectively. LC-HRMS was applied to an aliquot of the same mouse hepatocyte samples, which were used for target reduction assessment in order to identify the key cleavage products and/or metabolites.

Table 2 summarizes the results obtained for all ASOs investigated. Metabolite identification (MetID) experiments revealed that NSP-tagged ASO 2 showed instability with 11% of loss due to cleavage of the propionate and additionally by cleavage of the aminopropylglycerol-linker at the 3'-end after 72 h.

In contrast, ASOs tagged by NMM and NEM in mouse hepatocytes cells were almost unchanged for up to 72 h according to the LC-HRMS measurements. No relevant tag instability or metabolite formation was observed in the generic *all-ion fragmentation* (AIF) mass-chromatograms (**Figure 4:A,B**).

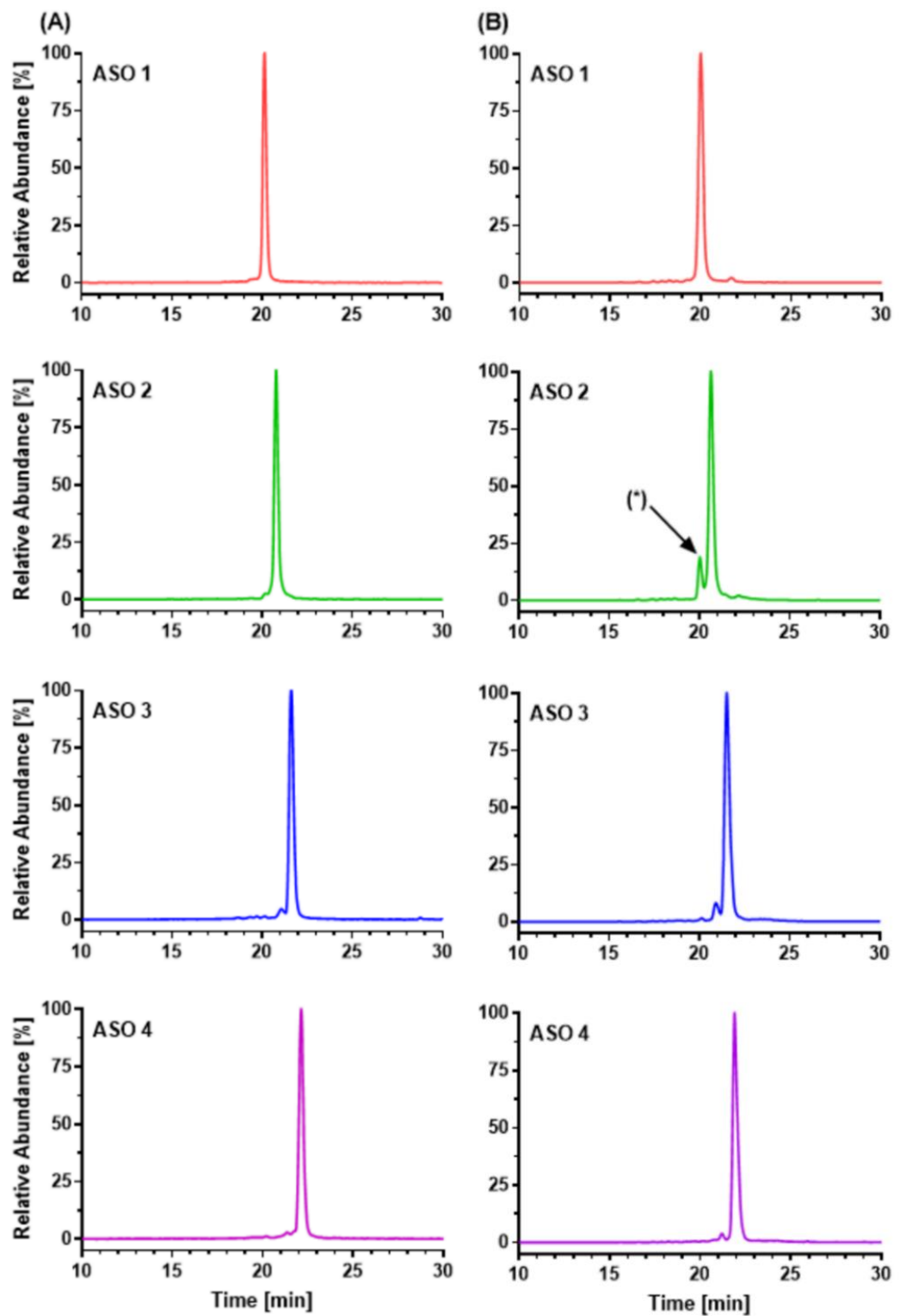


Figure 4: HPLC measurements (AIF, normalized) of naked ASO constructs from the MetID study. From the top: ASO 1 (untagged), ASO 2 (NSP), ASO 3 (NMM), and ASO 4 (NEM). Column (A): reference compounds; column (B) after 72 h incubation in primary mouse hepatocytes. (*) Arrow indicates the undesired degradation product of hydrolysis, which results in the loss of the tag.

Table 2: Degradation products for ASOs 1 to 6 from mouse hepatocyte metabolism identification study after 72 h of incubation. Capital letters in the oligonucleotide sequence describe LNA-modified nucleotides, and small letters describe DNA nucleotides. n.d.: not detectable.

ASO (Tag)	Oligonucleotide sequence 5' → 3'	Peak area [%]
1 (untagged)	5'-GAGtactgccaACT-3'	97.3
	5'-GAGtactgccaAC-3'	0.1
	5'-GAGtactgccaA-3'	n.d.
	5'-GAGtactgcca-3'	0.1
	5'-GAGtactgcc-3'	0.2
	5'-GAGtactgc-3'	0.3
	5'-GAGtactg-3'	0.4
	5'-GAGtact-3'	0.6
	5'-GAGtact-3'	0.5
	5'-GAGttac-3'	0.2
	5'-GAGtta-3'	0.1
2 (NSP)	5'-GAGtactgccaACT-3'-O-P(=O)(S)(O)-CH(OH)-CH ₂ -O-CH ₂ -CH ₂ -N(CH ₃) ₂	89.0
	5'-GAGtactgccaACT-3'-O-P(=O)(S)(O)-CH(OH)-CH ₂ -O-CH ₂ -NH ₂	5.9
	5'-GAGtactgccaACT-3'	
	5'-GAGtactgccaAC-3'	2.6
	5'-GAGtactgccaA-3'	n.d.
	5'-GAGtactgcca-3'	n.d.
	5'-GAGtactgcc-3'	n.d.
	5'-GAGtactgc-3'	0.2
	5'-GAGtactg-3'	0.3
	5'-GAGtact-3'	0.4
	5'-GAGtact-3'	0.8
5'-GAGttac-3'	0.5	
5'-GAGtta-3'	0.3	
5'-GAGtta-3'	0.1	
3 (NMM)	5'-GAGtactgccaACT-3'-O-P(=O)(S)(O)-(CH ₂) ₆ -S-C ₄ H ₃ N ₂ O ₂	98.7
	5'-GAGtactgccaACT-3'-O-P(=O)(S)(O)-(CH ₂) ₆ -S-C ₄ H ₃ N ₂ O	n.d.
	5'-GAGtactgccaACT-3'	0.2
	5'-GAGtactgccaAC-3'	n.d.
	5'-GAGtactgccaA-3'	n.d.
	5'-GAGtactgcca-3'	n.d.
	5'-GAGtactgcc-3'	0.1
	5'-GAGtactgc-3'	0.1
	5'-GAGtactg-3'	0.2
	5'-GAGtact-3'	0.3
	5'-GAGtact-3'	0.2
5'-GAGttac-3'	0.1	
5'-GAGtta-3'	n.d.	

4 (NEM)	$5\text{'-GAGtactgccACT-3' - O - } \overset{\ominus}{\underset{\text{S}}{\text{P}}} \text{O - (CH}_2\text{)}_6\text{-S - } \begin{array}{c} \text{O} \\ \diagup \\ \text{C} \\ \diagdown \\ \text{O} \\ \\ \text{N-CH}_2\text{-} \end{array}$	99.0
	$5\text{'-GAGtactgccACT-3' - O - } \overset{\ominus}{\underset{\text{S}}{\text{P}}} \text{O - (CH}_2\text{)}_6\text{-S - } \begin{array}{c} \text{O} \\ \diagup \\ \text{C} \\ \diagdown \\ \text{O} \\ \\ \text{NH} \end{array}$	n.d.
	5'-GAGtactgccACT-3'	n.d.
	5'-GAGtactgccAC-3'	n.d.
	5'-GAGtactgccA-3'	n.d.
	5'-GAGtactgccA-3'	n.d.
	5'-GAGtactgcc-3'	0.1
	5'-GAGtactgc-3'	0.1
	5'-GAGtactg-3'	0.1
	5'-GAGtact-3'	0.3
	5'-GAGtact-3'	0.2
	5'-GAGttac-3'	0.1
	5'-GAGtta-3'	n.d.
5 (GalNAc- conjugated, untagged)		47.2
		3.5
		2.6
	5'-GAGtactgccACT-3'	46.2
6 (GalNAc- conjugated, NEM)		45.2
		2.2
		2.3
	$5\text{'-GAGtactgccACT-3' - O - } \overset{\ominus}{\underset{\text{S}}{\text{P}}} \text{O - (CH}_2\text{)}_6\text{-S - } \begin{array}{c} \text{O} \\ \diagup \\ \text{C} \\ \diagdown \\ \text{O} \\ \\ \text{N-CH}_2\text{-} \end{array}$	50.3

The untagged GalNAc-ASO 5 and the corresponding NEM-tagged ASO 6 showed several metabolites in mouse hepatocytes mainly driven by the desired release of the naked ASO resulting from hydrolysis of the two diphosphate-linked nucleotide part (“cleavable linker”) and cleavages within the triantennary GalNAc construct. No undesired instability of the tag was observed. The main metabolites contained the maleimide derivative, demonstrating the applicability of using NEM to introduce tritium into ASOs. Therefore, the synthesis of tritium-labeled ASO for use in a proof-of-concept *in vivo* mouse study was pursued.

In Vivo Mouse Study

PK studies in mice were conducted using [³H]NEM-modified Malat1-based ASOs and their untagged counterparts. After a single subcutaneous dose of 1 mg/kg of body weight of untagged ASOs 1 (naked) and 5 (GalNAc), and their counterparts tagged with [³H]NEM: ASOs 7 (naked) and 8 (GalNAc), the concentrations in tissues (liver, kidney, spleen) were determined. Plasma concentrations and the recovery rate in urine and feces were monitored with the tritium-tagged ASOs. The most abundant metabolites were identified from the urine samples. In addition, the RNA levels after *in vivo* inhibition in tissues of tagged-ASOs and untagged counterparts were compared.

Tissue Concentrations in Liver, Kidney, and Spleen

Liver, kidney, and spleen tissues were collected after 1 d, 3 d, 14 d, and concentrations were determined for tritium-labeled ASOs by LSC or LC-MS/MS for untagged ASOs (**Figure 5**). As expected, GalNAc-conjugated ASOs of both untagged and tritium-tagged ASOs resulted in increased liver concentrations compared to their naked counterparts. The highest concentrations of naked ASOs were found in the kidney. For all tissues, the results obtained for the tagged vs untagged counterparts were comparable, which indicates a similar distribution in the respective examined tissues, liver, kidney, and spleen.

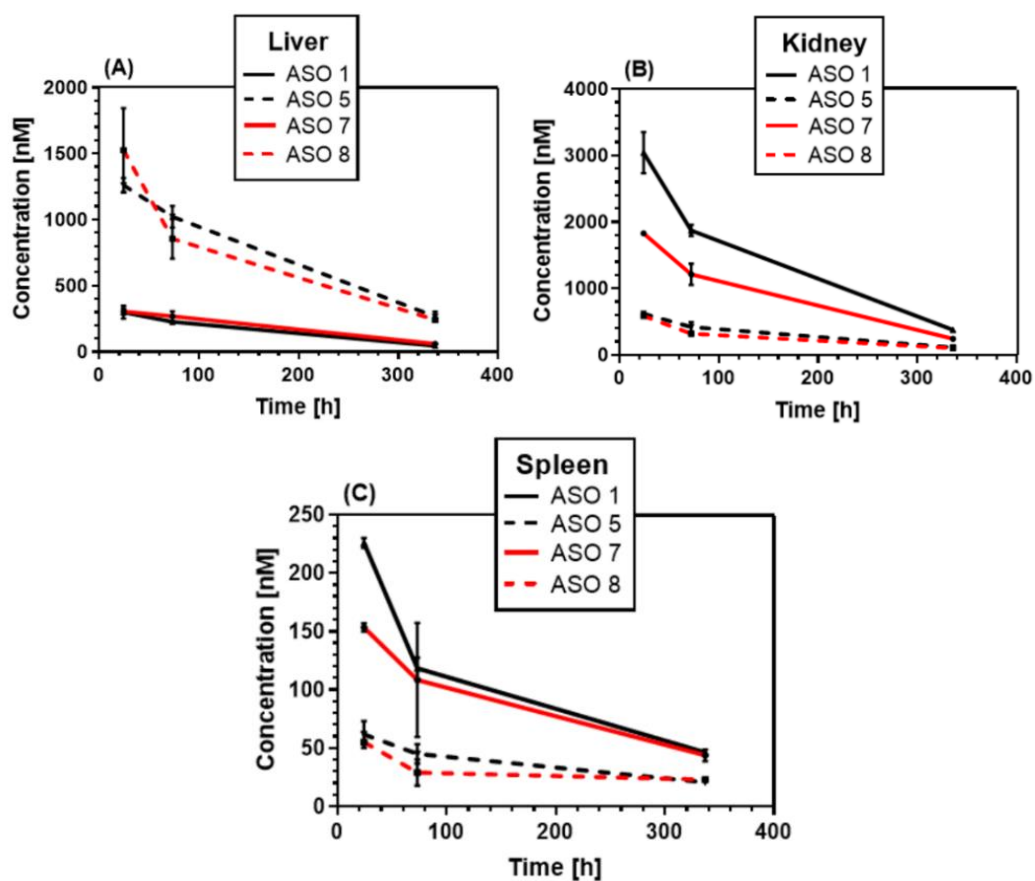


Figure 5: Tissue exposure of untagged ASOs 1 (naked), 5 (GalNAc), and tritium-tagged ASOs 7 (naked), 8 (GalNAc) in (A) liver, (B) kidney, and (C) spleen. (Mean, n=2)

Metabolism

Metabolic profiles were assessed using urine samples collected in the time interval from 0 - 24 h after administration. The main product in both cases, ASOs 7 and 8, was identified as the naked ASO-construct. In addition, several metabolites were observed at detectable signal intensities. A summary of the results is shown in **Table 3**. The metabolites found were mainly formed by hydrolysis of the phosphorothioate backbone, which resulted in shorter oligomers and confirmed the results of *in vitro* experiments. The metabolites identified in liver, kidney, and spleen are consistent with the main mode of ASO metabolism being initial endonuclease mediated hydrolysis at positions within the DNA chain of the parent compound, and by subsequent exonuclease mediated hydrolysis resulting in shorter metabolites.

Table 3: Most abundant metabolites observed in urine of mice from 0-24 h after a single dose of [³H]NEM-labeled ASOs 7 and 8. Capital letters in the oligonucleotide sequence describe LNA-modified nucleosides, and small letters describe DNA nucleosides. n.d.: not detectable.

ASO (Tag)	Oligonucleotide sequence 5' → 3'	MS Peak Area [%]
7 ([³ H]NEM)		1
		29
		56
		14
8 (GalNAc-conjugated, [³ H]NEM)		n.d.
		12
		39
		20
		29

Plasma and Excreta

The mean plasma concentration-time curves are shown in **Figure 6: A** as determined by LSC for ³H-labeled ASOs. Both tritium-labeled ASOs, naked and GalNAc, have a typically fast distribution phase. Plasma levels peaked at the first sampling time point. At 15 minutes after subcutaneous administration of 1 mg/kg of body weight of ASOs 7 (naked) and ASO 8 (GalNAc) in two animals, the mean maximum plasma concentration was 175 nM and 78 nM, respectively.

The major part of the radioactive dose was recovered within the first 24 h. 24% of the dose was collected of ASO 7, and 23% of ASO 8. The contribution of the

subsequent collection periods up to 72 h was only small for naked ASO 7 with an overall recovery of 32%. For GalNAc ASO 8, the overall recovery was 41% of the dose (Figure 6: B,C).

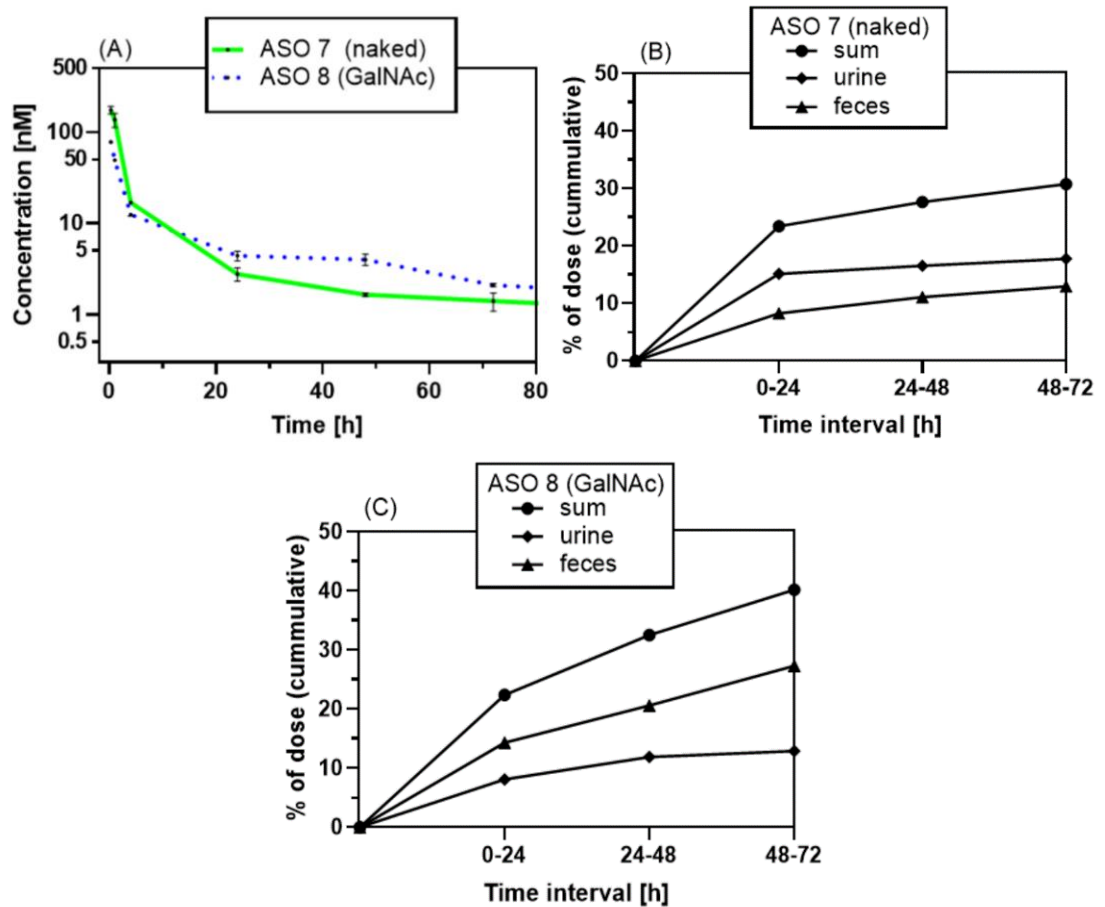


Figure 6: (A): Plasma concentration-time profile of ^3H -labeled ASO 7 (naked) and ^3H -labeled ASO 8 (GalNAc). (B,C): Excretion through urine and feces. (Mean, n=2)

Malat1 RNA-Levels after in vivo Inhibition

Next, the inhibitory effect of ASO exposure on Malat1-RNA levels in liver, kidney, and spleen was investigated after 1 day, 3 days, and 14 days. In the liver, a reduction of the RNA levels in the range of 5-12%, compared with untreated saline, was observed at each time point for all four ASOs. In kidney, the effect was slightly more pronounced, in particular for the tagged ASOs (naked and GalNAc), which showed a reduction in Malat1 RNA levels in the range of 5 to 20% and in 25-38% of their untagged counterparts. In spleen, no significant change in Malat1 RNA levels was observed after treatment with any ASO used in this study (Figure 7: A-C).

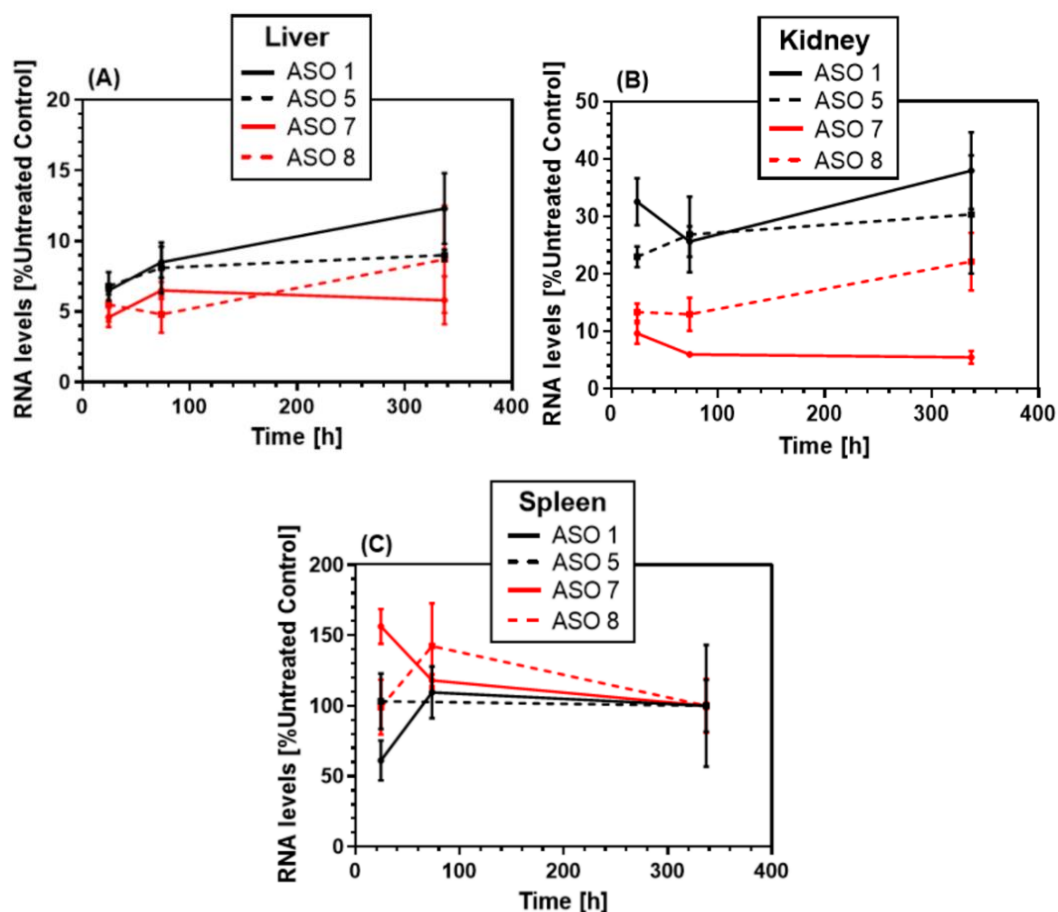


Figure 7: Malat1 RNA levels after *in vivo* inhibition of ASOs 1 (naked), 5 (GalNAc), and ^3H -labeled ASO 7 (naked), 8 (GalNAc) in liver (A), kidney (B), and spleen (C). (Mean, n=2)

Discussion

Investigating ADME characteristics of new small molecule drugs using radiolabeled drugs is well established as it enables reliable quantification, traceability and the generation of excretory mass balance data of the drug molecules, even after being transformed into various metabolites. For ASO drugs, however, the labeling with radioisotopes is far less established. The synthesis of radiolabeled ASO drugs is generally more complex and, despite the increasing importance of therapeutic ASOs in pre-clinical and clinical research, simple, straightforward chemical synthesis approaches to introduce radioisotopes into ASOs that achieve sufficient specific activity are not readily available. Therefore, we explored new approaches using *N*-succinimidyl propionate and maleimide-derivatives for a potential tritium-introduction into ASOs. Initially, NSP was used to introduce propionyl to the 3'-end. Conjugations at the 3'-end of amino linkers are known in the literature. Buntz and co-workers¹⁹ have reported conjugations of NHS-activated fluorescent labels to amino-modified oligonucleotides. Thus, an analogy to the smaller NSP, compared to fluorescent dyes, appears to be a feasible technique for labeling ASOs with tritium. Despite being synthetically favorable,

the tagged ASO resulting from this approach was unstable and showed considerable cleavage with the introduced propionate, resulting in loss of isotopic tag. This approach was therefore not further pursued. The second approach using NEM resulted in 3'-end tagged ASOs that were shown to be stable *in vitro* while maintaining the target affinity. Consequently, this conjugation approach was used to synthesize [³H]NEM analogs to be applied in proof-of-concept studies in mice to demonstrate the applicability in *in vivo* studies.

Hydrolysis by 3'-exonucleases may contribute to the instability of ASOs and 3'-end labeling could therefore result in label loss. For the ASOs used in this study for maleimide 3'-labeling, we could demonstrate that the 3'-end was largely stable against 3'-exonuclease activity. In cases of different ASOs where 3'-exonuclease activity is contributing significantly to instability, the 3'-end labeling approach shown here might be limited. For such cases, however, we assume that the conjugation concept can also be carried out on thiol-based linkers at 5'-end, as preliminary data already suggest with similar types of tritium-labeled maleimides.²⁰

In our study, we focused on the 3'-end, as the aim was to use modifications with GalNAc attached to the 5'-end of the ASO. In addition, ASOs are typically optimized to prevent exonuclease degradation as this improves the overall ADME properties. The decision as to whether the label is attached to the 5'-end or 3'-end eventually depends on the stability of the oligonucleotide 3'-end and of other conjugation interests, e.g., GalNAc conjugation. In this regard, an *in vitro* assessment of ASO uptake, target reduction, and metabolic stability could inform the selection of the best possible labeling position.

Known issues in the tritium-labeling of ASOs are related to the number of synthesis steps, which are associated with poor yields and low specific activity. For both factors, the approach shown here is beneficial, as only one principal modification step is required with the commercially available radioactive precursor [³H]NEM. The specific activity achievable (up to 629 GBq; 17 Ci/mmol) is, to the best of our knowledge,^{7,8,21,22} the highest specific activity that has been obtained so far with a tritiated oligonucleotide for use in *in vivo* studies. An even higher specific activity of the desired ASOs could be achieved by using more optimized maleimide derivatives with higher specific activity or by using more equivalents of tritium-labeled maleimide starting material (in contrast to an excess of oligonucleotides). The resulting specific activities in our study, however, still comfortably meet the requirements for *in vivo* disposition studies. In order to demonstrate the applicability of the labeling method for conducting *in vivo* studies with ASOs, mice were treated with a single dose of ASOs 7 and 8. In the collection periods up to 72 h for naked ASO 7 an overall recovery of 32% and for GalNAc ASO 8 an overall recovery of 41% of the dose was found. The main proportion of radioactivity was recovered in urine,

slightly less in feces. This is in line with literature reports that renal excretion is the dominant route of elimination for ASOs.^{22,23} Therefore, tritiated oligonucleotides labeled using this described conjugation technique might be well suited for mass balance and quantitative whole body autoradiography studies in order to gain a better understanding of the distribution and excretion of potential therapeutic ASOs.

Conclusions

Novel approaches to labeled antisense oligonucleotides with ³H were described. Conjugation of *N*-succinimidyl propionate (NSP) was attached to an amino-linker at the 3'-end, *N*-Methylmaleimide (NMM) and *N*-ethylmaleimide (NEM) were conjugated *via* Michael addition to sulfhydryl-linkers of oligonucleotides that target Malat1. Based on non-radiolabeled (cold) Malat1-ASO examples, *in vitro* experiments were carried out to investigate target efficiency and stability after the tag-modification. All cold-tagged Malat1 oligonucleotides showed similar RNA target reduction after 24 h, but metabolic instability of tag and linker in mouse hepatocyte cells was observed for the NSP-tagged ASO.

In contrast, the maleimide conjugates were metabolically stable *in vitro* up to 72 h. Consequently, [³H]NEM was selected as the conjugation agent of choice for this study, resulting in tritium-labeled ASO with high molar activity of up to 629 GBq/mmol (17 Ci/mmol). A single-dose PK experiment, including [³H]NEM-tagged GalNAc and naked ASO constructs, was performed in mice. It was demonstrated that the radiolabeled ASOs, despite the maleimide conjugation, show an equivalent PK behavior as their congeners. In conclusion, this new method to efficiently conjugate pre-labeled tags provides a powerful technique for fast and safe access to tritium-labeled oligonucleotides, e.g., for preclinical pharmacokinetic or autoradiography studies.

References


- (1) Stephenson, M. L., and Zamecnik, P. C. (1978) Inhibition of Rous sarcoma viral RNA translation by a specific oligodeoxyribonucleotide. *Proc. Natl. Acad. Sci. (USA)* 75, 285-288.
- (2) Wang, F., Zuroske, T., and Watts, J. (2020) RNA therapeutics on the rise. *Nat. Rev. Drug. Discov.* 19, 441-442.
- (3) Muntoni, F., and Wood, M. J. (2011) Targeting RNA to treat neuromuscular disease. *Nat. Rev. Drug. Discov.* 10, 621-637.
- (4) Havens, M. A., and Hastings, M. L. (2016) Splice-switching antisense oligonucleotides as therapeutic drugs. *Nucleic Acids Res.* 44, 6549-6563.
- (5) Sasaki, S., Sun, R., Bui, H. H., Crosby, J. R., Monia, B. P., and Guo, S. L. (2019) Steric Inhibition of 5' UTR Regulatory Elements Results in Upregulation of Human CFTR. *Mol. Ther.* 27, 1749-1757.
- (6) Shemesh, C. S., Rosie, Z. Y., Gaus, H. J., Greenlee, S., Post, N., Schmidt, K., Migawa, M. T., Seth, P. P., Zanardi, T. A., and Prakash, T. P. (2016) Elucidation

- of the biotransformation pathways of a Galnac3-conjugated antisense oligonucleotide in rats and monkeys. *Mol. Ther. Nucleic Acids* 5, e319.
- (7) Graham, M., Freier, S., Crooke, R., Ecker, D., Maslova, R., and Lesnik, E. (1993) Tritium labeling of antisense oligonucleotides by exchange with tritiated water. *Nucleic Acids Res.* 21, 3737-3743.
 - (8) Christensen, J., Natt, F., Hunziker, J., Krauser, J., Andres, H., and Swart, P. (2012) Tritium labeling of full-length small interfering RNAs. *J. Label. Compds. Radiopharm.* 55, 189-196.
 - (9) Tan, W., Iyer, R. P., Jiang, Z., Yu, D., and Agrawal, S. (1997) Method of tritium labeling oligonucleotides. *Patent US5668262A*.
 - (10) Palazzolo, A., Feuillastre, S., Pfeifer, V., Garcia-Argote, S., Bouzouita, D., Tricard, S., Chollet, C., Marcon, E., Buisson, D. A., Cholet, S., Fenaille, F., Lippens, G., Chaudret, B., and Pieters, G. (2019) Efficient access to deuterated and tritiated nucleobase pharmaceuticals and oligonucleotides using hydrogen-isotope exchange. *Angew. Chem.* 131, 4945-4949.
 - (11) Hagedorn, P. H., Persson, R., Funder, E. D., Albæk, N., Diemer, S. L., Hansen, D. J., Møller, M. R., Papargyri, N., Christiansen, H., and Hansen, B. R. (2018) Locked nucleic acid: modality, diversity, and drug discovery. *Drug Discov. Today* 23, 101-114.
 - (12) Sewing, S., Boess, F., Moisan, A., Bertinetti-Lapatki, C., Minz, T., Hedtjaern, M., Tessier, Y., Schuler, F., Singer, T., and Roth, A. B. (2016) Establishment of a predictive in vitro assay for assessment of the hepatotoxic potential of oligonucleotide drugs. *PLoS One* 11, e0159431.
 - (13) Straarup, E. M., Fisker, N., Hedtjärn, M., Lindholm, M. W., Rosenbohm, C., Aarup, V., Hansen, H. F., Ørum, H., Hansen, J. B. R., and Koch, T. (2010) Short locked nucleic acid antisense oligonucleotides potently reduce apolipoprotein B mRNA and serum cholesterol in mice and non-human primates. *Nucleic Acids Res.* 38, 7100-7111.
 - (14) Husser, C., Brink, A., Zell, M., Müller, M. B., Koller, E., and Schadt, S. (2017) Identification of GalNAc-conjugated antisense oligonucleotide metabolites using an untargeted and generic approach based on high resolution mass spectrometry. *Anal. Chem.* 89, 6821-6826.
 - (15) Husser, C., Koller, E., Brink, A., and Schadt, S. (2019) Studying the Biotransformation of Phosphorothioate-Containing Oligonucleotide Drugs by LC-MS, in *Oligonucleotide-Based Therapies* (Gissberg, O., Zain, R., and Lundin, K. E., Eds.) pp 307-315, Springer, Berlin.
 - (16) Grünweiler, A., and Hartmann, R. K. (2007) Locked nucleic acid oligonucleotides. *BioDrugs* 21, 235-243.
 - (17) Sewing, S., Gubler, M., Gérard, R., Avignon, B., Mueller, Y., Braendli-Baiocco, A., Odin, M., and Moisan, A. (2019) GalNAc conjugation attenuates the cytotoxicity of antisense oligonucleotide drugs in renal tubular cells. *Mol. Ther. Nucleic Acids* 14, 67-79.
 - (18) Disterer, P., Al-Shawi, R., Ellmerich, S., Waddington, S. N., Owen, J. S., Simons, J. P., and Khoo, B. (2013) Exon skipping of hepatic APOB pre-mRNA with splice-switching oligonucleotides reduces LDL cholesterol in vivo. *Mol. Ther.* 21, 602-609.
 - (19) Buntz, A., Killian, T., Schmid, D., Seul, H., Brinkmann, U., Ravn, J., Lindholm, M., Knoetgen, H., Haucke, V., and Mundigl, O. (2019) Quantitative fluorescence imaging determines the absolute number of locked nucleic acid oligonucleotides needed for suppression of target gene expression. *Nucleic Acids Res.* 47, 953-969.
 - (20) Edelmann, M. R., and Muser, T. (2021) Tritium O-Methylation of N-Alkoxy Maleimide Derivatives as Labeling Reagents for Biomolecules. *Bioconjug. Chem.* 32, 1027-1033.
 - (21) Post, N., Yu, R., Greenlee, S., Gaus, H., Hurh, E., Matson, J., and Wang, Y. (2019) Metabolism and disposition of volanesorsen, a 2'-O-(2 methoxyethyl) antisense oligonucleotide, across species. *Drug. Metab. Dispos.* 47, 1164-1173.

- (22) Yu, R. Z., Kim, T.-W., Hong, A., Watanabe, T. A., Gaus, H. J., and Geary, R. S. (2007) Cross-species pharmacokinetic comparison from mouse to man of a second-generation antisense oligonucleotide, ISIS 301012, targeting human apolipoprotein B-100. *Drug. Metab. Dispos.* 35, 460-468.
- (23) Bosgra, S., Sipkens, J., de Kimpe, S., den Besten, C., Datson, N., and van Deutekom, J. (2019) The pharmacokinetics of 2'-O-methyl phosphorothioate antisense oligonucleotides: experiences from developing exon skipping therapies for Duchenne muscular dystrophy. *Nucleic Acid Ther.* 29, 305-322.

Chapter Three

Tritium O-methylation of *N*-alkoxy maleimide derivatives as labeling reagents for biomolecules

This declaration concerns the article entitled:			
Tritium O-methylation of <i>N</i> -alkoxy maleimide derivatives as labeling reagents for biomolecules			
Publication status (tick one)			
Draft manuscript	<input type="checkbox"/>	Submitted	<input type="checkbox"/>
In review	<input type="checkbox"/>	Accepted	<input type="checkbox"/>
		Published	<input checked="" type="checkbox"/>
Publication details (reference)	Edelmann MR*, Muser T. (2021) <i>Bioconjug. Chem.</i> 32 :1027-1033		
Copyright status (tick the appropriate statement)			
I hold the copyright for this material	<input type="checkbox"/>	Copyright is retained by the publisher, but I have been given permission to replicate the material here	<input checked="" type="checkbox"/>
Candidate's contribution to the paper (provide details, and also indicate as a percentage)	<p>The candidate contributed to / considerably contributed to / predominantly executed the...</p> <p>Formulation of ideas: 90%</p> <p>Design of methodology: 100%</p> <p>Experimental work: 50%</p> <p>Presentation of data in journal format: 100%</p>		
Statement from Candidate	<p>"Reprinted with permission from <i>Bioconjugate Chem.</i> 2021, 32, 5, 1027–1033. Copyright 2021 American Chemical Society."</p> <p>https://pubs.acs.org/doi/full/10.1021/acs.bioconjchem.1c00202</p> <p>This paper reports on original research I conducted during the period of my Higher Degree by Research candidature.</p>		
Signed		Date	17.10.22

Introduction

Conjugations with functionalized maleimide derivatives have been popular in biochemistry or biotechnology.¹ The double bond of maleimides may undergo a Michael-type addition with sulfhydryl groups to form stable thioether bonds. The main use of maleimide derivatives is the bioconjugation to thiols, which are either naturally present in biomolecules or have been previously introduced. This technique is widely used in radio- or fluorescent labeling,^{2,3} or for the preparation of antibody-drug-conjugates.⁴ Thiol-maleimide additions take place quickly in the pH range of 6.5 to 7.5 in a high yield without the formation of byproducts, even in aqueous solution. Several functionalized maleimides are commercially available or accessible in a few synthesis steps. The simplest functionalization of maleimides is by formation of the equivalent *N*-alkyl derivatives.

Non-radiolabeled alkylated maleimide derivatives, such as *N*-ethylmaleimide (NEM) or *N*-methylmaleimide (NMM) are used in protein analytics, e.g. to identify free sulfhydryl groups in antibodies⁵ or for thiol-blocking in cysteine residues.^{6,7} Tritium labeled alkyl-maleimides, on the other hand, are used to determine the number of sulfhydryl groups in proteins,⁸ to identify surface-exposed cysteine residues,⁹ or in assays of protein palmitoylation.¹⁰ *N*-Alkylated tritium maleimide derivatives are also used in Michael-type additions to thiol-linkers in several types of biomolecules for tracking and monitoring, e.g. in oligonucleotides or proteins.^{11,12} A general disadvantage of NEM and NMM is their high volatility, which is a major challenge in dealing with them in radioactive conjugation reactions.

The most common way to access *N*-alkylated maleimides is the reaction of maleic anhydride with a primary amine, followed by dehydration.¹³ However, the translation of the aforementioned synthetic strategy for the preparation of tritiated analogues becomes a challenge due to the high volatility of the required primary amines. Methylamine with its boiling point of -6 °C and ethylamine (17 °C) pose a safety risk when handling radioactive compounds. In addition to the high volatility of these alkylamines, the corresponding tritiated compounds are only commercially available with a molar activity in the range of 370 – 740 GBq/mmol (10 - 20 Ci/mmol). For this reason, an alternative and safe synthetic route was required for the introduction of a tritium label on maleimide derivatives.

Palladium-catalyzed reduction of *N*-alkylated maleimides bearing an exocyclic carbon-carbon double or triple bond in the presence of tritium gas is not a viable option, since the maleimide double bond, required for a subsequent Michael-addition, will be reduced as well. A promising concept can be designed by late-stage alkylation of nucleophiles, such as amines or alcohols.

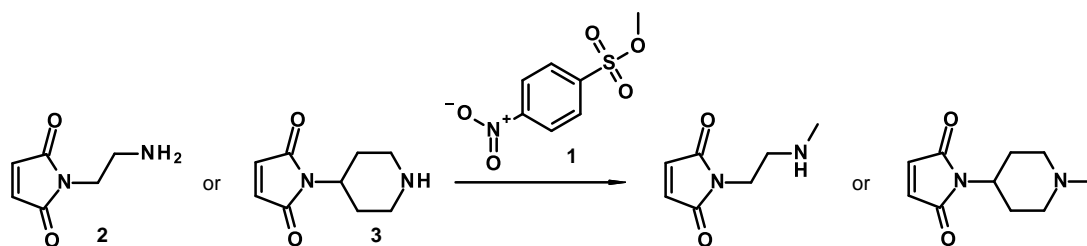
In this article, an alternative strategy to access tritium-labeled maleimide derivatives using *N*-hydroxyalkyl *exo*-maleimide-2,5-dimethylfuran cycloadducts in good yields and high molar activities (> 1.5 TBq/mmol; 40 Ci/mmol) is described. The synthesis avoids the use of volatile radioactive reagents and therefore significantly mitigates the safety risks in the preparation of tritiated *N*-alkyl maleimides. For a safe and robust concept with regard to late-stage labeling, we have examined *N*- and *O*-methylation with methyl nosylate.

Results & Discussion

Since Pounds' report in 2004,¹⁴ [³H]methyl nosylate **1** ([³H]methyl-4-nitrobenzene sulfonate) has been used in tritium-based chemistry as a radiochemically stable reagent for methylation of alcohols or amines. [³H]Methyl nosylate is commercially available at a molar activity of > 3 TBq/mmol (80 Ci/mmol) and in contrast to the corresponding methylation reagent [³H]methyl iodide it is not volatile. The fastest and easiest way to synthesize methylated maleimide derivatives is the direct alkylation of an amine or hydroxy functionalized maleimide precursor.

Direct methylation of *N*-substituted maleimides containing amino and hydroxy functionalities with [³H]methyl nosylate

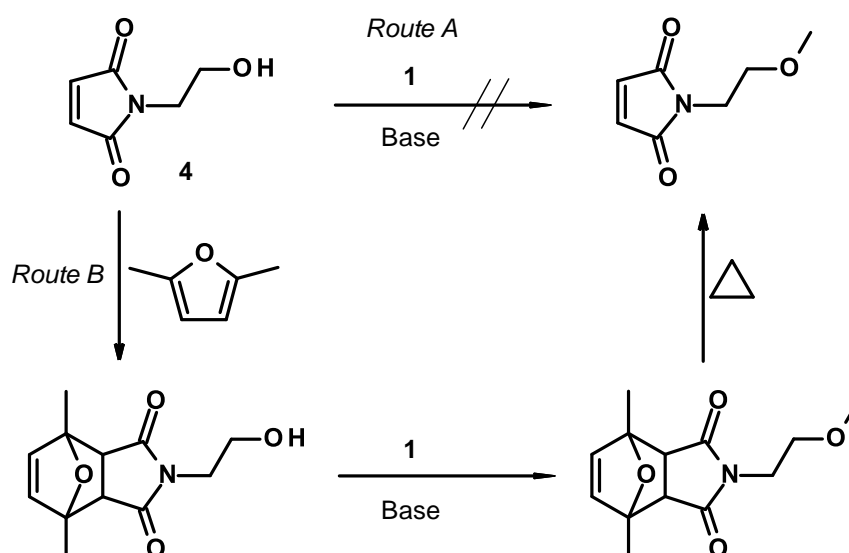
In the first experiments, it was aimed for an *N*-methylation and therefore two maleimide derivatives *N*-(2-aminoethyl)-maleimide **2** and *N*-(4-piperidyl)-maleimide **3** were selected (**Scheme 1**). Although the methylated products were isolated in low yield but in high purity, the stability of the products in solution was low and the compounds decomposed over 24 hours. It was hypothesized for **2** that this inherent instability might originate from the unprotected amine functionality, which is prone to react intramolecularly with the electrophilic imide carbonyls or intermolecularly with the activated olefin. In addition for **2** and **3**, the basicity of the methylated amine may promote hydrolysis of the maleimide core, which leads to ring opening. This observation confirms results reported in previous articles on the hydrolysis of maleimides in alkaline solutions.¹⁵ For this reason, the strategy was changed from *N*-methylation to *O*-methylation of a primary alcohol by using *N*-(2-hydroxyethyl)-maleimide **4** as substrate. Since a base, such as sodium hydride, sodium *tert*-butoxide, or lithium bis(trimethylsilyl)amide, was required for deprotonation of primary alcohols to perform a methylation with methyl nosylate, this synthesis route was also unsuccessful (**Scheme 2: Route A**).



Scheme 1: N-Methylation of maleimide derivatives containing amine functionality.

Using Diels Alder cycloadduct as a protecting group for hydroxyethyl-maleimide prior to methylation with [³H]methyl nosylate

N-(2-Hydroxyethyl)-maleimide **4** was selected as starting material to investigate the O-methylation of maleimide derivatives, which involves three steps: 1) protection of the maleimide core; 2) methylation on deprotonated hydroxy functionality; 3) deprotection to the final maleimide (**Scheme 2: Route B**).



Scheme 2: Investigated synthesis routes to methylate N-(2-hydroxyethyl)-maleimide **4** from methyl nosylate **1**. *Route A:* direct methylation starting from unprotected **4** and **1** did not lead to the desired product under basic conditions. *Route B:* protected **4** can be methylated in the presence of bases and deprotected by heating to achieve the target methylated maleimide derivative.

The introduction of a protecting group is essential for a chemical modification of maleimides under basic conditions. Maleimides can generally be easily protected under mild heating with furan analogues, resulting in a [4+2] Diels-Alder (DA) cycloadduct.¹⁶ The formed furan-maleimide cycloadduct prevents the possibility of a nucleophilic attack and allows O-alkylation under strongly basic conditions. Two relevant aspects are to be considered for a successful methylation labeling concept under basic conditions: 1) the

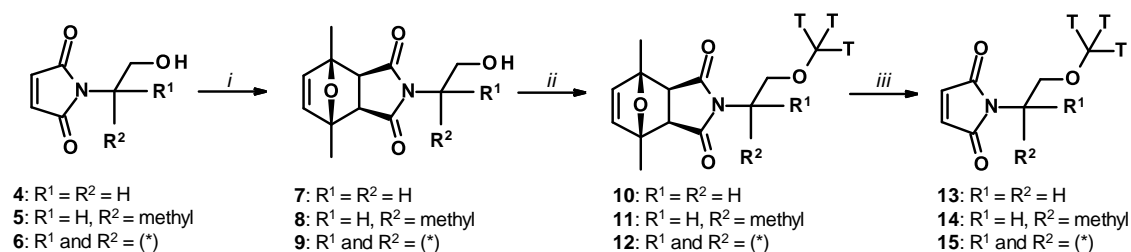
selection of the furan analogue for the protection, and 2) the selection of the diastereoisomer after the [4+2]-cycloaddition for the subsequent deprotection.

It is well known that the DA reaction between electron-deficient maleimides and dienes such as furans leads to a mixture of two diastereomers: *endo*, the kinetically controlled compound, and *exo*, the thermodynamically more stable compound.¹⁷ Although the *endo* compound can be deprotected more easily under retro-Diels-Alder (rDA) reaction conditions by heating,¹⁸ it is also less stable towards a base compared to the *exo* compound.^{19,20}

A comparison of different furan derivatives as a protecting group, namely furan, 2-methylfuran and 2,5-dimethylfuran, showed that 2,5-dimethylfuran has the best stability towards bases.²¹ Based on this knowledge, the synthesis route was adjusted as shown in **Scheme 3**.

After DA protection with 2,5-dimethylfuran, the obtained *exo/endo* intermediates formed in a diastereomeric mixture ratio of 4:1 were separated into the pure *exo* compound in 55-60% yield by the use of silica-based flash chromatography. In order to achieve a simpler handling on small scale for the methylation step, commercially available [³H]methyl nosylate (**1**, 3.3 TBq/mmol; 88 Ci/mmol) was diluted with non-labeled methyl nosylate to achieve a molar activity of 1.6 TBq/mmol (44 Ci/mmol), which comfortably still meets the requirements (> 37 GBq/mmol; 1 Ci/mmol) for tracking of molecules (< 10,000 Da) after conjugation to tritium labeled maleimides. A solid phase supported workup was carried out by using strong ion exchange (SCX-2/SAX) cartridges.²² This method allows a fast, safe, and efficient work-up for tritium labeled compounds with high recovery rates. Deprotection was carried out by a retro-Diels-Alder reaction by heating at 110 °C to give the desired tritium labeled *N*-[³H]-2-methoxyethyl maleimide **13** in an overall radiochemical yield of 15%.

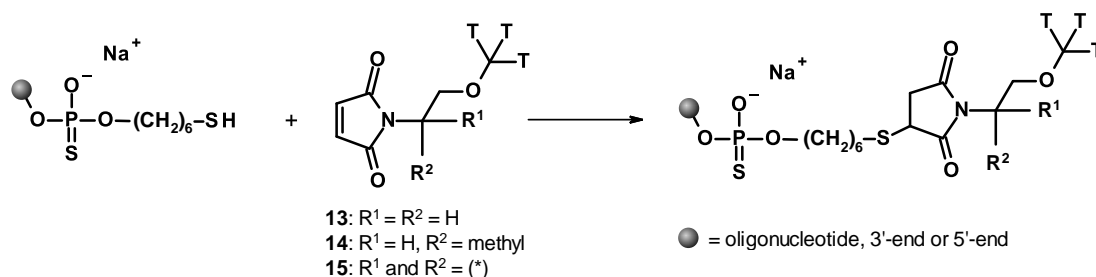
The robustness of this synthetic route was confirmed by repeating it with *N*-(2-hydroxy-1-methyl-ethyl)maleimide **5** and *N*-[1-(hydroxymethyl) cyclopropyl]maleimide **6** as starting materials. In both cases similar yields of 13%-15% were observed.



Scheme 3: Synthesis route to tritium-methylated *N*-alkoxy maleimide derivatives **13**, **14**, **15**: i: 2,5-dimethylfuran, acetonitrile, 65 °C, 16 h. ii: [³H]methyl nosylate **1**, sodium tert-butoxide, toluene, 22 °C, 2.5 h. iii: toluene, 110 °C, 2 h. (*): R¹ and R² together with the carbon atom to which they are attached form a cyclopropyl ring.

Conjugation of ³H-Maleimides on Thiol-functionalized Oligonucleotides

To prove the reactivity of the tritium-labeled maleimides **13**, **14**, and **15**, 2 different tool-oligonucleotides were used for conjugation experiments. The oligonucleotides contain a phosphorothioate-hexylenethiol-linker, either at 5'-end or 3'-end, which can be used for a Michael-type addition (**Scheme 4**). For the conjugation experiments, the purified tritium-labeled maleimides **13**, **14**, and **15** were used directly from the preparative HPLC-fractions without solvent exchange and added to a pH 7 buffered oligonucleotide solution. In order to achieve the highest possible conversion of tritiated maleimides, the oligonucleotide was used for the conjugation in a double molar excess, followed by a post-conjugation with the corresponding cold (non-radioactive) maleimide derivative in a 10-fold molar excess. In this way, a lower specific activity was consciously accepted. However, the resulting molar activities of 370 GBq/mmol to 740 GBq/mmol (10-20 Ci/mmol) still comfortably meet the requirements for *in vivo* disposition and QWBA studies. In order to determine the specific activity of the conjugates, the activity concentration [MBq/mL] of the oligonucleotide solution was determined by liquid scintillation counting and divided by the content concentration [mg/mL] measured using a spectrometer to give the specific activity in [MBq/mg]. Based on the molecular weight, the molar activity in [GBq/mmol] was calculated for each tritium-labeled oligonucleotide.



Scheme 4: General conjugation reaction of thiol-functionalized oligonucleotides with maleimide derivatives **13**, **14**, **15**. (*): R¹ and R² together with the carbon atom to which they are attached form a cyclopropyl ring.

Conclusions

In this manuscript, we have disclosed a facile and efficient method for radiolabeling of *N*-alkoxy maleimide derivatives from [³H]methyl nosylate. One of the most important features of these tritium-methyl-labeled compounds is that they are less volatile than the corresponding *N*-alkylated maleimides *N*-ethylmaleimide (NEM) or *N*-methylmaleimide (NMM). The standard molar enthalpy of sublimation of NMM ($\Delta_{\text{sub}}H_m^\circ = 73.3$ KJ/mol at 293.15 K)²³ is comparable to that of naphthalene ($\Delta_{\text{sub}}H_m^\circ = 73.0$ KJ/mol at 298.15 K).²⁴ No data could be found in the literature on NEM. However, a rapid weight loss of NEM was observed during previous conjugation preparations. Since tritium-labeled NEM is

supplied in a pentane solution, a solvent exchange must be carried out prior to bioconjugations. This handling bears the risk of undesired release of radioactivity and loss of NEM.

Starting from *N*-substituted maleimides containing exocyclic hydroxy functionality, base-stable intermediates of *O*-methylations were obtained by a Diels-Alder [4+2] cycloaddition reaction in the presence of 2,5-dimethylfuran. Protected maleimides enable the methylation of primary alcohols under basic conditions and prevent nucleophilic attack from Michael-type donors. A solid-phase supported work-up by the use of strong ion exchange cartridges (SCX-2/SAX) leads to pure intermediates. The final products were gained *via* a retro Diels-Alder reaction by heating the protected tritium-labeled maleimides. Although multi-step synthesis of tritium-labeled compounds is a particular challenge, this synthetic route is characterized by mild reaction conditions, efficient work-up, and high radiochemical purities. This is also reflected in the overall radiochemical yields of 13-15%, which is a notable result for a 3-step synthesis with tritiated compounds. The purified radioactive maleimides can be used directly from the preparative HPLC fractions without a solvent exchange for subsequent bioconjugations. Consequently, this allows quantitative use without loss of radioactivity and enables safe handling. The reactivity of the novel tritium-labeled maleimide derivatives was proven by a conjugation step on thiol-functionalized oligonucleotides.

This concept opens up new possibilities for safe, fast and cost-saving access to tritium-labeled maleimide derivatives. These radiotracers find wide applications in biology and biotechnology, such as tracking biomolecules in *in vitro* and *in vivo* studies.

Experimental

Material and Methods

All chemical starting materials are commercially available and have been used without further purification. Tritium labeled [³H]methyl nosylate (molar activity: 3.3 TBq/mmol = 88 Ci/mmol) was obtained from RC Tritec (Teufen, Switzerland) as solution in toluene. Liquid scintillation counting was accomplished using a HIDEX 300 SL and ULTIMATE GOLD™ cocktail (PerkinElmer Inc., Waltham, MA, USA). Analytical HPLC for maleimide-based derivatives were performed using an Agilent 1200 series HPLC system (Santa Clara, CA, USA) using a Waters XBridge C18 column (4.6 mm x 150 mm, 3.5 μm). HPLC conditions: mobile phase [A]: (H₂O+0.05% TFA), [B]: (acetonitrile/H₂O+0.05% TFA), gradient 10% [B] to 70% [B] over 12 min. Radiochemical purity was measured using the β Radioactivity HPLC detector RAMONA with internal solid scintillator (Elysia-raytest, Straubenhardt, Germany). Preparative purification for tritium labeled maleimides was performed by the use of Gilson PLC 2050 (Middleton, WI, USA), equipped with a Waters

XBridge C18 column (10 mm x 300 mm, 5 μ m) under the following conditions: Solvent [A] was water + 5% acetonitrile + 0.05% trifluoroacetic acid (v/v/v) and solvent [B] was acetonitrile + 0.05% trifluoroacetic acid (v/v). The column was initially equilibrated at 10% [B] using a flow rate of 6 mL/min, with the absorbance monitored at 214 nm. Starting with isocratic conditions of 10% [B] for 4 minutes, a linear gradient to 70% [B] followed over 15 minutes. The desired products eluted from the column at about 25% [B]. For purification of DA adducts, an Isco Combiflash[®] Rf+. (Lincoln, NE, USA) in combination with Disposable RediSep[™] silica gel columns (4 g) was used for flash column chromatography under the following conditions: Solvent [A] was heptane and solvent [B] was methyl *t*-butyl ether. The column was initially equilibrated at 20% [B] using a flow rate of 18 mL/min, with the absorbance monitored at 214 nm. The elution gradient consisted of isocratic conditions at 20% [B] for 4 minutes, followed by linear gradients to 100% [B] in 14 minutes, and finally isocratic conditions at 100% [B] over 5 minutes. Proton nuclear magnetic resonance (¹H NMR) spectra were recorded on a Bruker Avance III (600 MHz) instrument. ¹H chemical shifts (δ) are reported in parts per million (ppm) and referenced using residual solvent resonance relative to tetramethylsilane. Signal multiplicity is described using the following abbreviations: s (singlet), d (doublet), m (multiplet), dd (doublet of doublets), and br s (broad singlet). Coupling constants (*J*) are in hertz (Hz). Tritium-labeled intermediates and products were identified by HPLC comparison with commercially available non-radioactive materials or characterized compounds from Roche pharma Research and Early Development (pRED). Both oligonucleotides used as starting materials were synthesized from Roche pRED using standard phosphoramidite chemistry and consist of a complete phosphorothioate backbone. PBS buffer was purchased from Thermo Fisher Scientific (Paisley, UK), in one (1x) and tenfold (10x) concentration. Conjugated oligonucleotides were analyzed using UPLC Agilent 1290 at 260 nm wavelength and ACQUITY UPLC Oligonucleotide BEH C18, 2.1 x 50 mm, 1.7 μ m column at 80 °C under the following conditions: Solvent [A] was water/methanol/hexafluoro *i*-propanol/triethylamine: 950/25/21/2.3 mL; solvent [B] was water/methanol/hexafluoro *i*-propanol/triethylamine : 175/800/21/2.3 mL, and the following linear gradient of 10% [B] to 25% [B] in 13 min by a flow of 0.5 mL/min. Concentration of conjugated oligonucleotides were determined by Eppendorf Biospectrometer[®] basic (Hamburg, Germany) at 260 nm wavelength and the corresponding calculated molar extinction coefficient.

General Procedure of Maleimide Protection

To a solution of commercially available maleimide derivatives **4**, **5**, or **6** (1.42 mmol) in acetonitrile (2.0 mL) was added at 22 °C 2,5-dimethylfuran (720 mg, 800 µL, 7.5 mmol). The mixture was stirred at 65 °C in a sealed glass tube for 20 h. Removal of the solvent by evaporation and drying under high vacuum (3×10^{-2} mbar) gave the crude Diels-Alder adduct as a light yellow oil. The *endo/exo* mixture was purified by flash chromatography to isolate the *exo* compound **7**, **8**, or **9** in purities of > 95% and yields in the range 55 - 60%.

General Procedure of Methylation

1.67 GBq (45 mCi) of [³H]methyl nosylate **1** (125 µg, 0.561 µmol) as solution in toluene was diluted with non-radioactive methyl nosylate (122 µg, 0.561 µmol) in a 1:1 ratio to achieve a molar activity of approximately 1.6 TBq/mmol (44 Ci/mmol). The solution was evaporated, transferred into a sealed tube and concentrated to dryness under an argon flow. To the solid residue was added at 22 °C a solution of DA cycloadduct **7**, **8**, or **9** (2.81 µmol) in 80 µL toluene followed by the addition of 2 M sodium *t*-butoxide solution in THF (1.7 µL, 3.37 µmol). The mixture was stirred in a sealed tube at 22 °C for 2.5 h. HPLC analysis showed the desired intermediate products **10**, **11**, or **12** with a radiochemical purity of 50%. The reaction mixture was diluted with dichloromethane (DCM) (1 mL) and directly purified by filtration through a SCX-2/SAX cartridge (Silicycle, 500 mg, pre-conditioned with DCM) to remove basic and acidic impurities. The cartridge was washed with DCM (5 mL) and the resulting solution was concentrated by evaporation to a volume of 100 µL to give the radiolabeled intermediates **10**, **11**, or **12** in radiochemical purities of > 80%. The intermediates were used without further purification for the subsequent deprotection.

General Procedure of Deprotection

The obtained crude solution of **10**, **11**, or **12** was transferred into a sealed tube, diluted with toluene (70 µL) and heated at 110 °C for 2 h. HPLC analysis showed full conversion to the deprotected final product. The reaction mixture was allowed to cool to 22 °C. The solvent was concentrated to dryness under an argon flow. The residue was purified by preparative HPLC. The corresponding preparative HPLC fractions, containing the tritium labeled maleimide derivatives **13**, **14**, or **15**, were directly used for subsequent conjugation experiments. Radiochemical yields: 13 - 15%. Radiochemical purity: > 98%. The low sample concentration of tritiated maleimide derivatives made it impossible to determine the specific activity by mass spectrometry, since the ionization signal was too

low. Due to previous dilution of hot and cold methyl nosylate in 1:1 ratio, a molar activity of 1.6 TBq/mmol (44 Ci/mmol) is expected. Conjugation products of ^3H -maleimide derivatives on thiol-functionalized oligonucleotides, however, provided a clearer determination of the specific activity.

According to the *General Procedure of Maleimide Protection*, the following intermediates were synthesized:

exo-2-(2-hydroxyethyl)-4,7-dimethyl-3a,7a-dihydro-4,7-epoxyisoindole-1,3-dione (7).

This compound was isolated as a colorless solid in 55% yield and purity of > 95%; ^1H NMR (DMSO- d_6) δ ppm 6.36 (s, 2 H), 4.69 (br s, 2 H), 3.41 (s, 4 H), 2.88 (s, 2 H), 1.53 (s, 6 H); ESI-MS: m/z [M + H] $^+$ calcd for $\text{C}_{12}\text{H}_{15}\text{NO}_4$: 237.1001; found: 237.1001.

exo-2-(2-hydroxy-1-methyl-ethyl)-4,7-dimethyl-3a,7a-dihydro-4,7-epoxyisoindole-1,3-

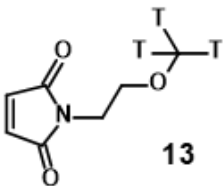
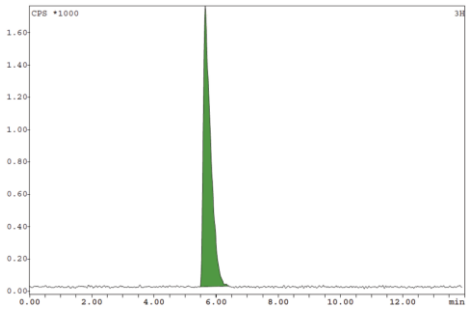
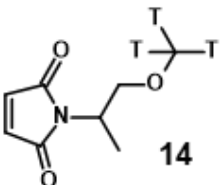
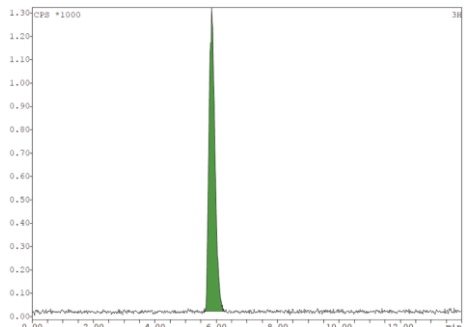
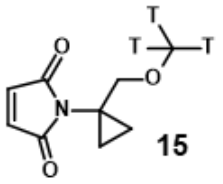
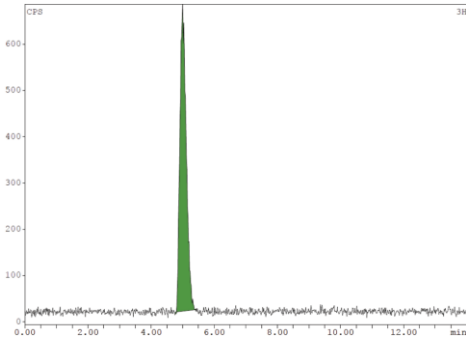
dione (8). This compound was isolated as a colorless oil in 60% yield and purity of > 90%; ^1H NMR (DMSO- d_6) δ ppm 6.36 (d, $J=1.6$ Hz, 2H), 4.54-5.09 (m, 1 H), 3.90-4.15 (m, 1 H), 3.67 (dd, $J=10.8, 8.1$ Hz, 1 H), 3.49 (dd, $J=10.8, 6.4$ Hz, 1 H), 2.82-2.87 (m, 1 H), 2.77-2.81 (m, 1 H), 1.53 (d, $J=4.0$ Hz, 6 H), 1.17 (d, $J=7.0$ Hz, 3 H); ESI-MS: m/z [M + H] $^+$ calcd for $\text{C}_{13}\text{H}_{17}\text{NO}_4$: 251.1158; found: 251.1152.

exo-2-[1-(hydroxymethyl)cyclopropyl]-4,7-dimethyl-3a,7a-dihydro-4,7-epoxyisoindole-

1,3-dione (9). This compound was isolated as a colorless solid in 60% yield and purity of > 95%; ^1H NMR (DMSO- d_6) δ ppm 6.35 (s, 2 H), 4.70 (br s, 1 H), 3.38 (s, 2 H), 2.78 (s, 2 H), 1.50 (s, 6 H), 0.89-0.93 (m, 2 H), 0.63-0.67 (m, 2 H); ESI-MS: m/z [M + H] $^+$ calcd for $\text{C}_{14}\text{H}_{17}\text{NO}_4$: 263.1158; found: 263.1169.

According to the *General Procedure of Deprotection*, the following products shown in **Table 1** were synthesized:

Table 1: Chemical structure of **13,14,15**, overall radiochemical yield, radiochemical purity, and the corresponding radio-HPLC traces.

Compound	Yield [%]	Purity [%]	Radio-HPLC Trace
 <p>13 <i>N</i>-(2-[³H]methoxyethyl)maleimide</p>	15.3	> 99	
 <p>14 <i>N</i>-(2-[³H]methoxy-1-methylethyl)maleimide</p>	13.2	> 99	
 <p>15 <i>N</i>-[1-(³H)methoxymethyl]cyclopropyl]maleimide</p>	15.2	> 99	

General Procedure of Maleimide Conjugation to Oligonucleotides

2 equivalents of oligonucleotide, containing 5'-end or 3'-end thiol-linker, was dissolved in PBS (10x) (volume factor: 250 mL/g). 1 equivalent of **13**, **14**, or **15**, directly used from preparative HPLC fraction eluent with a radio-concentration of 30.3 MBq/mL - 34.8 MBq/mL (0.82 - 0.94 mCi/mL), was added to the aqueous oligonucleotide solution and stirred at 22 °C for 1.5 h. UPLC analysis showed a conjugation rate of 30% to 50%.

10 equivalent of the corresponding cold (non-radioactive) maleimide derivative, dissolved in THF (volume factor: 700 mL/g), was added and stirred at 22 °C for 1 h. UPLC showed a complete conjugation. The reaction mixture was transferred into an Amicon® Pro purification system (MWCO: 3,000 Da) and centrifuged at 4,000 rpm. PBS (1x) was added, the process was repeated 4 times to complete the solvent exchange and to receive the purified product. The content concentration and activity concentration of the resulting buffered solution were determined. Radiochemical yields: 69% - 99%. Molar activities: 389 GBq/mmol - 770 GBq/mmol (10.5 Ci/mmol - 20.8 Ci/mmol). Radiochemical purities: 93.4% - 98.4%.

According to the *General Procedure of Maleimide Conjugation to Oligonucleotides*, the following oligonucleotides have been conjugated with **13**, **14**, or **15** (**Table 2**):

Table 2: Oligonucleotide-maleimide conjugates used for reactivity testing. Capital letters in sequence describe LNA modified nucleosides, small letters describe DNA nucleosides. Linker: -3'-C₆-SH = hexylene thiol at 3'-end; HS-C₆-5'- = hexylene thiol at 5'-end; SA: molar activity.

Sequence 5' → 3'	Linker	Label	Yield [%]	Purity [%]	SA [GBq/mmol] - [Ci/mmol]
5'-GAGttacttgccaACT-3'	-3'-C ₆ -SH	13	69	96.0	611 - 16.5
5'-TTAcActtaattatactTCC-3'	HS-C ₆ -5'-	13	72	98.4	677 - 18.3
5'-GAGttacttgccaACT-3'	-3'-C ₆ -SH	14	87	94.3	444 - 12.0
5'-TTAcActtaattatactTCC-3'	HS-C ₆ -5'-	14	89	93.4	387 - 10.5
5'-GAGttacttgccaACT-3'	-3'-C ₆ -SH	15	90	98.1	629 - 17.0
5'-TTAcActtaattatactTCC-3'	HS-C ₆ -5'-	15	99	97.3	770 - 20.8


References

- (1) Renault, K., Fredy, J. W., Renard, P.-Y., and Sabot, C. (2018) Covalent modification of biomolecules through maleimide-based labeling strategies. *Bioconjug. Chem.* **29**, 2497-2513.
- (2) Morais, M., and Ma, M. T. (2018) Site-specific chelator-antibody conjugation for PET and SPECT imaging with radiometals. *Drug Discov. Today Technol.* **30**, 91-104.
- (3) Kim, Y., Ho, S. O., Gassman, N. R., Korlann, Y., Landorf, E. V., Collart, F. R., and Weiss, S. (2008) Efficient site-specific labeling of proteins via cysteines. *Bioconjug. Chem.* **19**, 786-791.
- (4) Girish, S., Gupta, M., Wang, B., Lu, D., Krop, I. E., Vogel, C. L., Burris III, H. A., LoRusso, P. M., Yi, J.-H., and Saad, O. (2012) Clinical pharmacology of trastuzumab emtansine (T-DM1): an antibody–drug conjugate in development for the treatment of HER2-positive cancer. *Cancer Chemother. Pharmacol.* **69**, 1229-1240.
- (5) Robotham, A. C., and Kelly, J. F. (2019) Detection and quantification of free sulfhydryls in monoclonal antibodies using maleimide labeling and mass spectrometry. *MAbs* **11**, 757-766.

- (6) Chen, H., Liu, S., Li, S., Chen, J., Ni, J., and Liu, Q. (2018) Blocking the thiol at cysteine-322 destabilizes tau protein and prevents its oligomer formation. *ACS Chem. Neurosci.* 9, 1560-1565.
- (7) Reisz, J. A., Bechtold, E., King, S. B., Poole, L. B., and Furdui, C. M. (2013) Thiol-blocking electrophiles interfere with labeling and detection of protein sulfenic acids. *FEBS J.* 280, 6150-6161.
- (8) Baliga, B. S., Nelson, E., and Munro, H. N. (1976) A simple procedure for measuring small amounts of [¹⁴C] N-ethylmaleimide. *Anal. Biochem.* 72, 661-663.
- (9) Opalka, N., Beckmann, R., Boisset, N., Simon, M. N., Russel, M., and Darst, S. A. (2003) Structure of the filamentous phage pIV multimer by cryo-electron microscopy. *J. Mol. Biol.* 325, 461-470.
- (10) Drisdell, R. C., Alexander, J. K., Sayeed, A., and Green, W. N. (2006) Assays of protein palmitoylation. *Methods* 40, 127-134.
- (11) Edelmann, M. R. (2019), F. Hoffmann-La Roche AG.
- (12) Inoue, I., Pant, H. C., Tasaki, I., and Gainer, H. (1976) Release of proteins from the inner surface of squid axon membrane labeled with tritiated N-ethylmaleimide. *J. Gen. Physiol.* 68, 385-395.
- (13) Göksu, H., Topal, M., Keskin, A., Gültekin, M. S., Çelik, M., Gülçin, İ., Tanc, M., and Supuran, C. T. (2016) 9, 10-Dibromo-N-aryl-9, 10-dihydro-9, 10-[3, 4] epipyrroloanthracene-12, 14-diones: Synthesis and Investigation of Their Effects on Carbonic Anhydrase Isozymes I, II, IX, and XII. *Arch. Pharm.* 349, 466-474.
- (14) Pounds, S. (2004) Synthesis and Applications of Isotopically Labelled Compounds, (Dean, D. C., Filer, C. N., and MacCarthy, K. E., Eds.) pp 63-66, John Wiley & Sons Ltd.
- (15) Barradas, R. G., Fletcher, S., and Porter, J. D. (1976) The hydrolysis of maleimide in alkaline solution. *Can. J. Chem.* 54, 1400-1404.
- (16) Kappe, C. O., Murphree, S. S., and Padwa, A. (1997) Synthetic applications of furan Diels-Alder chemistry. *Tetrahedron* 53, 14179-14233.
- (17) Diels, O., and Alder, K. (1928) Synthesen in der hydroaromatischen Reihe. *Justus Liebigs Ann. Chem.* 460, 98-122.
- (18) Discekici, E. H., St. Amant, A. H., Nguyen, S. N., Lee, I.-H., Hawker, C. J., and Read de Alaniz, J. (2018) Endo and exo Diels–Alder adducts: temperature-tunable building blocks for selective chemical functionalization. *J. Am. Chem. Soc.* 140, 5009-5013.
- (19) Elduque, X., Sanchez, A., Sharma, K., Pedroso, E., and Grandas, A. (2013) Protected maleimide building blocks for the decoration of peptides, peptoids, and peptide nucleic acids. *Bioconjug. Chem.* 24, 832-839.
- (20) Paris, C., Brun, O., Pedroso, E., and Grandas, A. (2015) Exploiting protected maleimides to modify oligonucleotides, peptides and peptide nucleic acids. *Molecules* 20, 6389-6408.
- (21) Sánchez, A., Pedroso, E., and Grandas, A. (2011) Maleimide-dimethylfuran exo adducts: Effective maleimide protection in the synthesis of oligonucleotide conjugates. *Org. Lett.* 13, 4364-4367.
- (22) Muri, D., and Edelmann, M. R. (2018) Tools for work-up and prepurification of tritium-labeled small molecules. *J. Label. Compds. Radiopharm.* 61, 912-915.
- (23) Roux, M. V., Jiménez, P., Martín-Luengo, M. Á., Dávalos, J. Z., Sun, Z., Hosmane, R. S., and Liebman, J. F. (1997) The elusive antiaromaticity of maleimides and maleic anhydride: Enthalpies of formation of N-methylmaleimide, N-methylsuccinimide, N-methylphthalimide, and N-benzoyl-N-methylbenzamide. *J. Org. Chem.* 62, 2732-2737.
- (24) Irving, R. (1972) The standard enthalpy of sublimation of naphthalene. *J. Chem. Thermodyn.* 4, 793-794.

Chapter Four

Tritium-labelling of neuromedin S by conjugation with [³H]N-succinimidyl propionate

This declaration concerns the article entitled:			
Tritium-labelling of neuromedin S by conjugation with [³ H]N-succinimidyl propionate			
Publication status (tick one)			
Draft manuscript	<input type="checkbox"/>	Submitted	<input type="checkbox"/>
In review	<input type="checkbox"/>	Accepted	<input type="checkbox"/>
		Published	<input checked="" type="checkbox"/>
Publication details (reference)	Edelmann MR*, Erny J, Guba W, Hierl M. (2022) <i>ACS Omega</i> 8(2):2367-2376		
Copyright status (tick the appropriate statement)			
I hold the copyright for this material	<input checked="" type="checkbox"/>	Copyright is retained by the publisher, but I have been given permission to replicate the material here	<input type="checkbox"/>
Candidate's contribution to the paper (provide details, and also indicate as a percentage)	<p>The candidate contributed to / considerably contributed to / predominantly executed the...</p> <p>Formulation of ideas: 100%</p> <p>Design of methodology: 100%</p> <p>Experimental work: 70%</p> <p>Presentation of data in journal format: 100%</p>		
Statement from Candidate	This paper reports on original research I conducted during the period of my Higher Degree by Research candidature.		
Signed		Date	17.10.22

Introduction

Human neuromedin S (NMS) is a 33 amino acid neuropeptide belonging to the tachykinin family. It has been identified in brain as an endogenous ligand for the orphan G-protein-coupled receptor (GPCR) FM-4/TGR-1, and acts on the neuromedin U (NMU) receptor 2 (NMUR₂) in the regulation of body weight homeostasis.¹⁻³ The "S" nomenclature derives from the fact that NMS is highly expressed in the suprachiasmatic nucleus (SCN) of the hypothalamus. NMS is structurally related to human NMU (25-mer), first described in 1985 and named for its ability to stimulate smooth muscle contraction in the uterus.⁴ NMS and NMU both share an identical C-terminal heptapeptide (FLFRPRN-NH₂) including the amidated asparagine at the C-terminus in different species (e.g. chicken, mouse, Chinese softshell turtle, spotted gar, Nile tilapia),⁵ indicating the importance of this peptide segment for receptor recognition. It was shown that this heptapeptide and the amidated asparagine are closely related to binding activity.^{6,7}

Radioisotope labelling of peptides is an essential tool to determine fate in *in vitro* and *in vivo* experiments. As all peptides contain hydrogen and carbon, the corresponding radioisotopes are the most commonly used in biological studies. Tritium as a low-energy (19 keV) beta emitter has gained importance mainly because its half-life (12.6 y) is relatively long and the compounds can reach a high specific activity. However, the introduction of a tritium atom into a peptide is not straightforward. The incorporation of a tritiated amino acid into a peptide sequence is theoretically possible, but in practice, it is difficult and time-consuming when larger peptides are to be labelled. Catalytic titration is often complicated by the presence of interfering functional groups (e.g. thiol) within the peptide sequence, which can deactivate the catalyst during a reduction or exchange reaction. While tritium labelling has been reported for numerous neuropeptides, such as neuromedin N (6-mer)⁸, neuromedin U-8 (8-mer)⁹, angiotensin II (8-mer), and neurotensin 8-13 (6-mer),¹⁰ no tritium labelling concept for NMS has been published to date.

Considerations for Tritiating Peptides

Tritium labelling chemistry is often simple and labelling can usually be performed late in the synthesis. The most stable labelling position is found in a carbon-tritium bond. There are various considerations for the introduction of a tritium atom into NMS, which are illustrated in **Figure 1** and divided into four main routes. A) Derivatisation with a tritium-labelled conjugate. B) Catalytic hydrogen/tritium exchange (HTE) starting from the native

NMS. C) Tritiation of NMS precursor. D) Solid-phase NMS synthesis using tritiated amino acid.

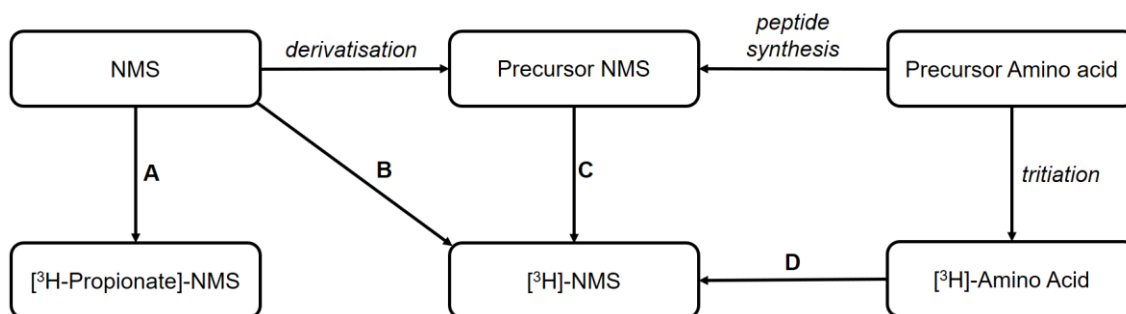


Figure 1: Considerations to tritium-labelled Neuromedin S (NMS). **A:** Derivatisation of peptide using [³H]*N*-succinimidyl propionate [³H]NSP; **B:** Catalytic hydrogen/tritium exchange starting from the native peptide; **C:** Tritiation of NMS-precursor; **D:** Peptide synthesis using tritiated amino acid.

Late-stage tritium-labelling by catalysed HTE finds wide application in small molecules.¹¹⁻¹³ These methods can only be applied to a limited extent for peptides. Promising approaches have been described, such as photoredox catalytic HTE in peptide backbone.¹⁴ As this exchange is based on a radical mechanism, the consequence is the loss of existing chiral stereocenters in the peptide backbone. Another approach to late-stage labelling of peptides is the high-temperature solid-state catalytic isotope exchange reaction (HSCIE) described by Zolotarev and co-workers.¹⁵ HTE mainly occurs in the aromatic part of tyrosine residues, with an exchange at the *ortho*-position to the OH group. For small peptides, there is the possibility of total synthesis using tritiated amino acids as starting materials, either by solid-phase synthesis¹⁶ or by enzymatic couplings.¹⁷ The advantage is that the labelling position is known using characterised amino acids and the specific activity can be adjusted as desired depending on the use of several ³H-amino acids.

An alternative strategy for the synthesis of tritiated peptides is to use an appropriate peptide precursor. Access to peptide precursors can be achieved either by peptide synthesis using modified amino acids or by post-modification of the native peptide. Halogenated aromatic amino acids or amino acids containing double or triple bonds are widely used in peptide synthesis to design peptide precursors. Subsequent metal-catalysed halogen-tritium exchange¹⁸ or reduction of the double/triple bond¹⁹ with tritium gas leads to the desired ³H-peptide. Derivatisation of a native peptide by direct iodination with non-radioactive iodine (¹²⁷I) using sodium iodide and an oxidising agent, such as Iodo-Gen or chloramine-T, also leads to a peptide precursor. This results in iodination primarily at tyrosine residues, but also at histidine residues in the sequence. Recently, the direct photochemical halogenation of peptides in a direct irradiation device and the single-pulse irradiation capillary reactor has been reported.²⁰ The specific

halogenation occurs with a bromination at tyrosine, histidine, and tryptophan residues as well as with an iodination at tyrosine and histidine residues. The halogens can subsequently be exchanged for tritium with tritium gas under metal catalysis.⁸

Another approach for tritiated peptides, especially larger peptides, is derivatisation with a relatively small tritiated group. In analogy to protein derivatisation,^{21,22} peptides can be tritiated by conjugation with the electrophilic *N*-succinimidyl-[2,3-³H₃]propionate ([³H]NSP). [³H]NSP preferentially reacts with primary amines such as the *N*-terminal amine or with lysine residues.²³ Keller and co-workers were able to introduce amine functionality into peptides lacking lysines by modifying arginine residues with an amine linker and used this for conjugation with [³H]NSP.¹⁰

Results and Discussions

Preliminary Labelling Experiments on NMS: Preparation of Iodinated Precursor

Commercially available NMS (human) has the following sequence: H-Ile-Leu-Gln-Arg-Gly-Ser-Gly-Thr-Ala-Ala-Val-Asp-Phe-Thr-Lys-Lys-Asp-His-Thr-Ala-Thr-Trp-Gly-Arg-Pro-Phe-Phe-Leu-Phe-Arg-Pro-Arg-Asn-NH₂. The synthesis of an NMS precursor was the first strategy explored. As described above in *Considerations for Tritiating Peptides*, derivatisation with iodine on Tyr is a common method for accessing peptide precursors. However, the peptide sequence of human NMS does not contain a Tyr, but does contain a His residue. For this purpose, the reaction conditions of iodination at the His residue of NMS were optimised to synthesise an iodinated precursor. The peptide was treated at pH 5 and pH 10 with sodium iodide in four different oxidising agents namely: chloramine-T, Iodo-Beads (polymer-supported version of chloramine-T), iodogen, and the recently described chloramine oxidant.²⁴ The highest iodine incorporation was obtained using chloramine-T at pH 10 with 35% I₁ and 65% I₂ (**Table 1**).

Table 1: Iodine incorporation in NMS dependent on pH and oxidation agent after 1 h, analysed by mass spectrometry.

#	Oxidation Agent	pH	I ₀ [%]	I ₁ [%]	I ₂ [%]
1	Chloramine-T	5	35	56	9
2	Chloramine-T	10	0	35	65
3	Iodo-Beads	5	76	24	0
4	Iodo-Beads	10	57	23	20
5	Iodogen	5	90	10	0
6	Iodogen	10	54	25	21
7	Chloramine	5	93	7	0
8	Chloramine	10	86	14	0

The catalytic exchange of iodine to tritium is described in the literature exclusively on iodinated Tyr residues, although for the tritium labelling approach of peptides, iodination on His is also mentioned.²⁵ Therefore, the conditions were adopted in analogy to the iodine-tritium exchange on Tyr to tritiate the NMS precursor.²⁶ The iodinated precursor #2 (chloramine-T, pH 10) was selected for the exchange experiments, as it yielded the highest iodine incorporation in His. PdO/BaSO₄ (10 % Pd) and Pd/C (10 % Pd) were tested as catalysts for an iodine-His isotope exchange in dimethylformamide as solvent. As a further variation, the experiments were each carried out with and without the addition of 1 µL triethylamine in the presence of deuterium gas at 22 °C for 2 h. However, a successful exchange was not achieved at the deuterium manifold in any of the experiments. As the reaction optimisation was too time-consuming in this case, the approach of tritium labelling of NMS by means of oxidative iodination followed by reductive tritium dehalogenation was discontinued.

Preliminary Labelling Experiments on NMS: Derivatisation using NSP

The feasibility of derivatisation on amine residues was investigated. NMS consists of three primary amines that can be tagged with NSP: Ile-1, Lys-15, and Lys-16. Compared to the size of NMS (3,790 Da), derivatisation from a small [³H₃]propionate (62 Da) contributes only a marginal difference in mass. However, the derivatisation changes the molecular structure and this could lead to altered biological or physico-chemical behaviour. For this reason, the corresponding non-radioactive NSP was specifically placed at different positions of the peptide and these derivatives were subsequently investigated for their functionality and binding behaviour towards NMUR₂. In a first preliminary experiment, NMS was treated in an equimolar ratio with NSP in PBS pH 8.5 for 30 min at 22 °C. Following the 1:1 reaction, theoretically, a maximum of eight NMS

derivatives with a modification at the following amino acids can be present: 1) unlabelled; 2) Ile-1; 3) Lys-15; 4) Lys-16; 5) Ile-1 + Lys-15; 6) Ile-1 + Lys-16; 7) Lys-15 + Lys-16; 8) Ile-1 + Lys-15 + Lys-16. However, HPLC analysis of the crude reaction mixture showed seven peaks (**Figure 2**). Five fractions were isolated from the preparative HPLC, with fractions "b" and "d" each consisting of two non-separable products.

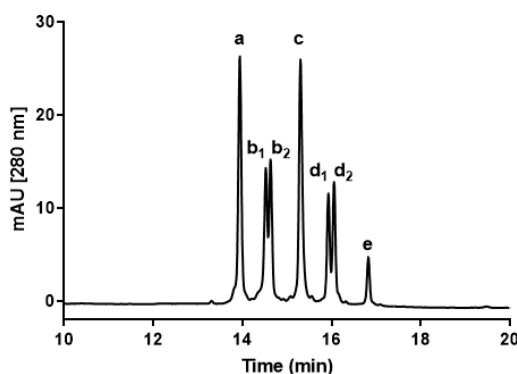


Figure 2: HPLC analysis of the crude solution on NMS treated with 1 eq. NSP showed seven peaks with retention times between 14 and 17 min.

In the next preliminary experiment, NMS was treated with 3 equivalents of NSP under identical reaction conditions to the equimolar approach. The main product from the crude reaction solution was assigned to peak e. Furthermore, the peptide derivatives related to the peaks d₁ and d₂ were found in the reaction mixture. Finally, an excess of 3 equivalents of NMS was treated with NSP. Analytical HPLC showed that the major component in the reaction solution after 30 min was the unlabelled peptide as expected, but fractions b₁ and b₂, and c were also detected. It was shown in the preliminary experiments that when treating NMS with different molar ratios of NSP, the distribution of the products formed can be controlled. The next steps are to identify the labelling positions of fractions a-e and to determine which labelling position has the least influence on the biological behaviour compared to the unlabelled peptide.

Identification of Labelling Position using LC-ESI-MS/MS

From the five isolated fractions (a-e) of the preparative purification from the equimolar labelling experiment with non-radioactive NSP, the labelling positions were identified by LC-ESI-MS/MS. In this process, a separation of the mixed fractions b and d was achieved, which ensured an investigation of the main peaks from the mass trace of the total ion chromatogram (TIC) (**Figure 3**).

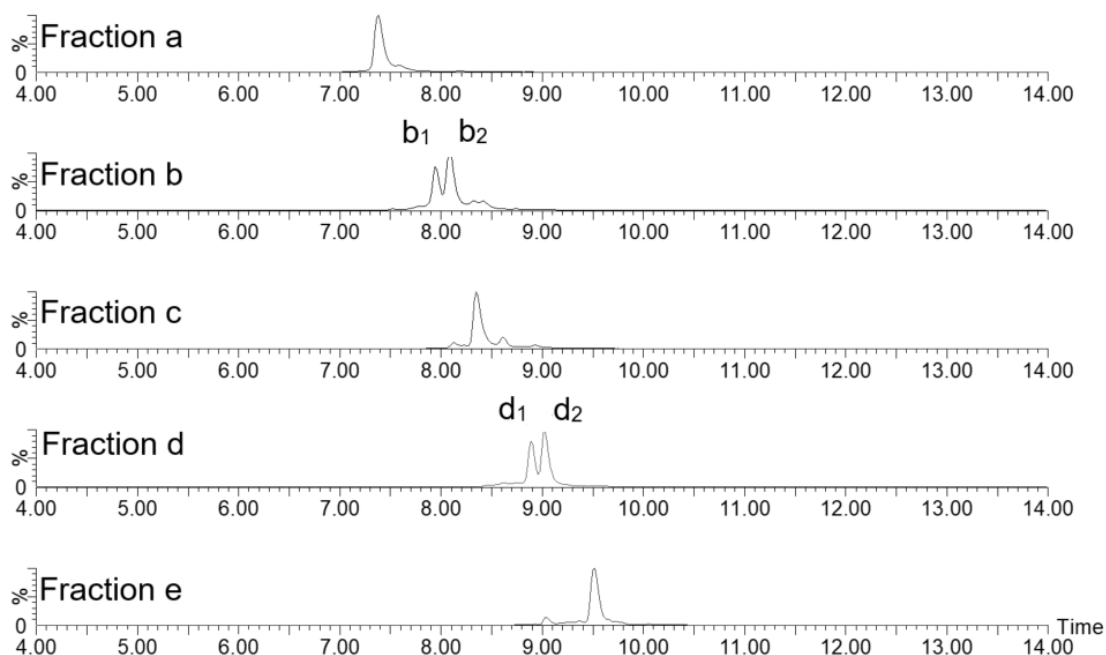


Figure 3: LC/MS chromatograms (MS trace, TIC: 100-2000 Da) of the fractions a-e.

Each spectrum below the low-energy MS trace was summed up and deconvoluted. The resulting mass spectra (**Figure 4**) showed the monoisotopic mass ($[M+H]^+$) of the intact peptides from fractions a-e and indicated the number of labelled amino acids of the peptide. In the case of unlabelled NMS, the calculated $[M+H]^+$ is 3,790.0206 Da. For each labelling event that would take place, the calculated mass increases by +56.0262 Da. From these intact masses, it can be concluded how often the activated propionic acid was conjugated to the three possible positions of the peptide.

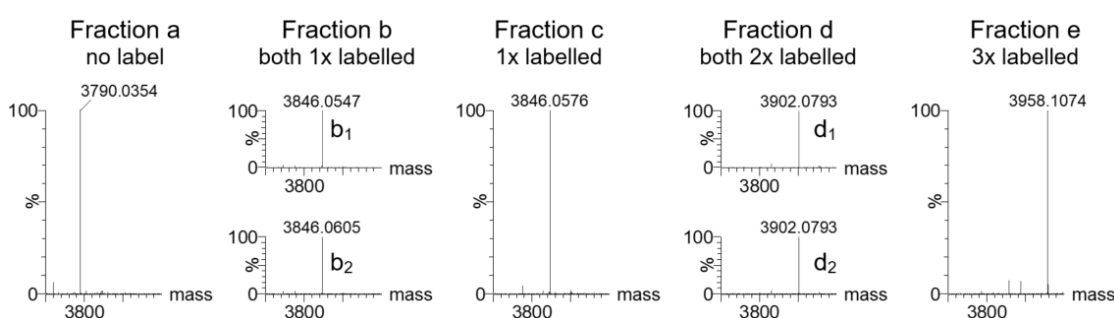


Figure 4: Deconvoluted low-energy mass ($[M+H]^+$) spectra of the main peaks of the fractions a-e.

Table 2 shows the theoretical masses of NMS containing 0 to 3 labels of propionate as well as the found masses of the intact peptides. The masses of fractions a-e were assigned as follows: Unlabelled NMS has been found in fraction a. Fraction b, which consisted of two peaks (b_1 and b_2), and fraction c gave a mass suggestive of a single label. In each of the two peaks of fraction d (d_1 and d_2) a double labelling event of NSP was detected. In fraction e, a mass increase of three labels was found, indicating

that conjugation occurred at all three possible positions of the primary amines present in the peptide.

Table 2: Found masses underneath chromatographic peaks in low-energy trace.

Fraction/ Peak	Retention time [min]	Found mass [Da]	Assignment	Theoretical mass [Da]	Mass error [ppm]
a	7.4	3,790.0354	NMS	3,790.0206	3.9
b₁	7.9	3,846.0547	1x labelled NMS	3,846.0468	2.1
b₂	8.1	3,846.0605	1x labelled NMS	3,846.0468	3.6
c	8.3	3,846.0576	1x labelled NMS	3,846.0468	2.8
d₁	8.9	3,902.0793	2x labelled NMS	3,902.0730	1.6
d₂	9.0	3,902.0793	2x labelled NMS	3,902.0730	1.6
e	9.5	3,958.1074	3x labelled NMS	3,958.0992	2.1

Although it is possible to determine the number of labels from the masses of intact proteins from the low-energy trace, it is not possible to obtain information about the exact label position. The most common peptide fragments observed in high-energy collisions are **b** ions and **y** ions.²⁷ The **b** ions appear to extend from the *N*-terminus while the **y** ions appear to extend from the *C*-terminus. The mass pattern in the high-energy trace has shown a more prominent **y** ion series (compared to the **b** ion series) in the mid mass and high mass range (**Figure 5**).

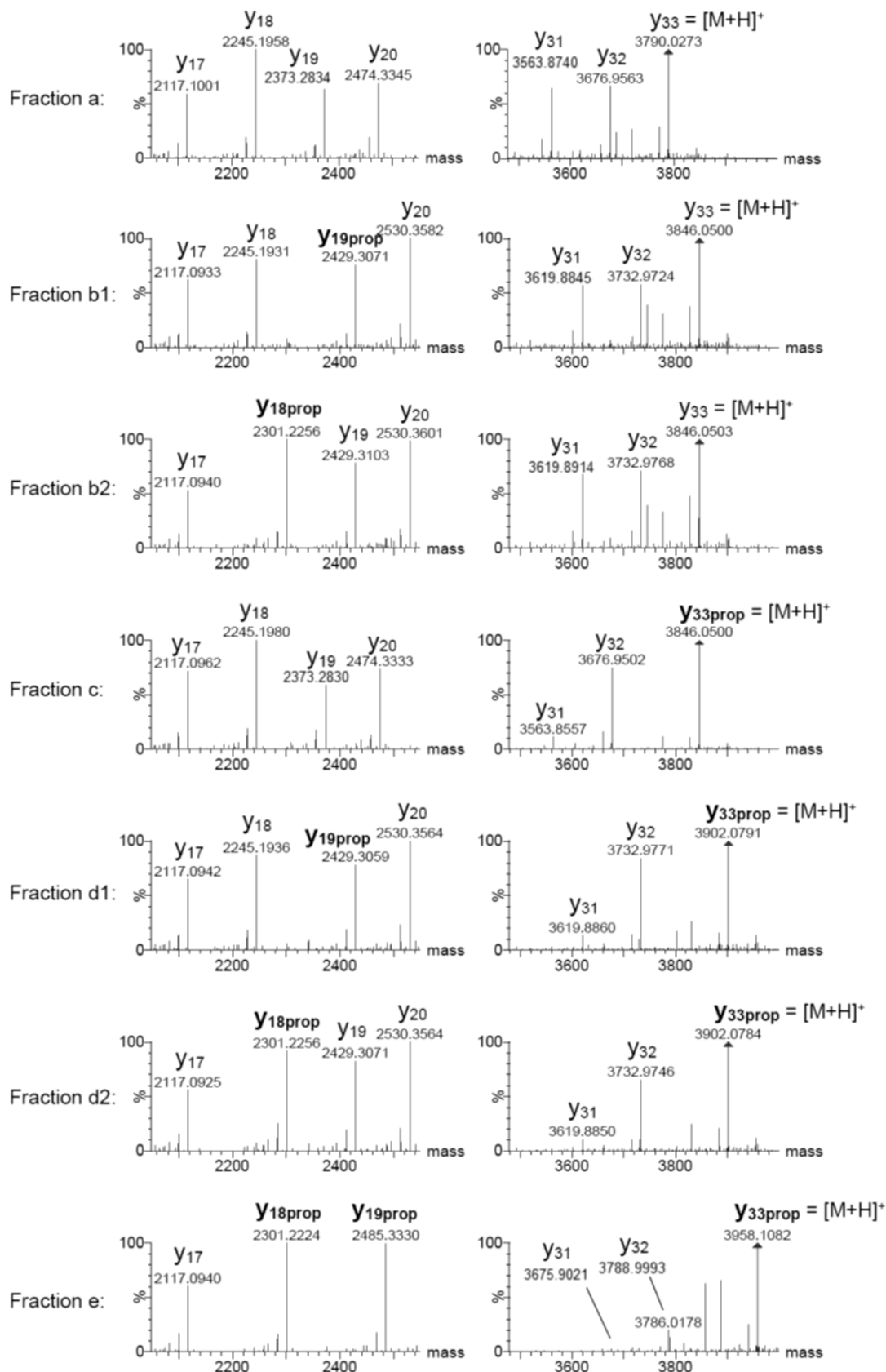
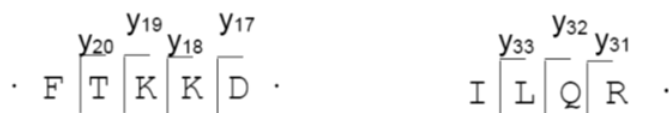


Figure 5: y ion pattern of high-energy MS spectra of fractions a-e. y ions marked with "prop" indicate the labelling positions. Zoom left column: 2050 Da – 2550 Da; zoom right column: 3480 Da – 4000 Da.

As already mentioned, the mass from fraction a correlates with the unlabelled NMS. In fraction b, which consists of two peaks, it was shown in b₁ that the mass shift occurred in the y₁₉ ion, which corresponds to the Lys-15 from the peptide sequence. In peak b₂, the mass shift happened in y₁₈ ion, which represents a label on Lys-16. With respect to fraction c, in which the peptide was also singly labelled, there is no mass shift in y₁₈ and y₁₉, whereas a mass shift was observed in y₃₃. This shows that the labelling took place at the *N*-terminal amino acid Ile-1. In fraction d, which also consisted of two peaks and each showed a double labelling in the low-energy trace, both peaks were assigned. The y ions 19 and 33 from peak d₁ showed a mass shift resulting in labelling at Ile-1 and Lys-15. For d₂, the shift was at y ions 18 and 33, resulting in labelling at Ile-1 and Lys-16. As already known, the peptide from fraction e was triply labelled and the mapping confirmed a mass shift at y₁₈, y₁₉, and y₃₃. Consequently, conjugation with NSP took place at amino acids Ile-1, Lys-15, and Lys-16. The exact labelling positions in the peptide sequence was assigned to each fraction or peak and are listed in **Table 3**. However, one compound was not found: a double labelling of NMS on Lys-15 and Lys-16. This is surprising, as conjugation to both lysine residues was observed with the triple-labelled NMS. The labelling experiments also did not show which amine reacts first with NSP. This raises the question of whether the *N*-terminal Ile-1 has an influence on the reactivity of the lysines or whether it is a sterically hindered effect.

Table 3: Propionyl-labelled amino acids of the peptide sequences from fractions a-e are marked with "*" according to the high-energy trace mass spectrometry analyses.

Fraction/ Peak	Labelling Position	Peptide Sequence
a	non	ILQRGSGTAAVDFTKKDHTATWGRPFFLFRPRN-NH ₂
b ₁	Lys-15	ILQRGSGTAAVDFTK*KDHTATWGRPFFLFRPRN-NH ₂
b ₂	Lys-16	ILQRGSGTAAVDFTKK*DHTATWGRPFFLFRPRN-NH ₂
c	Ile-1	I*LQRGSGTAAVDFTKKDHTATWGRPFFLFRPRN-NH ₂
d ₁	Ile-1, Lys-15	I*LQRGSGTAAVDFTK*KDHTATWGRPFFLFRPRN-NH ₂
d ₂	Ile-1, Lys-16	I*LQRGSGTAAVDFTKK*DHTATWGRPFFLFRPRN-NH ₂
e	Ile-1, Lys-15, Lys-16	I*LQRGSGTAAVDFTK*K*KDHTATWGRPFFLFRPRN-NH ₂

Functional In Vitro Fluorometric Imaging Plate Reader Assay

To compare the functional activities of modified and unlabelled NMS derivatives, an *in vitro* Fluorometric Imaging Plate Reader (FLIPR) assay was performed. The aim is to demonstrate whether the degree of labelling as well as the labelling position has an influence on the half maximal effect concentration (EC₅₀). The NMUR₂ FLIPR assay was run in homogeneous format in 384-wells format. All tested fractions are shown in

Figure 6. Fraction b ($pEC_{50} = 8.75 \pm 0.12$), fraction c ($pEC_{50} = 8.99 \pm 0.20$), fraction d ($pEC_{50} = 9.01 \pm 0.05$), and fraction e ($pEC_{50} = 9.00 \pm 0.12$) all show similar activities compared to the unlabelled NMS (fraction a, $pEC_{50} = 9.11 \pm 0.27$), indicating that the modifications are not interfering with the binding and functional activity of the peptides at the receptor.

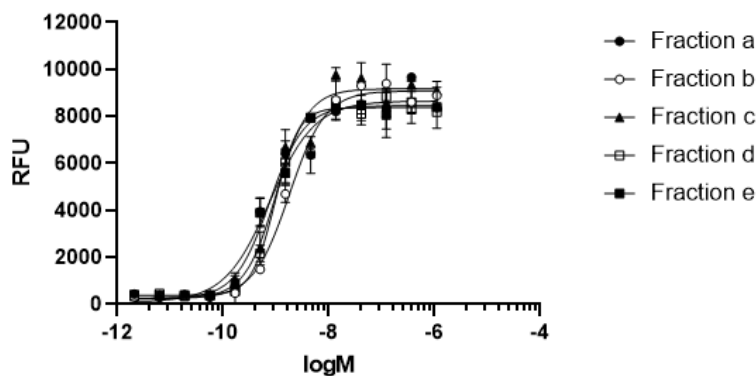


Figure 6: Concentration response curves (CRC) for fractions a-e in *in vitro* FLIPR assay. The y-axis represents the maximum minus baseline fluorescence signal for each sample. The x-axis represents the log of the molar concentration. Data were fitted by Hill equation and data points represent mean \pm standard deviation of 2 individual experiments.

***In Vitro* Affinity Receptor Binding**

The results from the functional *in vitro* FLIPR assay were confirmed by a second assay. The affinities of unlabelled and modified NMS with respect to specific binding to the human NMUR₂ receptor were compared in a competitive binding assay using ¹²⁵I-labelled NMU-8. The obtained dose response curves are shown in **Figure 7**. The resulting IC₅₀ values as well as the calculated negative logarithms of the IC₅₀ values (pIC_{50}) and the inhibition constants (K_i) of fractions a-e were similar (**Table 4**). It is noticeable that the unlabelled NMS (fraction a) showed the identical IC₅₀ value as the *N*-terminally single-labelled NMS derivative of fraction c. Whereas single labelling of one of the two Lys within the sequence (fraction b) showed a minor influence on the IC₅₀. In fraction d, in which there was double labelling of Ile-1 and one of the two Lys, the IC₅₀ was almost identical to that of fraction b. This also suggests that labelling at the *N*-terminal amino acid Ile-1 has no influence on the inhibition concentration. The triple-labelled NMS derivative from fraction e showed the highest influence on the IC₅₀ value.

These results are in line with the data obtained from the functional *in vitro* FLIPR assay, in which all tested fractions also showed similar effects and no significant differences in their functional activities. A single label at the *N*-terminal Ile-1 seems to have no influence on the functionality as well as on binding to NMUR₂, suggesting a modification at Ile-1 is preferred.

Table 4: IC₅₀, calculated pIC₅₀, and K_i values of fraction a-e. The values are given as the mean value in molarity [M] of two independent experiments.

Compound/ Fraction	IC ₅₀ [M]	pIC ₅₀ [M]	K _i [M]
NMU-8	1.5*10 ⁻¹⁰	9.82	1.2*10 ⁻¹⁰
a	2.2*10 ⁻⁹	8.66	1.8*10 ⁻⁹
b	4.0*10 ⁻⁹	8.39	3.3*10 ⁻⁹
c	2.2*10 ⁻⁹	8.66	1.8*10 ⁻⁹
d	4.3*10 ⁻⁹	8.37	3.5*10 ⁻⁹
e	6.3*10 ⁻⁹	8.20	5.2*10 ⁻⁹

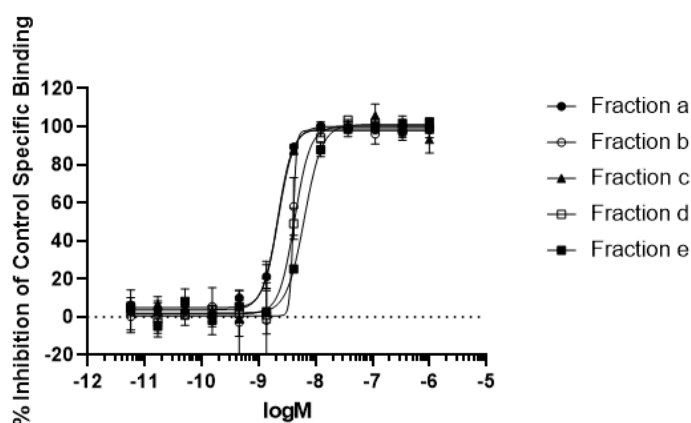


Figure 7: Concentration response curves (CRC) for fractions a-e in *in vitro* affinity receptor binding assay. The y-axis represents the percentage of inhibition of specific binding for the radiolabelled ligand [¹²⁵I]NMU-8 for each sample. The x-axis represents the log of the molar concentration. Data were fitted by Hill equation and data points represent mean ± standard deviation of 2 individual experiments.

Molecular Dynamics Simulation

Yi Jiang *et al.* recently published cryo-electron microscopy (cryoEM) structures of Gq chimera-coupled NMUR₁ and NMUR₂ together with bound human NMU-25 and NMS.²⁸ In the NMUR₂-NMS structure, only the final 11 C-terminal NMS amino acids Gly-23 to Asn-33 are visible (**Figure 8**). Of those residues Gly-23 to Pro-25 are not engaged in interactions with the protein.

As the labelling positions are obviously distant from the peptide-binding pocket, the derivatisation with NSP is not expected to interfere with binding of the peptide to the protein. This was indeed confirmed by FLIPR and receptor binding data with the modified peptides, which did not show an impact on functional activity. Therefore, it is reasonable to assume that the derivatised residues do not interact with the protein.

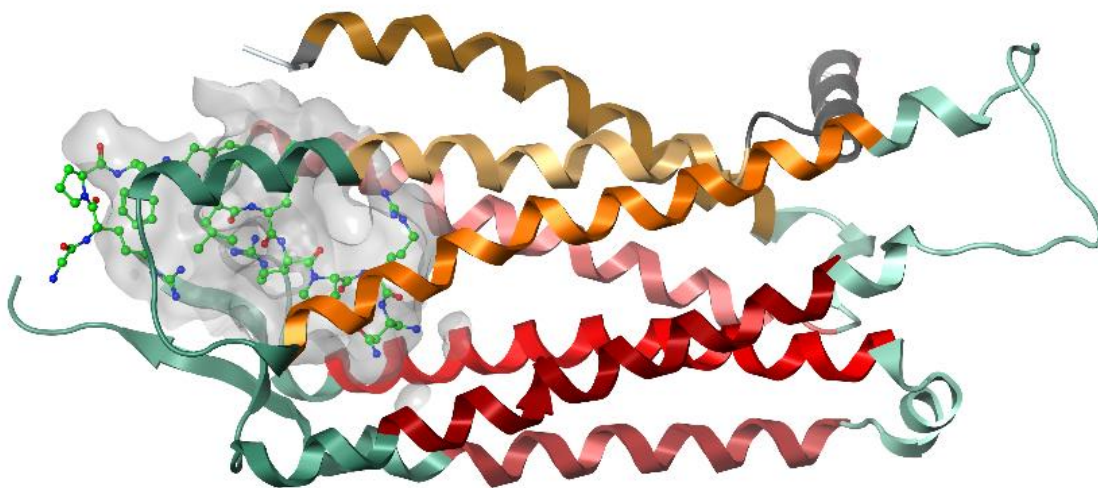


Figure 8: NMS in the binding pocket of NMUR₂ (PDB code 7W57). Phe-26 to Asn-33 are engaged in intermolecular interactions with the receptor.

Tritium-labelling of NMS

Based on the results of the functional activity and competitive binding assay, as well as the confirmation from molecular dynamic simulation, a modification at the amine residue of Ile-1 has no influence on the binding of the derivatised NMS to the protein NMUR₂. Therefore, in analogy to the non-radioactive preliminary experiments, the conjugation was carried out with radioactive [³H]NSP (1 eq.) and NMS (4 eq.). An HPLC analysis using UV and radio detector of the crude solution (**Figure 9: A**) showed, as expected, the unlabelled NMS as the major compound. Peak b showed a double peak in the UV, corresponding to conjugation to the Lys-15 and Lys-16, respectively, but there was no separation in the radio-peak. Furthermore, the desired product of the *N*-terminal conjugation at Ile-1 was formed.

By means of preparative HPLC, peak b, as a mixture of b₁ and b₂, and peak c was isolated in high purity (**Figure 9: B,C**). The radiochemical yields at b and c of 13 % and 7 %, respectively, indicate that a high amount of [³H]NSP was hydrolysed during the conjugation process. This was confirmed by a radioactivity measurement of the waste obtained from the dialysis of 50% of the initiated radioactive amount. On careful inspection of **Figure 9: C**, a tailing can be found in the isolated peak c, especially in the radioactive detection. A similar tailing can also be found in the UV trace of the unlabelled NMS peak in **Figure 9: A**. This tailing is probably due to the fact that in an analysis of the commercial NMS batch used for the radioactive conjugation, an impurity of about 8% (data not shown) of the corresponding *C*-terminal carboxylic acid is detected instead of the amide. This tailing is also seen in the non-radioactive NSP/NMS (3:1) preliminary experiment, as the identical batch was used here. In the equimolar preliminary experiment, which was the first conjugation experiment in this study, a different batch

was used and in this case, the HPLC analysis shows no tailing. It is worthwhile to carefully analyse the commercially available starting material before radiolabelling.

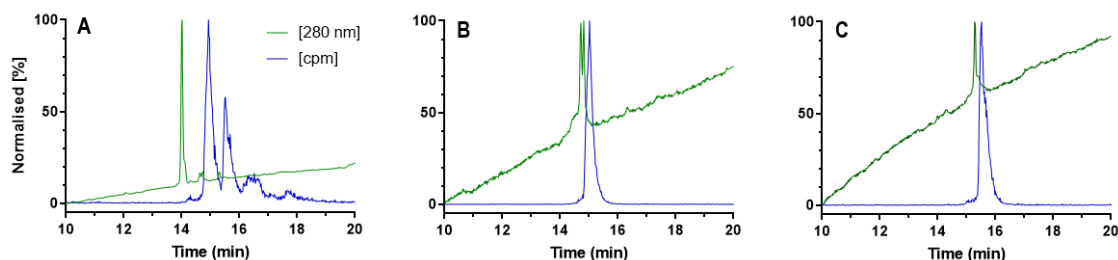


Figure 9: Analytical HPLC show the normalised chromatograms of **A** crude solution after dialysis; **B** isolated fraction from peak B; **C** isolated fraction C. Green lines: Absorbances at wavelength of 280 nm. Blue lines: time-shifted radio detection in counts per min (cpm).

Conclusions

Two approaches were investigated for the incorporation of tritium into human NMS: 1) halogenation of NMS followed by metal-catalysed halogen-tritium exchange. 2) Derivatisation of primary amine residues using [^3H]NSP. Halogenation was achieved with sodium iodide and chloramine-T at His residues (0%, I₀, 35% I₁, and 65% I₂), but subsequent exchange of iodine to deuterium was unsuccessful. In a non-radioactive preliminary experiment, NSP was conjugated to primary amines available at the following amino acids in the peptide sequence: Ile-1, Lys-15, and Lys-16. In a functional *in vitro* FLIPR and competitive binding assay, it was demonstrated that the binding behaviour between the modified NMS derivatives and the protein NMUR₂ is comparable to that of the unlabelled NMS, regardless of the degree of labelling and the labelling position, with the preferred labelling position at the *N*-terminal amino acid Ile-1. These results allowed conjugation with radioactive NSP to NMS. After preparative HPLC purification, two main fractions with radioactive peptide derivatives were isolated. The first fraction consisted of a mixture of a single conjugation at Lys-15 and another product with a label at Lys-16 (total yield: 13%), which was not separable due to the almost identical retention time. The second major fraction consisted of the desired conjugation product with a single label at the *N*-terminal Ile-1 (yield: 7%) in high purity (>95%) and a molar activity of 3.3 TBq/mmol (90 Ci/mmol). This study reports, to the best of our knowledge, the first approach to tritiated NMS, which opens the door for further studies to characterise and investigate NMS or corresponding ligands.

Materials and Methods

All chemical starting materials are commercially available and have been used without further purification. Neuromedin S (NMS) peptide (human) was purchased from Abbexa

Ltd (Cambridge, UK). Non-radioactive *N*-succinimidyl propionate (NSP) was obtained from FUJIFILM Wako (Osaka, Japan). Tritium-labelled [³H]*N*-succinimidyl propionate ([³H]NSP) (molar activity: 3.3 TBq/mmol; 90 Ci/mmol) was obtained from Pharmaron (Cardiff, Wales, UK) as a solution in toluene (185 MBq/mL; 5 mCi/mL). Dulbecco's Phosphate Buffered Saline (PBS, Gibco, Paisley, UK) was adjusted with 1 M NaOH to pH 8.5. Liquid scintillation counting was accomplished using a HIDEX 300 SL and ULTIMATE GOLD™ cocktail (PerkinElmer Inc., Waltham, MA, USA). Analytical HPLC was performed using an Agilent 1210 series HPLC system (Santa Clara, CA, USA) using a Waters XBridge Phenyl column (4.6 mm x 150 mm, 3.5 μm). HPLC conditions: mobile phase [A]: H₂O + 5% acetonitrile + 0.1% TFA (v/v/v), [B]: acetonitrile + 0.1% TFA (v/v), gradient 5% [B] to 65% [B] over 20 min with a flow rate of 1 mL/min. Radiochemical purity was measured using the β Radioactivity-HPLC flow detector RAMONA* (Elysia-raytest, Straubenhardt, Germany), combined with RAMONA-HPLC-pump for continuous admixture of liquid-scintillator cocktail (flow rate: 2 mL/min) to the eluate of the HPLC system. Preparative purification was performed by the use of Gilson PLC 2050 (Middleton, WI, USA), equipped with a Waters XBridge Phenyl column (300 mm x 10 mm, 5 μm) under the following conditions: Solvent [A] was water + 5% acetonitrile + 0.1% trifluoroacetic acid (v/v/v) and solvent [B] was acetonitrile + 0.1% trifluoroacetic acid (v/v). The column was initially equilibrated at 5% [B] using a flow rate of 6 mL/min, with the absorbance monitored at 280 nm. Starting with isocratic conditions of 5% [B] for 2 min, a linear gradient to 65% [B] followed over 38 min. Float-A-Lyzer Dialysis Devices were obtained from Thermo Fisher Scientific (Waltham, MA, USA), with volume sizes of 1 mL or 5 mL and a molecular weight cut-off of 500-1,000 Da.

Direct Iodination of NMS

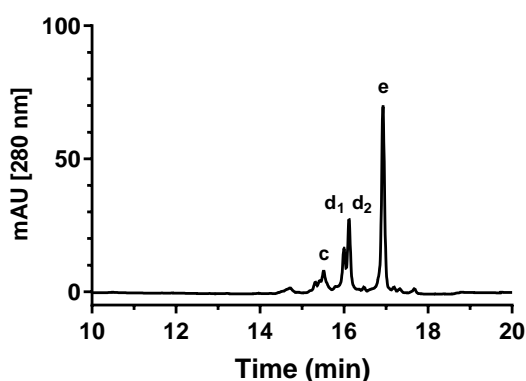
Direct iodination was investigated with 4 oxidising agents at pH 5 and pH 10, respectively. 0.5 mg (0.13 μmol) NMS was dissolved in 0.5 mL PBS (pH 5 or pH 10) in a 1.5 mL LoBind Eppendorf tube. 59 μg (0.40 μmol, 3 eq) sodium iodide, dissolved in 3.7 μL PBS pH 7.3, was added. 4 equivalents (0.53 μmol) of oxidising agents chloramine-T (0.12 μg in 8.5 μL PBS pH 7.3), iodogen (0.23 μg in 11.8 μL PBS pH 7.3), and freshly prepared chloramine according to a published procedure²⁴ was added. When using polymer-bound chloramine-T (loading: 0.2 mmol/g), a single bead with a weight of 15 mg was used, which corresponds to an amount of substance of about 3 μmol (22.7 eq). The 8 samples were shaken at 22 °C by a horizontal rotation of 600 rpm. After 1 h, the samples were analysed for their incorporation of iodine by mass spectrometry.

Equimolar treatment of NMS with NSP

4.5 mg (1.19 μmol) of NMS was dissolved in 1 mL PBS pH 8.5 in a 5 mL LoBind Eppendorf tube to give a colourless solution. 203 μg (1.19 μmol) of NSP, dissolved in 6.8 μL DMSO, was added and the solution was shaken orbitally at 22 $^{\circ}\text{C}$ for 30 min. The solution was diluted with 4 mL water transferred into a 5 mL Float-A-Lyzer for solvent exchange into water. The water was exchanged three times after 30 min and stored in the fridge at 4 $^{\circ}\text{C}$ for 16 h. Analytical HPLC at 280 nm showed the following ratios of the peaks with the corresponding retention time in brackets: 33% a (14.0 min); 11% b₁ (14.6 min); 11% b₂ (14.7 min); 23% c (15.4 min); 8% d₁ (16.0 min); 10% d₂ (16.2 min); 4% e (16.9 min). The crude protein solution was lyophilised and the residue dissolved in 1 mL water + 0.5% trifluoroacetic acid for preparative purification. The five fractions a-e (**Figure 1**) were separated as a colourless solid from the crude mixture and resulted in the following weights after lyophilisation: a: 1.1 mg; b: 0.7 mg; c: 1.0 mg; d: 0.8 mg; e: 0.3 mg. The corresponding labelling positions are described in the results section.

Treatment of NMS with 3-fold excess of NSP

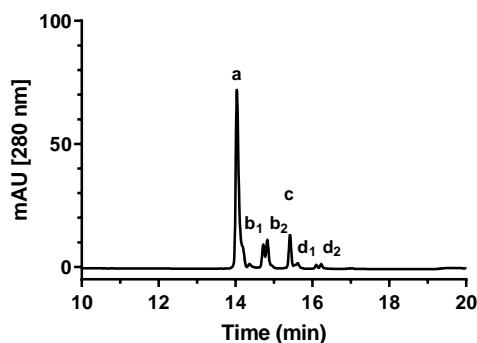
The conjugation of NMS with 3 equivalents of NSP was carried out in analogy to the described equimolar procedure with the following amounts: 3.3 mg (0.88 μmol) of NMS in 1.5 mL PBS pH 8.5 in a 5 mL LoBind Eppendorf tube and 462 μg (2.70 μmol) of NSP, dissolved in 9.5 μL DMSO. Analytical HPLC at 280 nm showed the following ratios of the peaks with the corresponding retention time in brackets: 8% c (15.4 min); 12% d₁ (16.0 min); 20% d₂ (16.2 min); 61% e (16.9 min). After preparative purification and lyophilisation, 2.2 mg (0.56 μmol ; yield: 64%) of the major peak e was isolated as a colourless solid with a purity of 97%.



HPLC analysis of the crude solution on NMS treated with 3 eq. NSP.

Treatment of 3-fold excess of NMS with NSP

The conjugation of 3 equivalents NMS with NSP was carried out in analogy to the described equimolar procedure with the following amounts: 3.3 mg (0.88 μmol) of NMS in 1.5 mL PBS pH 8.5 in a 5 mL LoBind Eppendorf tube and 462 μg (2.70 μmol) of NSP, dissolved in 9.5 μL DMSO. Analytical HPLC at 280 nm showed the following ratios of the peaks with the corresponding retention time in brackets: 70% a (14.0 min); 7% b₁ (14.7 min); 9% b₂ (14.8 min); 11% c (15.4 min); 1% d₁ (16.1 min); 2% d₂ (16.2 min).



HPLC analysis of the crude solution on NMS:NSP 3:1.

LC-MS/MS Analysis

LC-ESI-MS/MS was carried out on a Waters iClass HPLC system using a Waters UPLC BEH C18 column (1.0 mm x 150 mm, 1.7 μm), the column temperature was set to 40 °C, mobile phase [A]: H₂O + 0.1% formic acid (v/v), [B]: acetonitrile + 0.1% formic acid (v/v). Starting with isocratic conditions of 5% [B] for 1 min followed by the gradient 5% [B] to 40% [B] over 10 min and 40% [B] to 95% [B] over 6 min. The flow rate was set to 80 $\mu\text{L}/\text{min}$. Detection was performed first on a UV detector at 214 nm and 280 nm (TUV, Waters iClass) followed by a Synapt G2 HDMS QTof (Waters, Manchester, UK) equipped with an ESI source and adjusted with common voltages for MS peptide analysis. The collision energy for low-energy trace was switched off and ramped from 16 V up to 42 V for the high-energy trace. The data were acquired, processed, and analysed in Waters MassLynx software.

Functional in vitro FLIPR Assay

Recombinant Chem-1 cells overexpressing the full length human NMUR₂ were cultured at 37 °C and 5% CO₂ in growth medium consisting of DMEM with High Glucose, 10% FBS, 1x pen/strep, 1x non-essential amino acids, and appropriate selection antibiotics. At the time of the harvest, the cell density was 80% confluent. One day prior to the assays, cells were harvested by washing with 10 to 20 mL of PBS and treatment with

4 mL of Trypsin solution. After an approximately 5 min incubation at 37 °C, cell suspension was transferred to a 10 mL conical tube and pipette several times to break up cell clusters. After centrifugation, cells were resuspended and prepared in growth medium at a density of 5×10^5 cell/mL and seeded in 384 well plates for incubation at 37 °C for 16 h in an atmosphere of 5% CO₂. All assays were performed using clear-bottom 384-wells plates (Corning, Catalog 3764) on the FLIPR Penta (Fluorescence imaging plate reader) from Molecular Devices (Sunnyvale, CA). The FLIPR Calcium 6 Assay Kit (Molecular Devices, Catalog R8190) was used for the detection of Calcium mobilisation upon receptor activation. Prior to the readout, supernatant was removed from the cells and 20 µL per well of the FLIPR Calcium 6 Assay Kit was added, containing 2 mM probenecid. Plates were incubated with the Assay Kit for 60 min at 37 °C and 5% CO₂. Kinetic data was acquired by the FLIPR at the rate of 0.5 Hz. The activity for each individual well activity is interpreted as the difference of the maximum signal after compound addition minus the average baseline fluorescence signal determined before the online addition of compounds. For dose response experiments, 384-wells assay ready serial dilution plates were prepared. The plates contained the five different fractions with 12 different dilutions steps (1:3 serial dilution) for each fraction. All samples were diluted in 1x HBSS (Hank's Balanced Salt Solution), 20 mM Hepes, and 0.1% (w/v) BSA. The final compound concentrations in the dose response experiments ranged from 1.1 µM to 2.1 pM. For concentration response curves, the following equation was used for the calculations: $Y = \text{Bottom} + \frac{\text{Top} - \text{Bottom}}{1 + 10^{(\text{LogEC}_{50} - X) \cdot \text{HillSlope}}}$, where "Y" is a given response, "X" is log of concentration, "EC₅₀" is the concentration that gives a response half way between Top and Bottom; "HillSlope" describes the steepness of the curve, "Top" and "Bottom" are plateaus in the units of Y-axis.

In vitro affinity receptor binding assay

Membrane preparations from human recombinant HEK-293 cells overexpressing NMUR₂ and [¹²⁵I]NMU-8 were used for the radioligand displacement-binding assay. The specific binding of [¹²⁵I]NMU-8 in the radioligand binding assay was determined with a K_d (dissociation constant) of 0.13 nM.²⁹ When testing the fractions a-e in the competition binding assay 0.05 nM of [¹²⁵I]NMU-8 was used, and non-specific binding was determined by replacing the radiolabelled NMU-8 with 100 nM of unlabelled NMU-8. The incubation times during the various experiments was 60 min at 22 °C using scintillation counting as detection method. Fractions a-e were tested in 12 point serial dilutions starting from 1 µM to 5.65 pM. Results are expressed as the percentage of control binding ($= \frac{\text{measured specific binding}}{\text{control specific binding}} * 100$) and as a percentage inhibition of control specific

binding ($= 100 - \left[\frac{\text{measured specific binding}}{\text{control specific binding}} * 100 \right]$), obtained in the presence of the test compounds. The IC_{50} values (concentration causing a half-maximal inhibition of control specific binding) and Hill coefficients (nH) were determined by non-linear regression analysis of the competition curves generated with mean replicate values using Hill equation curve fitting $Y = D + \frac{A-D}{1 + \left(\frac{C}{C_{50}}\right)^{nH}}$, where Y = specific binding, A = left asymptote of the curve, D = right asymptote of the curve, C = compound concentration, $C_{50} = IC_{50}$, and nH = slope factor. This analysis was performed using GraphPad Prism™ software. The inhibition constants (K_i) were calculated using the following Cheng Prusoff equation $K_i = \frac{IC_{50}}{\left(1 + \frac{L}{K_D}\right)}$, where L = concentration of ligand in the assay, and K_D = affinity of the ligand for the receptor. All radioligand binding experiments were performed at Eurofins Cerep (Celle l'Evescault, France).

Molecular Modelling

Molecular Modelling software: *Molecular Operating Environment (MOE)*, 2022.02; Chemical Computing Group ULC, 1010 Sherbrooke St. West, Suite #910, Montreal, QC, Canada, H3A 2R7, 2022.

³H-Labeling of NMS

A toluene solution of 4 mCi (8 µg, 45 nmol; 1 eq) [³H]NSP was transferred into a 5 mL LoBind Eppendorf tube. The solvent was removed by a gentle stream of argon and the residue was dissolved in 25 µL of DMSO. NMS (713 mg, 188 nmol; 4 eq) of, dissolved in 0.5 mL PBS pH 8.5, was added to the [³H]NSP solution and shaken horizontally at 250 rpm for 30 min at 22 °C. The solution was into a 1 mL Float-A-Lyzer for solvent exchange into water. The water was exchanged three times after 30 min and stored in the fridge at 4 °C for 16 h. The crude reaction solution was purified by preparative HPLC to isolate two radioactive peaks that correlate with peaks b and c from the non-radioactive preliminary experiments. Radiochemical purities were >95% for both isolated fractions, with fraction containing peak b in the UV, as in the non-radioactive experiments, consisting of two peaks. Isolated radioactive amount for b was 0.5 mCi and for c was 0.3 mCi, corresponding to radioactive yields of 13% and 7%, respectively, based on 4 mCi started. A determination of the specific activity by means of isotope peak patterns from a mass spectrometric analysis was not possible. For this reason, the molar activity of [³H]NSP was taken as 3.3 TBq/mmol (90 Ci/mmol).


References

- (1) Novak, C. M. (2009) Neuromedin S and U. *Endocrinology* 150, 2985-2987.
- (2) Mitchell, J., Maguire, J., and Davenport, A. (2009) Emerging pharmacology and physiology of neuromedin U and the structurally related peptide neuromedin S. *Br. J. Pharmacol.* 158, 87-103.
- (3) Mori, K., Miyazato, M., Ida, T., Murakami, N., Serino, R., Ueta, Y., Kojima, M., and Kangawa, K. (2005) Identification of neuromedin S and its possible role in the mammalian circadian oscillator system. *EMBO J.* 24, 325-335.
- (4) Minamino, N., Kangawa, K., and Matsuo, H. (1985) Neuromedin U-8 and U-25: novel uterus stimulating and hypertensive peptides identified in porcine spinal cord. *Biochem. Biophys. Res. Commun.* 130, 1078-1085.
- (5) Wan, Y., Zhang, J., Fang, C., Chen, J., Li, J., Li, J., Wu, C., and Wang, Y. (2018) Characterization of neuromedin U (NMU), neuromedin S (NMS) and their receptors (NMUR₁, NMUR₂) in chickens. *Peptides* 101, 69-81.
- (6) Takayama, K., Mori, K., Taketa, K., Taguchi, A., Yakushiji, F., Minamino, N., Miyazato, M., Kangawa, K., and Hayashi, Y. (2014) Discovery of selective hexapeptide agonists to human neuromedin U receptors types 1 and 2. *J. Med. Chem.* 57, 6583-6593.
- (7) Brighton, P. J., Szekeres, P. G., and Willars, G. B. (2004) Neuromedin U and its receptors: structure, function, and physiological roles. *Pharmacol. Rev.* 56, 231-248.
- (8) Tóth, F., Mallareddy, J. R., Tourwé, D., Lipkowski, A. W., Bujalska-Zadrozny, M., Benyhe, S., Ballet, S., Tóth, G., and Kleczkowska, P. (2016) Synthesis and binding characteristics of [³H] neuromedin N, a NTS2 receptor ligand. *Neuropeptides* 57, 15-20.
- (9) De Prins, A., Martin, C., Van Wanseele, Y., Skov, L. J., Tömböly, C., Tourwé, D., Caveliers, V., Van Eeckhaut, A., Holst, B., and Rosenkilde, M. M. (2018) Development of potent and proteolytically stable human neuromedin U receptor agonists. *Eur. J. Med. Chem.* 144, 887-897.
- (10) Keller, M., Kuhn, K. K., Einsiedel, J., Hübner, H., Biselli, S., Mollereau, C., Wiffling, D., Svobodova, J., Bernhardt, G., and Cabrele, C. (2016) Mimicking of arginine by functionalized N ω-carbamoylated arginine as a new broadly applicable approach to labeled bioactive peptides: high affinity angiotensin, neuropeptide Y, neuropeptide FF, and neurotensin receptor ligands as examples. *J. Med. Chem.* 59, 1925-1945.
- (11) Yang, H., and Hesk, D. (2020) Base metal-catalyzed hydrogen isotope exchange. *J. Label. Compds. Radiopharm.* 63, 296-307.
- (12) Pfeifer, V., Certiat, M., Bouzouita, D., Palazzolo, A., Garcia-Argote, S., Marcon, E., Buisson, D. A., Lesot, P., Maron, L., and Chaudret, B. (2020) Hydrogen isotope exchange catalyzed by Ru nanocatalysts: Labelling of complex molecules containing N-heterocycles and reaction mechanism insights. *Chem. Eur. J.* 26, 4988-4996.
- (13) Loh, Y. Y., Nagao, K., Hoover, A. J., Hesk, D., Rivera, N. R., Colletti, S. L., Davies, I. W., and MacMillan, D. W. (2017) Photoredox-catalyzed deuteration and tritiation of pharmaceutical compounds. *Science* 358, 1182-1187.
- (14) Valero, M., Weck, R., Güssregen, S., Atzrodt, J., and Derdau, V. (2018) Highly selective directed iridium-catalyzed hydrogen isotope exchange reactions of aliphatic amides. *Angew. Chem. Int. Ed.* 57, 8159-8163.
- (15) Zolotarev, Y. A., Dadayan, A., Bocharov, E., Borisov, Y. A., Vaskovsky, B., Dorokhova, E., and Myasoedov, N. (2003) New development in the tritium labelling of peptides and proteins using solid catalytic isotopic exchange with spillover-tritium. *Amino Acids* 24, 325-333.
- (16) Wilkes, B. C., Hruby, V. J., Yamamura, H. I., Akiyama, K., Castrucci, A. M. d. L., Hadley, M. E., Andrews, J. R., and Wan, Y.-P. (1984) Synthesis of tritium labeled Ac-[Nle⁴, D-Phe⁷]-α-MSH₄₋₁₁-NH₂: A superpotent melanotropin with prolonged biological activity. *Life Sci.* 34, 977-984.

- (17) Hellio, F., Lecocq, G., Morgat, J., and Gueguen, P. (1990) Total synthesis of fully tritiated leu-enkephalin by enzymatic coupling. *J. Label. Compds. Radiopharm.* 28, 991-999.
- (18) Pedersen, M. H. F., and Baun, M. (2012) Tritium labelling of PACAP-38 using a synthetic diiodinated precursor peptide. *J. Label. Compds. Radiopharm.* 55, 1-4.
- (19) Shevchenko, V., Nagaev, I. Y., and Myasoedov, N. (2018) Heterogeneous catalytic synthesis of organic compounds labeled with hydrogen isotopes without using solvents. *Radiochemistry* 60, 105-139.
- (20) Luo, P., Liu, Z., Zhang, T., Wang, X., Liu, J., Liu, Y., Zhou, X., Chen, Y., Hou, G., and Dong, W. (2021) Photochemical bromination and iodination of peptides and proteins by photoexcitation of aqueous halides. *Chem. Commun.* 57, 11972-11975.
- (21) Schadt, S., Hauri, S., Lopes, F., Edelmann, M. R., Staack, R. F., Villaseñor, R., Kettenberger, H., Roth, A. B., Schuler, F., and Richter, W. F. (2019) Are biotransformation studies of therapeutic proteins needed? Scientific considerations and technical challenges. *Drug Metab. Dispos.* 47, 1443-1456.
- (22) Edelmann, M. R., Kettenberger, H., Knaupp, A., Schlothauer, T., and Otteneder, M. B. (2019) Radiolabeled IgG antibodies: Impact of various labels on neonatal Fc receptor binding. *J. Label. Compds. Radiopharm.* 62, 751-757.
- (23) Wang, M., Zhan, Y., O'Neil, S. P., Harris, S., Henson, C., McEwen, A., Webster, R., and O'Hara, D. M. (2018) Quantitative biodistribution of biotherapeutics at whole body, organ and cellular levels by autoradiography. *Bioanalysis* 10, 1487-1500.
- (24) Kumar, K., and Woolum, K. (2021) A novel reagent for radioiodine labeling of new chemical entities (NCEs) and biomolecules. *Molecules* 26, 4344.
- (25) Peng, C., Hua, R., Souers, P., and Coronado, P. (1988) Tritium labeling of amino acids and peptides with liquid and solid tritium. *Fus. Technol.* 14, 833-839.
- (26) Tóth, G., Lovas, S., and Ötvös, F. (1997) Tritium Labeling of Neuropeptides, in *Neuropeptide Protocols* (Irvine, G. B., and Williams, C. H., Eds.) pp 219-230, Humana Press, Totowa, NJ.
- (27) Roepstorff, P., and Fohlman, J. (1984) Proposal for a common nomenclature for sequence ions in mass spectra of peptides. *Biomed. Mass. Spec.* 11, 601.
- (28) You, C., Zhang, Y., Xu, P., Huang, S., Yin, W., Eric Xu, H., and Jiang, Y. (2022) Structural insights into the peptide selectivity and activation of human neuromedin U receptors. *Nat. Commun.* 13, 2045.
- (29) Funes, S., Hedrick, J. A., Yang, S., Shan, L., Bayne, M., Monsma Jr, F. J., and Gustafson, E. L. (2002) Cloning and characterization of murine neuromedin U receptors. *Peptides* 23, 1607-1615.

Chapter Five

Functional *in vitro* assessment of modified antibodies: Impact of label to protein properties

This declaration concerns the article entitled:			
Functional <i>in vitro</i> assessment of modified antibodies: Impact of label to protein properties			
Publication status (tick one)			
Draft manuscript	<input type="checkbox"/>	Submitted	<input type="checkbox"/>
In review	<input type="checkbox"/>	Accepted	<input type="checkbox"/>
		Published	<input checked="" type="checkbox"/>
Publication details (reference)	Edelmann MR*, Hauri S. (2021) <i>PLoS One</i> 16 (9):e0257342		
Copyright status (tick the appropriate statement)			
I hold the copyright for this material	<input checked="" type="checkbox"/>	Copyright is retained by the publisher, but I have been given permission to replicate the material here	<input type="checkbox"/>
Candidate's contribution to the paper (provide details, and also indicate as a percentage)	<p>The candidate contributed to / considerably contributed to / predominantly executed the...</p> <p>Formulation of ideas: 90%</p> <p>Design of methodology: 50%</p> <p>Experimental work: 100%</p> <p>Presentation of data in journal format: 75%</p>		
Statement from Candidate	This paper reports on original research I conducted during the period of my Higher Degree by Research candidature.		
Signed		Date	17.10.22

Introduction

In drug discovery and development of therapeutic antibodies, the implementation of protein labelling techniques is an extremely valuable tool for *in vitro* and *in vivo* testing to gain a better understanding the fate of therapeutic proteins in the body.¹ Radioactive or fluorescent labels attached to monoclonal antibodies (mAbs) or antibody fragments are routinely used in preclinical development, e.g. in biotransformation,² biodistribution,³ or binding⁴ studies. The labels allow tracking, monitoring, and imaging mAbs within complex biological matrices to evaluate their stability and disposition. Several types of labels are available, largely differentiated in fluorescent dyes for light and electron microscopy, and radioactive isotopes for imaging applications. Both can also be analysed by high-performance liquid chromatography (HPLC) combined with the appropriate detectors. It should be considered that the introduction of labels poses a risk of changes in the physicochemical properties of the labelled protein. Not only can the degree of label (DoL) change the properties of modified IgGs⁵, but the type of label may as well. For example, fluorescent labels often contain sulfonic acids, which upon conjugation add negative charges to the surface of the protein. Even more drastic, the labelling process could rely on harsh reaction conditions, such as oxidation or reduction, and damage the structure of the antibody entirely.

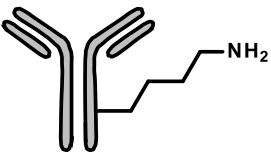
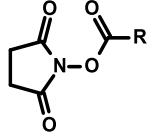
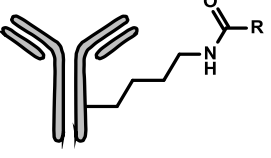
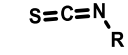
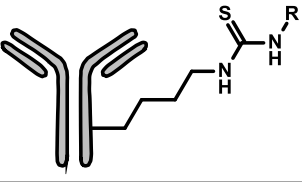
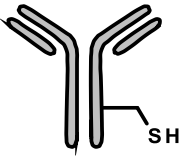
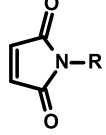
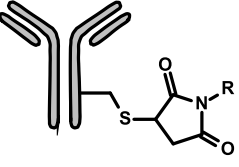
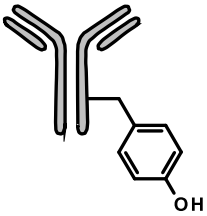

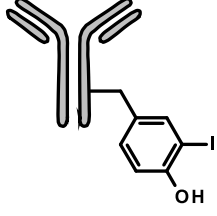
A quality control workflow was established which, in addition to the classic purity determination by size-exclusion chromatography (SEC), assesses changes in cell-specific receptor affinities and surface charges of the labelled protein. The involved analytical methods are SEC, neonatal Fc receptor (FcRn) and heparin affinity chromatography, as well as intact mass spectrometry (MS). This article describes the quality control workflow for labelled antibodies and compares the analytical results with their unlabelled counter-parts. It is not covering protein modifications for radioimmuno conjugates⁶ or antibody drug conjugates⁷ in which a radiolabel or toxic payload is desired. The main question addressed in this study is whether the label has an impact on the pharmacokinetic (PK) properties and how they can be extrapolated back to the parent antibody.

Labelling of Amino Acid Residues

A successful protein labelling technique depends on two chemically compatible requirements: A reactive group on a derivatisation reagent and surface accessible functional groups from amino acids in the antibody. This study included two types of protein labelling: 1) the direct introduction of radioactive atoms, e.g. ¹²⁵I to functional groups without the use of chemical spacers, and 2) by conjugation on functional groups

in the amino acid sequence of proteins using reactive tags. An overview of the labelling techniques used for this study is given in **Table 1**.

Table 1: Overview of labelling techniques used in this study. Amino acid residues schematically represent the majority of the amino acids on which labelling or modification takes place. Reactive group describes the part of the label that conjugates with the corresponding amino acid side chain. The reaction product shows the formed chemical structural formula after the covalent linkage of the label to the protein.

Amino acid residue	Reactive group	Reaction product
 Lysine	 N-Hydroxysuccinimide esters	
	 Isothiocyanates	
 Cysteine	 Maleimides	
 Tyrosine	 Iodonium	

Conjugation of Lysine Residues

There are around 80 lysine residues on average across a humanized monoclonal IgG₁ protein. Peptide-mapping experiments could identify almost 40 lysine residues for a potential conjugation.⁸ *N*-Hydroxysuccinimide esters (NHS) and isothiocyanates (SCN) are the most common reactive groups for a protein modification on ϵ -amino group of lysine residues or the *N*-terminal α -amine group. NHS ester-containing reagents react with amines in a pH range of 7-8 to form a stable amide bond. *N*-Succinimidyl propionate (NSP) was selected for this study since the corresponding tritium variant of NSP⁹ is suitable for a fast and efficient technique for incorporating the radio isotope tritium into a protein. In contrast to NHS reagents, the electrophilic carbon of the isothiocyanate-group reacts almost selectively with amines to form a stable thiourea. A consequence of amine

conjugation is the loss of the positive charge from lysine residues, which may have an impact on (at least) unspecific binding to the cell surface.

Conjugation of Cysteine Residues

An alternative to conjugation of lysine residues is the introduction of maleimide-based labels on cysteines.¹⁰ Cysteine residues form intramolecular disulfide bridges, which stabilize the protein tertiary structures. Disulfides do not react with maleimides. Therefore, it is necessary to reduce disulfides prior to the conjugation. Reducing agents such tris(2-carboxyethyl) phosphine (TCEP) can break disulfide bonds, which then can be used for a maleimide-containing labelling modification. This labelling process, however, can lead to damage of the protein.

Iodination of Tyrosine Residues

Radioiodination of proteins has a long tradition.^{11,12} Wilbur¹³ reported a detailed overview about radiohalogenation of proteins including various methods and reagents for conjugate labelling. An *in situ* generated mixture of halogen iodo-chloride species performs an electrophilic substitution of hydrogen under oxidative conditions on tyrosine or histidine residues. The sites of radioiodination vary with the choice of oxidizing agent and the pH of the labelling reaction. In general, formation of iodinated tyrosyl residues predominates near pH 7 and yields primarily monoiodotyrosine.¹⁴ Non-radioactive sodium iodide was used for the test labelling experiments in order to avoid working with specialist equipment and laboratory facilities with regards to radiation safety.

Materials and Methods

Chemicals and Reagents

Antibodies for this study were produced in house. Alexa Fluor 488 (AF488)-Maleimide and Alexa Fluor 488-NHS were purchased from Invitrogen (Carlsbad, CA, USA), thulium (III) 2-(4-isothiocyanatobenzyl)-1,4,7,10-tetraazacyclododecane-1,4,7,10-tetraacetic acid (Tm-*p*-SCN-Bn-DOTA) from Macrocyclics (Plano, TX, USA). *N*-Succinimidyl propionate (NSP) was purchased from Wako-Chemicals (Richmond, VA, USA), DOTA-NHS from Synchem (Felsberg / Altenburg, Germany), and the water-soluble Bolton-Hunter reagent sulfosuccinimidyl-3-(4-hydroxyphenyl)-propionate sodium salt (Sulfo-SHPP) from Apollo Scientific (Cheshire, UK). Sodium iodine (Sigma-Aldrich Chemie, Munich, Germany) and Pierce pre-coated IODO-GEN iodination tubes (Thermo Fisher

Scientific, Waltham, MA, USA) as an oxidizing agent were used for iodination experiments. All reagents were used without further purification.

Analytical Equipment

Protein concentrations were determined by Eppendorf (Hamburg, Germany) BioSpectrometer® basic in combination with an Eppendorf µCuvette® G1.0 with 1 mm path length at 280 nm wavelength and the corresponding calculated molar extinction coefficient. For the fluorescence-labelled mAbs, the absorbance at 494 nm was measured to calculate the degree of labelling with AF488 dye. Chromatographic analysis for size-exclusion, FcRn affinity, and heparin affinity was performed on an Agilent 1200 series HPLC system (Santa Clara, CA, USA). Agilent ChemStation software was used for data evaluation.

Labelling Procedure

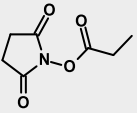
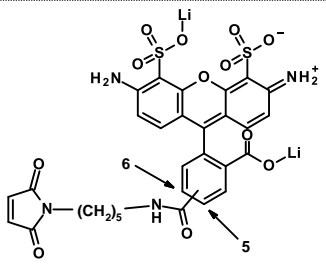
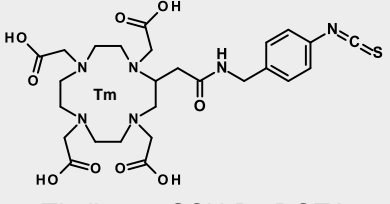
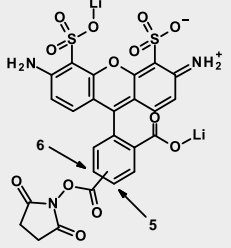
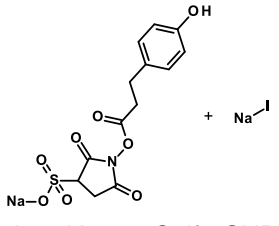
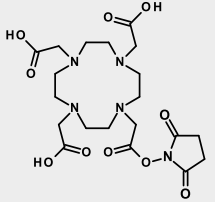
In this study, 2 different subclass 1 immunoglobulin G were modified with various labels. mAb_A is a human wild-type antibody, the second protein mAb_B is a concept antibody with reduced affinity to Fc-gamma receptor Fc-γR (LALA-PG mutation).¹⁵ An overview of the antibodies with different type of labels and the corresponding chemical structures is given in **Table 2**. The aim was to obtain 1 to 3 labels per protein with all labelling techniques in order to achieve the highest comparability.

N-Hydroxysuccinimide (NHS) modifications were carried out in analogy to previously published procedures.¹⁶ Briefly, an IgG solution in PBS (protein concentration: 1 to 5 mg/mL; pH 7.5 to 8.5) was added to NHS-based labels (3 molar equivalents, dissolved in DMSO), and shaken orbitally for 30 minutes.

mAbs, conjugated with Alexa Fluor 488-maleimide, were labelled strictly according to Invitrogen's kit-manuals: *Thiol-Reactive Probes*. In summary, reduction of thiol-residues with tris(2-carboxyethyl) phosphine (TCEP, 10 equivalents) in PBS pH 7.5 and a protein concentration of 2 mg/mL. Maleimide (11 equivalents in DMSO) was added to the protein solution and incubated for 2 hours.

Conjugations with Tm-*p*-SCN-Bn-DOTA (20 equivalents in DMSO) was performed in HEPES (4-(2-hydroxyethyl)-1-piperazineethansulfonic acid (Gibco, Paisley, UK), at pH 7.5 by a protein concentration of 20 to 30 mg/mL by mild shaking for 3 hours.

Table 2: Labels used in this study. Chemical structures of labels used in this study. Label Code describes the abbreviations of each label mentioned in this study. Column “Amino acid” shows the corresponding amino acid involved in the labelling process. Alphanumeric links to the modified mAbs are given in the two right-hand columns: mAbA1-4: wildtype mAb; mAbB1-7: research concept mAb.

Label	Label Code	Amino acid	mAb #	
 <p>N-Succinimidyl propionate</p>	NSP	Lysine	A1	B1
 <p>Alexa Fluor 488-maleimide</p>	AFM	Cysteine	A2	B2
 <p>Thulium-<i>p</i>-SCN-Bz-DOTA</p>	SCN	Lysine	A3	B3
<p>I^+</p> <p>Iodonium</p>	DI	Tyrosine	A4	B4
 <p>Alexa Fluor 488-NHS</p>	AFN	Lysine	---	B5
 <p>Bolton-Hunter Sulfo-SHPP</p>	BHN	Lysine	---	B6
 <p>DOTA-NHS</p>	DN	Lysine	---	B7

Direct iodination on tyrosine residues was carried out according to Thermo Fisher Scientific manual 0016379; Example Protocol II: *Direct Method for Iodination*. Indirect iodination, using water soluble Bolton Hunter-NHS reagent, was performed in analogy to Thermo Fisher Scientific's Example Protocol III: *Iodination of Crosslinkers*. Pierce™ Pre-Coated Iodination Tubes (Iodo-Gen®) were used for both iodination techniques, direct and indirect.

All labelled antibodies were buffer exchanged into 20 mM histidine, 140 mM sodium chloride, pH 6 formulation buffer using a PD MidiTrap G-25 desalting cartridge (GE Healthcare, Chicago, IL, USA). The DMSO volume of the label solutions never exceeded 5% of the total volume. Solutions for fluorescence labelling were protected from light as much as possible by wrapping all containers in aluminum foil.

Chromatography

Whenever possible, a common baseline was drawn and the peaks were split at minima or plateaus. A plateau is reached at a position where the chromatogram is parallel to the baseline. The highest peak retention time was used for the evaluation. The chromatograms of all mAbs used in this study can be found in **Figures S1-S3**.

Size-Exclusion Chromatography

Samples were analysed using a TSKgel G3000 SW_{XL} column (Tosoh Bioscience, Tokyo, Japan), 7.8 x 300 mm, 5 µm with 0.2 M potassium phosphate, 0.25 M potassium chloride, pH 7.0 as the mobile phase at a flow rate of 0.5 mL/min. Absorbance at 280 nm and in addition 494 nm for the fluorescence-labelled mAbs were used for detection and quantification. The injection volume was 10 µL and the protein concentration 1 mg/mL. The target concentration of 1 mg/mL was set by adding the eluent to the protein stock solution.

FcRn Affinity Chromatography

Analytical FcRn affinity chromatography¹⁷ was carried out with an FcRn affinity column (Roche Custom Biotech, Mannheim, Germany), column volume of 0.5 mL containing 1.5 mg FcRn protein. For detection and quantification, an absorbance at 280 nm and in addition 494 nm for fluorescence-labelled mAbs were used. The 45-min continuous gradient was applied with a flow rate of 0.5 mL/min (**Table 3**). The injection volume was 30 µL and the protein concentration 1 mg/mL. The target concentration of 1 mg/mL was set by adding eluent A to the protein stock solution.

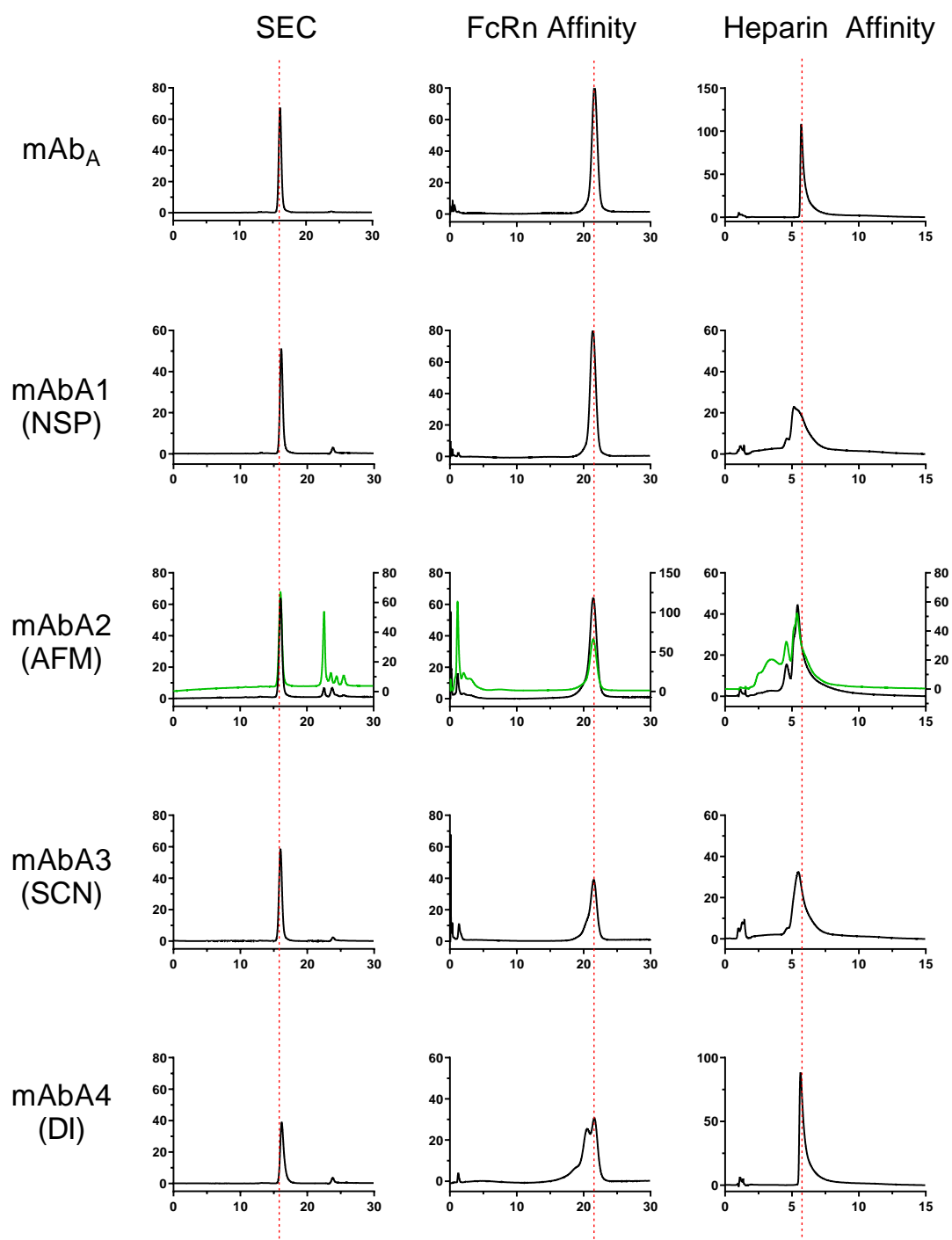


Figure S1: Chromatograms of mAbA1 to mAbA4 from the mAb_A series. Left column: SEC; center column: FcRn affinity chromatography; right column: heparin affinity chromatography. X-axis: time in min; left Y-axis: absorbance at 280 nm in black; right Y-axis: absorbance at 494 nm in green.

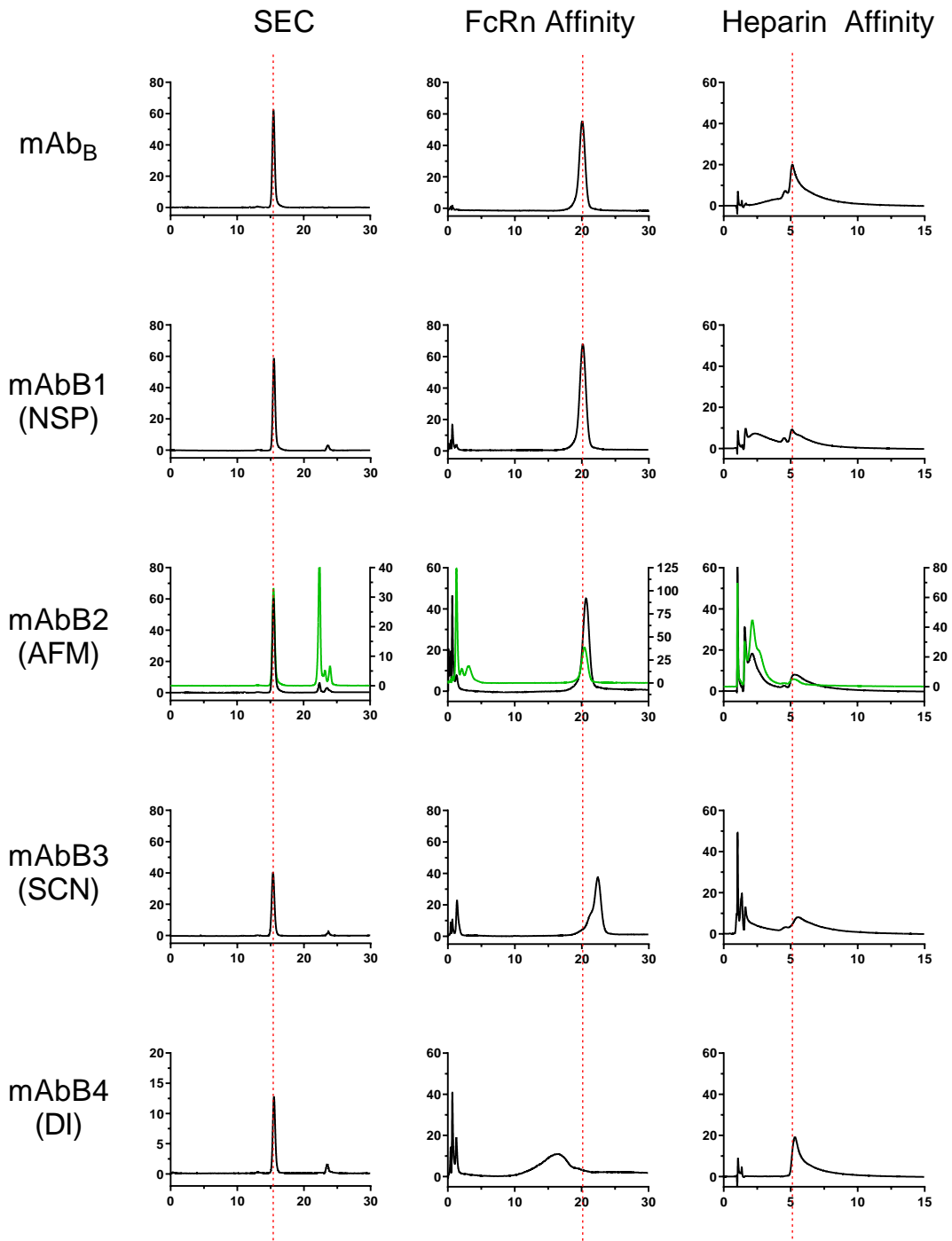


Figure S2: Chromatograms of mAbB1 to mAbB4 from the mAb_B series. Left column: SEC; center column: FcRn affinity chromatography; right column: heparin affinity chromatography. X-axis: time in min; left Y-axis: absorbance at 280 nm in black; right Y-axis: absorbance at 494 nm in green.

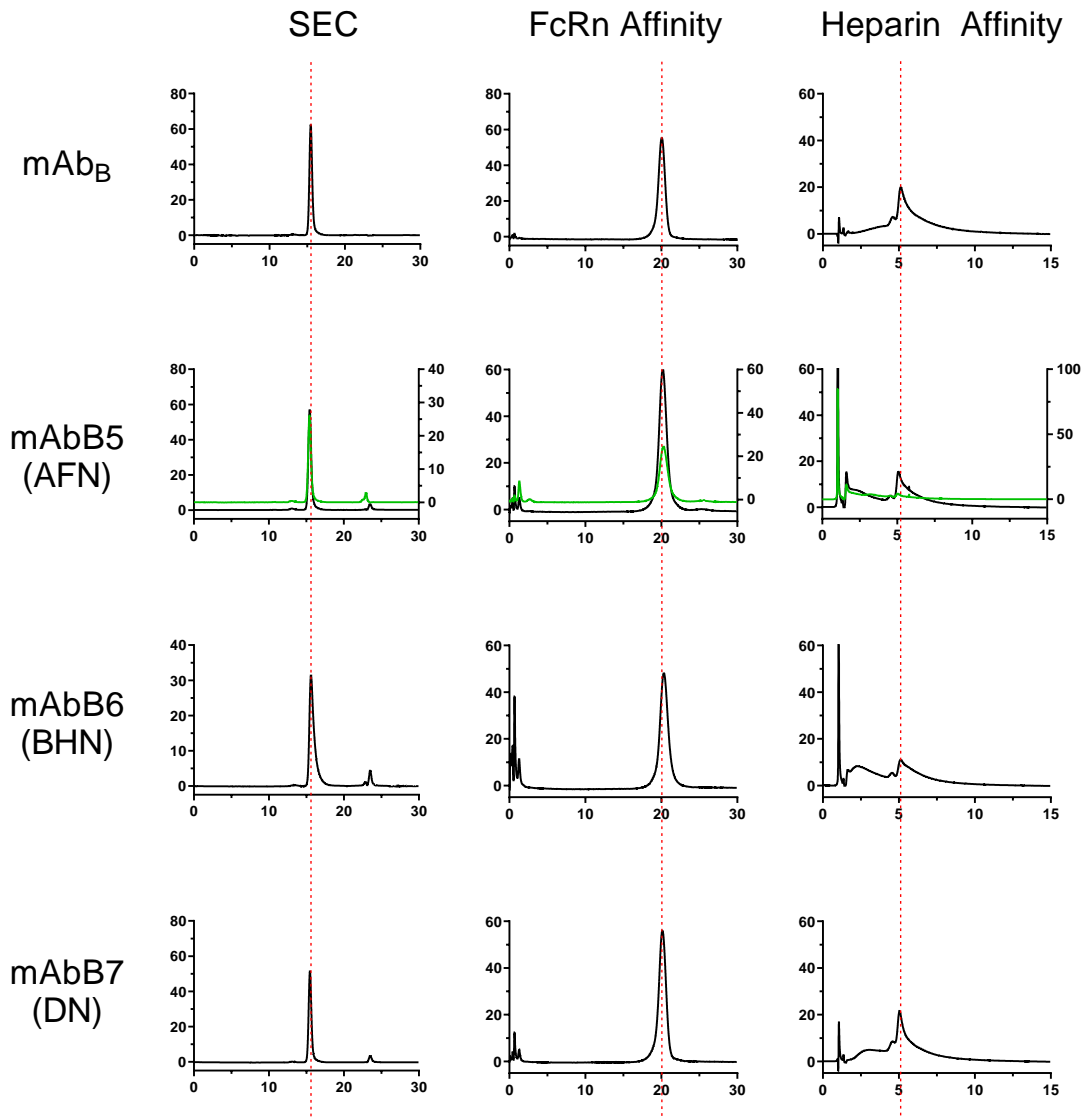


Figure S3: Chromatograms of mAbB5 to mAbB7 from the mAb_B series. Left column: SEC; center column: FcRn affinity chromatography; right column: heparin affinity chromatography. X-axis: time in min; left Y-axis: absorbance at 280 nm in black; right Y-axis: absorbance at 494 nm in green.

Table 3: Chromatographic method used for FcRn affinity chromatography. Eluent A: 20 mM 2-(N-morpholino)ethanesulfonic acid (MES), 140 mM NaCl buffer, pH 5.5; Eluent B: 20 mM tris(hydroxymethyl)aminomethan (Tris), 140 mM NaCl buffer, pH 8.8.

Time [min]	Eluent A [%]	Eluent B [%]
0	80	20
5	80	20
40	0	100
45	0	100
46	80	20
51	80	20

Heparin Affinity Chromatography

A commercially available heparin column (TSK-Gel Heparin-5PW, 5 x 50 mm, Tosoh Bioscience, Tokyo, Japan) was equilibrated with eluent A, followed by a 23 min continuous gradient to 100% eluent B was applied with a flow rate of 0.8 mL/min (**Table 4**). The injection volume was 30 μ L and the protein concentration 1 mg/mL. The target concentration of 1 mg/mL was set by adding eluent A to the protein stock solution.

Table 4: Chromatographic method used for heparin affinity chromatography. Eluent A: 50 mM Tris, pH 7.4; Eluent B: 50 mM Tris, 1 M NaCl, pH 7.4.

Time [min]	Eluent A [%]	Eluent B [%]
0	100	0
2	100	0
18.5	45	55
19	0	100
23	0	100
24	100	0
32	100	0

Mass Spectrometry

For mass spectrometry analysis, a Waters (Baden, Switzerland) nanoAcquity pump equipped with Waters LCT Premier XE and a Acquity UPLC Protein C4 column, 300 Å, 1.7 μ m, 1 x 50 mm was used in ESI positive mode at a flow rate of 70 μ L/min. Mobile phases used were (A) water/acetonitrile 9:1 with 0.1% trifluoroacetic acid and (B) acetonitrile/water 9:1 with 0.1% trifluoroacetic acid, from 10% (B) to 65% (B) within 10 minutes. Proteins have been analysed (if not otherwise mentioned) reduced and deglycosylated by the use of Rapid PNGase F (New England Biolabs, Ipswich, MA, USA) according to the following representative procedure: 5.7 μ L miliQ water was added to 10.3 μ L (12 μ g) protein solution. 4 μ L Rapid PNGase F buffer, containing dithiothreitol

(DTT) for mild reduction of disulfide bonds (5x) and 1 μ L Rapid PNGase F¹⁸ for deglycosylation was added. The mixture was incubated at 50 °C for 15 minutes.

Results and Discussion

This section explains the quality assessment package that compares antibodies, which have been modified with different type of labels, to the original, unlabelled parent proteins. The degree of labelling was calculated using mass spectrometry and supplemented by light spectroscopy in case of fluorescence-labelled variants. Size-exclusion chromatography provides a quantitative assessment of the degradation and aggregation of intact proteins. The affinity for neonatal Fc receptor and heparin were carried out using commercially available chromatography columns and the resulting retention times of labelled versus unlabelled protein were compared. These results allowed a correlation with both kinds of affinity chromatography and a prediction of the influence of the label on a change in PK properties of the protein.

Mass Spectrometry Analysis

The incorporation of labels at the proteins were identified by mass spectrometry. All labelled IgGs were analysed in reduced and deglycosylated form. Using this method, the heavy chain and the light chain are separated from each other by HPLC measured by intact mass spectrometry (**Figure 1**). By assuming a Poisson distribution, the percentage of incorporated labels could be determined on both the light and heavy chain. The degree of labelling (DoL) describes how many labels in average are bound to a protein. For example, a DoL of 1 refers to a label:protein molar ratio of 1:1. Considering the Poisson distribution (**Formula 1**), the actual number of labels conjugated to an antibody at a DoL of 1 reflect 37% of the antibody molecules are unlabelled, 37% will contain one label, 18% will contain two labels, 6% will contain three labels, and 2% four or more labels. The theoretical calculations from the Poisson distribution are also reflected in the label pattern of the conjugated intact antibody samples from the total ion chromatogram (**Figure 2: C**). Considering the labelling distribution on the light chain and heavy chain of each conjugated antibody (**Table 5**), the degree of labelling of the intact protein was calculated and listed in **Figure 2: D**.

Table 5: Labelling distribution on light and heavy chain calculated by ion peak integration in mass spectrometry. Label distribution calculation of intact protein follows the probability of Poisson distribution (**Formula 1**).

mAb #	Label light chain [%]				Label heavy chain [%]				Label intact protein [%]				
	0	1	2	3	0	1	2	3	0	1	2	3	4
A1	54	38	8	0	66	29	5	0	16	29	27	17	8
A2	43	57	0	0	25	64	10	1	6	16	23	22	16
A3	66	32	2	0	80	20	0	0	33	37	21	8	2
A4	59	38	3	0	65	30	5	0	19	31	26	15	6
B1	57	34	9	0	48	30	11	7	8	21	26	21	13
B2	58	42	0	0	54	44	2	0	17	30	27	16	7
B3	66	31	3	0	49	41	10	1	13	27	27	18	9
B4	77	20	3	0	24	39	26	12	5	14	22	22	17
B5	71	26	2	0	69	26	5	0	27	35	23	10	3
B6	65	34	1	0	63	33	4	0	21	33	25	13	5
B7	91	9	0	0	66	31	3	0	40	37	17	5	1

$$P(k) = \frac{\lambda^k * e^{-\lambda}}{k!}$$

Formula 1

Probability (P) of events for a Poisson distribution. λ is the average number of events per interval; e represents the Euler's number (2.7182...); k takes values 0, 1, 2, 3, 4, ...; k! is the factorial of k.

$$c(M)_{AF-mAbs} = \frac{[A_{280} - (A_{494} * 0.11)]}{\epsilon(M) * d}$$

Formula 2

Calculation of molar protein concentration labelled with Alexa Fluor 488. Absorbance of the protein solution at 280 nm (A_{280}) and 494 nm (A_{494}) in a cuvette with $d = 0.1$ cm path length, and the corresponding molar extinction coefficient ϵ (M).

$$DoL_{AF-mAbs} = \frac{A_{494}}{\epsilon(AF488) * c(M) * d}$$

Formula 3

Calculation of degree of labelling (DoL) for fluorescence-labelled conjugates based on spectrometric analysis. Absorbance of the protein solution at 494 nm (A_{494}) in a cuvette with $d = 0.1$ cm path length, approximate molar extinction coefficient of Alexa Fluor 488 dye ϵ (AF488) = 71,000 $\text{cm}^{-1} \text{M}^{-1}$ at 494 nm, molar protein concentration c (M) was calculated by the use of **Formula 2**.

$$t_{relative\ labelled} = \frac{t_{labelled}}{t_{unlabelled}}$$

Formula 4

Calculation of relative retention time for FcRn and heparin affinity chromatography.

DoL determination of mAbB6, labelled with Bolton-Hunter-NHS (BHN) reagent, was more complex, as two different labelling steps were required: 1) the labelling of BHN with iodine and 2) the conjugation to lysine residues using NHS-technology. The iodination of BHN did not result in a homogenous product, but rather a mixture of uniodinated, singly, and doubly iodinated BHN. Mass spectrometric analyses consequently showed a mixture of Bolton-Hunter-conjugate with no iodine, single and double iodine. Regardless the number of iodine on BHN, it was considered as one label when calculating the DoL for mAbB6.

In addition to mass spectrometry analysis, the degree of labelling of the fluorescence-labelled samples was calculated by light spectroscopy using **Formula 2** and **Formula 3**. The results of mAbB5, Alexa Fluor 488-NHS conjugation, from MS and spectroscopy analysis are comparable. An analytical deviation was encountered in the determination of DoL of mAbA2 and mAbB2, which were conjugated using the maleimide-cysteine technique. The result from the spectroscopy shows a 3-fold higher DoL than calculated by mass spectrometry (**Table 6**). An additional MS analysis of proteins without prior reduction during sample preparation provides an explanation: almost no intact protein was found in these analysis. Most of the mass signals showed protein fragments derived from a labelled light chain as well as labelled IgG without a light chain or without both light chains. The protein damage was most likely caused by the labelling process. After the partial reduction of inter-chain disulfide bonds and the subsequent addition of maleimide-dyes to cysteine residues, the corresponding thiols are blocked to form a disulfide bond again, however the quaternary structure is kept intact through inter-molecular forces.

Table 6: Absorbance of fluorescent-labelled antibodies. mAbs A2, B2, and B5 absorbances at 280 nm (A_{280}) and 494 nm (A_{494}). ϵ : molar extinction factor; d : path length of cuvette; c : protein concentration in molarity [M] and mass per volume [mg/mL]; DoL: degree of label.

<i>mAb#</i>	A_{280}	A_{494}	ϵ [$cm^{-1} M^{-1}$]	d [cm]	c [M]; [mg/mL]	DoL
A2	0.185	0.416	198,420	0.1	6.5×10^{-6} ; 0.95	9.0
B2	0.188	0.296	213,890	0.1	7.8×10^{-6} ; 1.11	5.3
B5	0.210	0.125	213,890	0.1	9.9×10^{-6} ; 1.41	1.7

Another major observation was that the incorporation rate of bulky labels on lysine residues is different for the light and heavy chains of the antibody. Alexa Fluor 488 (mAbB5) and DOTA (mAbB7), conjugated by NHS chemistry, showed a lower label incorporation in light chains compared to isothiocyanate based conjugated Tm-DOTA in mAbA3 and mAbB3. This is particularly noteworthy that NHS and SCN functionalized

labels react to lysine residues. *N*-Succinimidyl propionate as a small label in contrast, a higher incorporation at the light chain was observed (**Figure 2: A,B**).

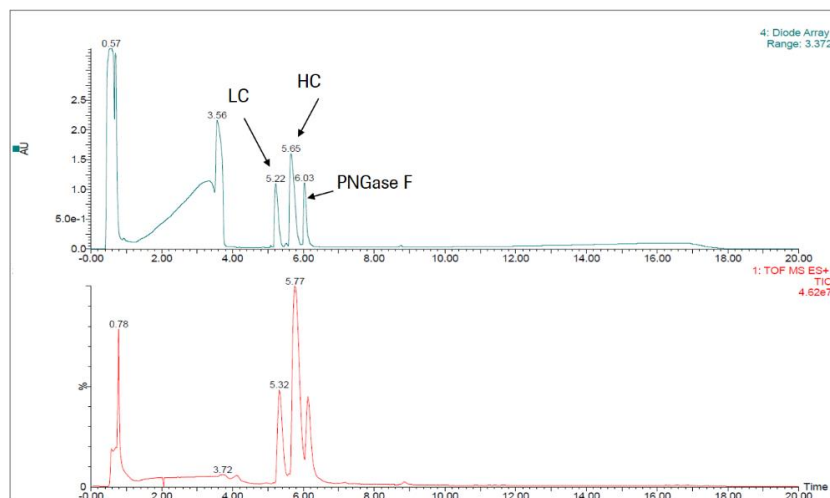


Figure 1: Representative example of a chromatographic separation for subsequent mass spectrometric analysis. LC: light chain; HC: heavy chain; PNGase F: peptide *N*-glycosidase F.

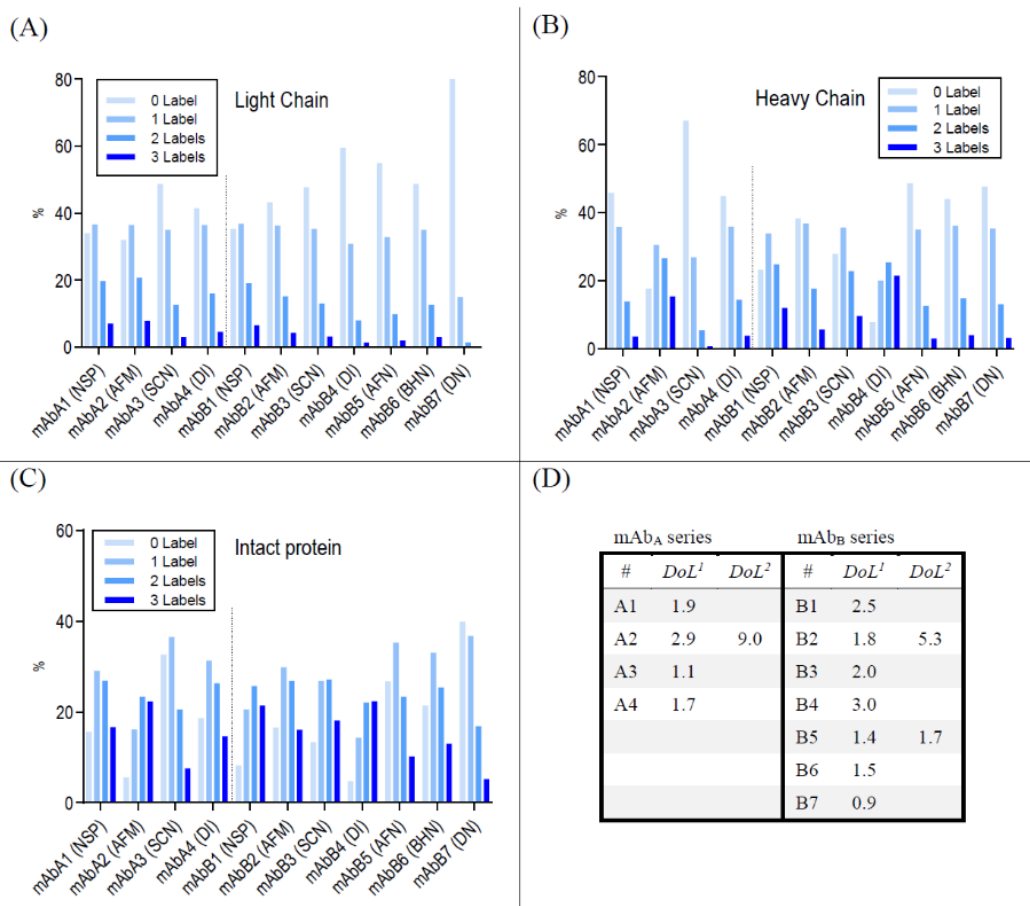


Figure 2: Labelling distribution of mAbA1-4 and mAbB1-7. (A): light chain; (B): heavy chain; (C) intact protein, according to Poisson distribution; (D): calculated degree of labelling (DoL). DoL¹: based on labelling distribution determined by mass spectrometry analysis; DoL²: based on spectroscopic calculation for fluorescence-labelled mAbs (**Formula 2**). Label Code: NSP: *N*-succinimidyl propionate; AFM: Alexa Fluor 488-maleimide; SCN: Tm-*p*-SCN-Bz-DOTA; DI: direct iodination; AFN: Alexa Fluor 488-NHS; BHN: Bolton-Hunter-NHS; DN: DOTA-NHS.

Size-Exclusion Chromatography (SEC)

SEC is an established application for the routine monitoring of therapeutic proteins with respect to purity and the identification of low as well as high molecular weight impurities.¹⁹ The retention time is a function of the HPLC flow rate, column pore size, and the hydrodynamic radius of the protein, and its potential fragments and aggregates. After conjugating a label to an antibody, the molecular weight does not change dramatically. A change in the hydrodynamic radius, in contrast, can induce a shift in migration time even with a negligible increase in molecular weight.²⁰ This phenomenon is observed in particular by introducing multiple charged labels such as chelators or fluorescence dyes. The difference in the retention times of the modified antibodies from this study are, however, too low to give a meaningful trend (**Table 7**).

Antibodies that have been treated with maleimide-based labels show an obvious degradation and confirm the finding from mass spectrometry of a fragmented antibody. The corresponding SEC shows a peak at the expected migration time of the unlabelled antibody at 16.1 min (mAbA2) and 15.5 min (mAbB2). An additional protein fragment with absorbance at 494 nm at around 22.4 min appeared. Although the molecular weight decreases due the cleavage of light chains, the retention times at around 16 min remains almost the same. The relatively unaltered retention time of the antibody fragments to the unlabelled proteins can be explained by an increase of the hydrodynamic sizes of human IgGs, which was observed after partial reduction of inter-chain disulfide bonds.²¹ In an additional SEC experiment, maleimide-labelled mAbB2 was treated by the addition of 0.1% formic acid (protein solution to formic acid 1:1 v/v) prior to injection. The main peak (mAbB2) at 15.5 min has disappeared and several peaks eluted at 16.0 min, 16.8 min, 20.4 min, 24.1 min, and 24.9 min (**Figure 3**). So, possibly, under non-denaturing conditions of the SEC, the reduced antibody was stabilized through a non-covalent interaction (ionic, hydrogen bonds, Van der Waals, or hydrophobic) and remained as intact protein at 15.5 min. However, after denaturation at low pH, the molecule divided into individual chains. This indicates that the disulfide bridges could not be reestablished after the labelling. Free thiol groups may have an unexpected impact on the PK properties of the therapeutic protein and should be avoided if possible.

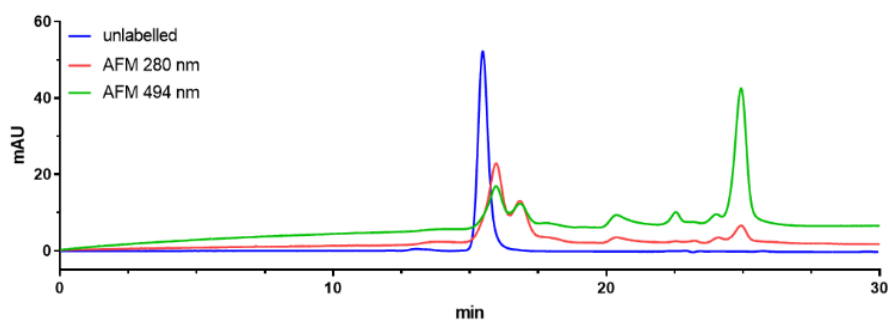


Figure 3: SEC of mAbB2 (Alexa Fluor 488-maleimide), denatured with 0.1% formic acid. Blue line: unlabelled mAb_B showed a single peak. Red line: absorbance of modified mAb₆ at 280 nm. Green line (494 nm) showed several peaks that indicate (labelled) protein fragments.

Table 7: Retention times in size-exclusion chromatography. ^(a): Peak area of 67%, additional peak at 22.6 min (33%). ^(b): Peak area of 49%, additional peak at 22.4 min (51%). Label Code: NSP: *N*-succinimidyl propionate; AFM: Alexa Fluor 488-maleimide; SCN: Tm-*p*-SCN-Bz-DOTA; DI: direct iodination; AFN: Alexa Fluor 488-NHS; BHN: Bolton-Hunter-NHS; DN: DOTA-NHS.

<i>mAb</i> #	Label Code	Retention time [min]	<i>mAb</i> #	Label Code	Retention time [min]
mAb _A	---	16.1	mAb _B	---	15.5
A1	NSP	16.1	B1	NSP	15.5
A2	AFM	16.1 ^(a)	B2	AFM	15.5 ^(b)
A3	SCN	16.0	B3	SCN	15.4
A4	DI	16.2	B4	DI	15.5
			B5	AFN	15.5
			B6	BHN	15.6
			B7	DN	15.5

***FcRn* Affinity Chromatography**

The neonatal Fc receptor (*FcRn*) is expressed by many cells types all over the body and structurally related to class I major histocompatibility complex (MHC I).²² The receptor is able to bind IgGs in a strictly pH-dependent manner with high affinity at pH 6 in the acidified endosome and low affinity at physiological pH of 7.4 in plasma.²³ The IgG:*FcRn* complexes are recycled back to the surface of the cell, whereas unbound proteins undergo lysosomal degradation.

For the setup of the antibody quality control package, we used an affinity chromatography based method,²⁴ which can sensitively detect differences in the pH-dependent interaction between IgGs and *FcRn*. The chromatography column contains biotinylated heterodimeric *FcRn*, immobilized onto sepharose streptavidin beads. The protein elution, driven by a pH gradient, resolves protein species according to their pH-dependent affinity to *FcRn* in a process that mimics the events that take place when recycling endosomes emerge at the cell surface. The result is an antibody-specific retention time. An early elution from the column predicts low affinity to the receptor at endosomal pH and thus a potentially short serum half-life. In contrast, late elution from

the column represents a high affinity and a potential long serum half-life, if the pH level is still below 7.4.²⁵ After comparing the retention times (**Table 8**), the results of two labelling techniques are particularly noticeable. First, for IgGs that were labelled by direct iodination, 2 additional peaks appear with a lower retention time. The higher the DoL (mAbA4: 1.7 and mAbB4: 3.0), the more the peak ratio shifts to the left in the chromatogram, which indicates a lower affinity for the neonatal Fc receptor. Apparently, during the labelling process with IODO-GEN, not only was the iodine ion oxidized to form the reactive iodo-chloride species, but the antibody was oxidized within the FcRn binding interface as well. Two surface exposed methionine residues located at position 252 in the C_H2 domain and position 428 in the C_H3 domain (EU numbering)²⁶ interact with the IgG binding region on cellular neonatal Fc receptor. Oxidation of Met252 and Met428 was shown to impair affinity to FcRn and consequently change PK properties of IgGs.^{27,28}

A second anomaly was found in chromatograms derived from antibodies conjugated with isothiocyanate-based labels. A pre-peak occurred with both examples mAbA3 and mAbB3, which were modified with Tm-*p*-SCN-Bz-DOTA. This phenomenon of the additional pre-peak in the FcRn affinity chromatography of IgGs, labelled with isothiocyanate-tags, has already observed. As the DoL is gradually increased, the pre-peak also increases.²⁹ Interaction with the stationary phase can be excluded, since mAbB3 shows no retention in a negative control with a sepharose (without FcRn) column (**Figure 4**). Our conclusion is that conjugation with an SCN-functionalized label creates a new variant that has, depending on DoL, a lower affinity to FcRn. Furthermore, mAbA3 showed a similar retention time to the unlabelled wild-type mAb_A, whereby the identical label in mAbB3 caused a significantly higher affinity to FcRn.

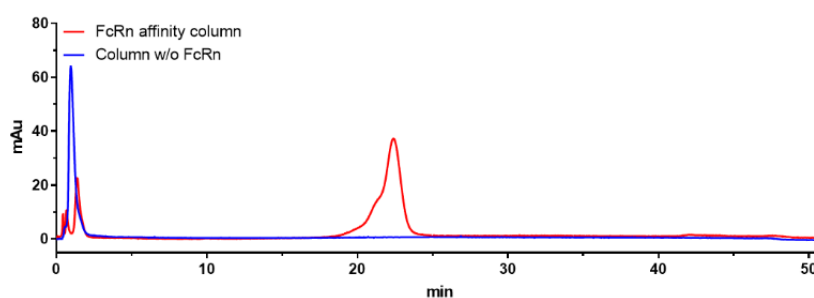


Figure 4: Negative control of mAbB3. Negative control of mAbB3 (Tm-*p*-SCN-Bz-DOTA) using sepharose column without FcRn (blue). The red line shows mAbB3 measured with FcRn affinity chromatography.

Heparin Affinity Chromatography

As a polysulfated polysaccharide, heparin is a strongly (poly-) negatively charged glucosaminoglycan. Such polymers are commonly found on cell surfaces of vascular endothelial cells and immune cells, such as monocytes or macrophages.³⁰ IgGs that bind to heparin are exposed of the risk of unspecific pinocytosis and thus the degradation of

the protein.³¹ Heparin chromatography offers a second way to control the influence of labels on changes in protein properties by charge-based glyocalyx interaction on a heparin affinity column.³² Starting with low-salt condition, heparin chromatography retains antibodies even with a low affinity for heparin. The elution is driven by a salt gradient and separates proteins according to difference in their ionic binding strength.

The corresponding retention times of the labelled antibodies are shown in **Table 8**. mAbB2, which has been labelled with Alexa Fluor 488-maleimide, has a large discrepancy. This is not surprising since previous controls (MS and SEC) showed that the antibody is no longer intact after the labelling process. The NSP-labelled mAb from the mAb_A series differs most clearly from the unlabelled antibody. The significant increase in heparin affinity for mAbB3 (Tm-*p*-SCN-Bz-DOTA) is surprising. When incorporating a negatively charged DOTA-label, it would be assumed that the affinity for negatively charged heparin decreases, as can be observed for mAbA3 with the same label from the mAb_A series.

Table 8: Retention times in FcRn and heparin affinity chromatography. ^(a): Peak area of 52%, additional peaks at 2.3 (10%), 2.1 min (9%), and 1.2 min (27%). ^(b): Peak area of 76%, additional peak at 20.3 min (24%). ^(c): Peak area of 41%, additional peaks at 21.6 min (47%), and 18.8 min (12%). ^(d): Peak area of 45%, additional peaks at 3.1 min (18%), 2.1 min (7%), and 1.3 min (35%). ^(e): Peak area of 74%, additional peak at 21.0 min (26%). Label Code: NSP: *N*-succinimidyl propionate; AFM: Alexa Fluor 488-maleimide; SCN: Tm-*p*-SCN-Bz-DOTA; DI: direct iodination; AFN: Alexa Fluor 488-NHS; BHN: Bolton-Hunter-NHS; DN: DOTA-NHS.

mAb #	Label Code	Retention time FcRn [min]	Retention time Heparin [min]
mAb _A	---	21.6	5.7
A1	NSP	21.4	5.2
A2	AFM	21.4 ^(a)	5.4
A3	SCN	21.5 ^(b)	5.5
A4	DI	20.5 ^(c)	5.6
mAb _B	---	20.1	5.1
B1	NSP	20.2	5.1
B2	AFM	20.4 ^(d)	2.2
B3	SCN	22.4 ^(e)	5.6
B4	DI	16.5	5.3
B5	AFN	20.1	5.1
B6	BHN	20.3	5.1
B7	DN	20.2	5.1

FcRn/Heparin Correlation

A combination of FcRn and Heparin affinity chromatography strengthen an assessment of the quality of therapeutic antibodies after modification. The retention times of labelled and unlabelled protein in both affinity chromatographies, FcRn and heparin, are set in proportion according to **Formula 4** to calculate a relative retention time of each labelled IgG (**Table 9**). A correlation of FcRn and heparin retention (**Figure 5**) identifies

deviations in affinities for the unlabelled antibody. For the labelled IgG, a relative retention time of < 1 in FcRn affinity chromatography indicates a lower IgG:FcRn binding. In contrast to heparin affinity, a relative retention time of > 1 may be indicative of a higher unspecific uptake in cells.

Direct iodinations (mAbA4 and mAbB4) lead to a significant decrease in FcRn affinity due to oxidation of the protein in the neonatal Fc receptor binding interface. All antibodies from the mAb_B series labelled with the *N*-hydroxysuccinimide technique (NSP, AFN, BHN, DN) are closely related in their correlation. In contrast, the only antibody from the mAb_A series that was labelled with the NHS technique (NSP) shows a deviation, although mAbA1 has a lower DoL (1.9) compared to mAbB1 (2.5).

Table 9: Calculated relative retention times. Calculated relative retention times from FcRn and heparin affinity chromatography by the use of **Formula 4**. Label Code: NSP: *N*-succinimidyl propionate; AFM: Alexa Fluor 488-maleimide; SCN: Tm-*p*-SCN-Bz-DOTA; DI: direct iodination; AFN: Alexa Fluor 488-NHS; BHN: Bolton-Hunter-NHS; DN: DOTA-NHS.

mAb #	Label Code	Relative t_R FcRn	Relative t_R Heparin
mAb _A	---	1.00	1.00
A1	NSP	0.99	0.90
A2	AFM	0.99	0.95
A3	SCN	0.99	0.96
A4	DI	0.95	0.99
mAb _B	---	1.00	1.00
B1	NSP	1.01	1.00
B2	AFM	1.02	0.42
B3	SCN	1.12	1.09
B4	DI	0.82	1.04
B5	AFN	1.01	0.99
B6	BHN	1.01	1.00
B7	DN	1.00	0.99

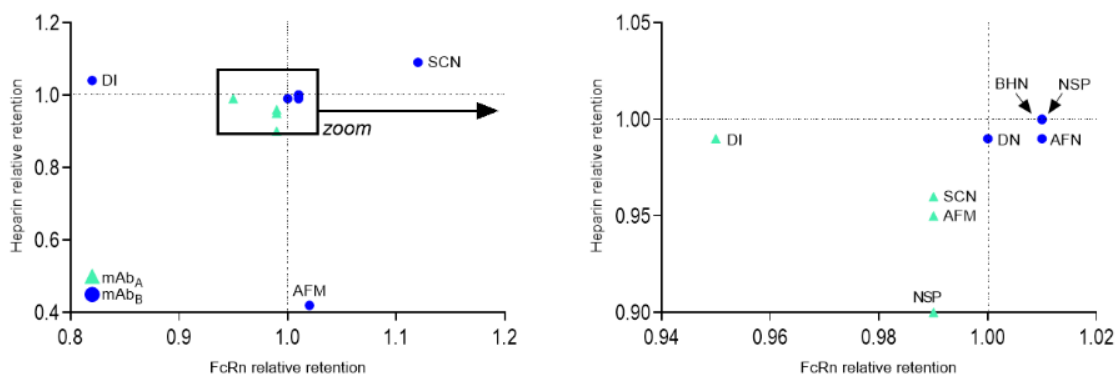


Figure 5: Correlation of FcRn and heparin column retention of labelled antibodies. Green triangle: mAb_A series, blue dot: mAb_B series. Left: full graphic, right represents the framed area. Dotted lines indicate a relative retention of 1.00. Label Code: NSP: *N*-succinimidyl propionate; AFM: Alexa Fluor 488-maleimide; SCN: Tm-*p*-SCN-Bz-DOTA; DI: direct iodination; AFN: Alexa Fluor 488-NHS; BHN: Bolton-Hunter-NHS; DN: DOTA-NHS.

Conclusions

The main purpose of this investigation was to develop an *in vitro* assessment workflow to predict a change of physiological properties of antibodies after incorporation of a label. These combinations of several analytical methods reveal changes after label conjugation that might otherwise have remained undetected. Besides classical size-exclusion chromatography, the core element of this analysis package consists of correlating relative retention times (t_R) for FcRn and heparin affinity chromatography of labelled mAbs with its congeners. So far, it has been a challenge to decide which shift in retention time is crucial for the application of the labelled protein in biological experiments. In a t_R range of 0.94 to 1.02 for FcRn and 0.90 to 1.05 for heparin affinity chromatography, however, no critical effect of the label is expected. These ranges have been tentatively selected and may shift with increasing empirical data collection.

It has been demonstrated that direct iodination can damage mAbs, which has been shown using FcRn affinity chromatography. During the labelling process, the protein is oxidized and leads to a lower affinity for the neonatal Fc receptor and consequently to a higher antibody clearance. An alternative to direct iodination is indirect iodination using the Bolton-Hunter reagent. The quality assessment after protein modification by conjugation of the iodinated Bolton-Hunter reagent shows a less pronounced change in the protein properties compared to direct iodination. Protein modifications with maleimide-based labels, which requires a previous partial reduction of the protein, can lead to an impairment of the quaternary protein structure. SEC analysis under denatured sample preparation conditions was indicative for free heavy and light chain after maleimide-based labelling. During the reduction step, cystine disulfide bonds are reduced to allow free Cys to conjugate with the labelling reagent. However, unconjugated cysteines are not re-oxidized and the antibody's quaternary structure is only maintained through intermolecular forces, e.g., ionic and hydrogen bonds. At denaturing conditions caused by low pH and organic solvent, these bonds are released and, as there are no longer any covalent disulfide bridges, the antibody degrades into heavy and light chains. This could be of importance in an *in vivo* setting when, during FcRn recycling, the endosomal pH is dropping and the antibody is degraded instead of being reintroduced into circulation.

In conclusion, both type and degree of label of modified IgGs lead to changes in the physico-chemical protein properties. In addition, harsh labelling conditions can also impact the behaviour of labelled mAbs. Finally, identical labels on separate constructs of IgG₁ can lead to different affinities for FcRn and heparin. This finding underlines the importance to assess the impact of the label for each new antibody construct individually and, unfortunately, the findings from this study cannot be taken as a general guide to

which labelling strategy is best suited in all cases. Considering the assessment data, only 6 of the 11 modified mAbs in this study can be recommended for use in *in vitro* or *in vivo* experiments.

The benefits of conducting a quality assessment prior to mechanistic studies are manifold. Obviously, time and resources can be saved by minimising the risk of using unsuitable or even instable test molecules that generate questionable data. Another crucial advantage is the reduction of animal experiments by avoiding proteins that have been impacted by the labelling process. From an ethical point of view, this analytical workflow is a contribution to the 3Rs-principles, so that animal experiments that could lead to incorrect results or conclusions (with respect to human data/clinical trials) are not conducted.

This *in vitro* quality assessment has become the analytical standard for labelled antibodies at Roche. Therefore, this analysis package is an important tool for characterization of labelled antibodies that ensures reliable extrapolation to the respective unlabelled antibodies.

References


- (1) Kaplan, M., Coons, A., and Deans, H. (1950) Localization of antigens in tissue cells. *Journal of Experimental Medicine* 91, 1-13.
- (2) Schadt, S., Hauri, S., Lopes, F., Edelmann, M. R., Staack, R. F., Villaseñor, R., Kettenberger, H., Roth, A. B., Schuler, F., and Richter, W. F. (2019) Are biotransformation studies of therapeutic proteins needed? Scientific considerations and technical challenges. *Drug Metab. Dispos.* 47, 1443-1456.
- (3) Allen, K. J., Jiao, R., Malo, M. E., Frank, C., and Dadachova, E. (2018) Biodistribution of a radiolabeled antibody in mice as an approach to evaluating antibody pharmacokinetics. *Pharmaceutics* 10, 262 (article number).
- (4) Bernhard, W., El-Sayed, A., Barreto, K., Gonzalez, C., Hill, W., Parada, A. C., Fonge, H., and Geyer, C. R. (2018) Near infrared fluorescence imaging of EGFR expression in vivo using IRDye800CW-nimotuzumab. *Oncotarget* 9, 6213-6227.
- (5) Vira, S., Mekhedov, E., Humphrey, G., and Blank, P. S. (2010) Fluorescent-labeled antibodies: Balancing functionality and degree of labeling. *Anal. Biochem.* 402, 146-150.
- (6) Kraeber-Bodéré, F., Bodet-Milin, C., Rousseau, C., Eugène, T., Pallardy, A., Frampas, E., Carlier, T., Ferrer, L., Gaschet, J., and Davodeau, F. (2014) Radioimmunoconjugates for the treatment of cancer. *Semin. Oncol.* 41, 613-622.
- (7) Beck, A., and Reichert, J. M. (2014) Antibody-drug conjugates: present and future. *MAbs* 6, 15-17.
- (8) Wang, L., Amphlett, G., Blättler, W. A., Lambert, J. M., and Zhang, W. (2005) Structural characterization of the maytansinoid–monoclonal antibody immunoconjugate, huN901–DM1, by mass spectrometry. *Protein Science* 14, 2436-2446.
- (9) Muller, G. (1980) Protein labelling with ³H-NSP (N-succinimidyl-[2,3-³H] propionate). *J. Cell Sci.* 43, 319-328.
- (10) Hempel, K. (1963) Über eine neue, autoradiographische Methode zum histochemischen Nachweis proteingebundener Sulfhydryl-gruppen mit tritiiertem N-Phenyl-maleinimid. *Exp. Cell Res.* 31, 594-596.

- (11) Fraker, P. J., and Speck Jr, J. C. (1978) Protein and cell membrane iodinations with a sparingly soluble chloroamide, 1, 3, 4, 6-tetrachloro-3a, 6a-diphenylglycoluril. *Biochem. Biophys. Res. Commun.* 80, 849-857.
- (12) Greenwood, F. C., Hunter, W. M., and Glover, J. (1963) The preparation of ¹³¹I-labelled human growth hormone of high specific radioactivity. *Biochem. J.* 89, 114-123.
- (13) Wilbur, D. S. (1992) Radiohalogenation of proteins: an overview of radionuclides, labeling methods and reagents for conjugate labeling. *Bioconjug. Chem.* 3, 433-470.
- (14) Knight, L. C., and Welch, M. J. (1978) Sites of direct and indirect halogenation of albumin. *Biochim. Biophys. Acta* 534, 185-195.
- (15) Lo, M., Kim, H. S., Tong, R. K., Bainbridge, T. W., Vernes, J.-M., Zhang, Y., Lin, Y. L., Chung, S., Dennis, M. S., and Zuchero, Y. J. Y. (2017) Effector-attenuating substitutions that maintain antibody stability and reduce toxicity in mice. *J. Biol. Chem.* 292, 3900-3908.
- (16) Jaramillo, C. A. C., Belli, S., Cascais, A.-C., Dudal, S., Edelmann, M. R., Haak, M., Brun, M.-E., Otteneder, M. B., Ullah, M., and Funk, C. (2017) Toward in vitro-to-in vivo translation of monoclonal antibody pharmacokinetics: Application of a neonatal Fc receptor-mediated transcytosis assay to understand the interplaying clearance mechanisms. *MAbs* 9, 781-791.
- (17) Cymer, F., Schlothauer, T., Knaupp, A., and Beck, H. (2017) Evaluation of an FcRn affinity chromatographic method for IgG1-type antibodies and evaluation of IgG variants. *Bioanalysis* 9, 1305-1317.
- (18) Maley, F., Trimble, R. B., Tarentino, A. L., and Plummer Jr, T. H. (1989) Characterization of glycoproteins and their associated oligosaccharides through the use of endoglycosidases. *Anal. Biochem.* 180, 195-204.
- (19) Cordoba-Rodriguez, R. V. (2008) Aggregates in MAbs and recombinant therapeutic proteins: a regulatory perspective. *BioPharm Int.* 21, 3 (article number).
- (20) Al-Ejeh, F., Darby, J. M., Thierry, B., and Brown, M. P. (2009) A simplified suite of methods to evaluate chelator conjugation of antibodies: effects on hydrodynamic radius and biodistribution. *Nucl. Med. Biol.* 36, 395-402.
- (21) Liu, H., and May, K. (2012) Disulfide bond structures of IgG molecules: structural variations, chemical modifications and possible impacts to stability and biological function. *MAbs* 4, 17-23.
- (22) Simister, N. E., and Mostov, K. E. (1989) An Fc receptor structurally related to MHC class I antigens. *Nature* 337, 184-187.
- (23) Eigenmann, M. J., Fronton, L., Grimm, H. P., Otteneder, M. B., and Krippendorff, B.-F. (2017) Quantification of IgG monoclonal antibody clearance in tissues. *MAbs* 9, 1007-1015.
- (24) Schlothauer, T., Rueger, P., Stracke, J. O., Hertenberger, H., Fingas, F., Kling, L., Emrich, T., Drabner, G., Seeber, S., and Auer, J. (2013) Analytical FcRn affinity chromatography for functional characterization of monoclonal antibodies. *MAbs* 5, 576-586.
- (25) Borrok, M. J., Wu, Y., Beyaz, N., Yu, X.-Q., Oganesyanyan, V., Dall'Acqua, W. F., and Tsui, P. (2015) pH-dependent binding engineering reveals an FcRn affinity threshold that governs IgG recycling. *J. Biol. Chem.* 290, 4282-4290.
- (26) Edelman, G. M., Cunningham, B. A., Gall, W. E., Gottlieb, P. D., Rutishauser, U., and Waxdal, M. J. (1969) The covalent structure of an entire γ G immunoglobulin molecule. *Proc. Natl. Acad. Sci. (USA)* 63, 78-85.
- (27) Wang, W., Vlasak, J., Li, Y., Pristatsky, P., Fang, Y., Pittman, T., Roman, J., Wang, Y., Prueksaritanont, T., and Ionescu, R. (2011) Impact of methionine oxidation in human IgG1 Fc on serum half-life of monoclonal antibodies. *Mol. Immunol.* 48, 860-866.
- (28) Pan, H., Chen, K., Chu, L., Kinderman, F., Apostol, I., and Huang, G. (2009) Methionine oxidation in human IgG2 Fc decreases binding affinities to protein A and FcRn. *Protein Science* 18, 424-433.

- (29) Edelmann, M. R., Kettenberger, H., Knaupp, A., Schlothauer, T., and Otteneder, M. B. (2019) Radiolabeled IgG antibodies: Impact of various labels on neonatal Fc receptor binding. *J. Label. Compds. Radiopharm.* 62, 751-757.
- (30) Meneghetti, M. C., Hughes, A. J., Rudd, T. R., Nader, H. B., Powell, A. K., Yates, E. A., and Lima, M. A. (2015) Heparan sulfate and heparin interactions with proteins. *J. R. Soc. Interface* 12, 20150589 (article number).
- (31) Tabrizi, M. A., Tseng, C.-M. L., and Roskos, L. K. (2006) Elimination mechanisms of therapeutic monoclonal antibodies. *Drug Discov. Today* 11, 81-88.
- (32) Kraft, T. E., Richter, W. F., Emrich, T., Knaupp, A., Schuster, M., Wolfert, A., and Kettenberger, H. (2020) Heparin chromatography as an in vitro predictor for antibody clearance rate through pinocytosis. *MAbs* 12, # 1683432.

Chapter Six

Biodistribution of drug/ADA complexes: the impact of immune complex formation on antibody distribution

This declaration concerns the article entitled:			
Biodistribution of drug/ADA complexes: the impact of immune complex formation on antibody distribution			
Publication status (tick one)			
Draft manuscript	<input checked="" type="checkbox"/>	Submitted	<input type="checkbox"/>
In review	<input type="checkbox"/>	Accepted	<input type="checkbox"/>
Published	<input type="checkbox"/>		
Publication details (reference)	Opolka-Hoffmann E*, Edelmann MR, Otteneder MB, Hauri S, Lechmann M, Staak R, Jordan G. (2023)		
Copyright status (tick the appropriate statement)			
I hold the copyright for this material	<input type="checkbox"/>	Copyright is retained by the publisher, but I have been given permission to replicate the material here	<input type="checkbox"/>
Candidate's contribution to the paper (provide details, and also indicate as a percentage)	<p>The candidate contributed to / considerably contributed to / predominantly executed the...</p> <p>Formulation of ideas: 30%</p> <p>Design of methodology: 30%</p> <p>Experimental work: 60%</p> <p>Presentation of data in journal format: 50%</p>		
Statement from Candidate	This paper reports on original research I conducted during the period of my Higher Degree by Research candidature.		
Signed		Date	17.10.22

Introduction

Monoclonal antibodies (mAbs) and other biotherapeutics enable the targeted treatment of a broad spectrum of diseases.¹ While great efforts are being made in drug development to reduce the immunogenicity of antibody therapeutics, one of the most challenging aspects of this class of therapeutics remains immunogenicity. Undesirable events such as abrogation of pharmacologic effects or hypersensitivity reactions can be triggered by the binding of anti-drug antibodies (ADAs) to the circulating drug.² ADAs can act in a neutralizing or non-neutralizing manner. Neutralization of therapeutic mAbs is largely driven by binding of ADAs to the complementary-determining region (CDR) and can consequently lead to abrogation of pharmaceutical activity.^{3,4} These ADAs, which target the CDR of a therapeutic mAb, have been reported from both humanized and fully human molecules.^{5,6} In addition to hindering the binding of the drug to its target, the formation of ADA can lead to the formation of immune complexes (IC). ICs are rapidly removed from the circulation by reticulo-endothelial cells. Such ADA are also named as clearing antibodies.^{7,8}

Although the detailed interaction between ADA and drug to form ICs is well understood,^{9,10} as well as known from the literature that large ICs are cleared faster than smaller ICs, quantitative information on the exact size or structure of the ICs as well as their disposition has not been investigated so far.^{11,12}

A recent publication has reported on the study of the formation and characterisation of non-radioactively labelled drug/ADA ICs and their bioanalysis in biological matrices and the influence of these ICs on the PK of antibody-based drugs.¹³ The formed ICs consisted of dimeric, tetrameric, hexameric, octameric, and high-molecular weight (HMW) ICs (**Figure 1**). Rapid clearance of larger ICs (larger than hexamers) only 5 min after administration without dissociation into smaller ICs or their non-complexed components raised the question of where the ICs ended up in the body.

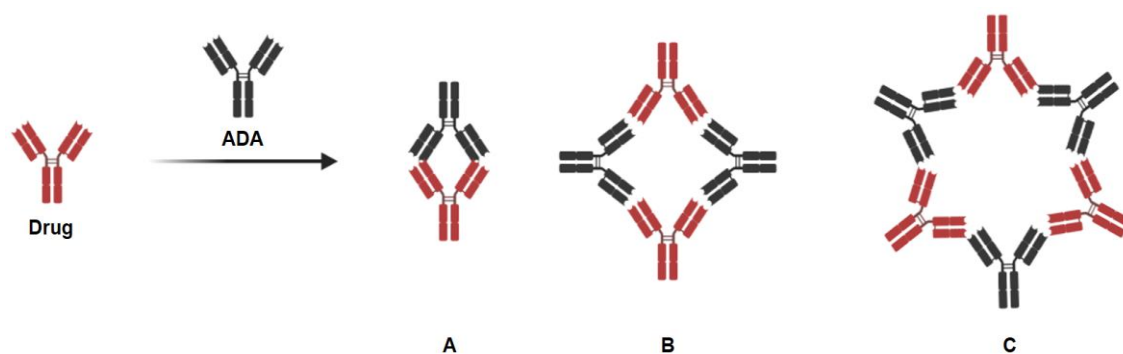


Figure 1: Schematic illustration of different IC species. **A** dimeric; **B** tetrameric; **C** hexameric. Red: drug; black: ADA.

To explore the effects of IC formation on the PK behaviour of therapeutic mAbs, *in vivo* studies were performed in rats receiving different ICs, which consist out of ^3H -IgG and anti-drug-antibodies (ADA), generated by immunization of rabbits. The ADA are directed against different regions of the ^3H -labelled IgG resulting in different formation of ICs. The disposition of ^3H -labelled IgG (hereafter referred to as " ^3H -drug") was compared to ICs (hereafter referred to as " ^3H -IC"). The radioactive label is used to gain quantitative information about the fate of the immune complexes by whole-body autoradiography and radioactive measurements.

Results

Formation and characterization of the immune complex (IC) dosing solution

The preparation of the dosing solutions was performed as previously described by Hoffmann and coworker.¹² As drug surrogate, a non-targeting IgG₁ was used, which had a silencing mutation in the Fc part that altered Fc effector function.¹⁴ The drug was labelled with tritium (^3H -drug) in analogy to the previous reported method by conjugation of [^3H]N-succinimidyl propionate to lysine in the protein sequence.¹⁵

For the dosing solution, the ^3H -drug was mixed at a ratio of 1:1.5 with a polyclonal anti-drug antibody (pADA) surrogate directed against the complementarity-determining regions (CDR) of the drug (pADA_{<CDR>}) to generate ^3H -IC. This dosing solution was analysed by size exclusion chromatography (SEC), detected at 280 nm, to evaluate the pattern of formed ICs and for better comparison of the IC patterns after administration. The formed ICs consisted of dimeric, tetrameric, hexameric, and high-molecular weight (HMW) ICs (**Figure 2**).

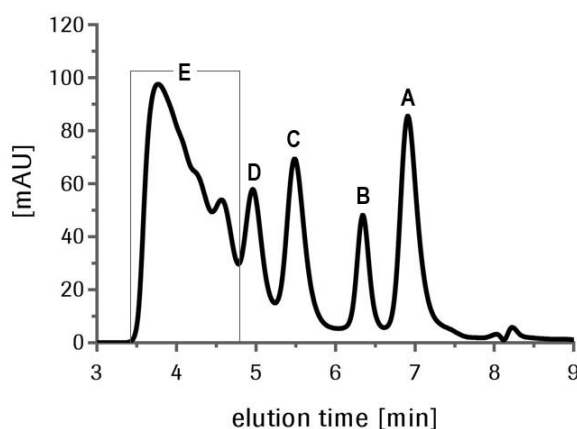


Figure 2: SEC of dosing solution (^3H -IC), detected at 280 nm. **A:** residual ADA; **B:** dimeric IC; **C:** tetrameric IC; **D:** hexameric IC; **E:** HMW ICs.

Quantitative whole-body autoradiography (QWBA)

In order to track the distribution of radiolabelled proteins *in vivo*, QWBA was performed after a single-dose animal study in rats with ^3H -drug (control animal) and ^3H -IC (IC animal). Both animals were sacrificed after 15 min. The short *in vivo* phase was based on findings from previous reports, where fast clearance of immune complexes from the circulation was observed.¹³ The whole-body slices were analysed and radioactivity in organs was quantified (**Figure 3, Table 1**). To provide a better comparison of the radioactive uptake of the organs, the tissue-to-blood ratio was calculated.

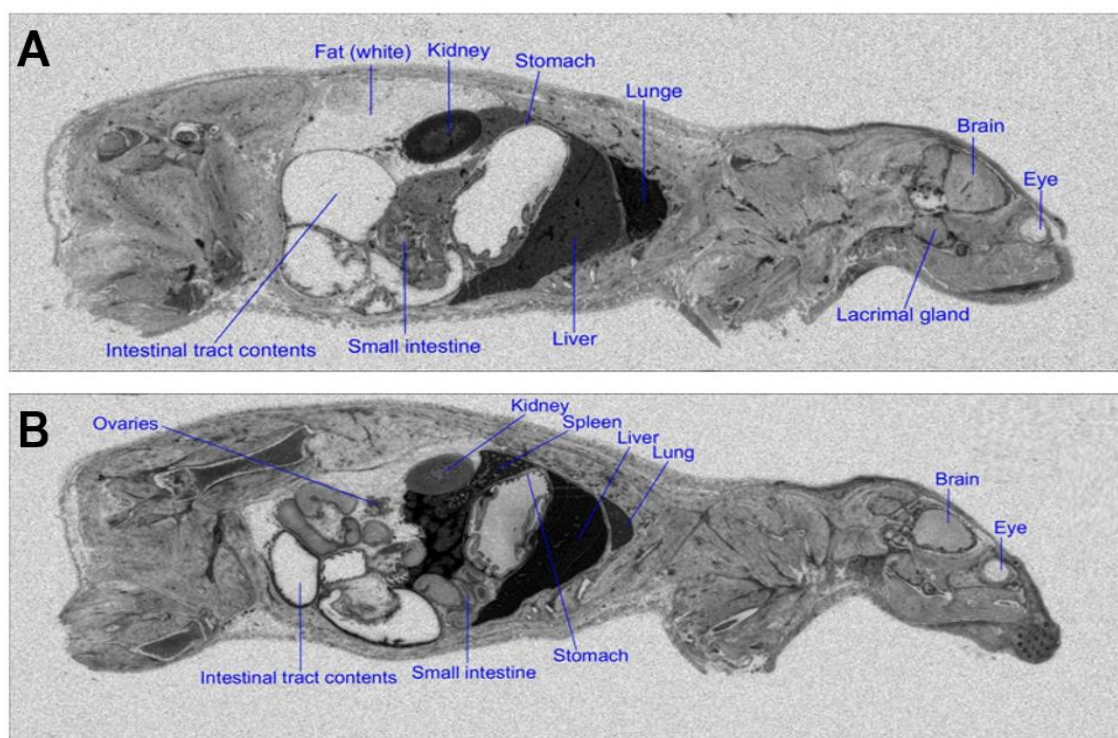


Figure 3: Representative example of layers obtained from the QWBA study. **A:** control animal after ^3H -drug administration; layer 5. **B:** IC animal after application of ^3H -IC; layer 4.

Table 1: Quantitative evaluation of radioactive uptake in tissues and calculated ratio of radioactivity in tissues to radioactivity in blood from the control animal and the IC animal. Tissue-to-blood ratios greater than 1 are highlighted in green.

Tissue	Control animal		IC animal	
	[ng-eq/g]	Ratio to blood	[ng-eq/g]	Ratio to blood
Adrenal (cortex)	13207	0.24	13381	0.63
Adrenal (medulla)	48626	0.88	17790	0.83
Blood	55029	1.00	221357	1.00
Blood vessel wall	33155	0.60	11498	0.54
Bone marrow	8496	0.15	12629	0.59
Brain (cerebellum)	1429	0.03	811	0.04
Brain (cortex)	825	0.01	531	0.02
Brain (plexus choroideus)	12866	0.23	13016	0.61
Conchae nasales	5017	0.09	656	0.03
Epiphysis	4538	0.08	6053	0.28
Eye (choroid)	1540	0.03	1326	0.06
Eye (lens)	-8	0.00	-7	0.00
Fat (brown)	28822	0.52	6894	0.32
Fat (white)	65	0.00	147	0.01
Harderin gland	2194	0.04	824	0.04
Heart (myocardium without blood)	11604	0.21	6608	0.31
Hypophysis	10470	0.19	4650	0.22
Kidney (cortex)	26890	0.49	6722	0.21
Kidney (medulla)	29710	0.54	8908	0.42
Kidney (papilla)	15505	0.28	7208	0.34
Lacrimal gland	1857	0.03	1126	0.05
Large intestine (wall)	2897	0.05	9416	0.44
Liver	18828	0.34	52284	2.45
Lung	49740	0.90	22058	1.03
Muscle	3391	0.06	1338	0.06
Ovaries	11533	0.21	5704	0.27
Pancreas	4423	0.08	101545	4.75
Salivary gland	2637	0.05	2353	0.11
Skin	638	0.01	795	0.04
Small intestine (wall)	6757	0.12	3820	0.18
Spinal cord	919	0.02	611	0.03
Spleen	8303	0.15	25854	1.12
Stomach	1204	0.02	5496	0.26
Thymus	1304	0.02	6199	0.29
Thyroid	6324	0.11	6118	0.29
Urinary bladder	2680	0.05	5595	0.26
Uterus	15980	0.29	7821	0.37

For the control animal dosed with ^3H -drug, increased radioactivity was detected in lung, liver, and kidney. In general, the total concentrations of radioactivity in the tissues were lower than in the blood. The highest ratios were found in the lung and adrenal medulla with 0.90 and 0.88, respectively. For the animal dosed with the pre-formed ^3H -IC, an increased concentration of radioactivity was detected in several tissues, such

as spleen, liver, and pancreas, giving tissue-to-blood ratios of 1.21, 2.45, and 4.75, respectively.

Biodistribution study

In order to understand the time kinetics and get further insights in the mechanism, a biodistribution study in rats with ^3H -labeled IgG and pre-formed ^3H -immuno complexes. Blood samples were collected after 0.25 hr, 1 hr, 3 hr, 7 hr, 24 hr, 48 hr, and 72 hr for IC analysis. Organs were collected and prepared for determination of radioactive concentration. In addition, urine and faeces were collected for radioactive measurements.

Immune complex analysis

To study the pattern of ICs, samples from the IC group were analysed by size-exclusion chromatography (SEC) and radioactive measurement. **Figure 4** shows the reconstructed IC profiles of serum samples from different time points. In direct comparison with the dosed IC pattern (**Figure 2**), it can be shown that HMW and hexameric ICs disappeared very fast. Dimeric and tetrameric ICs stay much longer in circulation. Between 24 hr and 72 hr, the tetrameric IC content seemed to be very similar. The dimeric IC content showed few changes between 7 hr and 72 hr. During the observed time, no monomeric drug was detected, indicating that ICs did not dissociate *in vivo*.

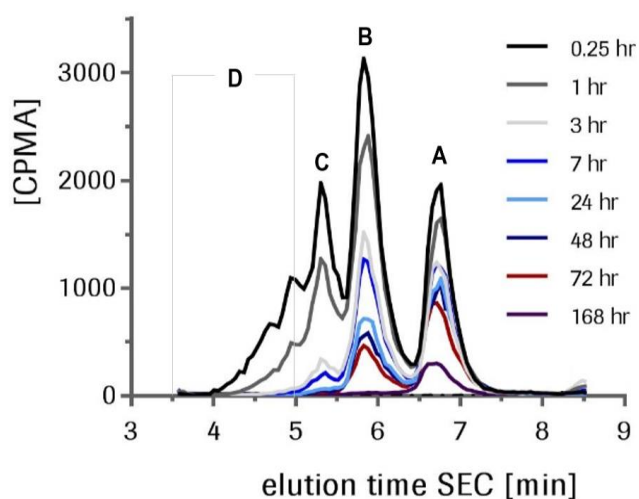


Figure 4: SEC of serum samples after different time points. **A:** dimeric IC; **B:** tetrameric IC; **C:** hexameric IC; **D:** HMW ICs.

This observation is consistent with previous data obtained from a previous study,¹³ in which the identical molecules were used, but without a radioactive label. For this reason, in the "non-radioactive" study, drug-specific ELISA determined the IC

patterns after SEC separation. This comparison (**Figure 5**) shows that the radioactive labelling has no influence on the drug or IC concentration in serum and provides comparable results to the ELISA method.

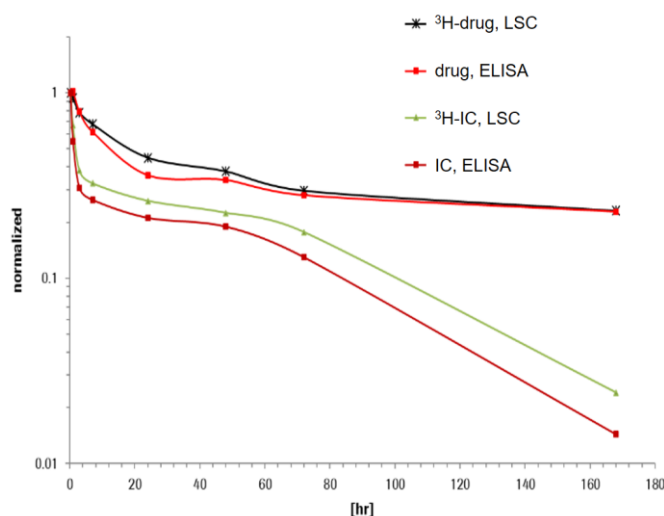


Figure 5: Comparison of normalised serum concentrations from the radioactive study, detected by LSC and the recently reported non-radioactive study, detected by ELISA.

Radioactivity in organs

At 0.25 hr, 3 hr, 7 hr, and 168 hr liver, lung, spleen, muscle, kidney, skin, heart, bone marrow, and pancreas were collected from one animal per group. The collected organs were homogenised and the radioactivity was determined by liquid scintillation counting (LSC). For better comparison between organs and between the groups, the ratio between organ in counts per minutes per gram tissue (CPM/g) and serum in CPM per mL was calculated (**Figure 6**).

For the control group, an increased tissue-to-plasma ratio (T:P) was observed in the liver at 0.25 hr, followed by a rapid decrease. In all other organs investigated, T:P increased over time. After 0.25 hr, the liver of the IC group had the highest radioactivity, followed by spleen and lung. By 3 hr after dosing, the T:P in the liver increased more than 2-fold. In general, all organs showed an increase in T:P after 3 hr. For the liver, T:P decreased again by the next measured time point of 7 hr. For the lung, spleen, bone marrow, and pancreas T:P remained relatively constant during the observed time period. The skin, however, showed the highest T:P after 168 hr.

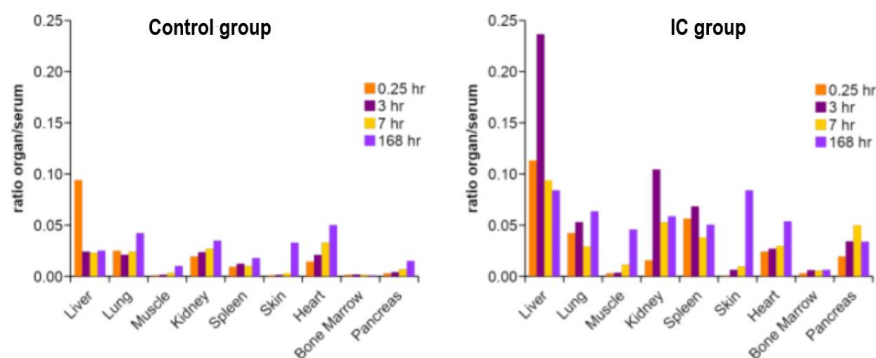


Figure 6: Radioactivity ratios of [CPM/g] in organs and [CPM/mL] serum from control group and IC group.

Comparing the tissue-to-plasma ratio between the control group and the IC group (**Figure 7**), the most significant differences were detected in the liver, muscle, spleen, and pancreas. Although the total radioactivity in the pancreas is relatively low compared to other organs, the amount of radioactivity in the IC group is 5-fold higher than in the control group.

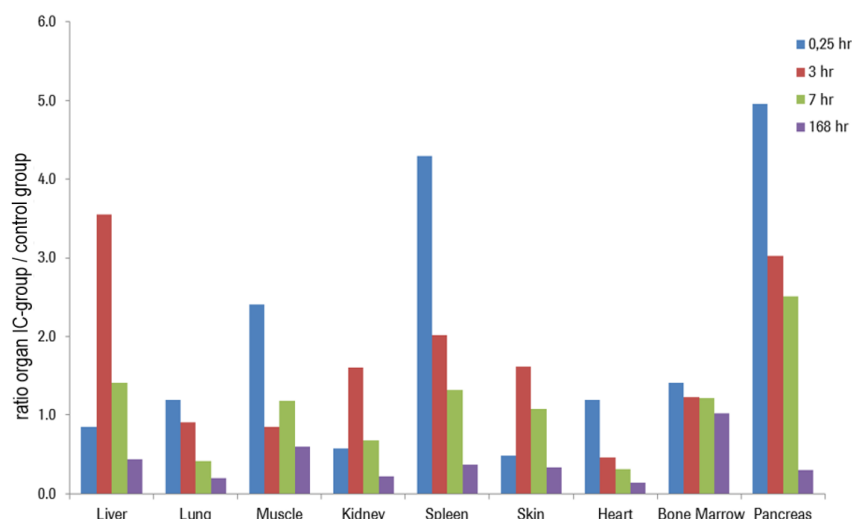


Figure 7: Ratio of radioactivity levels measured in the organs of the IC group to the control group.

Radioactivity in urine and faeces

Urine and faeces of the animals were collected in the time intervals of 0 - 24 hr and 24 - 48 hr. **Figure 8** shows the percentage of administered dose, determined by LSC, of the administered radioactive dose in the corresponding time intervals. For faeces, the overall radioactivity determined was very low, with a maximum of approx. 0.3% in the IC group (0 - 24 hr). In the urine samples, the control group had a maximum of approx. 6% of the administered dose in the 0 - 24 hr time interval. In contrast, approx. 65 % was observed in the IC group in the first 24 hr, indicating a much faster excretion of the ICs.

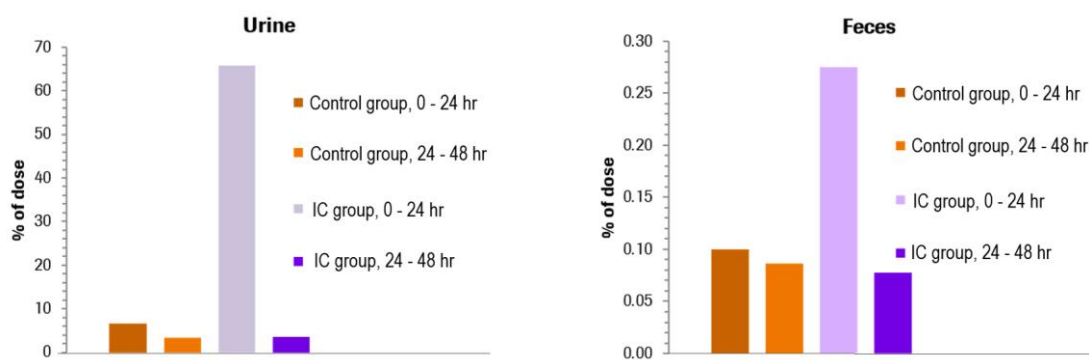


Figure 8: Radioactivity measurements of urine and faeces from the control group and IC group over time intervals of 0 - 24 and 24 - 48 hr in % of dose.

To better understand the excreted molecular substance(s) in the urine of the IC groups, the urine was analysed by peptide-level SEC determining counts per minutes (CPM, **Figure 9**). The radioactivity detection plot of the urine showed the same retention time in the control and the IC group, but different signal intensities. While a maximum of 3,700 CPM was measured in the control group, the IC group had a significantly higher radioactivity of 23,000 CPM.

The radioactivity detection plot shows only one signal as a single peak. It cannot be clearly determined whether this is a single compound or a mixture of compounds with a similar hydrodynamic radius. A commercially available calibration standard was used to narrow down the molecular weight of the excreted substance. The radioactive signal eluted near the calibrator with a molecular weight of 1.2 kDa. Considering the influence of the spatial structure on the elution behaviour, this molecular weight can only be regarded as a rough approximation. A mass spectrometric analysis was unsuccessful and thus the unknown compound, or the mixture of compounds, could not be identified so far.

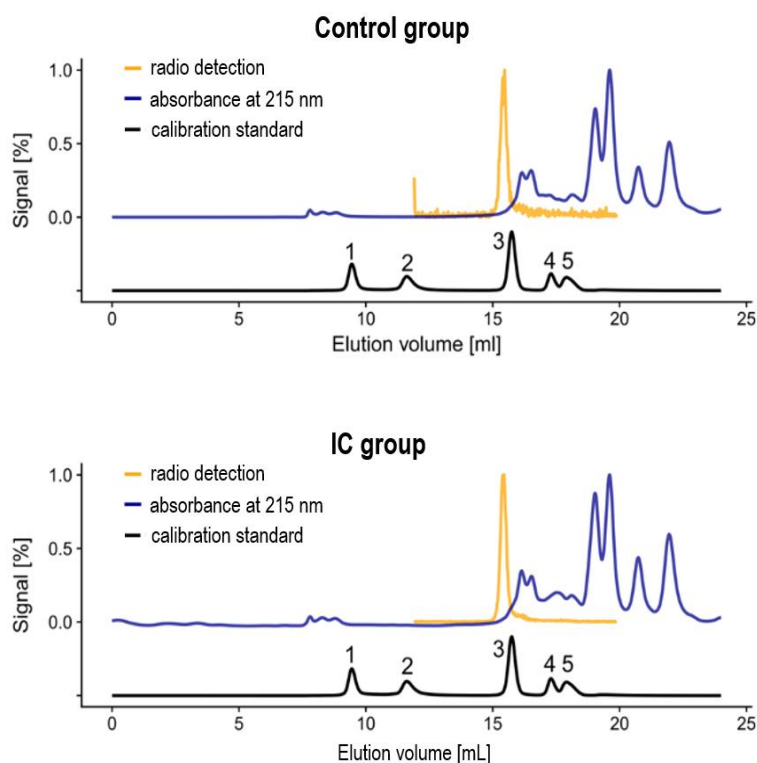


Figure 9: SEC plots of serum samples on peptide level. Top shows the control group, bottom IC group. Yellow line represents radio detection, blue line the absorbance at 215 nm and black line the commercial calibration mixture that consist of: **1** Cytochrome C (12.4 kDa); **2** Aprotinin (6.5 kDa); **3** Vitamin B12 (1.2 kDa); **4** Triglycine (189 Da); **5** Glycine (75 Da).

Discussion

The formation of ICs plays an important role in various preclinical and clinical aspects, such as autoimmunity or immunogenicity against biotherapeutics. Previous publications have reported on the study of the formation and characterisation of drug/ADA ICs and their bioanalysis in biological matrices, as well as the impact of these ICs on the PK of antibody-based drugs.¹³ The rapid clearance of larger ICs (larger than hexamers) after just 5 minutes after administration, without dissociation into smaller ICs or their non-complexed component, raised the question of where the ICs ended up in the body.

To investigate this matter, quantitative whole-body autoradiography (QWBA) was performed with a tritium-labelled antibody (³H-drug) in a control animal and in parallel with a polyclonal ADA immunocomplex (³H-IC) directed against the CDR of the ³H-drug. The QWBA slide received from the control animal showed high radioactivity in the lung, kidney, and liver 0.25 hr after administration, which was the only time point in this study. On the slide of the IC animal, a high level of radioactivity was observed in the lung, liver, spleen and, surprisingly, also in the pancreas. The high T:P ratio in pancreas is difficult to interpret, as it could be caused by the disposition of IC in the pancreas, but also by the uptake of catabolites released into the circulation after degradation in the reticulo-endothelial system.

In a second experiment, the time dependent disposition of ^3H -IgG and ^3H -IC was investigated. The T:P ratio in various organs was similar to that previously determined by QWBA. In addition, the change in pattern of circulating immune complexes was determined. As previously observed, the large immune complexes are rapidly cleared from circulation. This rapid clearance might be due to a fast hydrolysis of the proteins in peptides and amino acids. These fragments might contribute to the T:P ratio observed in the different organs. After 15 min, most of the multi-complexed ICs had already been cleared from the circulation, whereas the dimeric IC was still detectable after 168 hr. Interestingly, T:P in pancreas was only moderate compared to the QWBA study. However, T:P increased with time (up to 7 hr), indicating accumulation in the pancreas.

This could be due to two reasons: the pancreas takes up the ICs in an increased amount, or the ICs were proteolyzed in the liver and the radiolabelled amino acid was then taken up by the pancreas due to its high protein expression rate.¹⁶ In the second case, this means that the ^3H -labelled lysines could be recycled during protein expression and processed into new proteins by the natural protein expression machinery. This could also explain the increase in radioactivity with time of the control animal, as uptake and proteolytic degradation of the monomeric agent is significantly slower compared to ICs, as shown. Assuming that the labelled amino acids are recycled for new proteins, the radioactivity in the pancreas was not primarily caused by the ICs, but was a side effect of the increased proteolytic degradation of the ICs in the liver.¹⁷ This possibly applies to all organs in which increased activity could be detected with increasing time.

In the biodistribution study, the collected urine from the IC animals showed that 65% of the administered radioactivity was excreted in the first 24 hr, compared to only 6% in the control group. This is a clear indication that ICs are internalised, proteolytically digested and excreted much faster than the non-complexed drug. Notably, only one distinct peak was identified in peptide SEC analysis with radioactive detection, indicating the presence of a single molecular species, or several molecules with comparable hydrodynamic radius. The same pattern was observed in both the IC group and the control group in the radioactive detection. A commercial SEC size standard was used to better estimate the size of these encountered species. The results indicate that the radioactive species (or several) in the urine is a degradation product(s) with a molecular size of about 1.2 kDa, which is indicative of peptide size.

So far, a structure identification has not been successful and it could not yet be determined whether it is a matter of several peptide fragments or a single degradation product. Further analyses of the urine samples are required to investigate the species present by mass spectrometry.

Materials and Methods

Reagents and antibodies used

The drug surrogate IgG₁ for this study was produced in-house. Polyclonal anti-drug antibody (pADA) was generated by immunization of rabbits in-house.¹⁸ Sodium chloride (1.06404) was obtained from Merck KGaA (Germany). Histidine was ordered from Sigma (H6034 and 56190). Antibodies and buffers used to generate the *in vivo* dosing solutions were tested and approved for endotoxin levels. The custom synthesized [³H]*N*-succinimidyl propionate ([³H]NSP) was purchased from Pharmaron (Cardiff, Wales, UK) as a solution in toluene. Protein concentration was determined by Eppendorf (Hamburg, Germany) BioSpectrometer® basic in combination with an Eppendorf µCuvette® G1.0 with 1 mm path length at 280 nm wavelength and the corresponding calculated molar extinction coefficient. Dulbecco's phosphate-buffered saline (DPBS, Thermo Fisher Scientific, Paisley, UK, 14190-094), which consists of 2.67 mM potassium chloride, 1.47 mM potassium phosphate monobasic, 8.60 mM sodium phosphate dibasic, and 138 mM sodium chloride, was used as labelling buffer. The pH was adjusted to 8.4 by addition of 1 M sodium hydroxide (Merck KGaA, Darmstadt, Germany, 1.09956.0001). Formulation buffer consisted of 20 mM L-Histidine (Sigma, Steinheim, Germany, H-8000 for L-histidine and H-5659 for L-histidine monohydrochloride monohydrate), 140 mM sodium chloride (Sigma, Steinheim, Germany, 71376) at pH 6.0. Buffer exchange was performed with Slide-A-Lyzer G2 Dialysis Cassettes, 10K MWCO, 3 mL (Thermo Fisher Scientific, Paisley, UK, 87730).

Tritium-labelling of drug (³H-drug)

Methods

Radiolabelled antibody was analysed using an Agilent 1200 series HPLC system (Santa Clara, CA, USA), equipped with β Radioactivity HPLC detector RAMONA* with internal liquid scintillator admixture (Elysia-raytest, Straubenhardt, Germany). Absorbance at 280 nm and 320 nm were used for detection and quantification. For size-exclusion chromatography (SEC), a TSKgel G3000 SW_{XL} column (Tosoh Bioscience, Tokyo, Japan), 7.8 x 300 mm, 5 µm with 0.2 M potassium phosphate, 0.25 M potassium chloride, pH 7.0 as the mobile phase at a flow rate of 0.5 mL/min was used. The injection volume was 10 µL and the protein concentration 1 mg/mL. The target concentration of 1 mg/mL was set by adding the eluent to the protein stock solution. Analytical FcRn affinity chromatography was carried out with an FcRn affinity column (Roche Custom Biotech, Mannheim, Germany), column volume of 0.5 mL containing 1.5 mg FcRn protein.¹⁹ The 45-min analytical method was applied with a flow rate of 0.5 mL/min under the following

condition: Eluent [A] was 20 mM 2-(*N*-morpholino)ethanesulfonic acid (MES), 140 mM sodium chloride, pH 5.5; eluent [B] was 20 mM tris(hydroxymethyl)aminomethane (Tris), 140 mM sodium chloride, pH 8.8. Starting with isocratic conditions of 20% [B] for 5 min, a linear gradient to 100% [B] followed over 35 min to keep 100% [B] for 5 minutes. The injection volume was 30 μ L and the protein concentration 1 mg/mL. The target concentration of 1 mg/mL was set by adding eluent [A] to the protein stock solution. Liquid scintillation counting was accomplished using a HIDEX 300 SL (Mainz, Germany) and ULTIMATE GOLD cocktail (PerkinElmer Inc., Waltham, MA, USA).

Labelling procedure

The drug surrogate was transferred into a Slide-A-Lyzer Cassette and buffer exchanged into DPBS (14 mg, 97.9 nmol, in 2.8 mL formulation buffer). The buffer was changed 4 times after 30 min and stored overnight at 6 °C. The protein solution was warmed to 22 °C; a protein concentration determination resulted in 4.9 mg/mL. 925 MBq (25 mCi, 44.5 μ g, 245 nmol) of [³H]NSP as a solution in toluene was transferred in portions into a 5 mL Eppendorf LoBind tube. Toluene was removed by an argon stream and the solid residue was dissolved in 35 μ L DMSO. 2.8 mL of the protein solution was added and the tube was shaken horizontally at 150 rpm for 30 min. The solution was transferred into a Slide-A-Lyzer Cassette and buffer exchanged into formulation buffer. The buffer was changed 4 times after 30 minutes and stored for 16 hr at 6 °C. The solution was transferred to a 5 mL Eppendorf LoBind tube at 22 °C and resulted in a protein concentration of 4.4 mg/mL in a volume of 2.9 mL. A total activity of 396 MBq (10.7 mCi) was obtained, resulting in a specific activity of 31 MBq/mg (839 μ Ci/mg). The radiochemical purity using SEC was 98.1%; the low molecular weight impurity was 1%. A comparison of unlabelled with the tritium-labelled protein using FcRn affinity chromatography revealed no shift in retention times, which indicates that the label has no influence on FcRn affinity.²⁰ The protein solution was sterile-filtered using a Millex-GV Durapore (PVDF) filter (Merck Millipore, Darmstadt, Germany), divided into two portions, and stored at -80 °C.

Generation and characterization of dosing solutions (³H-drug and ³H-IC)

An endotoxin free 20 mM histidine/HCl, 140 mM NaCl, pH 6 buffer was used to generate the dosing solutions for the *in vivo* studies. For the control groups, 2 mg/mL drug was prepared in the buffer. For the IC groups, a 1:1.5 solution of 2 mg/mL ³H-drug and 3 mg/mL ADA was prepared and incubated for 1 hr at 22 °C on a shaker at 450 rpm before administration. Aliquots of the solutions were stored at -80 °C for further analysis by SEC using a Dionex Ultimate 3000 system like described previously.^{9,13}

Study design QWBA

QWBA study was conducted with the approval of the local veterinary authorities in strict adherence to the German regulations on animal protection and to the rules of the Association for Assessment and Accreditation of Laboratory Animal Care International (AAALAC). Female Wistar rats (CrI:WI, Charles River Laboratories) received a single intravenous injection of ^3H -drug or ^3H -IC into the tail vein. A dose of 4 mg/kg for ^3H -drug and 6 mg/kg of ^3H -IC was administered. The animals were sacrificed by inhalation of an increasing dose of carbon dioxide 15 minutes after administration. The body of the animals was embedded as a whole in a frozen state. Concentrations of radioactivity in tissues and organs were determined in whole-body sections of the animals by means of QWBA technique. Total radioactivity was measured in whole blood, plasma, and in blood cell pellets by LSC.

Determination of activity in QWBA slides

After sacrifice, the animals were immediately frozen as a whole at approximately $-80\text{ }^\circ\text{C}$ in a mixture of hexane/solid carbon dioxide for 30 min. Thereafter, the frozen animals were stored for at least one day in the freezer at $-20\text{ }^\circ\text{C}$ for temperature equilibration. The tail and limbs were removed and the carcasses were placed on a specimen frame. An aqueous solution of methyl cellulose (Methylan, Henkel, Düsseldorf, Germany) was poured over the carcasses. The specimen frame containing the animal were put into a freezer ($-20\text{ }^\circ\text{C}$, minimally 24 hr). Prior sectioning, the embedded animals were allowed to equilibrate for 1-2 hr to the temperature of the cryostat ($-20 \pm 2\text{ }^\circ\text{C}$). The frozen blocks were cut in a cryo-microtome at a temperature of $-20 \pm 2\text{ }^\circ\text{C}$. Sections of $40\text{ }\mu\text{m}$ thickness were sliced to the level of interest. Prior to the removal of the section for radioluminography, a piece of adhesive transparent tape (Scotch Tape 810; 3M, Neuss, Germany) was firmly placed onto the frozen surface of the carcass in order to adhere the section to the tape. Sections were taken at different levels through the embedded animal. About 6-7 levels were selected to cover all tissues. The selected sections allowed a quantitative evaluation of the radioactivity in tissues and organs as defined in this study plan. Two sections of each chosen level were taken per animal. One section was evaluated. The second section was kept as reserve until the evaluation of the first one was approved. Thereafter, this section was disposed. The sections were dehydrated in the microtome at $-20 \pm 2\text{ }^\circ\text{C}$ for at least 48 hr. The area of the adhesive tape was then reduced around the section to an area of about 0.5 to 1 cm.

The animal sections, together with a blood calibration set, were exposed to FUJI BAS-TR 2025 imaging plates sensitive for tritium (FUJI PHOTO FILM Co. Ltd., Tokyo, Japan, 20 x 25 cm) in light-tight cassettes, which were stored in a freezer at $-20\text{ }^\circ\text{C}$. In

brief: Tissue sections, the imaging plates and the cassettes were equilibrated to -20 °C for 30 min in the sectioning area of the Leica cryostat. One imaging plate was placed in the open cassette. Then the 3-4 sections were placed on this imaging plate and the cassette was closed. All these steps were done at -20 °C. The cassette was then moved to a freezer and the sections were exposed at -20 °C for 5 days (0.25 hr animals) or 7 days (24 hr animals). After the exposition, the cassette was equilibrated to 22 °C for 1 h. Then the cassette was opened under reduced light and the imaging plate was removed from the cassette. The tissue sections were carefully removed from the plates. The imaging plates were scanned in a FUJI BAS 5000 Bio-imaging-Analyzer with a resolution of 50 x 50 µm. The processing of the images and the integration of radioluminescence were performed using AIDA software (automatic imaging data analysis program version 5.0, Raytest, Straubenhardt, Germany). The tissues per protocol were marked manually as areas on the autoradiogram and the concentrations of radioactivity were calculated as integral of the marked area expressed in photo-stimulated luminescence (PSL) per mm² and converted to ng-eq/g, using the PSL/mm² and the radioactivity concentration calibration line and the respective specific radioactivity of the compound dosed.

Study design Biodistribution

Biodistribution study was conducted with the approval of the local veterinary authorities in strict adherence to the Swiss federal regulations on animal protection and to the rules of the Association for Assessment and Accreditation of Laboratory Animal Care International (AAALAC). Female Wistar rats (CrI:WI, Charles River Laboratories) received a single intravenous injection of ³H-drug or ³H-IC into the tail vein. A dose of 4 mg/kg for ³H-drug and 6 mg/kg of ³H-IC was administered. Urine and faeces were collected in time intervals of 0-24 hr and 24-48 hr. The study plan is described in the following table: **B** means collection of blood samples; **O** means sacrifice and removal of the organs liver, lung, spleen, muscle, kidney, skin, heart, bone marrow, and pancreas.

Rat #	0.25 hr	1 hr	3 hr	7 hr	24 hr	48 hr	72 hr	168 hr
1	B + O							
2	B	B	B + O					
3	B	B	B	B + O				
4	-	-	-	B	B	B	B	B + O
5	-	-	B	-	B	B	B	B + O

Size exclusion chromatography and reconstruction of complex profile by topcount

Protein separation was carried out by SEC on an Agilent 1290 Infinity II UHPLC system (Agilent Technologies Inc, Santa Clara, CA, USA) using an Acquity BEH SEC column (450 Å, 1.7 x 100 mm, Waters Corporation, Milford, MA, USA) with 100 mM sodium phosphate buffer at pH 7.4 containing 10% ethanol as mobile phase. The method run time was 10 min at 250 µL/min isocratic flow. Fractions were collected between 4 and 10 min for 0.05 min (12.5 µL) in a Deepwell LumaPlate384 (Perkin Elmer, Waltham, MA, USA). Small molecule size exclusion chromatography was carried with a Superdex 30 Increase 10/300 GL column (10 x 300 mm, Global Life Sciences Solutions USA LLC, Marlborough, MA, USA) with 100 mM sodium phosphate buffer at pH 7.4 containing 10% ethanol as mobile phase. The method run time was 70 min at 400 µL/min isocratic flow. Fractions were collected between 30 and 50 min for 0.05 min (20.9 µL) in a Deepwell LumaPlate384 (Perkin Elmer, Waltham, MA, USA). The collected radioactivity was measured on a TopCount NXT HTS Microplate Counter (Perkin Elmer, Waltham, MA, USA).

Conclusions

This study confirmed that drug/anti-drug antibody immune complexes are cleared from the circulation faster than the therapeutic drug. Until now, it was not well understood where and when these ICs are distributed or eliminated in the body. An important finding of these biodistribution studies with tritium-labelled compounds is that a high level of radioactivity accumulates in the pancreas. Also the finding that a high amount of radioactivity from the group that received the pre-complexed dose was found in the urine in the first 24 hours. So far, it has not been successful to identify the main degradation product. An estimation has only been possible by a molecular weight marker using SEC, which showed a peptide of a size of about 1.2 kDa. Further investigations need to be conducted to generate more findings on the degradation of IC.


References

- (1) Grilo, A. L., and Mantalaris, A. (2019) The increasingly human and profitable monoclonal antibody market. *Trends Biotechnol.* 37, 9-16.
- (2) Krishna, M., and Nadler, S. G. (2016) Immunogenicity to biotherapeutics—the role of anti-drug immune complexes. *Front. Immunol.* 7, 21.
- (3) Stubenrauch, K., Künzel, C., Vogel, R., Tuerck, D., Schick, E., and Heinrich, J. (2015) Epitope characterization of the ADA response directed against a targeted immunocytokine. *J. Pharm. Biomed. Anal.* 114, 296-304.
- (4) Harding, F. A., Stickler, M. M., Razo, J., and DuBridges, R. (2010) The immunogenicity of humanized and fully human antibodies: residual immunogenicity resides in the CDR regions. *MAbs* 2, 256-265.

- (5) Ritter, G., Cohen, L. S., Williams Jr, C., Richards, E. C., Old, L. J., and Welt, S. (2001) Serological analysis of human anti-human antibody responses in colon cancer patients treated with repeated doses of humanized monoclonal antibody A33. *Cancer Res.* 61, 6851-6859.
- (6) Cassinotti, A., Ardizzone, S., and Porro, G. B. (2008) Adalimumab for the treatment of Crohn's disease. *Biologics* 2, 763.
- (7) Ponce, R., Abad, L., Amaravadi, L., Gelzleichter, T., Gore, E., Green, J., Gupta, S., Herzyk, D., Hurst, C., and Ivens, I. A. (2009) Immunogenicity of biologically-derived therapeutics: assessment and interpretation of nonclinical safety studies. *Regul. Toxicol. Pharmacol.* 54, 164-182.
- (8) Chirmule, N., Jawa, V., and Meibohm, B. (2012) Immunogenicity to therapeutic proteins: impact on PK/PD and efficacy. *AAPS J.* 14, 296-302.
- (9) Hoffmann, E., Jordan, G., Lauer, M., Ringler, P., Kuszniir, E. A., Rufer, A. C., Huber, S., Jochner, A., Winter, G., and Staack, R. F. (2019) Generation, characterization, and quantitative bioanalysis of drug/anti-drug antibody immune complexes to facilitate dedicated in vivo studies. *Pharm. Res.* 36, 1-15.
- (10) van Schie, K. A., Kruithof, S., Ooijevaar-de Heer, P., Derksen, N. I., van de Bovenkamp, F. S., Saris, A., Vidarsson, G., Bentlage, A. E., Jiskoot, W., and Romeijn, S. (2018) Restricted immune activation and internalisation of anti-idiotypic complexes between drug and antidrug antibodies. *Ann. Rheum. Dis.* 77, 1471-1479.
- (11) Rojko, J. L., Evans, M. G., Price, S. A., Han, B., Waine, G., DeWitte, M., Haynes, J., Freimark, B., Martin, P., and Raymond, J. T. (2014) Formation, clearance, deposition, pathogenicity, and identification of biopharmaceutical-related immune complexes: review and case studies. *Toxicol. Pathol.* 42, 725-764.
- (12) Rojas, J. R., Taylor, R. P., Cunningham, M. R., Rutkoski, T. J., Vennarini, J., Jang, H., Graham, M. A., Geboes, K., Rousselle, S. D., and Wagner, C. L. (2005) Formation, distribution, and elimination of infliximab and anti-infliximab immune complexes in cynomolgus monkeys. *J. Pharmacol. Exp. Ther.* 313, 578-585.
- (13) Opolka-Hoffmann, E., Jordan, G., Otteneder, M., Kieferle, R., Lechmann, M., Winter, G., and Staack, R. F. (2021) The impact of immunogenicity on therapeutic antibody pharmacokinetics: A preclinical evaluation of the effect of immune complex formation and antibody effector function on clearance. *MAbs* 13, 1995929.
- (14) Schlothauer, T., Herter, S., Koller, C. F., Grau-Richards, S., Steinhart, V., Spick, C., Kubbies, M., Klein, C., Umaña, P., and Mössner, E. (2016) Novel human IgG1 and IgG4 Fc-engineered antibodies with completely abolished immune effector functions. *Protein Eng. Des. Sel.* 29, 457-466.
- (15) Edelmann, M. R., Kettenberger, H., Knaupp, A., Schlothauer, T., and Otteneder, M. B. (2019) Radiolabeled IgG antibodies: Impact of various labels on neonatal Fc receptor binding. *J. Label. Compds. Radiopharm.* 62, 751-757.
- (16) Sepp, A., Meno-Tetang, G., Weber, A., Sanderson, A., Schon, O., and Berges, A. (2019) Computer-assembled cross-species/cross-modalities two-pore physiologically based pharmacokinetic model for biologics in mice and rats. *J. Pharmacokinet. Pharmacodyn.* 46, 339-359.
- (17) Johansson, A., Erlandsson, A., Eriksson, D., Ullén, A., Holm, P., Sundström, B. E., Roux, K. H., and Stigbrand, T. (2002) Idiotypic-anti-idiotypic complexes and their in vivo metabolism. *Cancer* 94, 1306-1313.
- (18) Staack, R. F., Stracke, J. O., Stubenrauch, K., Vogel, R., Schleypen, J., and Papadimitriou, A. (2011) Quality requirements for critical assay reagents used in bioanalysis of therapeutic proteins: what bioanalysts should know about their reagents. *Bioanalysis* 3, 523-534.
- (19) Cymer, F., Schlothauer, T., Knaupp, A., and Beck, H. (2017) Evaluation of an FcRn affinity chromatographic method for IgG1-type antibodies and evaluation of IgG variants. *Bioanalysis* 9, 1305-1317.
- (20) Edelmann, M. R., and Hauri, S. (2021) Functional in vitro assessment of modified antibodies: Impact of label on protein properties. *PLoS One* 16, e0257342.

Chapter Seven

Multi-parameter optimization: development of a morpholin-3-one derivative with an improved kinetic profile for imaging monoacylglycerol lipase in the brain

This declaration concerns the article entitled:			
Multi-parameter optimization: development of a morpholin-3-one derivative with an improved kinetic profile for imaging monoacylglycerol lipase in the brain			
Publication status (tick one)			
Draft manuscript	<input type="checkbox"/>	Submitted	<input type="checkbox"/>
In review	<input type="checkbox"/>	Accepted	<input type="checkbox"/>
		Published	<input checked="" type="checkbox"/>
Publication details (reference)	He Y, Grether U, Taddio MF, Meier C, Keller C, Edelmann MR, Honer M, Huber S, Wittwer MB, Heer D, Richter H, Collin L, Hug MN, Hilbert M, Postmus A, Floor Steven, van der Stelt M, Krämer SD, Schibli R, Mu L*, Gobbi LC. (2022) <i>Eur. J. Med. Chem.</i> 243 :114750		
Copyright status (tick the appropriate statement)			
I hold the copyright for this material	<input checked="" type="checkbox"/>	Copyright is retained by the publisher, but I have been given permission to replicate the material here	<input type="checkbox"/>
Candidate's contribution to the paper (provide details, and also indicate as a percentage)	<p>The candidate contributed to / considerably contributed to / predominantly executed the...</p> <p>Formulation of ideas: 20%</p> <p>Design of methodology: 20%</p> <p>Experimental work: 20%</p> <p>Presentation of data in journal format: 25%</p>		
Statement from Candidate	This paper reports on original research I conducted during the period of my Higher Degree by Research candidature.		
Signed		Date	17.10.22

Introduction

The endocannabinoid system (ECS) is a versatile system that plays an important role in physiological and pathological conditions.¹ It consists of two major G-protein coupled receptors, cannabinoid receptor type-1 and type-2, and endogenous ligands such as 2-arachidonoyl-glycerol (2-AG) and *N*-arachidonoyl ethanolamine, which are referred as endocannabinoids. 2-AG is bio-synthesized 'on-demand' and functions as a retrograde signal to mediate neuronal excitability.² Upon the activation of cannabinoid receptor type-1, 2-AG is degraded mainly by monoacylglycerol lipase (MAGL) into fatty acid and glycerol. Pharmacological inhibition of MAGL, a serine hydrolase comprising 303 amino acid residues in the brain, leads to an elevation of 2-AG level in the central nervous system (CNS) and consequently reduces prostaglandin production that results in cytokine-lowering effects.³ Therefore, MAGL has received tremendous attention as a promising therapeutic target against neurological disorders such as Alzheimer's diseases, Parkinson's diseases, multiple sclerosis, amyotrophic lateral sclerosis, and traumatic brain injury.^{4,5}

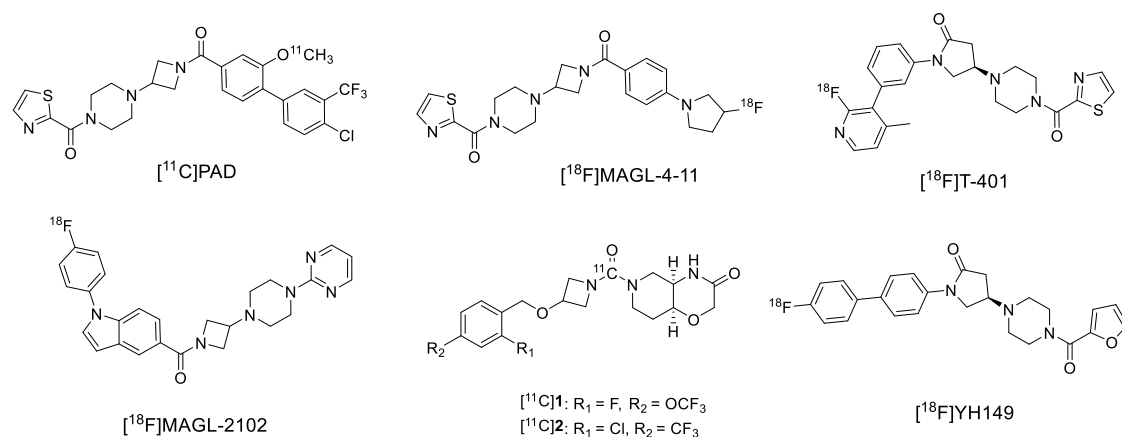


Figure 1: Chemical structures of reversible MAGL PET ligands.⁶⁻¹⁰

Positron emission tomography (PET) is a highly sensitive imaging technique that supports drug development and discovery by non-invasive quantification of pharmacological processes *in vivo*. Although a diverse set of MAGL inhibitors with various chemical scaffolds have been patented and published over the last decade,^{4,11,12} the development of MAGL PET tracers with adequate reversibility *in vivo* is lagging behind.¹³ The chemical structures of reversible MAGL PET tracers developed so far are summarized in **Figure 1**. Except [¹⁸F]T-401 and [¹⁸F]YH149,^{8,9} the rest of reversible MAGL PET tracers encountered a common issue: a relatively slow brain accumulation within the practical time frame.¹³ Among them, [¹¹C]1 and [¹¹C]2 were recently reported.¹⁰ Preliminary results showed that they were recognized by P-glycoprotein (P-gp) in rodents but not in humans. Although [¹¹C]2 was proved to be MAGL-specific in mice brain, its

brain uptake continuously increased during the whole PET scan time period indicating a slow kinetic profile. Similar observation was reported for other MAGL PET probes including [^{11}C]PAD, [^{18}F]MAGL-4-11 and [^{18}F]MAGL-2102 (**Figure 1**).^{6,7} Such kind of slow kinetics requires longer PET acquisition time to reach the equilibrium for a reliable quantification, complicating the measurement of the MAGL-drug interactions in the practical setting.

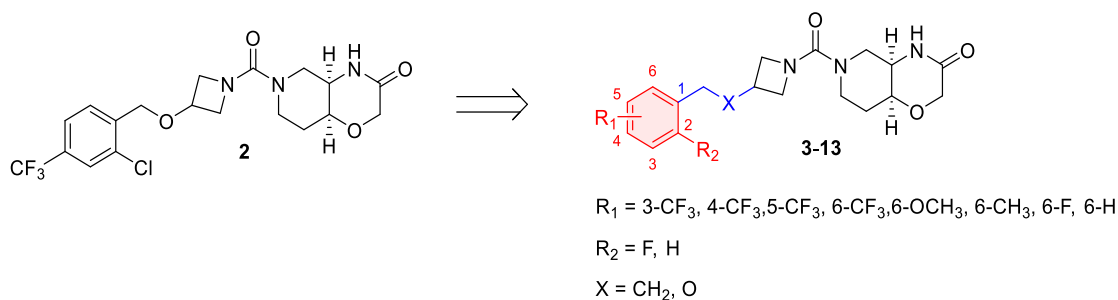
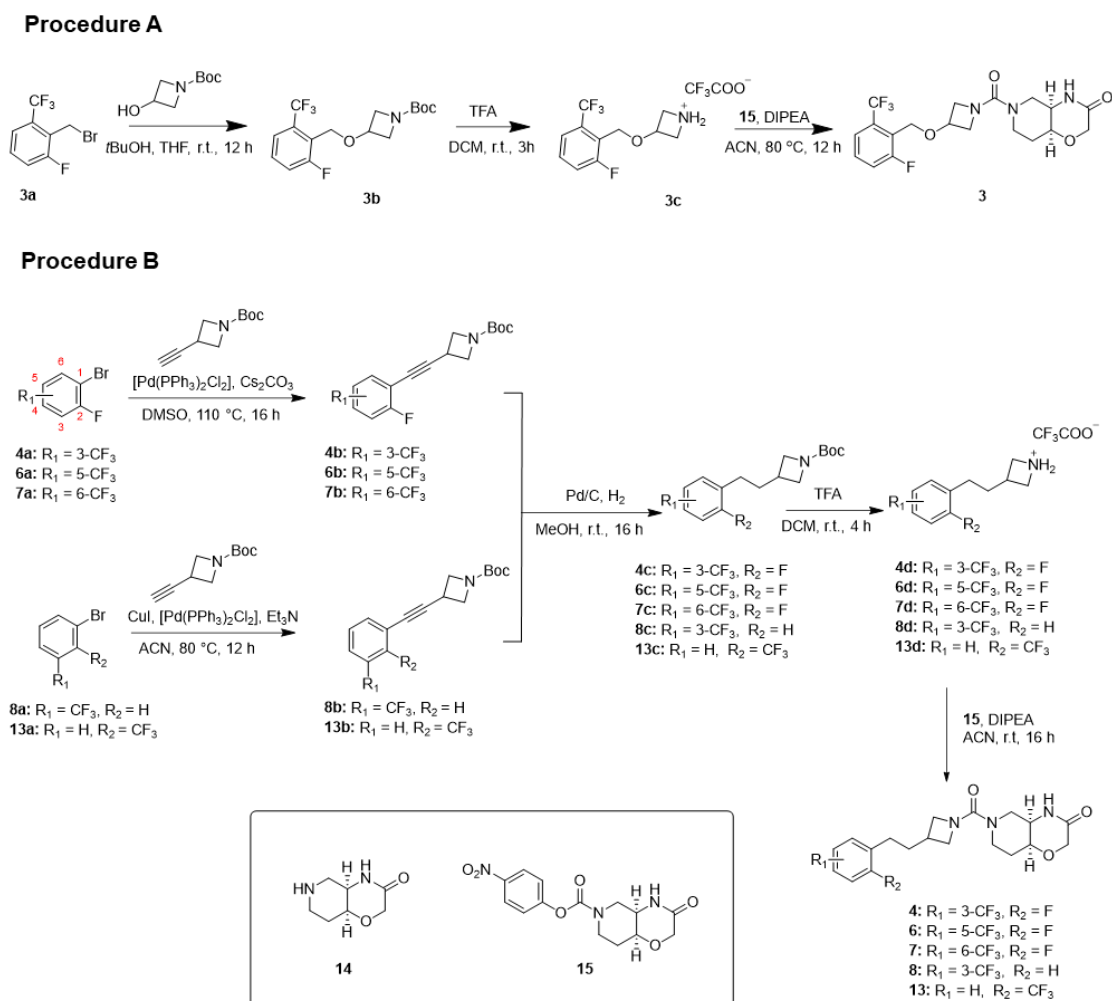


Figure 2: Chemical modification of compound **2**.

With the ultimate goal to develop a reversible MAGL PET tracer with rapid brain entry and fast clearance from CNS for clinical translation, a structural optimization program based on the chemical structure of compound **2** (as the current lead compound) is reported herein. The design concept is presented in **Figure 2**. The morpholine-3-one scaffold was conserved for non-covalent interactions with binding site residues. Meanwhile, the influences of aromatic substituents and the ether/alkyl linker on the target affinity, metabolic stability and binding kinetics were investigated. For this reason, it was envisioned the development of a novel reversible MAGL PET tracer with more favorable kinetics by accelerating the dissociation from the target site and elimination from the plasma, and thus from the brain. Aside from the determination of the half-maximal inhibitory concentration (IC_{50}) values of the novel structures, the *in vitro* metabolic stability in liver microsomes or hepatocytes was measured for predicting the *in vivo* clearance in periphery. Moreover, a surface plasmon resonance (SPR) assay was carried out to explore the association rate constants (k_{on}), dissociation rate constants (k_{off}) and dissociation constants (K_d) of the compounds in the target-binding site. The most promising candidate compound **7** with high MAGL inhibitory potency, a medium-to-high clearance and fast dissociation rate constant was selected for further *in vitro* and *in vivo* evaluations. [^{11}C]**7** was synthesized *via* direct $^{11}\text{CO}_2$ fixation method. MAGL knockout (KO) and wild-type (WT) mice were enrolled to assess its specificity and kinetic profiles. To investigate the influence of efflux transporters, a triple targeted mutation model (Mdr1a/b-Bcrp KO mice) were further included for *in vivo* evaluations.

Results

Chemistry

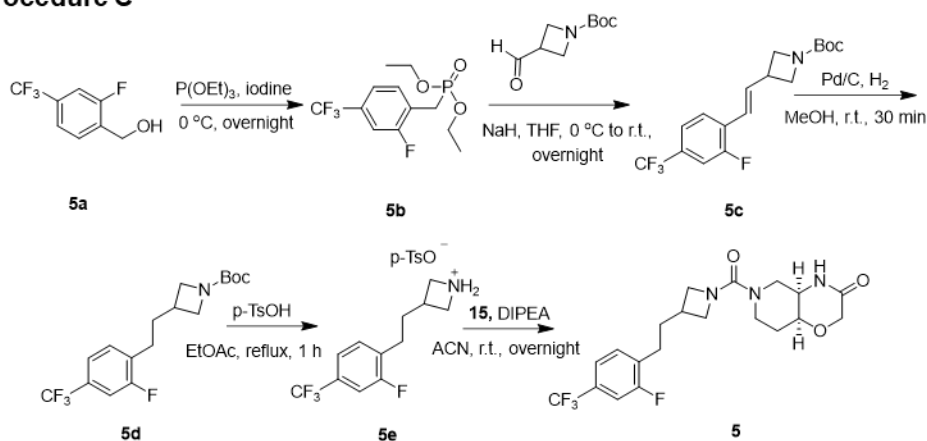


Scheme 1: Chemical syntheses of compounds **3**, **4**, **6-8**, and **13**.

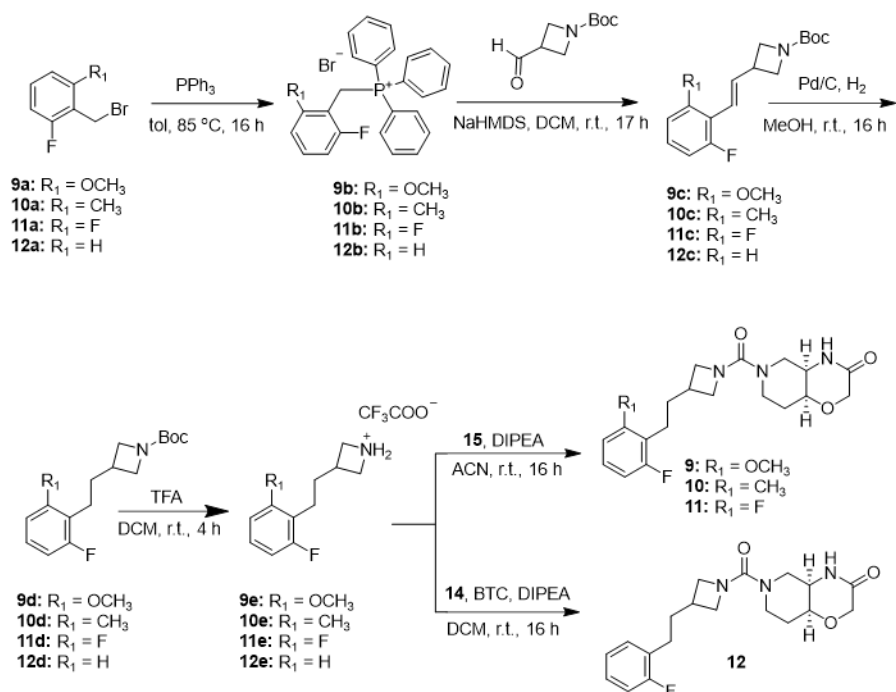
Four different procedures were employed to synthesize the desired compounds **3-13**. Similar to previously reported synthetic routine for compounds **1** and **2**, compound **3** was prepared *via* *O*-alkylation of *tert*-butyl 3-hydroxyazetidine-1-carboxylate with benzyl bromide **3a** (Procedure A in **Scheme 1**). Deprotection of azetidine **3b** by treatment with trifluoroacetic acid at room temperature provided intermediate **3c** which was subsequently reacted with nitro-phenol activated hexahydro-2*H*-pyrido-oxazin-one carboxylate (**15**) to form target compound **3** in 43% yield. Procedure B commences with a Sonogashira coupling of an aryl bromide with *tert*-butyl 3-ethynylazetidine-1-carboxylate to afford *N*-Boc protected intermediates **4b**, **6b-8b** and **13b**. After hydrogenation of the triple bond, removal of the Boc group, and subsequent urea formation with activated intermediate **15** in the presence of *N,N*-diisopropylethylamine (DIPEA), morpholine-3-ones **4**, **6-8**, and **13** were obtained as trifluoroacetate salts with

overall yields of 44-56%. As shown in **Scheme 2**, Procedures C and D began with the formation of phosphonate **5b** and phosphorous ylides **9b-12b** followed by a Wittig type reaction yielding *N*-Boc protected *E/Z* double-bond containing azetidines **5c** and **9c-12c**. In analogy to procedure B, the double bond was reduced by hydrogenation catalyzed by palladium on carbon to obtain intermediates **5d** and **9d-12d**. After the deprotection of the *N*-Boc group, the desired products **5** and **9-12** were obtained in yields of 14-60% by reacting azetidines **5e**, **9e-12e** with either compound **15** or (4*aR*,8*aS*)-hexahydro-2*H*-pyrido[4,3-*b*][1,4]oxazin-3(4*H*)-one (**14**) with triphosgene (BTC).

Procedure C



Procedure D



Scheme 2: Chemical syntheses of compounds **5** and **9-12**.

IC₅₀ measurement, in vitro metabolism, and SPR studies

The results from mouse MAGL IC₅₀, SPR assay, and *in vitro* metabolism using mouse liver microsomes and hepatocytes are summarized in **Table 1**. Compared to the lead compound **2**, compound **3** displayed a higher clearance in liver microsomes and hepatocytes by moving the trifluoromethyl (CF₃) group from 4- to 6-substitution in the aromatic ring. However, this modification also resulted in a dramatic reduction of its MAGL inhibitory activity. In contrast, replacement of the oxygen atom in the side chain with a methylene group profoundly enhanced MAGL inhibitory potency (**5** vs **2** and **7** vs **3** in **Table 1**). This may be partially explained by the lipophilic properties of the relevant MAGL binding pocket that is flanked by hydrophobic amino acid residues for matching the aliphatic chain of the natural substrat.¹⁵ Compounds **4-7** with CF₃-substituent in different positions of the aromatic ring showed comparable MAGL-inhibiting potency, their IC₅₀ values ranging from 6.5 nM to 17 nM. Compound **7** with CF₃-substituent at the 6-position of the aromatic ring exhibited the highest clearance (microsome CL_{int, app} = 99 μL/min/mg protein, hepatocyte CL_{int, app} = 51 μL/min/10⁶ cells), while compound **5** containing a 4-CF₃ substituent had much lower clearance (microsome CL_{int, app} = 11 μL/min/mg protein, hepatocyte CL_{int, app} = 4.9 μL/min/10⁶ cells). After identifying the pivotal role of the 6-position in the benzene for clearance, different substituents were used to replace the CF₃ moiety for studying their impact on the binding affinity and metabolic stability. Upon replacing 6-CF₃ to methoxy, methyl, or fluorine (**7** to **9**, **10**, or **11**), a reduction in MAGL inhibitory potency and increased metabolic clearance (except compound **11**) were observed. Mono-substituted aromatic compounds (**8**, **12**, and **13**) fell into two-digit nanomolar activities toward MAGL. The binding kinetics of the newly synthesized compounds with low nanomolar activity were further investigated using the SPR assay. The equilibrium dissociation constant (K_d), association rate constant (k_{on}), and dissociation rate constant (k_{off}) of the inhibitor-enzyme complex are shown in **Table 1**. All the tested compounds bind non-covalently to the immobilized MAGL proteins in the SPR real-time monitoring. The K_d values correlated well with the measured MAGL IC₅₀ data. The k_{off} values of compounds **4**, **7**, **10**, and **13** were in the range between 0.00558 and 0.00658 s⁻¹. Taking the multiple parameters into consideration, compound **7** with an IC₅₀ value of 9.4 ± 3.1 nM (n = 3), a K_d value of 30.0 nM, the highest dissociation rate constant (k_{off} = 0.00658 s⁻¹) and a high metabolic rate as predicted from microsomal and hepatocyte clearance, was selected for advanced profiling prior to radiolabeling.

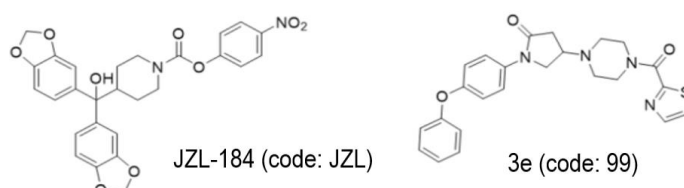
Table 1: The results of IC₅₀ measurements using mouse MAGL protein (n ≥ 3, values are means ± the standard deviation), K_d, k_{on}, and k_{off} values measured by SPR (n = 1–2) and *in vitro* metabolism using mouse liver microsomes and hepatocytes (*n.d* stands for ‘not determined’).

Compd	IC ₅₀ (nM)	K _d ^b (nM)	k _{off} (s ⁻¹)	k _{on} (M ⁻¹ s ⁻¹)	Liver microsome Cl _{int} (μL/min/mg protein)	Hepatocyte Cl _{int} (μL/min/10 ⁶ cells)
1 ^d	34 ± 4.8 ^a	24	0.00276	113850	<10 ^c	5.2
2	19 ± 6.5 ^a	5.7	0.00207	364200	<10 ^c	6.8
3	98 ± 40	<i>n.d</i>	<i>n.d</i>	<i>n.d</i>	30	32
4	6.5 ± 1.7	57	0.00588	103600	54	57
5 ^d	6.5 ± 1.6	6.1	0.00204	335200	11	4.9
6	17 ± 4.9	15	0.00392	255800	33	46
7 ^d	9.4 ± 3.1	30	0.00658	214900	99	51
8	19 ± 4.4	29	0.00443	152100	32	25
9	25 ± 6.0	41	0.00234	56570	96	156
10	30 ± 8.0	30	0.00622	208100	133	102
11	481 ± 74	<i>n.d</i>	<i>n.d</i>	<i>n.d</i>	38	36
12	88 ± 25	<i>n.d</i>	<i>n.d</i>	<i>n.d</i>	<i>n.d</i>	45
13	40 ± 4.4	27	0.00558	203500	155	200

^aResults from reference.¹⁰ ^bK_d was calculated from k_{off} divided by k_{on}. ^cThe clearance rate is below the assay sensitivity range. ^dThe SPR (k_{off} and k_{on}) was measured in duplicate and the mean value is provided.

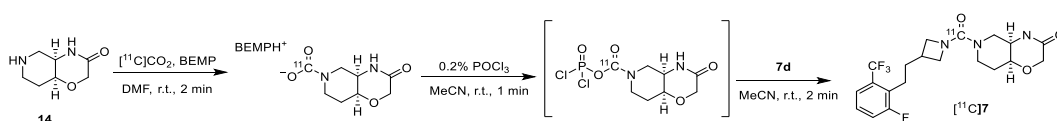
Advanced profiling of compound 7

To evaluate the selectivity of compound **7** over the relevant serine hydrolases in the ECS, a gel-based activity-based protein profiling (ABPP) assay was applied using mouse brain membrane and cytosol proteomes.¹⁶ Two selective and potent MAGL inhibitors (JZL-184 (code: JZL) and 3e (code: 99)) were employed as the positive controls.^{17,18} Compound **7** blocked only the fluorescent signals from MAGL under tested conditions, which suggests the high MAGL selectivity of compound **7** over the other hydrolases including fatty acid amide hydrolase (FAAH), diacylglycerol lipase α (DAGL-α), and α/β-hydrolase-domain containing enzymes 6 (ABHD6) and 12 (ABHD12). In P-gp *in vitro* transport experiments, the efflux ratios (ER) of compound **7** in the mouse and human P-gp-transfected cell lines were determined as 5.8 and 1.9, respectively, indicating that the structure could be a P-gp substrate in rodents but not in humans. Moreover, the IC₅₀ value of compound **7** towards human MAGL was determined as 3.7 ± 1.2 nM (n = 6), indicating its excellent MAGL potency across species. The free fractions of compound **7** in mouse and human plasma were measured to be 10% and 5%, respectively. These results suggest that a low risk of high non-specific binding *in vivo*, according to previously reported literature.¹⁹



Radiosynthesis of [¹¹C]7

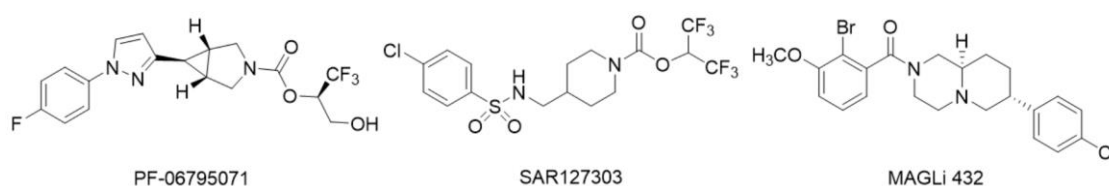
[¹¹C]7 was synthesized *via* direct [¹¹C]CO₂ fixation using **14** and **7d** as the precursors (**Scheme 3**). This one-pot, three-step reaction sequence comprises the trapping of [¹¹C]CO₂, the activation *via* a presumable [¹¹C]carbamoyl chloride, and the incorporation of azetidine **7d**. After the semi-preparative high performance liquid chromatography (HPLC) purification, [¹¹C]7 (1.37 ± 0.25 GBq) was obtained with a molar activity of 59.8 ± 22.9 GBq/μmol at the end of synthesis (n = 20). The radiochemical purity (RCP) was greater than 99%, and the total synthesis time from the end of bombardment was around 30 min.



Scheme 3: Radiosynthesis of [¹¹C]7.

In vitro autoradiography

Sagittal brain slices from Wistar rat were utilized to unveil the *in vitro* binding characteristics of [¹¹C]7. Representative autoradiograms are presented in **Figure 3**. The heterogeneous distribution of [¹¹C]7 followed the expression pattern of MAGL in the rat brain.^{20,21} High accumulation was found in the cortex, hippocampus, and striatum. Moderate accumulation was detected in the thalamus and cerebellum, followed by low accumulation in the brain stem where a low expression level of MAGL was reported.^{20,21} Co-incubation with a MAGL inhibitor, either PF-06795071 or SAR127303, led to a significant reduction of the radioactive signals confirming the *in vitro* specificity of [¹¹C]7 towards MAGL. Brain sections from MAGL KO and WT mice were further included to evaluate the selectivity of [¹¹C]7 *in vitro*. A heterogeneous distribution pattern of [¹¹C]7, reflecting the target expression patterns, was observed in the WT mouse brain sections. By contrast, low and homogenous signals were seen using brain sections from MAGL KO mouse. These results demonstrate the high specificity and selectivity of [¹¹C]7 towards MAGL *in vitro*.



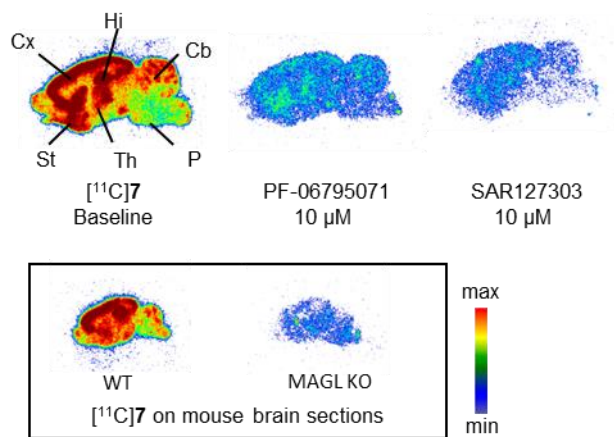


Figure 3: Representative *in vitro* autoradiograms of [¹¹C]7 on rat (top) and mouse (bottom) brain sections. Cx, cortex; St, striatum; Hi, hippocampus; Th, thalamus; Cb, cerebellum; P, pons (brainstem).

Lipophilicity and in vitro stability

The lipophilicity of [¹¹C]7 was determined as 2.65 ± 0.15 at pH 7.4 using the shake-flask method ($n = 3$),²² which falls into the optimal range for brain penetration. The radiochemical purity of [¹¹C]7 remained above 95% after 40 min incubation at 37 °C in mouse, rat, or human serum (**Figure 4**).

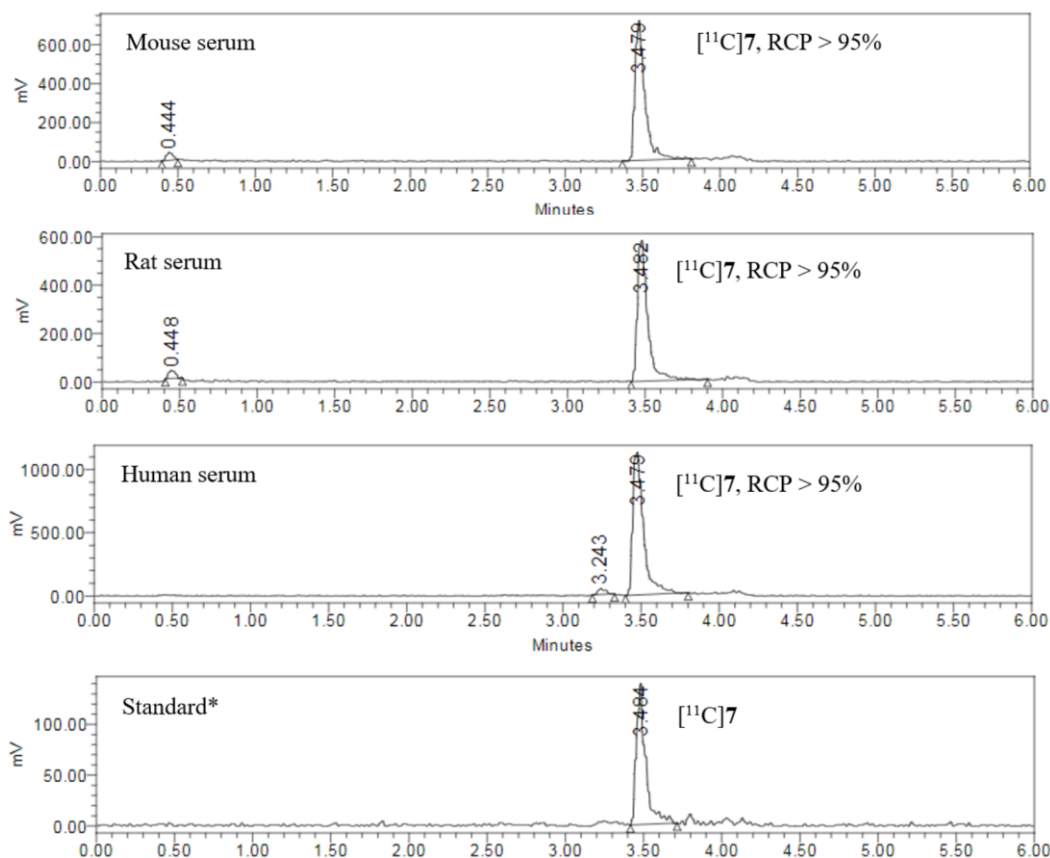


Figure 4. *In vitro* stability of [¹¹C]7 after 40 min incubation. *The standard run was the same as shown in **Figure 8A**.

In vivo PET imaging

MAGL KO and WT mice. To investigate the kinetic profile of [¹¹C]7 *in vivo*, dynamic PET scans were carried out in anaesthetized MAGL KO and WT mice. The time activity curves (TACs) of the whole brain uptake are shown in **Figure 5**. The radiotracer exhibited a maximal standardized uptake value (SUV_{max}) of ca. 0.4-0.5 in mice brain. Compared to the increasing brain accumulation of [¹¹C]2 overtime,¹⁰ [¹¹C]7 reached its maximal accumulation in WT mice within 20 min p.i. and slowly washed out afterwards. A strikingly faster clearance was observed in MAGL KO mice brain, confirming the specific and selective binding of the radioligand towards MAGL *in vivo*.

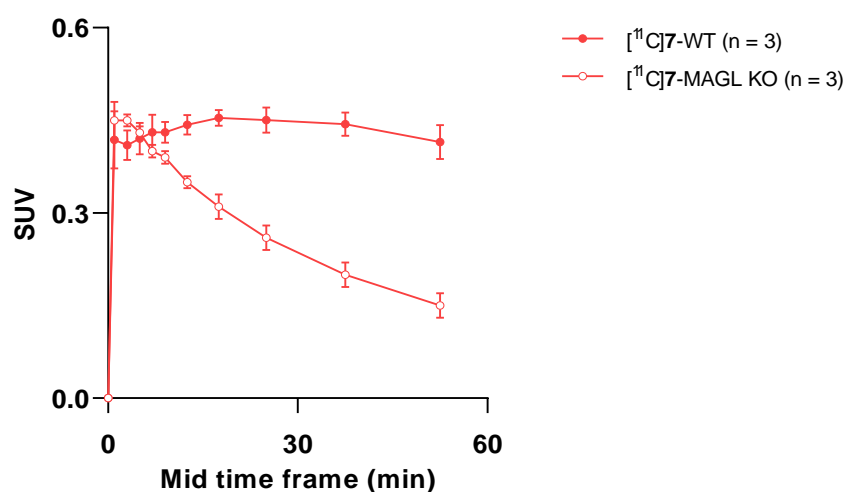


Figure 5: The whole brain TACs of [¹¹C]7 in MAGL KO and WT mice.

Mdr1a/b-Bcrp KO and WT mice

To investigate the influence from efflux transporters, Mdr1a/b-Bcrp KO mice carrying a disruption of the multi-drug resistance genes and WT mice were enrolled in dynamic PET scans. The whole brain TACs of [¹¹C]2 and [¹¹C]7 in Mdr1a/b-Bcrp KO and WT mice are depicted in **Figure 6**. Significantly higher brain uptakes were achieved by both radioligands in Mdr1a/b-Bcrp KO mice, confirming that the structures were P-gp substrates in rodents. Compared to [¹¹C]2, [¹¹C]7 exhibited a significantly higher radioactive accumulation and more appropriate kinetics in Mdr1a/b-Bcrp KO mice. To understand whether these increased radioactive signals was MAGL-specific, one mouse was pretreated with a potent and selective MAGL inhibitor MAGLi432²³ before the administration of radiotracer. As illustrated in **Figure 6** (blue color curve), a profoundly rapid washout of the radioactivity from the Mdr1a/b-Bcrp KO mouse brain was induced, which confirmed the high specificity of [¹¹C]7 *in vivo*. **Figure 7** showed the axial, sagittal and coronal brain PET images of [¹¹C]7 in the Mdr1a/b-Bcrp KO and WT mouse. The

low brain uptake of [^{11}C]7 in the WT mouse (**Figure 7A**) is in line with its high ER of 5.8 measured *in vitro*. In the Mdr1a/b-Bcrp KO mouse brain, high levels of radioactive signals were revealed for [^{11}C]7 and its distribution in the different brain regions reflected the MAGL expression pattern in the rodent (**Figure 7B**). Blocking with 5 mg/kg MAGLi432, a potent MAGL inhibitor, led to a profound reduction in the level of the radiotracer accumulated in the Mdr1a/b-Bcrp KO mouse brain, as shown in **Figure 7C**.

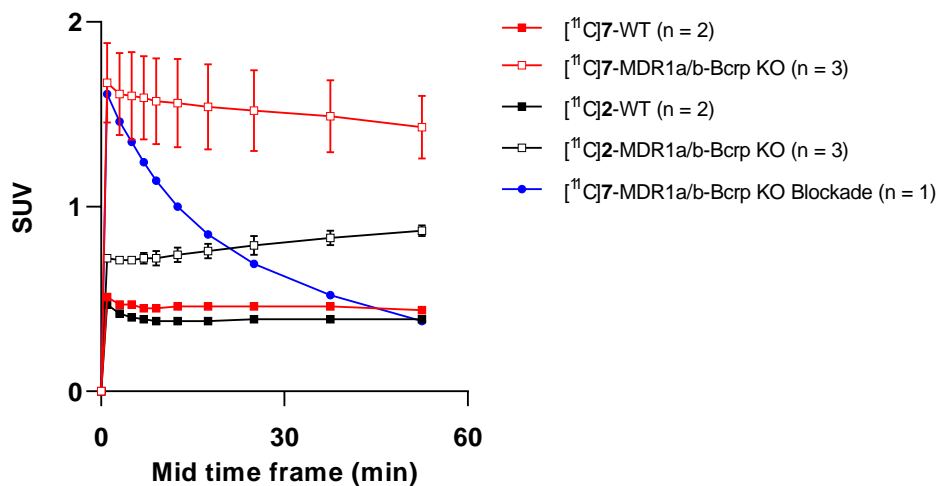


Figure 6: The whole brain TACs of [^{11}C]2 and [^{11}C]7 in Mdr1a/b-Bcrp KO and WT mice.

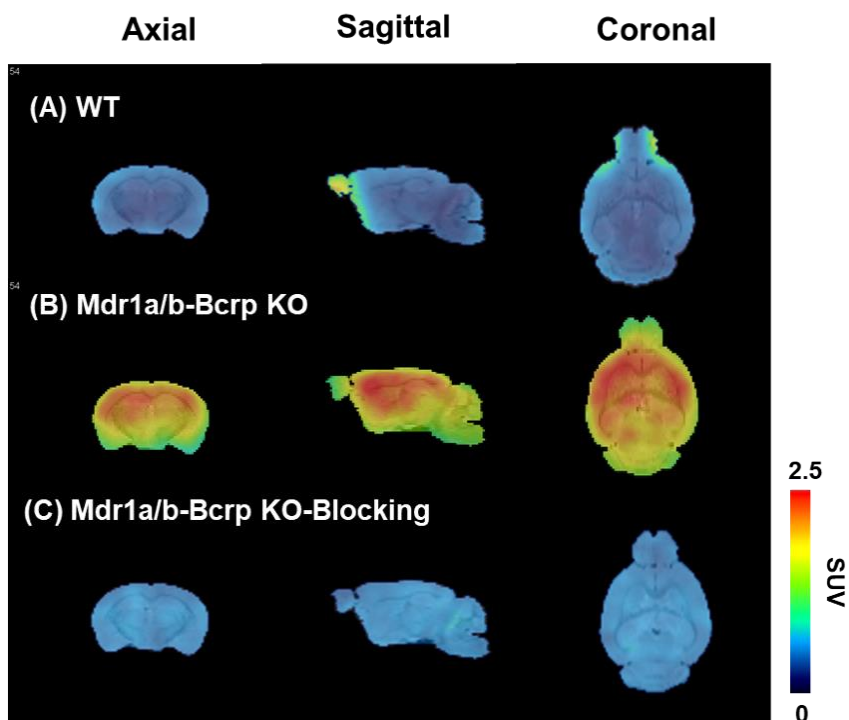


Figure 7: The axial, sagittal, and coronal PET brain images of [^{11}C]7 in WT mouse (A) and Mdr1a/b-Bcrp KO mouse under baseline (B), and blocking conditions (C) averaged from 13.5 min to 52.5 min p.i.

Radiometabolite analysis

The *in vivo* metabolic stability of [^{11}C]7 in the mouse brain was further investigated. **Figure 7** showed the radio-UPLC chromatograms from the final formulation and brain homogenates. At 40 min p.i., the intact radiotracer [^{11}C]7 was the only detectable radioactive peak in the brain extract. Therefore, we concluded that the radioactive signals in the mouse brain were dominantly presented by the intact structure and the radiometabolites of [^{11}C]7 showed limited ability to cross the blood-brain barrier.

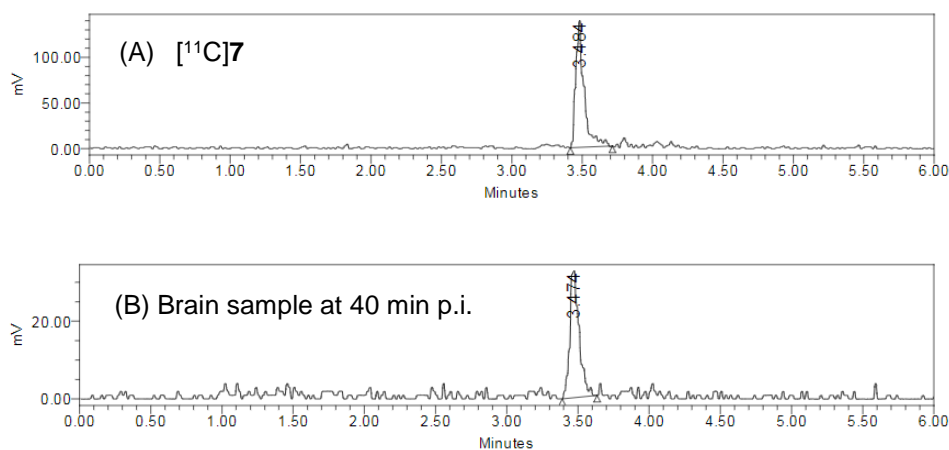


Figure 8: Radio-UPLC chromatograms of [^{11}C]7 in the final formulation (A) and the brain homogenate after 40 min p.i. of [^{11}C]7 (B).

Discussion

In a previous work, [^{11}C]2 was identified from an F. Hoffmann-La Roche Ltd internal morpholin-3-one library to serve as an entirely novel structure to image MAGL in the CNS.¹⁰ The specificity of [^{11}C]2 was confirmed *in vivo* using MAGL KO and WT mice. In the meanwhile, the slow kinetic profile of [^{11}C]2 was disclosed with increasing radioactivity accumulated in mouse brains up to 60 min p.i. This is somehow not surprising as compound 2 was initially designed as a reversible MAGL drug candidate, for which high metabolic stability and a long target residence time are favored for the pursuit of therapeutic efficacy in the treatment. Accordingly, the major objective of current study was to accelerate the brain clearance of [^{11}C]2 to consequently improve its kinetic profile as a suitable molecular probe for quantitative PET studies. Eleven compounds were designed and synthesized based on the lead structure 2. Their IC_{50} values indicated that the lipophilic property of the alkyl chain and the position of trifluoromethyl substituent in the aromatic ring are the essential elements for the regulation of MAGL inhibition potency. Although compounds 4-7 displayed high structural similarity and comparable IC_{50} values toward MAGL, compound 7 containing a CF_3 -substituent at the position 6 of the benzene ring showed a remarkably high clearance in metabolic stability assays. In

addition, compound **7** revealed a faster dissociation rate constant in the MAGL binding pocket compared to those of the other candidates. It was subsequently labeled with carbon-11 for further evaluations.

Remarkably, [¹¹C]**7** reached its peak uptake in the WT mouse brains within a distinctively shorter time period than [¹¹C]**2** (17.5 min p.i. for [¹¹C]**7** vs. 52.5 min p.i. for [¹¹C]**2**).¹⁰ This could be attributed to the faster metabolism of [¹¹C]**7** in periphery in addition to its increased dissociation from MAGL protein as determined in the SPR assay (**Table 1**). However, it is hard to speculate the major contributor based on the current results because the interactions between tracer and target macromolecules *in vivo* are more complex than in *in vitro* assays running under closed system conditions. Further PET kinetic studies with mathematical modelling are required to elucidate the key determinant behind this improved kinetic profile. The *in vivo* specificity of [¹¹C]**7** in the mouse brain was confirmed by 63% reduction of the radioactive signals in the MAGL KO mice compared to the WT mice. To investigate the impact of efflux transporters on mice brain uptake, PET studies were then conducted with triplet-mutated mice carrying a disruption of efflux transporters. As expected, higher brain uptakes were accomplished by [¹¹C]**2** and [¹¹C]**7** in Mdr1a/b-Bcrp KO mice brain. Of note, [¹¹C]**7** achieved a significantly higher brain penetration in Mdr1a/b-Bcrp KO mice than that of [¹¹C]**2** ([¹¹C]**7**: 1.67 SUV at 2 min p.i. vs. [¹¹C]**2**: 0.72 SUV at 2 min p.i.). This improvement might be contributed by the reduced molecular weight, slightly increased lipophilicity and decreased topological surface area (TPSA) of [¹¹C]**7** ($M_w=429.17$, $\log D_{7.4} = 2.65$, TPSA = 61.88 using ChemDraw 19.0) compared to [¹¹C]**2** ($M_w=447.12$, $\log D_{7.4} = 2.21$,¹⁰ TPSA = 71.11 using ChemDraw 19.0). Taken together with the low ER value of 1.9 obtained from porcine kidney epithelial cells overexpressing human P-gp, [¹¹C]**7** is not expected as a substrate for efflux transporters in humans, and therefore holds a great potential to achieve a high brain uptake in further clinical translation. So far, it remains unclear whether [¹¹C]**7** would have a slower brain washout in higher species and whether the volume of distribution could be stable and measurable within the practicable imaging time of carbon-11. In this perspective, a fluorine-18-labeled version of compound **7** without structural modification or the methyl-substituted analog compound **10** that has higher metabolic clearance capacity could offer a solution.

Conclusion

In conclusion, [¹¹C]**7** is a promising reversible MAGL probe that could serve as a potential clinical candidate with an entirely novel chemical scaffold for imaging MAGL in the brain. It demonstrated high specificity, selectivity, and reversible target binding towards MAGL *in vivo*, as well as the absence of confounding radiometabolites in the mouse brain. In

the structural optimization process, results of metabolic stability and surface plasmon resonance provided valuable guidance in the compound selection prior to the radiolabeling, and ultimately led to the identification of [¹¹C]7 with improved kinetic profile *in vivo*. This finding may provide useful hints for the structural optimization of PET probes that encountered slow pharmacokinetics for neuroimaging.

Experimental Section

General Information.

All chemicals, reagents, and solvents for the synthesis and analysis of compounds were purchased from commercial sources and used without further purification. The key intermediate, (4*aR*,8*aS*)-Hexahydro-2*H*-pyrido[4,3-*b*][1,4]oxazin-3(4*H*)-one (**14**), was prepared from its racemic commercial source (ChemBridge Corporation) and purified by preparative chiral HPLC (ReprosilChiral NR column) using an isocratic mixture of EtOH (containing 0.05% of NH₄OAc): *n*-heptane (30:70). The 4-nitrophenyl (4*aR*,8*aS*)-3-oxohexahydro-2*H*-pyrido[4,3-*b*][1,4]oxazine-6(5*H*)-carboxylate (**15**) was prepared according to the previously described method.¹⁰ All the reactions were monitored by thin-layer chromatography (TLC) performed on Merck TLC glass sheets (silica gel 60 F254) or a Waters Acquity ultra-performance liquid chromatography (UPLC) equipped with a single quadrupole mass spectrometer (MS). Fast column chromatography was carried out using silica gel (Sigma-Aldrich, mesh size 230 - 400). Nuclear magnetic resonance spectra were acquired on Bruker Avance FT-NMR spectrometer 300, 400, or 600 MHz instruments. Chemical shifts (δ) are reported in parts per million (ppm), relative to the residual solvent peak or tetramethylsilane (TMS). High resolution mass spectra were recorded by an Agilent liquid chromatography (LC) system consisting of Agilent 1290 high pressure gradient system, a CTC PAL auto sampler and an Agilent 6520 quadrupole time-of-flight MS. The separation in Agilent LC-system was achieved by Zorbax Eclipse Plus C18 column at 55 °C (2.1 × 50 mm, 1.8 μ m; mobile phase A = 0.02% formic acid in water, mobile phase B = acetonitrile with 0.01% formic acid at flow 0.8 mL/min; gradient: 0 min 5%B, 0.3 min 5%B, 4.5 min 99%B, 5 min 99%B). The injection volume was 2 μ L, and the ionization was performed in Agilent multimode source. The system was run in "2 GHz extended dynamic range" mode, resulting in a resolution of about 10 000 at *m/z* = 922. Mass accuracy was ensured by internal drift correction. Purity of all biologically tested compounds was determined by LC-MS, and greater than 95%.

Chemistry

Procedure A. *tert*-Butyl 3-((2-fluoro-6-(trifluoromethyl)benzyl)oxy)azetidine-1-carboxylate (**3b**). To a solution of *tert*-butyl 3-hydroxyazetidine-1-carboxylate (674 mg, 3.89 mmol) in anhydrous THF (5 mL), potassium *tert*-butoxide (1.0 M solution in THF, 5.84 mL, 5.84 mmol) and **3a** (1.00 g, 3.89 mmol) were added. After stirring at room temperature for 12 h, the mixture was poured into water (10 mL) and extracted three times with ethyl acetate (20 mL × 3). The combined organic layers were dried over anhydrous Na₂SO₄ and filtered. The filtrate was concentrated under reduced pressure, purified by flash chromatography (SiO₂, petroleum ether: ethyl acetate = 10/1 to 2/8) to obtain the desired product as a colorless oil (1100 mg, 81%). LC-MS (ESI): *m/z* = 294.0 [M-*t*Bu+H]⁺.

3-((2-Fluoro-6-(trifluoromethyl)benzyl)oxy)azetidine 2,2,2-trifluoroacetate (**3c**). To a solution of **3b** (400 mg, 1.15 mmol) in DCM (5 mL) was added TFA (2.00 mL). The reaction mixture was stirred at room temperature for 12 h. The reaction mixture was concentrated under reduced pressure and dried to afford crude product (300 mg) as a yellow oil, which was used in the next step without any further purification. LC-MS (ESI): *m/z* = 250.0 [M+H]⁺.

(4*aR*,8*aS*)-6-(3-((2-Fluoro-6-(trifluoromethyl)benzyl)oxy)azetidine-1-carbonyl)hexahydro-2*H*-pyrido[4,3-*b*][1,4] oxazin-3(4*H*)-one (**3**). To a solution of **15** (106 mg, 0.33 mmol) in MeCN (10 mL) was added DIPEA (107 mg, 0.83 mmol) and **3c** (100 mg, 0.28 mmol). The reaction mixture was stirred at 80 °C for 12 h. The solvent was removed under reduced pressure and the crude residue was purified by reversed-phase HPLC to yield the desired product as white solid (53 mg, 43%). ¹H NMR (600 MHz, Chloroform-*d*) δ 7.54–7.48 (m, 1H), 7.48-7.43 (m, 1H), 7.31 (t, *J* = 8.8 Hz, 1H), 6.18 (br d, *J* = 3.6 Hz, 1H, -NHCO-), 4.62 (s, 2H), 4.37 (tt, *J* = 6.6, 4.4 Hz, 1H), 4.32-4.26 (m, 1H), 4.23-4.15 (m, 2H), 4.12 (dd, *J* = 8.9, 7.0 Hz, 1H), 3.96 (d, *J* = 2.8 Hz, 1H), 3.93 (ddd, *J* = 9.2, 4.4, 0.8 Hz, 1H), 3.89-3.83 (m, 2H), 3.55-3.45 (m, 1H), 3.42-3.34 (m, 1H), 3.13–3.00 (m, 2H), 1.91 (dd, *J* = 14.4, 2.7 Hz, 1H), 1.85–1.74 (m, 1H). ¹³C NMR (151 MHz, Chloroform-*d*) δ 168.22, 162.25 (d, *J*_{C-F} = 250.2 Hz), 162.09, 131.41 (d, *J*_{C-F} = 34.6 Hz), 130.49 (d, *J*_{C-F} = 9.2 Hz), 123.43 (q, *J*_{C-F} = 274.1 Hz), 122.79 (d, *J*_{C-F} = 16.9 Hz), 122.02, 119.56 (d, *J*_{C-F} = 23.0 Hz), 69.47, 68.38, 67.68, 60.49, 58.44, 58.25, 49.57, 46.20, 39.77, 29.55. HRMS (ESI) calculated for [M+H]⁺/C₁₉H₂₂F₄N₃O₃⁺: 432.1541 *m/z*, found: 432.1546 *m/z*.

Procedure B. *tert*-Butyl 3-((2-fluoro-3-(trifluoromethyl)phenyl)ethynyl) azetidine-1-carboxylate (**4b**). To a solution of **4a** (405 mg, 1.67 mmol) and *tert*-butyl 3-ethynylazetidine-1-carboxylate (300 mg, 1.66 mmol) in DMSO (10 mL) were added

[Pd(PPh₃)₂Cl₂] (117 mg, 0.17 mmol) and cesium carbonate (1.08 g, 3.31 mmol) at 25 °C. The mixture was stirred at 110 °C for 16 h under N₂ protection, poured into brine (30 mL) and extracted with ethyl acetate (30 mL × 2). The organic layers were washed with water (20 mL × 2). The organic layers were dried over Na₂SO₄, filtered and concentrated *in vacuo* to give a residue, which was purified by column chromatography (SiO₂, petroleum ether : ethyl acetate = 10:1 to 3:1) to give the desired product as a colorless oil (139 mg, 22%). ¹H NMR (400 MHz, Methanol-*d*₄) δ 7.78–7.72 (m, 1H), 7.70-7.63 (m, 1H), 7.38-7.30 (m, 1H), 4.27 (t, *J* = 8.5 Hz, 2H), 4.03-3.92 (m, 2H), 3.80-3.63 (m, 1H), 1.46 (s, 9H). LC-MS (ESI): *m/z* = 288.0 [M-*t*Bu +H]⁺.

tert-Butyl 3-((2-fluoro-3-(trifluoromethyl)phenyl)ethynyl)azetidine-1-carboxylate (**4c**). To a mixture of **4b** (130 mg, 0.38 mmol) in methanol (5 mL) was added 10% Pd/C (50.0 mg, 0.05 mmol) and the mixture was stirred at 25 °C under H₂ (15 psi) for 16 h. The mixture was filtered and the filtrate was concentrated *in vacuo* to give a residue, which was purified by column chromatography (SiO₂, petroleum ether : ethyl acetate = 15:1 to 5:1) to the desired product as a colorless oil (88 mg, 57%). ¹H NMR (400 MHz, Chloroform-*d*) δ 7.49-7.43 (m, 1H), 7.39-7.33 (m, 1H), 7.19-7.13 (m, 1H), 4.00 (t, *J* = 8.3 Hz, 2H), 3.55 (dd, *J* = 8.3, 5.5 Hz, 2H), 2.72-2.58 (m, 2H), 2.56-2.39 (m, 1H), 1.91 (q, *J* = 7.7 Hz, 2H), 1.43 (s, 9H). LC-MS (ESI): *m/z* = 292.0 [M-*t*Bu+H]⁺.

3-(2-Fluoro-3-(trifluoromethyl)phenethyl)azetidine 2,2,2-trifluoroacetate (**4d**). To a solution of **4c** (80.0 mg, 0.23 mmol) in DCM (2 mL) was added trifluoroacetic acid (0.20 mL, 2.60 mmol) and the mixture was stirred at 25 °C for 4 h. The reaction solution was concentrated under reduced pressure to give a crude product, which was directly used in the next step without any further purification. LC-MS (ESI): *m/z* = 248.4 [M+H]⁺.

(4*aR*,8*aS*)-6-(3-(2-Fluoro-3-(trifluoromethyl)phenethyl)azetidine-1-carbonyl)hexahydro-2*H*-pyrido[4,3-*b*][1,4] oxazin-3(4*H*)-one (**4**). To solution of **4d** (40.0 mg, 0.11 mmol) and DIPEA (0.11 mL, 0.65 mmol) in MeCN (2 mL) was added **15** (36.0 mg, 0.11 mmol). Then the mixture was stirred at 25 °C for 16 h. The solution was concentrated *in vacuo* to give a residue, which was purified by preparative HPLC (column: Phenomenex Luna C18 75 × 30 mm, 3 μm, mobile phase: A/B = 0.1% TFA in water/acetonitrile, condition: 25 mL/min, A/B from 58/42 to 28/72) and then lyophilized to give the desired product as a colorless oil (25 mg, 53%). ¹H NMR (600 MHz, Chloroform-*d*) δ 7.48-7.45 (m, 1H), 7.39-7.34 (m, 1H), 7.16 (t, *J* = 7.7 Hz, 1H), 6.30 (br d, *J* = 3.0 Hz, 1H, -NHCO-), 4.32-4.28 (m, 1H), 4.21-4.17 (m, 1H), 4.09 (t, *J* = 8.3 Hz, 1H), 4.02 (t, *J* = 8.3 Hz, 1H), 3.96 (s, 1H), 3.88 (dd, *J* = 13.0, 4.9 Hz, 1H), 3.65 (dd, *J* = 8.3, 5.9 Hz, 1H), 3.59 (dd, *J* = 8.2, 5.9 Hz, 1H), 3.49-3.45 (m, 1H), 3.42-3.37 (m, 1H), 3.14-2.99 (m, 2H), 2.66 (t, *J* = 7.6 Hz, 2H),

2.60-2.55 (m, 1H), 1.95-1.90 (m, 3H), 1.81-1.75 (m, 1H). ¹³C NMR (151 MHz, Chloroform-*d*) δ 168.37, 162.29, 157.99 (d, *J*_{C-F} = 254.6 Hz), 134.47 (d, *J*_{C-F} = 5.4 Hz), 129.85 (d, *J*_{C-F} = 15.4 Hz), 125.16 (q, *J*_{C-F} = 4.3 Hz), 123.95 (d, *J*_{C-F} = 4.4 Hz), 122.71 (q, *J*_{C-F} = 272.3 Hz), 118.50, 69.48, 67.66, 56.57, 49.58, 46.17, 39.74, 34.72, 29.59, 28.94, 26.31. HRMS (ESI) calculated for [M+H]⁺/C₂₀H₂₄F₄N₃O₃⁺: 430.1748 m/z, found: 430.1750 m/z.

tert-Butyl 3-((2-fluoro-5-(trifluoromethyl)phenyl)ethynyl)azetidine-1-carboxylate (**6b**).

The procedure described for the synthesis of **4b** was applied to **6a** (675 mg, 2.78 mmol), *tert*-butyl 3-ethynylazetidine-1-carboxylate (500 mg, 2.76 mmol), [Pd(PPh₃)₂Cl₂] (195 mg, 0.28 mmol) and cesium carbonate (1.80 g, 5.52 mmol) in 10 mL DMSO to give the desired product as a colorless oil (214 mg, 20%). ¹H NMR (400 MHz, Chloroform-*d*) δ 7.73-7.67 (m, 1H), 7.59-7.52 (m, 1H), 7.18 (t, *J* = 8.7 Hz, 1H), 4.23 (t, *J* = 8.5 Hz, 2H), 4.05 (dd, *J* = 8.2, 6.4 Hz, 2H), 3.66-3.53 (m, 1H), 1.45 (s, 9H). LC-MS (ESI): m/z = 288.1 [M-*t*Bu+H]⁺.

tert-Butyl 3-(2-fluoro-5-(trifluoromethyl)phenethyl)azetidine-1-carboxylate (**6c**). The procedure described for the synthesis of **4c** was applied to **6b** (205 mg, 0.60 mmol) and 10% Pd/C (50.0 mg, 0.05 mmol) in methanol (5 mL) to give the desired product as a grey solid (128 mg, 56%). ¹H NMR (400 MHz, DMSO-*d*₆) δ 7.85-7.73 (m, 1H), 7.69-7.61 (m, 1H), 7.39 (t, *J* = 9.2 Hz, 1H), 3.88 (s, 2H), 3.47 (s, 2H), 2.64 (t, *J* = 7.7 Hz, 2H), 2.48-2.37 (m, 1H), 1.83 (q, *J* = 7.7 Hz, 2H), 1.37 (s, 9H). LC-MS (ESI): m/z = 292.3 [M-*t*Bu+H]⁺.

3-(2-Fluoro-5-(trifluoromethyl)phenethyl)azetidine 2,2,2-trifluoroacetate (**6d**). The procedure described for the synthesis of **4d** was applied to **6c** (120 mg, 0.35 mmol) and trifluoroacetic acid (0.30 mL, 3.89 mmol) to a crude product, which was directly applied to next step without any further purification. LC-MS (ESI): m/z = 248.4 [M+H]⁺.

(4*aR*,8*aS*)-6-(3-(2-Fluoro-5-(trifluoromethyl)phenethyl)azetidine-1-carbonyl) hexahydro-2*H*-pyrido[4,3-*b*][1,4]oxazin-3(4*H*)-one (**6**). The procedure described for the synthesis of **4** was applied to **6d** (40.0 mg, 0.11 mmol), DIPEA (0.11 mL, 0.65 mmol), **15** (36.0 mg, 0.11 mmol) in MeCN (2 mL). The crude was purified by preparative HPLC (column: Phenomenex Synergi C18 150 × 25 mm, 10 μm, mobile phase: A/B = 0.1%TFA in water/acetonitrile, condition: 25 mL/min, A/B from 59/41 to 29/71) and then lyophilized to give the desired product as a colorless oil (21 mg, 44%). ¹H NMR (400MHz, DMSO-*d*₆) δ 8.13 (d, *J* = 3.9 Hz, 1H, -NHCO-), 7.76 (d, *J* = 6.7 Hz, 1H), 7.69-7.63 (m, 1H), 7.40 (t, *J* = 9.0 Hz, 1H), 4.10-4.00 (m, 2H), 3.99-3.88 (m, 4H), 3.71 (dd, *J* = 4.5, 12.4 Hz, 1H), 3.60-3.52 (m, 2H), 3.48 (d, *J* = 13.7 Hz, 1H), 3.23-3.16 (m, 1H), 2.87-2.74 (m, 2H),

2.68-2.62 (m, 2H), 1.83 (q, $J = 7.7$ Hz, 2H), 1.78-1.66 (m, 2H). ^{13}C NMR (151 MHz, Chloroform- d) δ 168.55, 162.82 (d, $J_{\text{C-F}} = 250.5$ Hz), 162.26, 129.17 (d, $J_{\text{C-F}} = 17.5$ Hz), 127.85, 126.44, 125.39, 123.77 (q, $J_{\text{C-F}} = 271.9$ Hz), 115.90 (d, $J_{\text{C-F}} = 23.8$ Hz), 69.45, 67.59, 56.57, 49.55, 46.13, 39.72, 34.62, 29.56, 28.93, 26.48. HRMS (ESI) calculated for $[\text{M}+\text{H}]^+/\text{C}_{20}\text{H}_{24}\text{F}_4\text{N}_3\text{O}_3^+$: 430.1748 m/z, found: 430.1753 m/z.

tert-Butyl 3-((2-fluoro-6-(trifluoromethyl)phenyl)ethynyl)azetidine-1-carboxylate (**7b**). The procedure described for the synthesis of **4b** was applied to **7a** (270 mg, 1.11 mmol), *tert*-butyl 3-ethynylazetidine-1-carboxylate (200 mg, 1.10 mmol), $[\text{Pd}(\text{PPh}_3)_2\text{Cl}_2]$ (78.0 mg, 0.11 mmol) and cesium carbonate (719 mg, 2.21 mmol) in DMSO (5 mL) to give the desired product as a colorless oil (127 mg, 32%). ^1H NMR (400 MHz, DMSO- d_6) δ 7.77-7.57 (m, 3H), 4.22 (t, $J = 7.9$ Hz, 2H), 3.90-3.68 (m, 3H), 1.39 (s, 9H). LC-MS (ESI): m/z = 287.9 $[\text{M}-t\text{Bu}+\text{H}]^+$.

tert-Butyl 3-(2-fluoro-6-(trifluoromethyl)phenethyl)azetidine-1-carboxylate (**7c**). The procedure described for the synthesis of **4c** was applied to **7b** (110 mg, 0.32 mmol) and 10% Pd/C (50.0 mg, 0.05 mmol) in methanol (5 mL) to give the desired product as a yellow oil (95 mg, 68%). ^1H NMR (400 MHz, DMSO- d_6) δ 7.68-7.41 (m, 3H), 3.91 (s, 2H), 3.48-3.41 (m, 2H, overlapped with water residue), 2.73-2.60 (m, 2H), 2.57-2.52 (m, 1H, overlapped with solvent peak), 1.90-1.68 (m, 2H), 1.35 (s, 9H). LC-MS (ESI): m/z = 292.0 $[\text{M}-t\text{Bu}+\text{H}]^+$.

3-(2-Fluoro-6-(trifluoromethyl)phenethyl)azetidine (**7d**). The procedure described for the synthesis of **4d** was applied to **7c** (80.0 mg, 0.23 mmol) and trifluoroacetic acid (0.20 mL, 2.60 mmol) to give a crude product which was directly applied to next step without any further purification. LC-MS (ESI): m/z = 248.0 $[\text{M}+\text{H}]^+$. For precursor for radiolabeling, *p*-toluenesulfonic acid was employed as the acid for deprotection. To a solution of **7c** (800 mg, 2.3 mmol) in ethyl acetate (5 mL) was added 4-methylbenzenesulfonic acid monohydrate (438 mg, 2.3 mmol). The mixture was heated at reflux for 1 hour, cooled down to room temperature, and kept at 4 °C overnight. The suspension was filtered, washed with Et_2O , resolved in ethyl acetate, and treated with pentane/ Et_2O for recrystallization. ^1H NMR (600 MHz, DMSO- d_6) δ 8.63-8.31 (m, 2 H), 7.57 (ddd, $J = 9.6, 8.0, 1.0$ Hz, 1 H), 7.59 (dd, $J = 7.9, 1.0$ Hz, 1 H), 7.52 (td, $J = 8.1, 5.8$ Hz, 1 H), 7.47 (d, $J = 8.1$ Hz, 2 H), 7.11 (dd, $J = 8.5, 0.6$ Hz, 2 H), 4.06-3.97 (m, 2 H), 3.64-3.57 (m, 2 H), 2.87-2.76 (m, 1 H), 2.69-2.63 (m, 2 H), 2.28 (s, 3 H), 1.88-1.80 (m, 2 H). HRMS (ESI) calculated for $[\text{M}+\text{H}]^+/\text{C}_{12}\text{H}_{14}\text{F}_4\text{N}^+$: 248.1057 m/z, found: 248.1062 m/z.

(4a*R*,8a*S*)-6-(3-(2-Fluoro-6-(trifluoromethyl)phenethyl)azetidine-1-carbonyl)hexahydro-2*H*-pyrido[4,3-*b*][1,4]oxazin-3(4*H*)-one (**7**). The procedure described for the synthesis of **4** was applied to **7d** (30.0 mg, 0.08 mmol), DIPEA (0.08 mL, 0.49 mmol), **15** (27.0 mg, 0.08 mmol) in MeCN (2 mL). The crude was purified by preparative HPLC (column: phenomenex Luna C18 150 × 25 mm, 10 μm, mobile phase: A/B = 0.225% formic acid in water/acetonitrile, condition: 25 mL/min, A/B from 62/38 to 32/68) and then lyophilized to give the desired product as a yellow gum (20 mg, 56%). ¹H NMR (600 MHz, Chloroform-*d*) δ 7.44 (d, *J* = 7.9 Hz, 1H), 7.30 (td, *J* = 7.7, 5.8 Hz, 1H), 7.25-7.19 (m, 1H), 6.22 (br s, 1H, -NHCO-), 4.32-4.26 (m, 1H), 4.22-4.17 (m, 1H), 4.11 (t, *J* = 8.3 Hz, 1H), 4.06 (t, *J* = 8.3 Hz, 1H), 3.97 (br d, *J* = 2.6 Hz, 1H), 3.89 (br dd, *J* = 13.1, 4.6 Hz, 1H), 3.67 (dd, *J* = 8.2, 5.9 Hz, 1H), 3.62 (dd, *J* = 8.2, 5.8 Hz, 1H), 3.53-3.45 (m, 1H), 3.43–3.37 (m, 1H), 3.12-3.00 (m, 2H), 2.77-2.68 (m, 2H), 2.67-2.58 (m, 1H), 1.92 (br d, *J* = 6.3 Hz, 1H), 1.99-1.86 (m, 2H), 1.84-1.74 (m, 1H). ¹³C NMR (151 MHz, Chloroform-*d*) δ 168.29, 162.28, 161.69 (d, *J*_{C-F} = 246.1 Hz), 130.42 (q, *J*_{C-F} = 30.1 Hz), 127.91, 127.73, 123.89 (q, *J*_{C-F} = 273.6 Hz), 121.83, 119.00 (d, *J*_{C-F} = 23.3 Hz), 69.50, 67.67, 56.58, 56.52, 49.61, 46.18, 39.70, 34.88, 29.59, 23.47. HRMS (ESI) calculated for [M+H]⁺/C₂₀H₂₄F₄N₃O₃⁺: 430.1748 m/z, found: 430.1751 m/z.

tert-Butyl 3-((3-(trifluoromethyl)phenyl)ethynyl)azetidine-1-carboxylate (**8b**). To a mixture of **8a** (200 mg, 1.10 mmol) and 3-iodobenzotrifluoride (302 mg, 1.11 mmol) in MeCN (2 mL) was added copper (I) iodide (22.9 mg, 0.12 mmol), [Pd(PPh₃)₂Cl₂] (150 mg, 0.21 mmol) and triethylamine (0.40 mL, 2.87 mmol) at 25 °C. The mixture was stirred at 80 °C for 12 h under N₂. The mixture was added brine (30 mL) and extracted with ethyl acetate (30 mL). The organic layer was dried over Na₂SO₄, filtered and concentrated *in vacuo*. The residue was purified by flash column (SiO₂, petroleum ether : ethyl acetate = 20:1 to 5:1) to give the desired product as a colorless oil (77 mg, 18%). ¹H NMR (400 MHz, Methanol-*d*₄) δ 7.76-7.64 (m, 3H), 7.61-7.52 (m, 1H), 4.34-4.20 (m, 2H), 4.09-3.95 (m, 2H), 3.81-3.58 (m, 1H), 1.47 (s, 9H). LC-MS (ESI): m/z = 269.9 [M-*t*Bu+H]⁺.

tert-Butyl 3-(3-(trifluoromethyl)phenethyl)azetidine-1-carboxylate (**8c**). The procedure described for the synthesis of **4c** was applied to **8b** (72.0 mg, 0.22 mmol) and 10% Pd/C (30.0 mg, 0.03 mmol) in methanol (2 mL) to give the desired product as a colorless oil (55 mg, 70%). ¹H NMR (400 MHz, Methanol-*d*₄) δ 7.61-7.40 (m, 4H), 4.09-3.82 (m, 2H), 3.67–3.47 (m, 2H), 2.82-2.64 (m, 2H), 2.62-2.48 (m, 1H), 1.95 (q, *J* = 7.7 Hz, 2H), 1.44 (s, 9H). LC-MS (ESI): m/z = 274.3 [M-*t*Bu+H]⁺.

3-(3-(Trifluoromethyl)phenethyl)azetidine 2,2,2-trifluoroacetate (**8d**). The procedure described for the synthesis of **4d** was applied to **8c** (50.0 mg, 0.15 mmol) and

trifluoroacetic acid (0.08 mL, 1.08 mmol) in 1 mL DCM to obtain a crude product, which was directly applied in the next step without any further purification. LC-MS (ESI): $m/z = 230.0 [M+H]^+$.

(4*aR*,8*aS*)-6-(3-(3-(Trifluoromethyl)phenethyl)azetidine-1-carbonyl)hexahydro-2*H*-pyrido[4,3-*b*][1,4]oxazin-3(4*H*)-one (**8**). The procedure described for the synthesis of **4** was applied to **15** (46.8 mg, 0.15 mmol), **8d** (50.0 mg, 0.15 mmol) and DIPEA (0.15 mL, 0.85 mmol) in MeCN (2 mL). The crude was purified by preparative HPLC (column: Phenomenex Synergi C18 150 × 25 mm, 10 μm, mobile phase: A/B = 0.1%TFA in water/acetonitrile, condition: 27 mL/min, A/B from 63/37 to 23/67) and then lyophilized to give the desired product as a colorless oil (28 mg, 47%). ¹H NMR (400 MHz, DMSO-*d*₆) δ 8.14 (d, *J* = 4.3 Hz, 1H), 7.59 (s, 1H), 7.57-7.51 (m, 2H), 4.05 (d, *J* = 3.7 Hz, 2H), 4.02-3.90 (m, 3H), 3.72 (dd, *J* = 13.0, 5.1 Hz, 1H), 3.61-3.53 (m, 4H, overlapped with solvent peak), 3.25-3.14 (m, 1H), 2.89-2.73 (m, 2H), 2.70-2.58 (m, 2H), 1.90-1.81 (m, 2H), 1.78-1.68 (m, 2H). HRMS (ESI) calculated for $[M+H]^+/C_{20}H_{25}F_3N_3O_3^+$: 412.1843 m/z , found: 412.1850 m/z .

tert-Butyl 3-((2-(trifluoromethyl)phenyl)ethynyl)azetidine-1-carboxylate (**13b**). The procedure described for the synthesis of **8b** was applied to **13a** (151 mg, 0.56 mmol), *tert*-butyl 3-ethynylazetidine-1-carboxylate (100 mg, 0.55 mmol), copper(I) iodide (11.4 mg, 0.06 mmol), [Pd(PPh₃)₂Cl₂] (75.0 mg, 0.11 mmol) and trimethylamine (0.2 mL, 1.43 mmol) in MeCN (2 mL) to give the desired product as an off-white solid (110 mg, 59% yield). ¹H NMR (400 MHz, DMSO-*d*₆) δ 7.79-7.68 (m, 3H), 7.61-7.57 (m, 1H), 4.22-4.18 (m, 2H), 3.85-3.82 (m, 2H), 3.74-3.69 (m, 1H), 1.39 (s, 9H). LC-MS (ESI): $m/z = 269.9 [M-tBu+H]^+$.

tert-Butyl 3-(2-(trifluoromethyl)phenethyl)azetidine-1-carboxylate (**13c**). The procedure described for the synthesis of **4c** was applied to **13b** (97.0 mg, 0.30 mmol) and 10% Pd/C (30.0 mg, 0.03 mmol) in methanol (2 mL) to give the desired product as a colorless oil (68 mg, 59% yield). ¹H NMR (400 MHz, Methanol-*d*₄) δ 7.65 (d, *J* = 7.9 Hz, 1H), 7.60-7.54 (m, 1H), 7.46 (d, *J* = 7.7 Hz, 1H), 7.38 (t, *J* = 7.7 Hz, 1H), 4.08–3.96 (m, 2H), 3.61-3.48 (m, 2H), 2.87-2.70 (m, 2H), 2.70-2.55 (m, 1H), 2.06-1.82 (m, 2H), 1.45 (s, 9H). LC-MS (ESI): $m/z = 274.4 [M-tBu+H]^+$.

3-(2-(Trifluoromethyl)phenethyl)azetidine 2,2,2-trifluoroacetate (**13d**). The procedure described for the synthesis of **4d** was applied to **13c** (60.0 mg, 0.18 mmol) and trifluoroacetic acid (0.10 mL, 1.30 mmol) in 1 mL DCM. A crude product was obtained

and directly applied in the next step without any further purification. LC-MS (ESI): $m/z = 230.0$ $[M+H]^+$.

(4*aR*,8*aS*)-6-(3-(2-(Trifluoromethyl)phenethyl)azetidine-1-carbonyl)hexahydro-2*H*-pyrido[4,3-*b*][1,4]oxazin-3(4*H*)-one (**13**). The procedure described for the synthesis of **4** was applied to **15** (46.8 mg, 0.15 mmol), **13d** (50.0 mg, 0.15 mmol) and DIPEA (0.15 mL, 0.85 mmol) in MeCN (2 mL). The crude was purified by preparative HPLC (column: Phenomenex Synergi C18 150 × 25 mm, 10 μm, mobile phase: A/B = 0.1%TFA in water/acetonitrile, condition: 27 mL/min, A/B from 64/36 to 24/66) and then lyophilized to give the desired product as a colorless oil (30 mg, 49% yield). ¹H NMR (600 MHz, Chloroform-*d*) δ 7.62 (d, *J* = 7.6 Hz, 1H), 7.50-7.44 (m, 1H), 7.30 (d, *J* = 7.8 Hz, 1H), 7.30-7.28 (m, 1H), 6.21 (br d, *J* = 3.0 Hz, 1H, -NHCO-), 4.35-4.26 (m, 1H), 4.22-4.16 (m, 1H), 4.10 (t, *J* = 8.3 Hz, 1H), 3.97 (br d, *J* = 2.8 Hz, 1H), 3.88 (dd, *J* = 13.1, 4.9 Hz, 1H), 3.65 (dd, *J* = 8.3, 5.8 Hz, 1H), 3.60 (dd, *J* = 8.3, 5.8 Hz, 1H), 3.51-3.45 (m, 1H), 3.42-3.36 (m, 1H), 3.02-3.11 (m, 2H), 2.75-2.70 (m, 2H), 2.64-2.58 (m, 1H), 1.95-1.88 (m, 3H), 1.84-1.75 (m, 2H). ¹³C NMR (151 MHz, Chloroform-*d*) δ 168.67, 162.64, 140.46, 132.19, 131.30, 128.74 (q, *J*_{C-F} = 29.7 Hz), 126.55, 126.41 (q, *J*_{C-F} = 5.7 Hz), 124.94 (q, *J*_{C-F} = 273.8 Hz), 69.84, 67.99, 56.97, 49.95, 46.52, 40.06, 36.80, 30.43, 29.92, 29.58. HRMS (ESI) calculated for $[M+H]^+/C_{20}H_{25}F_3N_3O_3^+$: 412.1843 m/z , found: 412.1847 m/z .

Procedure C. Diethyl (2-fluoro-4-(trifluoromethyl)benzyl)phosphonate (**5b**). To an ice-cold solution of **5a** (530 mg, 2.73 mmol) in triethyl phosphite (1.17 mL, 6.82 mmol) was added iodine (693 mg, 2.73 mmol). After stirring at room temperature overnight, the crude was purified by silica gel chromatography on a 80 g column using a medium pressure liquid chromatography (MPLC) system eluting with a gradient of *n*-heptane : ethyl acetate (100 : 0 to 0 : 100) to get the desired compound as a colorless oil (85 mg, 10%). ¹H NMR (300 MHz, Chloroform-*d*) δ 7.56-7.47 (m, 1H), 7.42-7.30 (m, 2H), 4.18-3.99 (m, 4H), 3.24 (d, *J* = 22.0 Hz, 2H), 1.28 (t, *J* = 7.0 Hz, 6H). LC-MS (ESI): $m/z = 315.2$ $[M+H]^+$.

tert-Butyl 3-(2-fluoro-4-(trifluoromethyl)styryl)azetidine-1-carboxylate (**5c**). To an ice-cold solution of **5b** (160 mg, 0.51 mmol) in THF (1 mL), sodium hydride (55% in mineral oil, 22.2 mg, 0.51 mmol) was added. After stirring at 0 °C for 30 minutes, *tert*-butyl 3-formylazetidine-1-carboxylate (94.3 mg, 0.51 mmol) in THF (0.5 mL) was added to the mixture dropwise. The reaction was stirred at room temperature overnight. A mixture of H₂O/ethyl acetate was added to quench the reaction. The organic layer was separated, washed once with brine, and dried over MgSO₄. After filtration, the solvent was evaporated. The compound was purified by silica gel chromatography on a 4 g column

using an MPLC system eluting with a gradient of *n*-heptane/ethyl acetate (100 : 0 to 50 : 50) to get the desired compound as a colorless oil (123 mg, 70%). ¹H NMR (300 MHz, DMSO-*d*₆) δ 7.95-7.81 (m, 1H), 7.66 (d, *J* = 10.8 Hz, 1H), 7.56 (d, *J* = 8.2 Hz, 1H), 6.91-6.75 (m, 1H), 6.69-6.51 (m, 1H), 4.11-4.01 (m, 2H), 3.83-3.73 (m, 2H), 3.56-3.40 (m, 1H), 1.39 (s, 9H). MS (ESI): *m/z* = 290.1 [M-*t*Bu+H]⁺.

tert-Butyl 3-(2-fluoro-4-(trifluoromethyl)phenethyl)azetidone-1-carboxylate (**5d**). To a solution of **5c** (120 mg, 0.35 mmol) in EtOAc (1 mL) and MeOH (1 mL), 10% Pd/C (12.0 mg, 0.01 mmol) was added. The mixture was stirred under a hydrogen atmosphere at room temperature for 30 minutes. The suspension was filtered to get the desired compound as a colorless oil (111 mg, 92%). ¹H NMR (300 MHz, DMSO-*d*₆) δ 7.65-7.44 (m, 3H), 3.94-3.78 (m, 2H), 3.50-3.41 (m, 2H), 2.74-2.57 (m, 2H), 2.45-2.31 (m, 1H), 1.83 (q, *J* = 7.7 Hz, 2H), 1.36 (s, 9H). MS (ESI): *m/z* = 292.2 [M-*t*Bu+H]⁺.

3-(2-Fluoro-4-(trifluoromethyl)phenethyl)azetidone 4-methylbenzenesulfonate (**5e**). To a solution of **5d** (111 mg, 0.32 mmol) in EtOAc (1.20 mL), 4-methylbenzenesulfonic acid monohydrate (66.0 mg, 0.38 mmol) was added. The mixture was heated at reflux for 1 h. The clear, colorless solution was allowed to cool down to room temperature. The suspension was filtered, and washed with a small volume of EtOAc to get a crude product as a colorless solid, which was used in the next step without any further purification. MS (ESI): *m/z* = 248.2 [M-TsOH+H]⁺.

(4*aR*,8*aS*)-6-(3-(2-Fluoro-4-(trifluoromethyl)phenethyl)azetidone-1-carbonyl)hexahydro-2*H*-pyrido[4,3-*b*][1,4]oxazin-3(4*H*)-one (**5**). The procedure described for the synthesis of **1** was applied to **15** (45.0 mg, 0.14 mmol), DIPEA (73.4 μL, 0.42 mmol) and **5e** (58.7 mg, 0.14 mmol) to yield the desired product as a colorless solid (50 mg, 83%). ¹H NMR (600 MHz, Chloroform-*d*) δ 7.48-7.45 (m, 1H), 7.39-7.34 (m, 1H), 7.16 (t, *J* = 7.7 Hz, 1H), 6.30 (br d, *J* = 3.0 Hz, 1H, -NHCO-), 4.32-4.28 (m, 1H), 4.21-4.17 (m, 1H), 4.09 (t, *J* = 8.3 Hz, 1H), 4.02 (t, *J* = 8.3 Hz, 1H), 3.96 (s, 1H), 3.88 (dd, *J* = 13.0, 4.9 Hz, 1H), 3.65 (dd, *J* = 8.3, 5.9 Hz, 1H), 3.59 (dd, *J* = 8.2, 5.9 Hz, 1H), 3.49-3.45 (m, 1H), 3.42-3.37 (m, 1H), 3.14-2.99 (m, 2H), 2.66 (t, *J* = 7.6 Hz, 2H), 2.60-2.55 (m, 1H), 1.95-1.90 (m, 3H), 1.81-1.75 (m, 1H). ¹³C NMR (151 MHz, Chloroform-*d*) δ 168.37, 162.29, 157.99 (d, *J*_{C-F} = 254.6 Hz), 134.47 (d, *J*_{C-F} = 5.4 Hz), 129.85 (d, *J*_{C-F} = 15.4 Hz), 125.16 (q, *J*_{C-F} = 4.4 Hz), 123.95 (d, *J*_{C-F} = 4.4 Hz), 122.71 (q, *J*_{C-F} = 272.3 Hz), 118.50, 69.48, 67.66, 56.57, 49.58, 46.17, 39.74, 34.72, 29.59, 28.94, 26.32. HRMS (ESI) calculated for [M+H]⁺/C₂₀H₂₄F₄N₃O₃⁺: 430.1748 *m/z*, found: 430.1753 *m/z*.

Procedure D. (2-Fluoro-6-methoxybenzyl)triphenylphosphonium (**9b**). A solution of **9a** (202 mg, 0.93 mmol) and triphenylphosphine (242 mg, 0.92 mmol) in toluene (5 mL) was heated under reflux to 85 °C whilst vigorously stirring for 16 h. After the reaction mixture was cooled down to room temperature, the resulting precipitate was collected by vacuum filtration and washed with toluene and hexane. The residue was resolved in chloroform and dried *in vacuo* to obtain the title compound as a white foamy solid (449 mg, 100 %). ¹H NMR (400 MHz, Chloroform-*d*) δ 7.83-7.74 (m, 3H), 7.73-7.58 (m, 12H), 7.18-7.07 (m, 1H), 6.87 (d, *J* = 7.6 Hz, 1H), 6.64 (t, *J* = 9.0 Hz, 1H), 5.30 (dd, *J* = 13.9, 2.0 Hz, 2H), 2.06 (s, 3H). ¹³C NMR (101 MHz, CDCl₃) δ 141.81, 135.48, 134.68 (d, *J*_{C-P} = 10.9 Hz), 130.54, 130.40, 127.15, 118.56, 117.71, 113.31, 113.09, 24.59 (d, *J*_{C-P} = 48.3 Hz), 20.93. ¹⁹F NMR (376 MHz, Chloroform-*d*) δ -110.94. ³¹P NMR (162 MHz, Chloroform-*d*) δ 21.22. HRMS (ESI) calculated for [M+H]⁺/C₂₆H₂₃FP⁺: 385.1516 m/z, found: 385.1517 m/z.

tert-Butyl 3-(2-fluoro-6-methoxystyryl)azetidide-1-carboxylate (**9c**). Compound **9b** (421 mg, 1.05 mmol) was added into a dry reaction vessel that was subsequently evacuated and refilled with nitrogen three times. After the compound was dissolved in anhydrous DCM (6 mL), 1 M sodium bis(trimethylsilyl)amide in THF (1.1 mL) was added at 0 °C and stirred for 30 min. *tert*-Butyl 3-formylazetidide-1-carboxylate (168 mg, 0.91 mmol) was added dropwise to the solution, and then the reaction mixture was stirred at room temperature for 17 h. The solvent was removed *in vacuo*, and the residue was suspended in a mixture of ethyl acetate / saturated NaHCO₃ (*v/v* = 1/1, total volume: 40 mL) and extracted with ethyl acetate (30 mL × 3). The combined organic phases were washed with saturated NaCl solution (140 mL) and dried over MgSO₄. After filtration and evaporation, the crude was purified by column chromatography (SiO₂, petroleum ether: ethyl acetate = 10:1 to 5:1) to obtain the desired product as a clear yellow oil (94 mg, 34 %). ¹H NMR (400 MHz, Chloroform-*d*) δ 7.24-7.16 and 7.16-7.08 (m, 1H), 6.73-6.70 and 6.70-6.51 (m overlapped, 2H), 6.70-6.51 and 6.26-6.04 (m overlapped, 2H), 4.16 and 4.09 (t, *J* = 8.5 Hz, 2H), 3.86 and 3.82 (s overlapped, 3H), 3.84 and 3.73 (dd overlapped, *J* = 8.6, 5.7 Hz, 2H), 3.42-3.29 and 3.26-3.14 (m, 1H), 1.45 and 1.43 (s, 9H). ¹⁹F NMR (376 MHz, Chloroform-*d*) δ -113.06 and -114.48. HRMS (ESI) calculated for [M+Na]⁺/C₁₇H₂₂FNNaO₃⁺: 330.1476 m/z, found: 330.1476 m/z.

tert-Butyl 3-(2-fluoro-6-methoxyphenethyl)azetidide-1-carboxylate (**9d**). The procedure described for the synthesis of **4c** was applied to **9c** (184 mg, 0.60 mmol) and 10% Pd/C (28.5 mg, 0.03 mmol) in methanol (5 mL) to obtain the desired product as a clear colorless oil (112 mg, 60 %). ¹H NMR (400 MHz, Chloroform-*d*) δ 7.15-7.05 (m, 1H), 6.69-6.59 (m, 2H), 3.95 (t, *J* = 8.3 Hz, 2H), 3.81 (s, 3H), 3.53 (dd, *J* = 8.5, 5.5 Hz, 2H),

2.65-2.56 (m, 2H), 2.53-2.37 (m, 1H), 1.81 (q, $J = 7.5$ Hz, 2H), 1.43 (s, 9H). ^{19}F NMR (376 MHz, Chloroform- d) δ -117.96. HRMS (ESI) calculated for $[\text{M}+\text{Na}]^+/\text{C}_{17}\text{H}_{24}\text{FNNaO}_3^+$: 332.1632 m/z , found: 332.1631 m/z .

3-(2-Fluoro-6-methoxyphenethyl)azetidine 2,2,2-trifluoroacetate (**9e**) The procedure described for the synthesis of **4d** was applied to **9d** (110 mg, 0.36 mmol) and trifluoroacetic acid (0.30 mL, 4.27 mmol) to give a crude product, which was directly applied to the next step. LC-MS (ESI): $m/z = 210$ $[\text{M}+\text{H}]^+$.

(4a*R*,8a*S*)-6-(3-(2-Fluoro-6-methoxyphenethyl)azetidine-1-carbonyl)hexahydro-2*H*-pyrido[4,3-*b*][1,4]oxazin-3(4*H*)-one (**9**). The procedure described for the synthesis of **4** was applied to **15** (28.0 mg, 0.09 mmol), **9e** (30.0 mg, 0.09 mmol) and DIPEA (0.10 mL, 0.57 mmol) in MeCN (2 mL). The crude was purified by preparative HPLC (column: Phenomenex Luna C18 150 \times 25 mm, 10 μm , mobile phase: A/B = 0.1% TFA in water/acetonitrile, condition: 25 mL/min, A/B from 71/29 to 41/59) and then lyophilized to give the desired product as a colorless oil (17 mg, 44% yield). ^1H NMR (600 MHz, Chloroform- d) δ 7.12 (td, $J = 8.3, 6.8$ Hz, 1H), 6.71-6.59 (m, 2H), 6.05 (br d, $J = 2.5$ Hz, 1H, -NHCO-), 4.32-4.28 (m, 1H), 4.21-4.18 (m, 1H), 4.05 (t, $J = 8.3$ Hz, 1H), 3.99 (t, $J = 8.3$ Hz, 1H), 3.97 (br d, $J = 2.8$ Hz, 1H), 3.89-3.85 (m, 1H), 3.82 (s, 3H), 3.63 (dd, $J = 8.2, 6.0$ Hz, 1H), 3.58 (dd, $J = 8.3, 5.9$ Hz, 1H), 3.51-3.46 (m, 1H), 3.42-3.37 (m, 1H), 3.11-3.01 (m, 2H), 2.64-2.60 (m, 2H), 2.55-2.51 (m, 1H), 1.93-1.89 (m, 1H), 1.85-1.81 (m, 2H), 1.80-1.76 (m, 1H). ^{13}C NMR (151 MHz, Chloroform- d) δ 168.28, 162.32, 161.60 (d, $J_{\text{C-F}} = 242.5$ Hz), 158.59, 127.29 (d, $J_{\text{C-F}} = 10.7$ Hz), 116.92 (d, $J_{\text{C-F}} = 18.7$ Hz), 107.76 (d, $J_{\text{C-F}} = 23.3$ Hz), 105.95, 69.53, 67.65, 56.85, 55.81, 49.64, 46.18, 39.68, 33.81, 29.56, 29.07, 19.87. HRMS (ESI) calculated for $[\text{M}+\text{H}]^+/\text{C}_{20}\text{H}_{27}\text{FN}_3\text{O}_4^+$: 392.1980 m/z , found: 392.1983 m/z .

(2-Fluoro-6-methylbenzyl)triphenylphosphonium (**10b**). The procedure described for the synthesis of **9b** was applied to **10a** (200 mg, 0.98 mmol) and triphenylphosphine (260 mg, 0.98 mmol) in toluene (5 mL) to obtain the desired product as a foamy white solid (243 mg, 65 %). ^1H NMR (400 MHz, Chloroform- d): δ 7.87-7.76 (m, 3H), 7.71-7.57 (m, 12H), 7.25-7.18 (m, 1H), 6.57 (t, $J = 8.4$ Hz, 1H), 6.49 (d, $J = 8.4$ Hz, 1H), 4.85 (d, $J = 13.6$ Hz, 2H), 3.38 (s, 3H). ^{13}C NMR (100 MHz, Chloroform- d) δ 135.58, 134.31 (d, $J_{\text{C-P}} = 10.7$ Hz), 131.51, 131.40, 130.49 (d, $J_{\text{C-P}} = 13.5$ Hz), 118.46, 117.61, 108.53, 108.32, 107.00, 56.14, 21.36 (d, $J_{\text{C-P}} = 51.6$ Hz). ^{19}F NMR (376 MHz, Chloroform- d) δ -111.94. ^{31}P NMR (162 MHz, Chloroform- d) δ 21.17. HRMS (ESI): Calculated for $[\text{M}+\text{H}]^+/\text{C}_{26}\text{H}_{23}\text{FOP}^+$: 401.1465 m/z , found: 401.1465 m/z .

tert-Butyl 3-(2-fluoro-6-methylstyryl)azetidine-1-carboxylate (**10c**). Compound **10c** was synthesized by following the procedure for compound **9c** using **10b** (400 mg, 1.04 mmol), *tert*-butyl 3-formylazetidine-1-carboxylate (173 mg, 0.94 mmol) and 1 M sodium bis(trimethylsilyl)amide (1.14 mL, 1.14 mmol). The desired product was obtained as a yellow oil (233 mg, 39 %). ¹H NMR (400 MHz, Chloroform-*d*): δ 7.17-7.02 (m, 1H), 6.99-6.84 (m, 2H), 6.47-6.30 and 6.24-6.06 (m, 2H), 4.18 and 4.07 (t, *J* = 8.6 Hz, 2H), 3.84 and 3.72 (dd, *J* = 8.6, 5.9 Hz, 2H), 3.44-3.30 and 3.21-3.07 (m, 1H), 2.34 and 2.21 (s, 3H), 1.45 and 1.43 (s, 9H). ¹⁹F NMR (376 MHz, Chloroform-*d*) δ -114.62 and -115.24. HRMS (ESI): Calculated for [M+Na]⁺/C₁₇H₂₂FNNaO₂⁺: 314.1527 m/z, found: 314.1527 m/z.

tert-Butyl 3-(2-fluoro-6-methylphenethyl)azetidine-1-carboxylate (**10d**). The procedure described for the synthesis of **4c** was applied to **10c** (377 mg, 1.30 mmol) and 10% Pd/C (60.6 mg, 0.06 mmol) in methanol (5 mL) to obtain the title compound as yellow oil (370 mg, 98 %). ¹H NMR (400 MHz, Chloroform-*d*) δ 7.11-7.01 (m, 1H), 6.92 (d, *J* = 7.5 Hz, 1H), 6.90-6.81 (m, 1H), 4.00 (t, *J* = 8.5 Hz, 2H), 3.54 (dd, *J* = 8.6, 5.5 Hz, 2H), 2.65-2.56 (m, 2H), 2.57-2.43 (m, 1H), 2.31 (s, 3H), 1.87-1.76 (m, 2H), 1.43 (s, 9H). ¹³C NMR (101 MHz, Chloroform-*d*) δ 161.71 (d, *J*_{C-F} = 243.1 Hz), 156.75, 138.63, 127.28 (d, *J*_{C-F} = 10.5 Hz), 127.05, 126.09, 113.06 (d, *J*_{C-F} = 23.8 Hz), 79.55, 54.76, 34.27, 29.00, 28.77, 23.35, 19.39. ¹⁹F NMR (376 MHz, Chloroform-*d*) δ -118.77. HRMS (ESI) calculated for [M+Na]⁺/C₁₇H₂₄FNNaO₂⁺: 316.1683 m/z, found: 316.1682 m/z.

3-(2-Fluoro-6-methylphenethyl)azetidine 2,2,2-trifluoroacetate (**10e**). The procedure described for the synthesis of **4d** was applied to **10d** (100 mg, 0.341 mmol) and trifluoroacetic acid (0.30 mL, 4.09 mmol) to give a crude product, which was directly applied in the next step. LC-MS (ESI): m/z = 194 [M+H]⁺.

(4*aR*,8*aS*)-6-(3-(2-Fluoro-6-methylphenethyl)azetidine-1-carbonyl)hexahydro-2*H*-pyrido[4,3-*b*][1,4]oxazin-3(4*H*)-one (**10**). The procedure described for the synthesis of **4** was applied to **15** (32 mg, 0.10 mmol), **10e** (30.0 mg, 0.10 mmol) and DIPEA (0.10 mL, 0.57 mmol) in MeCN (2 mL). The crude was purified by preparative HPLC (column: Unisil 3-100 C18 Ultra 150 × 50 mm, 3 μm, mobile phase: A/B = 0.225% formic acid in water/acetonitrile, condition: 25 mL/min, A/B from 65/35 to 45/55) and then lyophilized to the desired product as a colorless oil (16 mg, 44% yield). ¹H NMR (600 MHz, Chloroform-*d*) δ 7.12-7.01 (m, 1H), 6.93 (d, *J* = 7.6 Hz, 1H), 6.86 (t, *J* = 8.9 Hz, 1H), 6.01 (br d, *J* = 0.8 Hz, 1H, -NHCO-), 4.36-4.27 (m, 1H), 4.23-4.14 (m, 1H), 4.08 (t, *J* = 8.3 Hz, 1H), 4.03 (t, *J* = 8.2 Hz, 1H), 3.97 (br d, *J* = 2.6 Hz, 1H), 3.87 (br dd, *J* = 13.0, 4.5 Hz, 1H), 3.64 (dd, *J* = 8.2, 5.9 Hz, 1H), 3.58 (dd, *J* = 8.2, 5.9 Hz, 1H), 3.52-3.45 (m, 1H),

3.43-3.37 (m, 1H), 3.14-2.90 (m, 2H), 2.68-2.39 (m, 3H), 2.32 (s, 3H), 1.91 (dd, $J = 14.4$, 2.7 Hz, 1H), 1.85-1.71 (m, 3H). ^{13}C NMR (151 MHz, Chloroform- d) δ 168.20, 162.14, 161.42 (d, $J_{\text{C-F}} = 267.6$ Hz), 138.31, 127.00, 126.65, 125.78, 112.71 (d, $J_{\text{C-F}} = 23.4$ Hz), 69.52, 67.68, 56.76, 49.64, 46.18, 39.69, 33.98, 29.57, 29.18, 22.96, 19.06. HRMS (ESI) calculated for $[\text{M}+\text{H}]^+/\text{C}_{20}\text{H}_{27}\text{FN}_3\text{O}_3^+$: 376.2031 m/z, found: 376.2037 m/z.

(2,6-Difluorobenzyl)triphenylphosphonium (**11b**). The procedure described for the synthesis of **9b** was applied to **11a** (100 mg, 0.49 mmol) and triphenylphosphine (127 mg, 0.49 mmol) in toluene (5 mL) to obtain the desired product as a white solid (150 mg, 78 %). ^1H NMR (400 MHz, Chloroform- d): δ 7.84-7.71 (m, 9H), 7.70-7.60 (m, 6H), 7.25-7.20 (m, 1H), 6.78-6.67 (m, 2H), 5.31 (d, $J = 14.0$ Hz, 2H). ^{13}C NMR (101 MHz, Chloroform- d) δ 135.63, 134.45 (d, $J_{\text{C-P}} = 10.7$ Hz), 131.42, 130.57 (d, $J_{\text{C-P}} = 13.9$ Hz), 118.15, 117.31, 112.21, 111.98, 21.49 (d, $J_{\text{C-P}} = 51.3$ Hz). ^{19}F NMR (376 MHz, Chloroform- d) δ -108.88. ^{31}P NMR (162 MHz, CDCl_3) δ 22.24. HRMS (ESI): Calculated for $[\text{M}+\text{H}]^+/\text{C}_{25}\text{H}_{20}\text{F}_2\text{P}^+$: 389.1265 m/z, found: 389.1270 m/z.

tert-Butyl 3-(2,6-difluorostyryl)azetidine-1-carboxylate (**11c**). Compound **11c** was synthesized by following the procedure for compound **9c** using **11b** (700 mg, 1.80 mmol), *tert*-butyl 3-formylazetidine-1-carboxylate (333.2 mg, 1.799 mmol) and 1 M sodium bis(trimethylsilyl)amide (2.16 mL, 2.16 mmol). The desired product was obtained as a yellow oil (413 mg, 72 %). ^1H NMR (400 MHz, Chloroform- d) δ 7.25-7.18 and 7.18-7.07 (m, 1H), 6.92-6.82 and 6.89-6.84 (m overlapped, 2H), 6.70 and 6.16 (dd overlapped, $J = 16.2$, 8.4 Hz, 1H), 6.44 and 6.22 (d overlapped, $J = 16.2$ Hz, 1H), 4.17 and 4.12 (t, $J = 8.5$ Hz, 2H), 3.84 and 3.74 (dd, $J = 8.6$, 5.9 Hz, 2H), 3.43-3.29 and 3.29-3.15 (m, 1H), 1.45 and 1.43 (s, 9H). ^{19}F NMR (376 MHz, Chloroform- d) δ -111.79 and -113.56. HRMS (ESI): Calculated for $[\text{M}+\text{Na}]^+/\text{C}_{16}\text{H}_{19}\text{F}_2\text{NNaO}_2^+$: 318.1276 m/z, found: 318.1276 m/z.

tert-Butyl 3-(2,6-difluorophenethyl)azetidine-1-carboxylate (**11d**). The procedure described for the synthesis of **4c** was applied to **11c** (413 mg, 1.40 mmol) and 10% Pd/C (65.6 mg, 0.06 mmol) in methanol (5 mL) to obtain the desired product as a colorless oil (350 mg, 84%). ^1H NMR (400 MHz, Chloroform- d) δ 7.19-7.08 (m, 1H), 6.89-6.78 (m, 2H), 3.98 (t, $J = 8.4$ Hz, 2H), 3.54 (dd, $J = 8.6$, 5.5 Hz, 2H), 2.64 (t, $J = 7.0$ Hz, 2H), 2.54-2.42 (m, 1H), 1.87 (q, $J = 7.6$ Hz, 2H), 1.43 (s, 9H). ^{13}C NMR (100 MHz, Chloroform- d) δ 161.89 (d, $J_{\text{C-F}} = 247.5$ Hz), 161.79 (d, $J_{\text{C-F}} = 247.4$ Hz), 156.71, 127.92 (t, $J_{\text{C-F}} = 10.7$ Hz), 117.12 (t, $J_{\text{C-F}} = 20.6$ Hz), 111.38 (d, $J_{\text{C-F}} = 28.6$ Hz), 79.53, 54.65, 34.24, 28.37, 20.06. ^{19}F NMR (376 MHz, Chloroform- d) δ -116.32. HRMS (ESI): Calculated for $[\text{M}+\text{Na}]^+/\text{C}_{16}\text{H}_{21}\text{F}_2\text{NNaO}_2^+$: 320.1433 m/z, found: 320.1436 m/z.

3-(2,6-Difluorophenethyl)azetidine 2,2,2-trifluoroacetate (**11e**). The procedure described for the synthesis of **4d** was applied to **11d** (60.0 mg, 0.20 mmol) and trifluoroacetic acid (0.11 mL, 1.44 mmol) to give a crude product, which was directly applied to the next step. LC-MS (ESI): $m/z = 198.5 [M+H]^+$.

(4*aR*,8*aS*)-6-(3-(2,6-Difluorophenethyl)azetidine-1-carbonyl)hexahydro-2*H*-pyrido[4,3-*b*][1,4]oxazin-3(4*H*)-one (**11**). The procedure described for the synthesis of **4** was applied to **15** (43.4 mg, 0.13 mmol), **11e** (42.0 mg, 0.13 mmol) and DIPEA (0.14 mL, 0.79 mmol) in MeCN (2 mL). The crude was purified by preparative HPLC (column: Phenomenex Synergi C18 150 × 25 mm, 10 μm, mobile phase: A/B = 0.1%TFA in water/acetonitrile, condition: 27 mL/min, A/B from 70/30 to 40/60) and then lyophilized to give the desired product as a colorless oil (33 mg, 60% yield). ¹H NMR (400MHz, DMSO-*d*₆) δ 8.14 (d, *J* = 3.8 Hz, 1H, -NHCO-), 7.37-7.26 (m, 1H), 7.12-7.03 (m, 2H), 4.09-4.00 (m, 2H), 3.99-3.94 (m, 1H), 3.92 (d, *J* = 8.2 Hz, 2H), 3.70 (dd, *J*=4.5, 12.6 Hz, 1H), 3.55 (br s, 4H), 3.20 (d, *J* = 8.3 Hz, 1H), 2.85–2.74 (m, 2H), 2.62–2.58 (m, 2H), 1.83-1.70 (m, 4H). HRMS (ESI) calculated for $[M+H]^+/C_{19}H_{24}F_2N_3O_3^+$: 380.1780 m/z , found: 380.1785 m/z .

(2-Fluorobenzyl)triphenylphosphonium (**12b**). The procedure described for the synthesis of **9b** was applied to **12a** (2.00 g, 10.6 mmol) and triphenylphosphine (2.79 g, 10.6 mmol) in toluene (5 mL) to obtain the desired product as white solid (539 mg, 92 %). ¹H NMR (400 MHz, Chloroform-*d*): δ 7.88–7.73 (m, 9H), 7.71-7.63 (m, 6H), 7.61-7.53 (m, 1H), 7.27-7.21 (m, 1H), 7.03 (t, *J* = 7.6 Hz, 1H), 6.88-6.79 (m, 1H), 5.55 (d, *J* = 14.3 Hz, 2H). ¹³C NMR (101 MHz, Chloroform-*d*) δ 135.40, 134.61 (d, *J*_{C-P} = 10.7 Hz), 134.13, 130.89, 130.49 (d, *J*_{C-P} = 14.0 Hz), 125.33, 118.43, 117.58, 115.60 (d, *J*_{C-F} = 23.6 Hz), 24.88 (d, *J*_{C-P} = 49.2 Hz). ¹⁹F NMR (376 MHz, Chloroform-*d*) δ -115.05. ³¹P NMR (162 MHz, Chloroform-*d*) δ 22.93. HRMS (ESI): Calculated for $[M+H]^+/C_{25}H_{21}FP^+$: 371.1359 m/z , found: 371.1361 m/z .

tert-Butyl 3-(2-fluorostyryl)azetidine-1-carboxylate (**12c**). Compound **12c** was synthesized by following the procedure for compound **9c** using **12b** (150 mg, 0.40 mmol), *tert*-butyl 3-formylazetidine-1-carboxylate (75.0 mg, 0.40 mmol) and 1 M sodium bis(trimethylsilyl)amide (0.49 mL, 0.49 mmol). The desired product was obtained as a yellow oil (61 mg, 55 %). ¹H NMR (400 MHz, Chloroform-*d*) δ 7.48-7.39 and 7.28-7.22 (m overlapped, 1H), 7.22-7.16 and 7.12-7.00 (m overlapped, 3H), 6.58 and 6.49 (d overlapped, *J* = 16.0 Hz, 1H), 6.44 and 6.03 (dd overlapped, *J* = 11.3, 9.3 Hz, 1H), 4.17 and 4.13 (t, *J* = 7.6 Hz, 2H), 3.83 and 3.75 (dd, *J* = 8.6, 5.9 Hz, 2H), 3.58-3.43 and 3.43-3.31 (m, 1H), 1.45 and 1.44 (s, 9H). ¹⁹F NMR (376 MHz, Chloroform-*d*) δ -108.87

and -108.88. HRMS (ESI): Calculated for $[M+Na]^+/C_{16}H_{20}FNNaO_2^+$: 300.1370 m/z, found: 300.1375 m/z.

tert-Butyl 3-(2-fluorophenethyl)azetidine-1-carboxylate (**12d**). The procedure described for the synthesis of **4c** was applied to **12c** (61.2 mg, 0.22 mmol) and 10% Pd/C (10.4 mg, 0.01 mmol) in methanol (5 mL) to obtain the title compound as a colorless oil (36 mg, 58%). 1H NMR (400 MHz, Chloroform-*d*) δ 7.23-7.09 (m, 2H), 7.09-6.95 (m, 2H), 3.98 (t, $J = 8.5$ Hz, 2H), 3.54 (dd, $J = 8.6, 5.5$ Hz, 2H), 2.60 (t, $J = 7.5$ Hz, 2H), 2.56-2.42 (m, 1H), 1.95–1.84 (m, 2H), 1.43 (s, 9H). ^{13}C NMR (101 MHz, Chloroform-*d*) δ 161.11 (d, $J_{C-F} = 245.0$ Hz), 156.39, 130.55 (d, $J_{C-F} = 5.7$ Hz), 128.18 (d, $J_{C-F} = 15.8$ Hz), 127.80 (d, $J_{C-F} = 8.7$ Hz), 124.05, 115.28 (d, $J_{C-F} = 22.8$ Hz), 79.19, 54.34, 34.81, 28.42, 26.57. ^{19}F NMR (376 MHz, Chloroform-*d*) δ -119.07. HRMS (ESI): Calculated for $[M+Na]^+/C_{16}H_{22}FNNaO_2^+$: 302.1527 m/z, found: 302.1530 m/z.

3-(2-Fluorophenethyl)azetidine 2,2,2-trifluoroacetate (**12e**). The procedure described for the synthesis of **4d** was applied to **12d** (62.0 mg, 0.22 mmol) and trifluoroacetic acid (0.20 mL, 2.67 mmol) to give a crude product, which was directly applied in the next step. LC-MS (ESI): $m/z = 180 [M+H]^+$.

(4a*R*,8a*S*)-6-(3-(2-Fluorophenethyl)azetidine-1-carbonyl)-hexahydro-2H-pyrido[4,3-*b*][1,4]oxazin-3(4*H*)-one (**12**). Triphosgene (37.4 mg, 0.13 mmol) was filled into a dried reaction vessel under nitrogen protection and dissolved in anhydrous DCM (1 mL) at 0 °C. A mixture of **14** (53.2 mg, 0.34 mmol) and DIPEA (88.8 μ L, 0.51 mmol) in anhydrous DCM (2 mL) was added over a time period of 30 min. The stirring was continued for another 10 min at 0 °C, and a mixture of compound **4d** (94.4 mg, 0.34 mmol) and DIPEA (0.15 mL, 0.88 mmol) in anhydrous DCM (2 mL) was added. Upon completion, the reaction mixture was diluted with saturated $NaHCO_3$ and extracted three times with DCM. The combined organic phases were dried over $MgSO_4$, filtered and the evaporated *in vacuo*. The residue was purified by column chromatography (SiO_2 , DCM: methanol =100:1 to 19:1) to give the desired product as a clear colorless oil (17.3 mg, 14%). 1H NMR (400 MHz, Chloroform-*d*) δ 7.22-7.11 (m, 2H), 7.08-6.97 (m, 2H), 6.52-6.41 (m, 1H, -NHCO-), 4.29 (d, $J = 16.9$ Hz, 1H), 4.18 (d, $J = 16.9$ Hz, 1H), 4.05 (dt, $J = 21.8, 8.3$ Hz, 2H), 3.98-3.94 (m, 1H), 3.92-3.85 (m, 1H), 3.69-3.57 (m, 2H), 3.54-3.45 (m, 1H), 3.44-3.37 (m, 1H), 3.13-2.98 (m, 2H), 2.64-2.57 (m, 3H), 1.94-1.87 (m, 3H), 1.85-1.71 (m, 1H). ^{13}C NMR (101 MHz, Chloroform-*d*) δ 168.71, 162.65, 160.23, 130.89 (d, $J_{C-F} = 6.3$ Hz), 128.42 (d, $J_{C-F} = 15.6$ Hz), 128.19 (d, $J_{C-F} = 8.5$ Hz), 124.44, 115.61 (d, $J_{C-F} = 22.9$ Hz), 69.81, 67.99, 57.01, 49.86, 46.51, 40.01, 35.21, 29.93, 29.29,

26.87. ^{19}F NMR (376 MHz, Chloroform-*d*) δ -119.04. HRMS (ESI): Calculated for $[\text{M}+\text{H}]^+/\text{C}_{19}\text{H}_{25}\text{FN}_3\text{O}_3^+$: 362.1874 m/z, found: 362.1875 m/z.

MAGL IC₅₀ measurement

The IC₅₀ values of compounds were measured using MAGL enzyme as previously described.⁹ The experiments were carried out at least in triplet using mouse or human MAGL.

Metabolism

Microsomal clearance and hepatocyte clearance of the compounds were measured as previously reported.^{24,25}

Microsomal clearance

Commercially available pooled liver microsomes (C57BL/6J mice) were purchased from Corning Incorporated (Woburn, USA). The NADPH generating system consists of 30 mM glucose-6-phosphate disodium salt hydrate, 10 mM NADP, 30 mM MgCl₂·6H₂O and 5 mg/mL glucose-6-phosphate dehydrogenase (Roche Diagnostics) in 0.1 M potassium phosphate buffer (pH = 7.4). The test compound was incubated at 1 μM with microsome concentrations of 0.5 mg/mL plus the cofactor NADPH in 96-well plates at 37 °C on TECAN (Tecan Group Ltd, Switzerland) equipped with Te-Shake shakers (Tecan Freedom EVO, Te-shake, orbital shaker silver) and a warming device (Tecan Group Ltd, Switzerland) at a shaking speed of 600 rpm and at 37 °C. At 1, 3, 6, 9, 15, 25, 35, and 45 min post-incubation, 40 μL solution was transferred and quenched with 120 μL acetonitrile containing 2-(8-aminotetralin-5-yl)-1,1,1,3,3,3-hexafluoro-propan-2-ol as an internal standard. Samples were then cooled and centrifuged before analysis by LC-MS/MS. Log peak area ratios (test compound/internal standard) are plotted against incubation time using a linear fit. The calculated slope is used to determine the intrinsic clearance, and expressed as μL per min per mg protein.

Hepatocyte Clearance

Pooled hepatocytes were purchased from BioreclamationIVT (NY, USA), and the cell culture medium was William's media supplemented with glutamine, antibiotics, insulin, dexamethasone and 10% fetal bovine serum. 96-well plates (Nunc Natural, 267245) are used for suspension cultures. The compound was tested at 1 μM concentration in suspension cultures of 1 million cell/mL (approx. 1 mg/mL protein concentration). The 96-well plates were incubated in a Thermo Forma incubator (Fischer Scientific, Wohlen, Switzerland) up to 2 h with 5% CO₂ atmosphere at 37 °C, and shook at 900 rpm

(Variomag Teleshake shaker, Sterico, Wangen, Switzerland) to maintain cell dispersion. At 3, 6, 10, 20, 40, 60, and 120 min post-incubation, 100 μ L cell suspension in each well was quenched by 200 μ L methanol containing 2-(8-aminotetralin-5-yl)-1,1,1,3,3,3-hexafluoro-propan-2-ol as an internal standard. The samples were then cooled and centrifuged for LC-MS/MS analysis. Log peak area ratios (test compound/internal standard) are plotted against incubation time using a linear fit. The calculated slope is used to determine the intrinsic clearance, and expressed as μ L per min per million cells.

SPR measurements

All SPR experiments were performed on the SPR instruments (Biacore 3000 and T200, GE Healthcare, Uppsala, Sweden) at 18 °C in the running buffer (10 mM HEPES, 150 mM NaCl, 0.05% (v/v) Surfactant P20, pH 7.4, 50 μ M EDTA supplemented with 1% DMSO (v/v) for binding assay if desired). Protein immobilization and binding assay were performed at flow rate of 5 and 30 μ L/min, respectively.

Protein immobilization

N-terminally tagged, full-length mouse His6-TEV-MAGL protein was immobilized on CM5 SPR sensor (Cat. No. BR-100530, GE Healthcare, Uppsala, Sweden) applying protected amino coupling surface chemistry. The target protein was first pre-diluted 40 times from stock (2.3 mg/mL) in the running buffer and further diluted in the coupling buffer (10 mM acetate, pH 5.5) containing 10 μ M reference compound to stabilize the protein while immobilization. The sensor surface was first activated by a mixture of 0.2 M 1-ethyl-3-(3-dimethylaminopropyl)-carbodiimide and 0.5 M *N*-hydroxysuccinimide for 10 min. Afterwards, the activated surface was contacted with the protein solution at final protein concentration of 0.06 mg/mL in acetate buffer in presence of the reference compound at saturating concentration until the desired protein surface density was achieved (Response: ca. 3000-4000 relative units). No deactivation of sensor surface was performed. Protein surface was prepared freshly to analyze each slow dissociating compound.

Binding assay

All samples were solubilized in DMSO to get 10 mM stock solutions. Further, samples were diluted with running buffer to get dilution series (adapted to the affinity of the compound) and analyzed in single cycle kinetic mode (5 concentrations with the dilution factor of 2). Injection of buffer (blank) was performed to collect buffer signal enabling further data proceeding. The protein binding activity was tested with (2-chlorophenyl)(3-(4-(pyrimidin-2-yl)piperazin-1-yl)azetid-1-yl)methanone) as a fast dissociating compound, prior to the injection of slow dissociating compounds.

Data proceeding

SPR resonance signals measured on the active channel (protein channel) were subtracted with signals collected on the reference channel (only activated sensor surface, no protein) and further subtracted with buffer (blank) signal. Kinetic and binding parameters were extracted from the experimental binding curves by fitting them into mathematical binding model for one-to-one interaction applying Biacore T200 Evaluation software (version 3.2.1).

Activity-based protein profiling assay (ABPP) of compound 7.

Sample preparation: Male mouse brain (27 weeks old) was homogenized with glass beads (2 x 1 min, bullet blender, speed 8) using cold lysis buffer (20 mM HEPES pH 7.2, 1 mM MgCl₂, 2 U/mL Benzonase). Membrane and cytosol were separated by centrifugation. Membrane fraction was resuspended in HEPES/DTT buffer. The protein concentration was determined with Bradford Assay and the samples were diluted to a final concentration of 2.0 mg/mL. Afterwards, the samples were snap frozen in liquid nitrogen and stored at -80 °C until further use.

Gel-based ABPP: Samples of cytosol and membrane fraction were thawed on ice. Samples were divided over tubes and incubated with either vehicle (2.5% DMSO), JZL-184 (10 µM, final concentration), piperazinyl pyrrolidin-2-one **3e** from Aida *et al.*¹⁸ (10 µM, final concentration) or one of the concentrations of compound **7** (1 nM, 3 nM, 10 nM, 30 nM, 100 nM, 300 nM, 1 µM, 3 µM, 10 µM final concentration) for 30 min at 22 °C. Samples were then incubated with the probe cocktail (MB064 100 nM final and FP-Bodipy 100 nM final)¹⁶ for 10 min at 22 °C. The reaction was quenched with 4x Laemmli buffer for 30 min at 22 °C. Samples were resolved by SDS-PAGE (10% AA gel, 15 slots, 0.75 mm, 75 min, 180V) along with a protein marker. In-gel fluorescence was measured in the Cy3-(MB064, 120s), Cy2-(FP-Bodipy, 80s) and Cy5 (Marker, 10s) channel. Gels were stained with Coomassie for 10 min after scanning and destained overnight in DEMI water for protein loading control.

Determination of the free fraction in plasma

Binding to mouse and human plasma proteins was determined by equilibrium dialysis as previously described.²⁶ The compound was incubated with mouse or human plasma with an equilibration time of 5 hours. The total concentrations of test compound in plasma (C_p) and in buffer (C_{buffer}) were then determined by LC-MS, and unbound fractions in plasma (f_p) were calculated based on the formular:

$$f_p = \frac{C_{buffer}}{C_p}$$

Drug recovery (Rec%) after equilibrium dialysis time was calculated as:

$$\text{Rec\%} = 100 \cdot \frac{(C_p + C_{buffer})_{t=5\text{hr}}}{(C_p)_{t=0\text{hr}}}$$

Only measurements with a recovery of 80-120% were considered valid.

Radiosynthesis

Compound **14** (0.672 mg, 4.3 μmol), BEMP (5 μL , 17.3 μmol), 0.2% POCl_3 (v/v, 2.15 μmol in 100 μL MeCN) and **7d** prepared as tosylate salt (4.7 μmol in 100 μL MeCN) was employed to obtain [^{11}C]**7** using the radiolabeling method described previously.¹⁰ Semi-preparative HPLC with a gradient method was applied for purification (ACE5 C18-300 column, 250 \times 10 mm, 5 μm ; mobile phase A: water containing 0.1% H_3PO_4 , mobile phase B: CH_3CN ; flow rate of 4 mL/min; 0.0–6.0 min, 30–50% B; 6.0–8.0 min, 50–55% B; 8.0–12.0 min, 55–60% B; 12.0–18.0 min, 60–95% B; 18.0–20.0 min, 95% B at a wavelength of 254 nm). The identification of the radioactive product was performed in an Agilent 1100 series HPLC system, equipped with UV detector and a GabiStar radiodetector (Raytest) using an ACE XDB-C18 Zobrax column (75 mm \times 4.6 mm, 3.5 μm ; mobile phase A: water containing 0.1% H_3PO_4 , mobile phase B: CH_3CN ; flow rate of 1 mL/min; 0.0–3.0 min, 30–50% B; 3.0–4.0 min, 50–55% B; 4.0–6.0 min, 55–60% B; 6.0–7.0 min, 60–70% B with a wavelength of 254/230 nm). The retention time of **7** and [^{11}C]**7** were 4.99 and 5.02 min, respectively. This difference in retention time was in agreement with the time lag between the UV and radioactivity detectors in our HPLC system. [^{11}C]**2** was synthesized according to the literature.¹⁰

Lipophilicity and in vitro stability

The lipophilicity and *in vitro* stability of [^{11}C]**7** were measured as previously described.⁹

In vitro autoradiography

The *in vitro* autoradiography of [^{11}C]**7** was carried out using an analogous procedure in the literature.¹⁰ An aqueous buffer comprising 30 mM HEPES, 1.2 mM MgCl_2 , 110 mM NaCl, 5 mM KCl, 2.5 mM CaCl_2 , and 1% fatty acid free bovine serum albumin (pH ~7.4) was employed as incubation buffer. The brain sections were incubated with [^{11}C]**7** (18 nM, 65.6 GBq/ μmol) in a humidified chamber for 30 min. Blocking experiments on Wistar brain sections were carried out in the presence of 10 μM SAR127303 or 10 μM

PF-06795071. Upon the completion of incubation, the slices were washed in the above-mentioned incubation buffer (pH 7.4, 0 °C, 1 × 2 min), washing buffer comprising 30 mM HEPES, 1.2 mM MgCl₂, 110 mM NaCl, 5 mM KCl, 2.5 mM CaCl₂ (pH 7.4, 0 °C, 2 × 2 min), followed by 2 quick dips in distilled water (0 °C, 2 × 5 s). After drying, the slices were attached to a phosphor image plate (Fuji, Dielsdorf, Switzerland) and the exposure lasted for 60 min. The film was scanned by BAS5000 reader (Fuji), and the autoradiogram was analyzed by AIDA 4.50.010 software (Raytest GmbH, Straubenhardt, Germany).

In vivo PET imaging

All animals were taken care in accordance with Swiss Animal Welfare legislation. The experiments were complied with ARRIVE guidelines and authorized by the Veterinary Office of the Canton Zurich (ZH28/2018). PET imaging was carried out in mouse under anesthesia with a Super Argus PET/CT tomograph (Sedecal, Madrid, Spain). The radiotracer (6.33–14.42 nmol/kg) was administrated *via* tail-vein injection, and dynamic PET data was acquired 1 min later. A 60 min scan protocol was applied in all animal studies. For blocking studies, MAGLi432 were injected into the mice 5 min prior to tracer injection (5 mg/kg, formulated in DMSO/Tween80/saline = 1/1/8, v/v/v). The resulting data were reconstructed in user-defined time frames with a voxel size of 0.3875 × 0.3875 × 0.775 mm³, and the data analysis were carried out using PMOD 4.002 software (PMOD Technologies Ltd., Zurich, Switzerland) as previously described.¹⁰ The radioactive accumulations in mice brain were expressed as standardized uptake values (SUVs), which is the decay-corrected regional radioactivity normalized to the injected radioactivity and body weight.

Radiometabolite analysis

[¹¹C]7 was concentrated and administered intravenously *via* tail vein (~190 MBq with a radiochemical purity greater than 97%), and the animal was scarified by decapitation at 40 min post-injection. The brain sample were collected and analyzed as previously described.¹⁰ Briefly, the brain homogenate was obtained in 1 mL PBS buffer after dissection. After centrifugation at 4 °C for 5 min, the supernatant was taken and 1 mL ice-cold MeCN was added for protein precipitation. The mixture was centrifuged, and the resulting supernatant was passed through a 0.22 μM Nalgene PES syringe filter. Afterwards, 10 μL sample was injected to a Waters Acquity ultra-performance liquid chromatography (UPLC) equipped with BEH C18 column (Acquity Waters, 130 Å, 1.7 μm, 2.1 mm × 50 mm) and FlowStar LB 513 Radioactivity Flow Detector. A gradient method using 10 mM NH₄HCO₃ in Milli-Q water as mobile phase A and MeCN as mobile

phase B was employed at the flow of 0.6 mL/min for analysis (0.0–2.0 min, 5–30% B; 2.0–3.5min, 30-50% B; 3.5–4.0 min, 50–90% B; 4.0–6.0 min, 90% B).


References

- (1) Aizpurua-Olaizola, O., Elezgarai, I., Rico-Barrío, I., Zarandona, I., Etxebarria, N., and Usobiaga, A. (2017) Targeting the endocannabinoid system: future therapeutic strategies. *Drug Discov. Today* 22, 105-110.
- (2) Ohno-Shosaku, T., and Kano, M. (2014) Endocannabinoid-mediated retrograde modulation of synaptic transmission. *Curr. Opin. Neurobiol.* 29, 1-8.
- (3) Piro, J. R., Benjamin, D. I., Duerr, J. M., Pi, Y., Gonzales, C., Wood, K. M., Schwartz, J. W., Nomura, D. K., and Samad, T. A. (2012) A dysregulated endocannabinoid-eicosanoid network supports pathogenesis in a mouse model of Alzheimer's disease. *Cell Rep.* 1, 617-623.
- (4) Gil-Ordóñez, A., Martín-Fontecha, M., Ortega-Gutiérrez, S., and López-Rodríguez, M. L. (2018) Monoacylglycerol lipase (MAGL) as a promising therapeutic target. *Biochem. Pharmacol.* 157, 18-32.
- (5) van Egmond, N., Straub, V. M., and van der Stelt, M. (2021) Targeting Endocannabinoid Signaling: FAAH and MAG Lipase Inhibitors. *Annu. Rev. Pharmacol. Toxicol.* 61, 441-463.
- (6) Chen, Z., Mori, W., Deng, X., Cheng, R., Ogasawara, D., Zhang, G., Schafroth, M. A., Dahl, K., Fu, H., Hatori, A., Shao, T., Zhang, Y., Yamasaki, T., Zhang, X., Rong, J., Yu, Q., Hu, K., Fujinaga, M., Xie, L., Kumata, K., Gou, Y., Chen, J., Gu, S., Bao, L., Wang, L., Collier, T. L., Vasdev, N., Shao, Y., Ma, J.-A., Cravatt, B. F., Fowler, C., and Josephson, L. (2019) Design, synthesis, and evaluation of reversible and irreversible monoacylglycerol lipase positron emission tomography (PET) tracers using a “tail switching” strategy on a piperazinyl azetidine skeleton. *J. Med. Chem.* 62, 3336-3353.
- (7) Rong, J., Mori, W., Xia, X., Schafroth, M. A., Zhao, C., Van, R. S., Yamasaki, T., Chen, J., Xiao, Z., and Haider, A. (2021) Novel reversible-binding PET ligands for imaging monoacylglycerol lipase based on the piperazinyl azetidine scaffold. *J. Med. Chem.* 64, 14283-14298.
- (8) Hattori, Y., Aoyama, K., Maeda, J., Arimura, N., Takahashi, Y., Sasaki, M., Fujinaga, M., Seki, C., Nagai, Y., and Kawamura, K. (2019) Design, synthesis, and evaluation of (4 R)-1-{3-[2-(¹⁸F) fluoro-4-methylpyridin-3-yl] phenyl}-4-[4-(1, 3-thiazol-2-ylcarbonyl) piperazin-1-yl] pyrrolidin-2-one ([¹⁸F] T-401) as a novel positron-emission tomography imaging agent for monoacylglycerol lipase. *J. Med. Chem.* 62, 2362-2375.
- (9) He, Y., Schild, M., Grether, U., Benz, J. r., Leibrock, L., Heer, D., Topp, A., Collin, L., Kuhn, B., and Wittwer, M. (2022) Development of high brain-penetrant and reversible monoacylglycerol lipase PET tracers for neuroimaging. *J. Med. Chem.* 65, 2191-2207.
- (10) He, Y., Gobbi, L. C., Herde, A. M., Rombach, D., Ritter, M., Kuhn, B., Wittwer, M. B., Heer, D., Hornsperger, B., Bell, C., O'Hara, F., Benz, J., Honer, M., Keller, C., Collin, L., Richter, H., Schibli, R., Grether, U., and Muac, L. (2022) Discovery, synthesis and evaluation of novel reversible monoacylglycerol lipase radioligands bearing a morpholine-3-one scaffold. *Nucl. Med. Biol.* 108, 24-32.
- (11) Granchi, C., Caligiuri, I., Minutolo, F., Rizzolio, F., and Tuccinardi, T. (2017) A patent review of Monoacylglycerol Lipase (MAGL) inhibitors (2013-2017). *Expert Opin. Ther. Pat.* 27, 1341-1351.
- (12) Bononi, G., Poli, G., Rizzolio, F., Tuccinardi, T., Macchia, M., Minutolo, F., and Granchi, C. (2021) An updated patent review of monoacylglycerol lipase (MAGL) inhibitors (2018-present). *Expert Opin. Ther. Pat.* 31, 153-168.
- (13) Hou, L., Rong, J., Haider, A., Ogasawara, D., Varlow, C., Schafroth, M. A., Mu, L., Gan, J., Xu, H., and Fowler, C. J. (2020) Positron emission tomography

- imaging of the endocannabinoid system: opportunities and challenges in radiotracer development. *J. Med. Chem.* **64**, 123-149.
- (14) Huang, S.-C., Barrio, J. R., and Phelps, M. E. (1986) Neuroreceptor assay with positron emission tomography: equilibrium versus dynamic approaches. *J. Cereb. Blood Flow Metab.* **6**, 515-521.
- (15) Labar, G., Bauvois, C., Borel, F., Ferrer, J. L., Wouters, J., and Lambert, D. M. (2010) Crystal structure of the human monoacylglycerol lipase, a key actor in endocannabinoid signaling. *Chembiochem* **11**, 218-227.
- (16) Janssen, A. P., Van Der Vliet, D., Bakker, A. T., Jiang, M., Grimm, S. H., Campiani, G., Butini, S., and Van Der Stelt, M. (2018) Development of a multiplexed activity-based protein profiling assay to evaluate activity of endocannabinoid hydrolase inhibitors. *ACS Chem. Biol.* **13**, 2406-2413.
- (17) Long, J. Z., Li, W., Booker, L., Burston, J. J., Kinsey, S. G., Schlosburg, J. E., Pavón, F. J., Serrano, A. M., Selley, D. E., Parsons, L. H., Lichtman, A. H., and Cravatt, B. F. (2009) Selective blockade of 2-arachidonoylglycerol hydrolysis produces cannabinoid behavioral effects. *Nat. Chem. Biol.* **5**, 37-44.
- (18) Aida, J., Fushimi, M., Kusumoto, T., Sugiyama, H., Arimura, N., Ikeda, S., Sasaki, M., Sogabe, S., Aoyama, K., and Koike, T. (2018) Design, synthesis, and evaluation of piperaziny pyrrolidin-2-ones as a novel series of reversible monoacylglycerol lipase inhibitors. *J. Med. Chem.* **61**, 9205-9217.
- (19) Zhang, L., Villalobos, A., Beck, E. M., Bocan, T., Chappie, T. A., Chen, L., Grimwood, S., Heck, S. D., Helal, C. J., and Hou, X. (2013) Design and selection parameters to accelerate the discovery of novel central nervous system positron emission tomography (PET) ligands and their application in the development of a novel phosphodiesterase 2A PET ligand. *J. Med. Chem.* **56**, 4568-4579.
- (20) Dinh, T., Carpenter, D., Leslie, F., Freund, T., Katona, I., Sensi, S., Kathuria, S., and Piomelli, D. (2002) Brain monoglyceride lipase participating in endocannabinoid inactivation. *Proc. Natl. Acad. Sci. (USA)* **99**, 10819-10824.
- (21) Yamasaki, T., Mori, W., Zhang, Y., Hatori, A., Fujinaga, M., Wakizaka, H., Kurihara, Y., Wang, L., Nengaki, N., Ohya, T., Liang, S. H., and Zhang, M.-R. (2018) First demonstration of in vivo mapping for regional brain monoacylglycerol lipase using PET with [¹¹C] SAR127303. *NeuroImage* **176**, 313-320.
- (22) Honer, M., Gobbi, L., Martarello, L., and Comley, R. A. (2014) Radioligand development for molecular imaging of the central nervous system with positron emission tomography. *Drug Discov. Today* **19**, 1936-1944.
- (23) Kemble, A. M., Hornsperger, B., Ruf, I., Richter, H., Benz, J., Kuhn, B., Heer, D., Wittwer, M., Engelhardt, B., Grether, U., and Collin, L. (2022) A potent and selective inhibitor for the modulation of MAGL activity in the neurovasculature. *PLoS One* **17**, e0268590.
- (24) Soethoudt, M., Grether, U., Fingerle, J., Grim, T. W., Fezza, F., De Petrocellis, L., Ullmer, C., Rothenhäusler, B., Perret, C., Van Gils, N., Finlay, D., MacDonald, C., Chicca, A., Dalghi Gens, M., Stuart, J., de Vries, H., Mastrangelo, N., Xia, L., Alachouzos, G., Baggelaar, M. P., Martella, A., Mock, E. D., Deng, H., Heitman, L. H., Connor, M., Di Marzo, V., Gertsch, J., Lichtman, A. H., Maccarrone, M., Pacher, P., Glass, M., and van der Stelt, M. (2017) Cannabinoid CB 2 receptor ligand profiling reveals biased signalling and off-target activity. *Nat. Commun.* **8**, 1-14.
- (25) Haider, A., Kretz, J., Gobbi, L., Ahmed, H., Atz, K., Bürkler, M., Bartelmus, C., Fingerle, J. r., Guba, W., Ullmer, C., Honer, M., Knuesel, I., Weber, M., Brink, A., Müller Herde, A., Keller, C., Schibli, R., Mu, L., Grether, U., and Ametamey, S. M. (2019) Structure–activity relationship studies of pyridine-based ligands and identification of a fluorinated derivative for positron emission tomography imaging of cannabinoid type 2 receptors. *J. Med. Chem.* **62**, 11165-11181.
- (26) Gobbi, L. C., Knust, H., Körner, M., Honer, M., Czech, C., Belli, S., Muri, D., Edelmann, M. R., Hartung, T., and Erbsmehl, I. (2017) Identification of three novel radiotracers for imaging aggregated tau in Alzheimer's disease with positron emission tomography. *J. Med. Chem.* **60**, 7350-7370.

Chapter Eight

Synthesis of radiolabeled tetrazine derivatives for pretargeted imaging within the central nervous system

This declaration concerns the article entitled:			
Synthesis of radiolabeled tetrazine derivatives for pretargeted imaging within the central nervous system			
Publication status (tick one)			
Draft manuscript	<input type="checkbox"/>	Submitted	<input type="checkbox"/>
Published	<input type="checkbox"/>	Accepted	<input checked="" type="checkbox"/>
In review	<input checked="" type="checkbox"/>		
Publication details (reference)	Edelmann MR*, Bredack C*, Belli S, Mohr P, Imhoff MP, Regiani F, Kuszir EA, Rufer AC, Holt DP, Valentine H, Wong DF, Dannals RF, Honer M, Gobbi LC. (2023) <i>Bioconjug. Chem.</i>		
Copyright status (tick the appropriate statement)			
I hold the copyright for this material	<input type="checkbox"/>	Copyright is retained by the publisher, but I have been given permission to replicate the material here	<input type="checkbox"/>
Candidate's contribution to the paper (provide details, and also indicate as a percentage)	<p>The candidate contributed to / considerably contributed to / predominantly executed the...</p> <p>Formulation of ideas: 40%</p> <p>Design of methodology: 30%</p> <p>Experimental work: 50%</p> <p>Presentation of data in journal format: 80%</p>		
Statement from Candidate	This paper reports on original research I conducted during the period of my Higher Degree by Research candidature.		
Signed		Date	17.10.22

Introduction

Monoclonal antibodies (mAbs) with their exquisite specificity and affinity are increasingly being investigated as positron emission tomography (PET) imaging agents.¹⁻³ The application of mAbs is particularly interesting for targets where imaging approaches with small molecules have proven difficult or methodologically intractable, incl. targets in the central nervous system (CNS).⁴ Recently, published preclinical data suggest that antibody-based PET imaging of CNS targets is feasible.⁵ MAbs are characterized by prolonged circulation in the body due to their molecular size (compared to small molecules) and the neonatal Fc receptor, which protects IgGs from degradation.⁶ This long biological half-life of mAbs in combination with the short physical half-life of preferred and typically used PET radionuclides for clinical imaging implies some challenges, both with regard to signal-to-noise ratios (due to radioactivity background in the blood pool) and to radiation exposure of healthy tissue. Pretargeted imaging, based on *in vivo* labeling of a target-bound large molecule with a small molecule PET tracer, provides a way to address this hurdle.⁷ Compared to conventional PET imaging approaches in which a large molecule is directly labeled with a radionuclide, a pretargeting approach offers a solution by uncoupling of the pharmacokinetic half-life of the biological molecule of interest from the physical half-life of the radionuclide. The pretargeting approach allows an antibody to be directed to a target before injecting a small radiolabeled effector to recognize and specifically bind to it, for instance *via* an *in vivo* click reaction.⁸ Well-known types of click chemistry include the [3+2] cycloaddition, such as the 1,3-dipolar azide-alkyne Huisgen cycloaddition,⁹ the [4+1] cycloaddition between isonitriles and tetrazines,¹⁰ or the inverse electron-demand Diels-Alder (IEDDA) reaction of strained alkenes with tetrazines.¹¹ The advantage of IEDDA reactions is not only due to the high reaction rate, but also to the fact that the *in vivo* click mechanism is bioorthogonal in nature, meaning that both the reactants and the product do not interact with a biological system. Tetrazine (Tz) ligation with *trans*-cyclooctene (TCO) exhibits probably the highest reported rate constants and is therefore amenable to *in vivo* imaging applications.¹²

While pretargeted mAb-based imaging of peripheral targets has been often reported,¹³⁻¹⁵ imaging of targets within the CNS is largely unexplored. Targets in the CNS represent a special challenge for pretargeted imaging since both click reaction partners must be able to cross the blood-brain barrier (BBB). In this case, it is daunting to use functionalized mAbs as a partner of the click chemistry and target binder, as a full-length antibody (MW: 150,000 Da) can usually only penetrate the BBB to a limited extent due to its size and hydrophilic properties. This issue can be elegantly addressed by the use of an engineered antibody containing a Brain Shuttle module, also known as 8D3,¹⁶ that

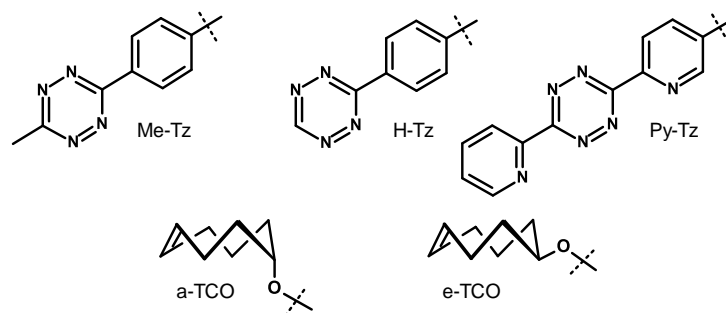
has a high affinity for the transferrin receptor (TfR), which enables the active transport of molecules across the BBB *via* receptor-mediated transcytosis.¹⁷⁻¹⁹ The Brain Shuttle version of an amyloid-beta (A β) antibody (referred to in this study as A β -mAb), which capitalizes on the monovalent binding mode to the TfR, increases A β target binding in brain tissue in a mouse model of Alzheimer's disease (AD) by 55-fold compared to the parent A β -mAb without 8D3-fusion.²⁰ Initial promising results in a mouse model of A β deposition were presented for an anti-amyloid A β antibody conjugated to 8D3 and directly radiolabeled with ¹²⁴I for PET imaging.⁵ Functionalization of such engineered A β -specific antibodies with a TCO-tag could therefore introduce an ideal partner for click reaction and a bioorthogonal pretargeting imaging approach. As second partner in the click reaction, Tz-derivatives must be identified, which are able to carry a radionuclide, such as ¹¹C, ¹⁸F, or ³H, pass the BBB for a pretargeted A β -mAb ligation, and are stable enough under physiological conditions. It is reported, that a high reactivity rate of a tetrazine towards TCO correlates with lower stability in the serum.²¹ However, the use of the Tz as a second reactant allows for a strategic optimization of the molecule, especially regarding brain uptake, as the LogD-values, which are a critical parameter for both brain permeability and non-specific tissue binding, of Tzs are in general in an acceptable range compared to the highly lipophilic TCO-derivatives.

The focus of this study aimed at the identification and optimization of the most important properties of Tzs to make them suitable tracers for pretargeted imaging of CNS targets. Covalent imaging probes such as Tzs share some common properties with classical reversible small molecule PET tracers, for example fast and high brain uptake or low non-specific binding. The identified radiolabeled Tzs are expected to be used, for example, as versatile tools for pretargeted PET imaging for CNS targets using *in vivo* IEDDA chemistry.

Results & Discussion

In order to identify tetrazine derivatives, which are suitable for a bioorthogonal click reaction on CNS targets, three sub-classes (**Figure 1**) were investigated: A) 3-methyl-6-aryl-tetrazine (Me-Tz); B) 3-H-6-aryl-tetrazine (H-Tz); and C) 3,6-bis(2-pyridyl)-tetrazine (Py-Tz). Furthermore, it was deemed necessary that the selected tetrazine derivatives allow the incorporation of a PET radionuclide such as ¹¹C and ¹⁸F. In addition, the feasibility of labeling with a β -emitter such as tritium was explored to complement the biological evaluation.

Figure 1: Three sub-classes of tetrazines used in this study: Me-Tz, H-Tz, Py-Tz. Structure of axial-substituted TCO (a-TCO) and equatorial TCO (e-TCO).

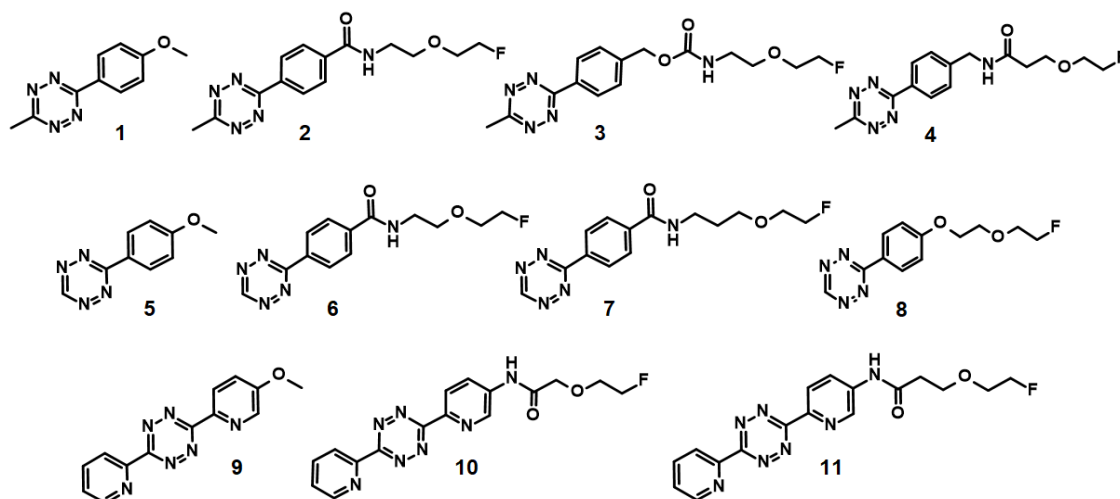


As reaction partner for the bioorthogonal IEDDA click reaction to the tetrazines, *trans*-cyclooctene (TCO) constructs previously described in the literature were selected. It is well known that *cis*-cyclooctene (CCO) is 5-6 orders of magnitude less reactive towards electron-deficient tetrazines than TCO.²² Furthermore, it was reported that the axial diastereomer of 5-hydroxy-TCO (a-TCO) is more reactive than the equatorial diastereomer (e-TCO).²³ Structures of a-TCO and e-TCO are shown in **Figure 1**. Based on these findings, an axial 5-hydroxy-*trans*-cyclooctene substructure was chosen for antibody functionalization.

Preparation of non-radioactive Tetrazine Derivatives

Eleven tetrazines (**Figure 2**) were synthesized and investigated. The design was based on modulating of the electronic properties of the Tz core and on varying the steric bulk in its proximity, both factors known to impact the reactivity towards TCOs. In addition, different side-chains with potential for a straightforward radiolabeling strategy were explored. The selection includes literature two reported (**1**, **5**)²⁴ and nine new tetrazines (**2-4**, **6-11**).

Figure 2: Structures of tetrazines investigated in this study.



The synthesis of tetrazine derivatives followed three general routes, depending on the substitution pattern of the tetrazine core: A) methylated tetrazines (Me-Tzs); B) mono-substituted tetrazines (H-Tzs); C) bis-pyridyl tetrazines (Py-Tzs). A classical route to 1,2,4,5-tetrazines is the addition of hydrazine to aromatic nitriles, followed by oxidation of the 1,2-dihydropyridazine intermediate.²⁵ However, this approach is not applicable to the preparation of tetrazines from alkyl nitriles. For these reasons, a general and robust metal-catalyzed method, described by Devaraj and co-workers,²⁶ was used to prepare asymmetric 1,2,4,5-tetrazines with a single substituent or a methyl moiety.

Tetrazine key-intermediates **12-17**, belonging to the Me-Tz and H-Tz series, were all synthesized in a similar manner as shown in **Figure 3: A, B**. Using 50 mol% nickel triflate (Ni(OTf)₂) or zinc triflate (Zn(OTf)₂), the Me-Tz and H-Tz key-intermediates were synthesized *via* 1,2-dihydropyridazine-intermediates that were subsequently oxidized with sodium nitrite/hydrogen chloride. Either Ni(OTf)₂ or Zn(OTf)₂ was tested for catalytic effectiveness in each case. In terms of the synthesis to Me-Tzs, the yields were slightly higher when the nickel catalyst was used, with the exception of the phenol-Tz **12**: The yield of 38% for **12** using the zinc catalyst was superior to a yield of 8% using the nickel catalyst. With respect to the synthesis of H-Tzs, the yields were uniformly significantly lower. The phenol-Tz **16** was isolated in 17% yield using the zinc catalyst, while only traces of the product was found when the corresponding nickel catalyst was tried. In contrast, the results for the synthesis of carboxylic acid-Tz **17** were different. In this case no product was obtained relying on the zinc catalyst, but use of the nickel catalyst resulted in a 14% yield. Py-Tz-based key-intermediates were formed with an excess of aqueous hydrazine, without the use of metal catalyst, followed by oxidation with sodium nitrite and hydrogen chloride to yield 12% of **18** and 20% of **19**, respectively (**Figure 3:C**).

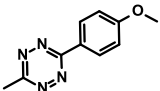
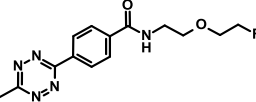
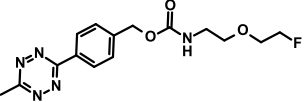
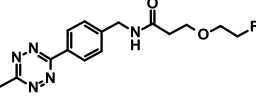
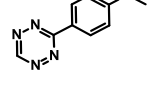
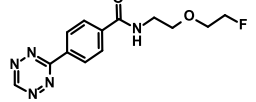
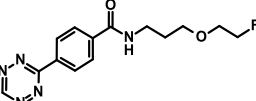
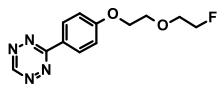
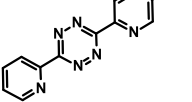
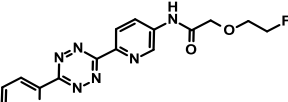
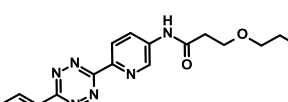
The final tetrazines **1-11** were synthesized starting from key-intermediates **12-19** that contain a unique reactive group for side chain modification and functionalization with potential for radio isotope incorporation. Hydroxyaryl precursors **12**, **16**, **18** were O-alkylated under Williamson etherification conditions. Using iodomethane as methyl source, **1** was alkylated in 80% yield. The isolated yield of 10% for the synthesis of **5** under identical conditions was significantly lower. This result can be explained by the instability of the monosubstituted tetrazine precursor under basic conditions (*vide infra*). A tosylated fluoroethoxyethyl-derivative was used in the alkylation to obtain **8**, which resulted in 24% yield. O-Methylation to **9** from the Py-Tz series with methyl nosylate (**22**) was achieved in 81% yield. Starting from **14**, the primary alcohol was activated by the use of carbonyldiimidazole in a first step and the desired carbamate-Tz **3** was prepared by quenching the intermediate with the corresponding amine in 74% yield. The remaining tetrazines were synthesized using standard amide coupling procedure. The resulting yields for Me-Tz series ranged from 57–74% and from the H-Tz series **6** was isolated in

Considerations on the Physicochemical Properties of Tetrazine Derivatives

From a pharmacological point of view, a viable PET tracer must be highly specific towards its intended target and exhibit low non-specific binding for reducing background signal. In principle, the requirements for tetrazines for use in pretargeted PET imaging based on bioorthogonal click reactions are equal to those of a PET tracer that binds directly to a CNS target. The target in this study represents a TCO-modified antibody that is pre-targeted to the CNS protein A β . A suitable tetrazine derivative must therefore be able to penetrate the brain in high concentration, have low non-specific binding (NSB), and be highly reactive towards the TCO group. In contrast to a classical small-molecule CNS-PET tracer, which binds with high affinity to its target, the tetrazine for the bioorthogonal click reaction must engage with the TCO in an efficient and fast reaction with very high reaction rate. At the same time, the tetrazine must show sufficient stability to maintain reactivity towards a TCO group for a sufficiently long time. This balance between stability and reaction kinetics must be carefully designed since, in general, high reaction rate results in low stability.

A slight modification of a previously described multiparameter optimization *in silico* descriptor for PET tracers targeting the central nervous system (CNS-PET-MPO) was used to guide the design of the compounds. The prediction is based on six calculated physicochemical properties: mlLogD (machine learning based prediction of partition coefficient at pH = 7.4), AlogP (atom-based partition coefficient), MW (molecular weight), TPSA (topological polar surface area), HBD (number of hydrogen bond donors), and pK_a (predicted ionization constant of the most basic center). This model estimates properties such as good brain permeability and moderate non-specific binding in the target tissue. The CNS-MPO desirability score for each compound can range from 0.0 to 6.0, with higher CNS-MPO scores (≥ 4.0) predicting a higher probability of success for the molecule to become a PET tracer for CNS use. Based on the calculated score using the CNS-PET-MPO assessment (**Table 1**), all selected tetrazines **1-11** meet the requirements of a potential CNS PET tracer. The physicochemical property of the ionization constant of the most basic center has limited applicability to tetrazines. Although four nitrogen atoms are present in 1,2,4,5-tetrazines, the basicity from the tetrazine ring is remarkably low, which can be attributed to the aromaticity criterion. Protonation disrupts the symmetry of the heterocycle and consequently reduces aromaticity, which ultimately destabilizes the protonated form.^{28,29} For this reason, in **Table 1**, a pK_a value can be calculated only from Tzs **9-11**, which resulted from the basicity of the pyridine residues.

Table 1: Calculated physicochemical properties of Tzs and CNS-PET-MPO scores.^a

Tz #	Structure	<i>m</i> logD	<i>A</i> logP	MW	TPSA	HBD	pK _a	CNS MPO Score
1		1.91	1.20	202	56	0	*	5.7
2		1.12	0.69	305	81	1	*	5.0
3		1.62	1.25	335	90	1	*	4.3
4		1.09	0.73	319	81	1	*	4.7
5		1.16	1.24	188	56	0	*	6.0
6		0.83	0.74	291	81	1	*	5.0
7		-0.10	0.80	305	81	1	*	5.0
8		1.30	1.51	264	64	0	*	5.7
9		1.12	1.42	266	76	0	2.2	5.0
10		0.88	0.69	355	100	1	2.5	4.0
11		0.95	0.94	369	99	1	2.2	4.0

^a *m*logD: prediction of the distribution coefficient (logD) at physiological pH = 7.4 based on an internal machine-learning model; *A*logP: atom-based partition coefficient; MW: molecular weight; TPSA: topological polar surface area; HBD: number of hydrogen bond donors; pK_a: predicted ionization constant of the basic center. *: Tzs **1-8** do not have a basic pK_a value.

pH-Dependent Aqueous Stability Assay

With the aim of narrowing down the number of tetrazines used for further studies, the synthesized compounds **1–11** were first tested for their chemical stability at different pH. The chemical stability of the Tzs was determined after incubation in buffers at pH 1.0, 4.0, 6.5, 8.0, and 10.0 for 2 hours at 37 °C. According to analytical-HPLC, the area under the curve of the 2 h-samples was compared to the sample at time zero and the percent recovery calculated. A systematic survey of stability assay results (**Table 2**) led to the following conclusions: Me-Tzs are the most stable ones at all pH values tested, with the exception of **2**, which was stable only in the pH range 4.0 to 6.5. H-Tzs **6** and **7** rapidly decompose under basic conditions (pH = 10.0), their stability already being problematic at pH = 8.0, whereas acidic conditions are well tolerated. Py-Tzs quickly decompose under strongly basic conditions (pH = 10.0), and under strongly acidic conditions (pH = 1.0). Tzs **5**, **6**, and **7** were excluded from the study due to their instability at pH 8; it can be assumed that the compounds are not sufficiently stable under physiological conditions and are therefore unsuitable for a PET tracer.

Table 2: Results from the pH-dependent aqueous stability assay in percent recovery after 2 hours. q* means quantitative recovery.

Tz #	Structure	pH				
		1.0	4.0	6.5	8.0	10.0
1		90	91	92	91	84
2		51	94	88	74	0
3		q*	q*	q*	q*	97
4		q*	q*	q*	q*	q*
5		56	61	60	60	38
6		92	q*	97	27	0
7		94	q*	95	34	0
8		q*	q*	q*	q*	16
9		60	q*	q*	q*	3
10		51	94	88	74	0
11		50	93	92	75	0

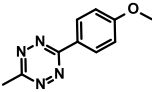
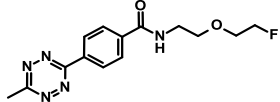
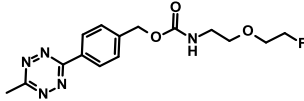
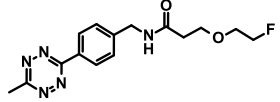
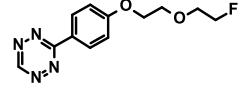
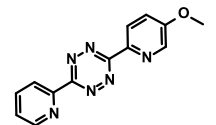
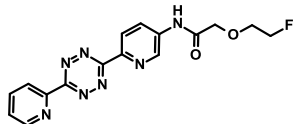
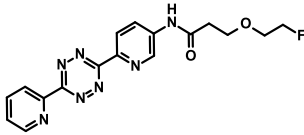
Results of the passive permeability, microsomal stability, and P-gp transport assays for *in vivo* ADME predictions

In order to rank compounds based on predicted ADME properties suitable for a PET tracer and select the most promising candidates for *in vivo* pharmacokinetic assessments, Tzs **1-4** and **8-11** were profiled in three key assays: stability in rodent (Rat) and human (Hu) liver microsomes to predict potential hepatic oxidative clearance (CL) *in vivo*, PAMPA to assess passive permeability across cell membranes at the BBB, and P-Glycoprotein (P-gp) transport in human (Hu) and rodent (Mo) cell lines to anticipate and minimize potential issues with brain uptake originating from active efflux at the BBB. The recently described apical efflux ratio (AP-ER) was determined in the P-gp transport assays and the passive transcellular permeability $P_{app}^{A \rightarrow B}(+I)$ was included in the evaluation.³⁰ Respective results are depicted in **Table 3**.

Most compounds displayed very low clearance in human microsomes outside the assay sensitive range, as indicated by CL values of 10 $\mu\text{L}/\text{min}/\text{mg}$. One notable exception is methyl-phenol ether **1**, exhibiting high clearance indicative of fast oxidative metabolism, most likely at the methoxy position. By contrast, medium to high clearance was observed in general on rat microsomes. While such a species difference is not surprising, these results indicate that longer tracer plasma pharmacokinetics might be observed when moving into imaging studies in higher species, possibly negatively affecting the PET image quality.

Passive cell membrane permeability was assessed in the PAMPA assay.³¹ All tetrazines displayed good ($P_{\text{eff}} \geq 2 \times 10^{-6} \text{ cm}^{\text{s}^{-1}}$) to excellent permeability, predictive for rapid and efficient BBB crossing. The high passive permeability was further corroborated by results from the P-Glycoprotein transport assay, where high values for the apical to basolateral permeability in presence of a P-gp inhibitor ($P_{app}^{A \rightarrow B}(+I) \gg 100 \text{ nm}/\text{s}$) were recorded. Small Tzs with no hydrogen-bond donor functionality (**1**, **8**) were not substrates for P-gp, as demonstrated by AP-ER values of ca. 1, and are thus expected to have excellent permeability at the BBB *in vivo*. By contrast, larger Tzs possessing an amide (**2**, **4**, **10**, **11**) or carbamate (**3**) as hydrogen bond donor started to suffer from some weak active efflux, in particular in the rodent model. While the absolute AP-ERs are only weak, no efflux at all is generally preferred for a PET tracer, as the injected dose is always small and limited by radiation burden consideration. Thus already weak to moderate efflux at the BBB can jeopardize the usefulness of a novel tracer candidate, and the issue cannot be resolved by adapting the dosage. Tzs **2** and **3** suffered from weak active efflux only at mouse P-gp, but not in human. While this might complicate preclinical tracer characterization and validation in rodents, these two compounds might still be valid tracer candidates for use in humans.

Table 3: Summary of results of the PAMPA, microsomal stability, and P-gp transport assays.

Tz #	Structure	PAMPA	MicroCL		P-gp AP-ER	
		[cm/s * 10 ⁻⁶] <i>P_{eff}</i>	Rat	Hu	(<i>P_{app}^{A→B}</i> (+I) [nm/s]) Hu	Mo
1		14.85	67	91	0.83 (206)	1.12 (250)
2		7.79	10	10	0.93 (255)	1.45 (261)
3		16.47	167	11	0.93 (270)	1.54 (287)
4		6.63	16	10	1.29 (247)	n.d.
8		17.99	n.d.	10	0.93 (318)	1.01
9		5.69	51	10	n.d.	n.d.
10		2.61	10	22	1.26 (225)	1.23
11		2.55	11	10	1.92 (156)	n.d.


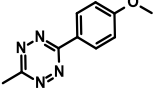
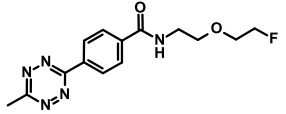
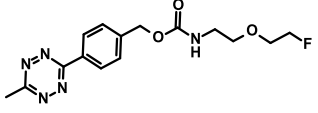
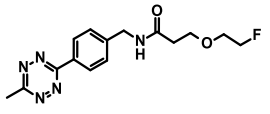
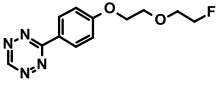
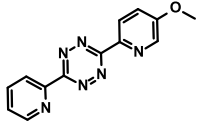
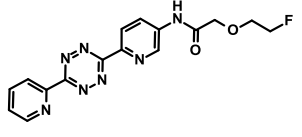
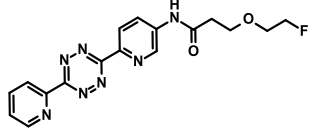
Bimolecular Reaction Kinetics

Selected tetrazines **1-4** and **8-11** were tested for their bimolecular reaction kinetic rates k_{bi} under pseudo-first order conditions against the commercially available TCO-OH **21**. The pseudo equatorial conformation of **21** differs from the pseudo axial conformation of **20**. Therefore, lower reaction kinetics are to be expected in the following experiments than with the TCO-modified antibody. The importance of these measurements is to compare reaction rates of Tzs with the same TCO derivative, to rank them and draw a conclusion about the reactivity behavior of each novel Tz.

The bimolecular reaction rates k_{bi} of the selected Tzs (dienes) and **21** (dienophile) were determined by stopped-flux kinetic measurements in fluorescence (Tzs **1-4**, **8**) or absorption (Tz **9-11**) mode in principle as described by Yang et al.³² and Blackman et al.³³ All reactions were performed at 20 °C in PBS and 10% (v/v) DMSO as solvent to achieve good solubility of the compounds in four concentration ratios (Tzs: 10 μ M; TCO: 100, 150, 200, 300 μ M). To determine the reaction rates, five technical replicates were measured and averaged for all reactant combinations and concentrations. The bimolecular reaction rates k_{bi} (k_{on} for the association reaction) were determined under pseudo-first order conditions, keeping the concentration of the tetrazine reactants constant and titrating with **21**. The changes in fluorescence and absorbance signals over time were fitted with a single exponential equation in all cases, and the observed reaction rates were linearly dependent on concentration, demonstrating the absence of additional rate-limiting reaction steps. The observed concentration-dependent rate constants k_{obs} were fitted to a linear equation in a secondary plot to determine k_{bi} from the slope. The intersection with the abscissa in the secondary plot corresponds to the rate constant of dissociation in the back reaction (k_{off}), which in this case is experimentally indistinguishable from zero. However, this is to be expected because nitrogen is released during the ensuing cycloreversion and the reverse reaction is thus entropically unfavorable.

The results of the bimolecular reaction kinetic measurements are summarized in **Table 4**. From the Me-Tz series, the reaction rates with **21** ranged from $k_{bi} = 166 \text{ M}^{-1}\text{s}^{-1}$ to $388 \text{ M}^{-1}\text{s}^{-1}$. Tz **8**, as the only remaining tetrazine derivative from the H-Tz series, had a significantly higher reaction rate of $7,638 \text{ M}^{-1}\text{s}^{-1}$. The fastest reaction rate was observed with Py-Tz **10** with $k_{bi} = 10,894 \text{ M}^{-1}\text{s}^{-1}$.

Table 4: Bimolecular association rate constants k_{bi} for the reaction of TCO **21** with selected tetrazines in $M^{-1}s^{-1}$. Values are given as averages \pm standard error of the fit to data of $n = 5$ experiments.

Tz #	Structure	 OH
1		166 ± 1
2		388 ± 5
3		287 ± 4
4		272 ± 5
8		$7,638 \pm 75$
9		$7,063 \pm 144$
10		$10,894 \pm 211$
11		$9,736 \pm 186$

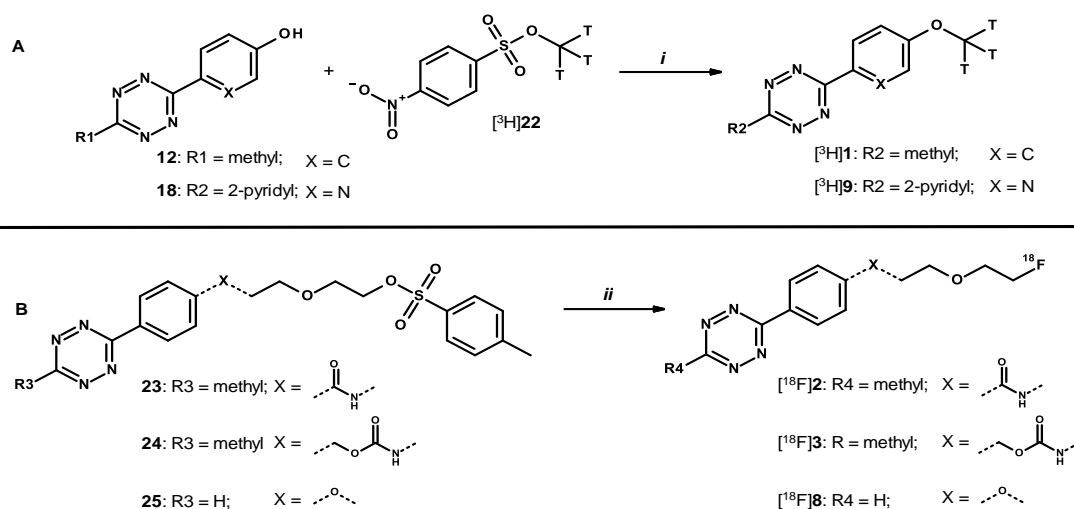
Preparation of Radiolabeled Tetrazine Derivatives

Tetrazines **1** and **9** were examined for their qualification for radiochemical labeling with tritium. In preclinical experiments, tritium, which belongs to the group of long-lived radionuclide is regularly used as a source of ionizing radiation due to its half-life of 12.6 years. The long half-life allows tritium-labeled compounds to be available for experiments over a longer period of time. For several decades, [3H]methyl nosylate ([3H]**22**, [3H]methyl-4-nitrobenzenesulfonate) has been used in tritium-based chemistry as a radiochemically stable reagent for methylation of amines, alcohols, or phenols.^{34,35} [3H]Methyl nosylate has the advantage that, in contrast to the corresponding methylation

reagent [^3H]methyl iodide, it is non-volatile and therefore less harmful from a radiation protection point of view. The methylation on tetrazine phenols (**Figure 4-A**) was run under basic conditions in aprotic solvents such as THF. A solid-phase supported work-up was carried out by using strong ion exchange (SCX-2/SAX) cartridges.³⁶ This method allows a fast, safe, and efficient work-up for tritium labeled compounds with high recovery rates.

Products of tritium-methylations of tetrazine phenols were difficult to isolate and the synthesis proceeded significantly worse than with non-tetrazine-functionalized phenols. This is reflected in the poor radiochemical yield as well as in the formation of numerous by-products. A reason for this might be the basic reaction conditions, since cesium carbonate was used as a base to deprotonate the hydrogen of the phenol-group. In the pH-dependent stability assay, Py-Tzs showed a high level of instability at pH > 8. [^3H]9 was isolated in a radiochemical yield of 2% with a 97% radiochemical purity. The best yield in this study was achieved with [^3H]1. In 3 independent [^3H]-methylation experiments, a 10% \pm 1% radiochemical yield with a radiochemical purity of > 97% were achieved after HPLC purification in each case.

Figure 4: General procedure for radiolabeling of tetrazine derivatives.^a



^a **A:** Tritium methylation on phenol residues. *i.* cesium carbonate, tetrahydrofuran, 16 h, 22 °C. **B:** Fluorine-18 labeling. *ii.* Elixys Flex/Chem, potassium bicarbonate, Krypofix, [^{18}F]2: 110 °C, 9 min; [^{18}F]3 and [^{18}F]8: microwave radiation, 30 s, 50 W.

The tetrazines **2**, **3**, and **8** were selected for testing the feasibility of labeling with the PET nuclide fluorine-18. ^{18}F -Tzs were synthesized using a custom-built ^{18}F -synthesis module at the Johns Hopkins University PET Center, which has been previously described.³⁷ Starting with methyl benzenesulfonate precursors, several ^{18}F -labeling experiments were carried out as described in **Figure 4-B**. Due to the high radiolytic decomposition, [^{18}F]3 could only be isolated in an insufficient radiochemical purity of of 34% at most.

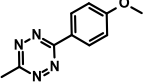
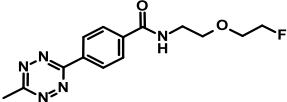
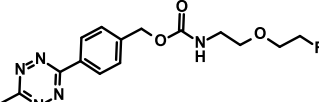
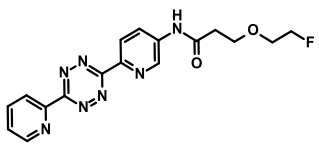
[¹⁸F]**2** and [¹⁸F]**8**, on the other hand, were isolated in a radiochemical purity of 86% and 95%, respectively.

Single-Dose Pharmacokinetic and brain/CSF uptake Studies in Rats

Based on the findings from the P-glycoprotein efflux transport assay and the pH-dependent stabilities, 4 tetrazines (**1**, **2**, **3**, **11**) were selected for the intravenous single-dose pharmacokinetic studies in Wistar rats to assess plasma PK and brain and CSF uptake *in vivo*. Since Tzs **10** and **11** showed similar behavior in the stability as well as in the *in vitro* PAMPA, MicroCL, and P-gp assays, an *in vivo* study with **10** was omitted, which represents a contribution to the 3R principles. The respective results are summarized in **Table 5**, including basic PK parameters such as systemic clearance (CL), apparent distribution volume (V_{ss}), and apparent terminal half-life (T_{1/2}), and furthermore CNS penetration expressed as the compound concentration ratio at 1 h post administration in CSF vs plasma, and in brain vs plasma.

Among the four tested compounds, Tz **1** displayed the highest CL in rat and the highest distribution volume, properties certainly desirable for a PET tracer to reduce unspecific background signal, distribute quickly and improve imaging resolution. All compounds showed a very short apparent elimination half-life from plasma ≤ 0.6 h. CNS penetration of unbound compound, and thus of the molecular species able to interact with its target in the brain, was assumed to be represented here by the concentration ratio in CSF vs plasma and was calculated to be 1 for Tz **2**, slightly lower than 1 for Tzs **1** and **3** but still acceptable, while markedly poor for Tz **11**, likely indicating a strong P-gp efflux in rodent (and possibly in human, see **Table 3**) for this last tetrazine. As a consequence, Tz **11** was excluded from further studies. In terms of brain vs plasma ratio, Tz **3** was the poorest. Due to this finding and the challenging fluorine-18 labeling, Tz **3** was withdrawn from the study.

Table 5: Summary of single-dose PK study results.^a

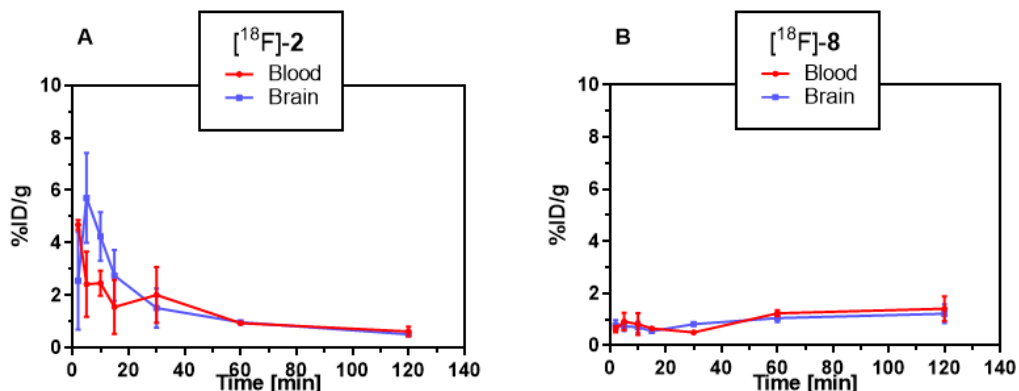
Tz #	Structure	Tested IV dose [mg/kg]	Syst. CL [mL/min kg]	Vss [L/kg]	T _{1/2} [h]	CSF-plasma conc. ratio	Brain-plasma conc. ratio
1		1	65.5	1.3	0.3	0.4	1
2		0.7	13.5	0.5	0.4	1	1.6
3		1	15.7	0.8	0.6	0.5	0.5
11		0.4	13.8	0.5	0.3	0.05	1.9

^a CL: systemic clearance; Vss: apparent distribution volume; T_{1/2}: apparent terminal half-life; CFS: cerebrospinal fluid.

Biodistribution Study of ¹⁸F-labeled Tzs

To investigate potential brain penetration, a biodistribution study was performed in male C57BL6 mice ($n = 3$ per group) using successful labeled ¹⁸F-labeled Tzs **2** and **8**. Each animal received a 7.4 MBq (200 μ Ci) single intravenous bolus injection of high specific activity [¹⁸F]**2** or [¹⁸F]**8** (in approximately 0.2 mL saline) *via* the tail vein. Three mice were sacrificed by cervical dislocation at each of the following post-injection time points: 2, 5, 10, 15, 30, 60, and 120 minutes. The aim of this study was to determine the ratio of the injected dose in the blood and in the brain. Other organs such as kidney, liver, and spleen were also taken into account. Average time-activity curves for blood and brain, which were dosimetrically evaluated are given in **Figure 5**. [¹⁸F]**2** showed an uptake in the brain of up to 6% of the injected dose per gram of tissue, which is an acceptable result for a tracer for CNS targets. In the case of [¹⁸F]**8**, there was a rapid accumulation of radiotracer activity in the kidneys (data not shown). Marginal uptake of radiotracer was observed in the brain, which consequently renders [¹⁸F]**8** unsuitable for bioorthogonal click chemistry for CNS targets. This is particularly surprising as [¹⁸F]**8** showed promising results for passive permeability and P-gp transport.

Figure 5: Mean biodistribution curves plotted for decay-corrected percentage injected dose per gram (%ID/g) of blood and brain mass versus time in minutes as mean \pm SD, $n = 3$. A: [^{18}F]2; B: [^{18}F]8.



Click-Chemistry

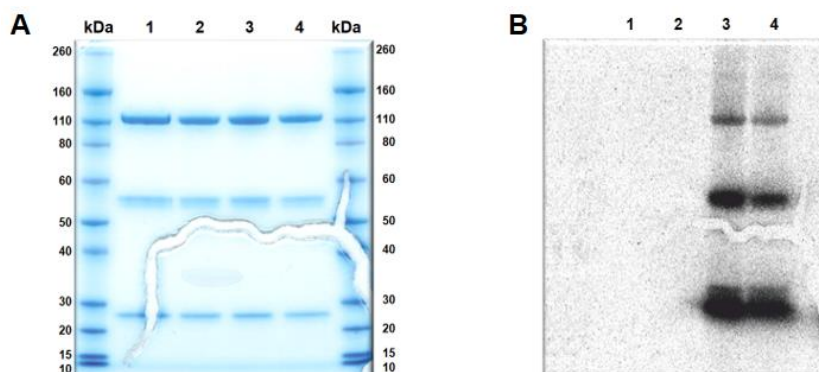
In order to demonstrate the reactivity of tetrazines towards a TCO-modified antibody, [^3H]1 was selected as a model example. For this purpose, the amyloid-beta specific, bispecific monoclonal antibody A β -mAb was functionalized with TCO to give A β -mAb-TCO. The functionalization took place *via* NHS-activated TCO **20** on lysine residues of the mAb in analogy to previously reported NHS conjugation chemistry.⁴ A β -mAb-TCO consists of 3 different types of chains: 1) two identical light chains with a molecular weight of 25 kDa; 2) one heavy chain of 55 kDa; 3) one heavy chain with a C-terminal fusion of a single-chain Fab fragment against the transferrin receptor (8D3, brain shuttle module) of total 110 kDa.

To determine the degree of labeling, the TCO-modified antibody was deglycosylated and the intact protein was analyzed by means of LC-MS. The MS data revealed an average of 2.5 TCO-moieties per antibody molecule (data not shown).

[^3H]1 was incubated with the A β -mAb-TCO in a molar ratio of 1:1 in PBS pH 7.4 for 1 h at 22 °C. After purification by dialysis against PBS pH 7, the tritiated mAb was obtained with a radiochemical purity of > 95%.

SDS-PAGE was used to separate the chains according to their molecular size. **Figure 6-A** shows a Coomassie Blue staining of A β -mAb (lane 1), A β -mAb-TCO (lane 2), and A β -mAb-TCO clicked with [^3H]1 from two independent labeling experiments (lanes 3, 4). Furthermore, an autoradiographic gel image obtained after a 5-day exposure is shown in **Figure 6-B**. Visual inspection of the bands at MW 110 kDa, 55 kDa, and 25 kDa reveals radiolabeling of all chains, which clearly shows that the selected tetrazine reacts with a TCO-functionalized antibody.

Figure 6: Gel electrophoresis separation of antibody constructs. **A:** Coomassie stained gel showing protein fragments of lane 1: A β -mAb; lane 2: A β -mAb-TCO; lanes 3, 4: A β -mAb-TCO after click reaction with [3 H]**1**. **B:** autoradiographic image of gel A shows tritium-labeled antibody fragments.



Conclusions

Eleven tetrazines were explored and classified with respect to their properties as potential CNS radiotracers and click partners for bioorthogonal PET imaging in combination with a TCO-modified brain-penetrating antibody based on multiple *in vitro* and *in vivo* experiments. These experiments included pH-dependent stability assessment, *in vitro* membrane permeability, P-gp efflux, and microsomal clearance. The biodistribution as well as the CFS/plasma ratios of selected tetrazines were determined in *in vivo* experiments. Out of the eleven tetrazines, Tzs **1** and **2** can be proposed as most promising candidates, which showed the best properties in terms of brain penetration and a decent balance between stability and reaction rate with a TCO moiety. In the next step, the selected tetrazines will be evaluated for their suitability as bioorthogonal click partners for PET imaging of misfolded proteins in the CNS on brain tissues and *in vivo*. The results obtained will be published separately.

Experimental Section

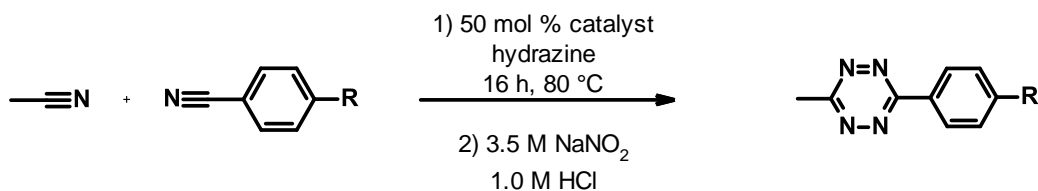
All chemical starting materials are commercially available and have been used without further purification. TCO-OH **21** was purchased from Fluorochem Ltd (Derbyshire, UK, #544896). Tritium labeled [3 H]methyl nosylate ([3 H]**22**, molar activity: 3.3 TBq/mmol = 88 Ci/mmol) was obtained from RC Tritec (Teufen, Switzerland) as solution in toluene. Liquid scintillation counting was accomplished using a HIDEX 300 SL and ULTIMATE GOLD™ cocktail (PerkinElmer Inc., Waltham, MA, USA). Analytical HPLC was performed using an Agilent 1200 series HPLC system (Santa Clara, CA, USA) using a Waters XBridge C18 column (4.6 mm x 150 mm, 3.5 μ m). HPLC conditions: mobile

phase [A]: (H₂O+0.05% TFA), [B]: (acetonitrile/H₂O+0.05% TFA), gradient 10% [B] to 70% [B] over 12 min. Radiochemical purity for tritium-labeled compounds was measured using the β Radioactivity HPLC detector RAMONA* with internal solid scintillator (Elysia-raytest, Straubenhardt, Germany). Preparative purification for tritium labeled tetrazine was performed by the use of Gilson PLC 2050 (Middleton, WI, USA), equipped with a Waters XBridge C18 column (10 mm x 300 mm, 5 μ m) under the following conditions: Solvent [A] was water + 5% acetonitrile + 0.05% trifluoroacetic acid (v/v/v) and solvent [B] was acetonitrile + 0.05% trifluoroacetic acid (v/v). The column was initially equilibrated at 10% [B] using a flow rate of 6 mL/min, with the absorbance monitored at 214 nm. Starting with isocratic conditions of 10% [B] for 4 minutes, a linear gradient to 70% [B] followed over 15 minutes. For purification of non-radiolabeled compounds, an Isco Combiflash[®] Rf+. (Lincoln, NE, USA) in combination with Disposable RediSep[™] silica gel columns (4 g) was used for flash column chromatography under the following conditions: Solvent [A] was heptane and solvent [B] was methyl *t*-butyl ether. The column was initially equilibrated at 20% [B] using a flow rate of 18 mL/min, with the absorbance monitored at 214 nm. The elution gradient consisted of isocratic conditions at 20% [B] for 4 minutes, followed by linear gradients to 100% [B] in 14 minutes, and finally isocratic conditions at 100% [B] over 5 minutes. Proton nuclear magnetic resonance (¹H NMR) spectra were recorded on a Bruker Avance III (300 MHz) instrument. ¹H chemical shifts (δ) are reported in parts per million (ppm) and referenced using residual solvent resonance relative to tetramethylsilane. Signal multiplicity is described using the following abbreviations: s (singlet), d (doublet), t (triplet), q (quartet) m (multiplet), dd (doublet of doublets), ddd (doublet of doublets of doublets), dt (doublet of triplets), br s (broad singlet), br d (broad doublet), and br dd (broad doublet of doublets). Coupling constants (*J*) are in hertz (Hz). LC-MS spectra were recorded with an Agilent LC-system high pressure gradient system, a CTC PAL auto sampler and an Agilent 6520 QTOF. The separation was achieved on a Zorbax Eclipse Plus C18 1.7 μ m 2.1 mm x 50 mm column at 55 °C; [A] = 0.01% formic acid in Water; [B] = 0.01% formic acid in acetonitrile at flow 1 mL/min. Gradient: 0 min 5% [B], 0.3 min 5% [B], 4.5 min 99 % [B], 5 min 99% [B]. The injection volume was 2 μ L. Ionization was performed in Agilent's Multimode source. Tritium labeled products were identified by HPLC comparison with characterized compounds from Roche pharma Research and Early Development (pRED). For ¹⁸F-radiochemistry, the semi-preparative high performance liquid chromatography system consisted of an Agilent 1260 Prep pump with a VICI injector, a Knauer 200 UV detector (254 nm), and a Bioscan Hot Cell interface with a diode radioactivity detector. The analytical chromatography system included an Agilent 1260 Infinity System equipped with a quaternary pump, HiP ALS autosampler, and DAD UV detector with a Max-Light flow cell set to 254 nm as well as a Bioscan Flow-Count interface with a NaI

radioactivity detector. Radioisotope production was performed by proton irradiation of [^{18}O]water (98%, Huayi Isotopes (Shanghai, China), approx. 1.7 mL) loaded into the niobium-body, high-yield ^{18}F -fluoride target of a General Electric Medical Systems (GEMS; Waukesha, WI) PETtrace cyclotron.

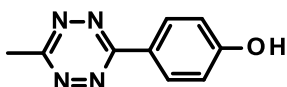
Synthesis of Tetrazine Derivatives

General procedure for 3-methyl-6-aryl-tetrazine (Me-Tz)-based intermediates



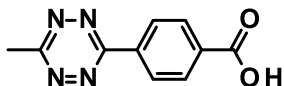
To a 25 mL sealable tube, equipped with a stir bar, 3.8 mmol of 4-cyanoaryl-derivative, 1.9 mmol catalyst ($\text{Ni}(\text{OTf})_2$ or $\text{Zn}(\text{OTf})_2$), 188 mmol hydrazine monohydrate, and 38 mmol acetonitrile (2 mL) was added to give a purple colored solution. The tube was sealed and the reaction solution was stirred for 16 h at 80 °C. The reaction solution was cooled to 22 °C and transferred into 250 mL three-neck round bottom flask. 3.5 M sodium nitrite solution (25 mL) was added with ice bath cooling, followed by dropwise addition of 1 M hydrogen chloride (75 mL) until no gas evolution was observed and a pH of 3-4 was reached. The mixture was extracted 3x with ethyl acetate, the organic phase was separated, dried over sodium sulfate, and concentrated in vacuo. The crude residue was purified using silica-based flash chromatography to yield 38 – 98% of the desired product.

4-(6-Methyl-1,2,4,5-tetrazine-3-yl)phenol (**12**)



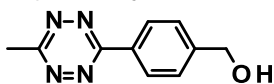
Starting from 4-hydroxybenzotrile and $\text{Zn}(\text{OTf})_2$, the title compound was isolated as an orange solid. Yield: 38%, purity: 98%. ^1H NMR (300 MHz, CDCl_3) δ 8.52 (d, $J = 9.08$ Hz, 2H), 7.03 (d, $J = 9.08$ Hz, 2H), 5.21 (s, 1H), 3.07 (s, 3H). LC-MS (ESI) m/z : 189.4 ($[\text{M}+\text{H}]^+$).

4-(6-Methyl-1,2,4,5-tetrazin-3-yl)benzoic acid (13)



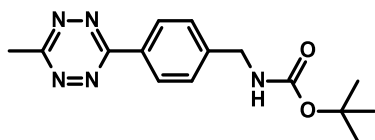
Starting from 4-cyanobenzoic acid and Ni(OTf)₂, the title compound was isolated as a pink solid. Yield: 93%, purity: 80%. ¹H NMR (300 MHz, CDCl₃) δ 8.59 (d, *J* = 8.48 Hz, 2H), 8.20 (d, *J* = 8.48 Hz, 2H), 3.03 (s, 3H). LC-MS (ESI) *m/z*: 215.3 ([M-H]⁻).

[4-(6-Methyl-1,2,4,5-tetrazine-3-yl)phenyl]methanol (14)



Starting from 4-(hydroxymethyl)benzotrile and Ni(OTf)₂, the title compound was isolated as a purple solid. Yield: 50%, purity: 95%. ¹H NMR (300 MHz, DMSO-*d*₆) δ 8.44 (d, *J* = 8.48 Hz, 2H), 7.60 (d, *J* = 8.48 Hz, 2H), 5.41 (t, *J* = 5.75 Hz, 1H), 4.64 (d, *J* = 5.75 Hz, 2H), 2.99 (s, 3H). LC-MS (ESI) *m/z*: 203.4 ([M+H]⁺).

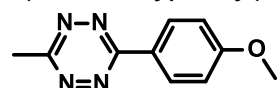
tert-Butyl N-[[4-(6-methyl-1,2,4,5-tetrazin-3-yl)phenyl]methyl]carbamate (15)



Starting from *tert*-butyl-4-cyanobenzylcarbamate and Ni(OTf)₂, the title compound was isolated as a pink solid. Yield: 47%, purity: 95%. ¹H NMR (300 MHz, CDCl₃) δ 8.56 (d, *J* = 8.36 Hz, 2H), 7.56-7.51 (br, 1H), 7.50 (d, *J* = 8.36 Hz, 2H), 4.44 (br d, *J* = 5.74 Hz, 2H), 3.10 (s, 3H), 1.48 (s, 9 H). LC-MS (ESI) *m/z*: 302.2 ([M+H]⁺).

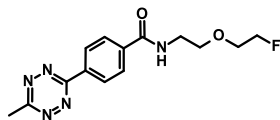
Synthesis of 3-methyl-6-aryl-tetrazines (Me-Tzs)

3-(4-Methoxyphenyl)-6-methyl-1,2,4,5-tetrazine (1)



21.5 mg (114 μmol) of **12** was dissolved in acetone (1.14 mL) to give a pink solution. Cesium carbonate (74.4 mg, 228 μmol) and iodomethane (16.2 mg, 7.13 μL, 114 μmol), dissolved in 0.1 mL acetone, were added to the solution. The solution was stirred at 22 °C. After 30 minutes, the reaction solution was poured in 10 mL 4 M ammonia hydrogen chloride and extracted 2 times with 15 mL ethyl acetate. The combined organic layers were dried over sodium sulfate, filtered, and concentrated to dryness. The crude material was purified by flash chromatography (silica gel, 4 g column, 25% EtOAc in Heptane in 16 minutes) to yield 18.6 mg (80%) of the title compound **1** as a pink solid. ¹H NMR (300 MHz, CDCl₃) δ 8.55 (d, *J* = 9.08 Hz, 2H), 7.09 (d, *J* = 9.08 Hz, 2H), 3.92 (s, 3H), 3.06 (s, 3H). LC-MS (ESI) *m/z*: 203.4 ([M+H]⁺).

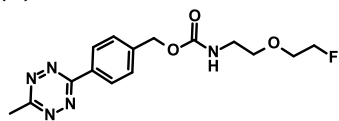
N-[2-(2-Fluoroethoxy)ethyl]-4-(6-methyl-1,2,4,5-tetrazin-3-yl)benzamide (**2**)



In a 10 mL two-necked flask, 2-(2-fluoroethoxy)ethanamine (40 mg, 373 μmol) was dissolved in 4 mL *N,N*-dimethylformamide. **13** (50 mg, 231 μmol) and Hünigs base (259 mg, 350 μL , 2.00 mmol) were added to the reaction mixture followed by 1-propanephosphonic acid cyclic anhydride (367 mg, 1.15 mmol). The reaction solution was stirred at 22 °C. After 16 h, the solution was poured into 10 mL water and extracted with ethyl acetate (2 x 25 mL). The organic layers were combined, dried over sodium sulfate, filtered and concentrated in vacuo. The crude material was purified by flash chromatography to get 40 mg (yield: 57%) of the title compound as a pink solid with a purity of 98%.

^1H NMR (300 MHz, $\text{DMSO-}d_6$) δ 8.80 (t, J = 5.45 Hz, 1H), 8.55 (d, J = 8.68 Hz, 2H), 8.11 (d, J = 8.68 Hz, 2H), 4.62-4.46 (m, 2H), 3.74-3.62 (m, 4H), 3.48 (q, J = 5.85 Hz, 2H), 3.02 (s, 3H). LC-MS (ESI) m/z : 306.4 ($[\text{M}+\text{H}]^+$).

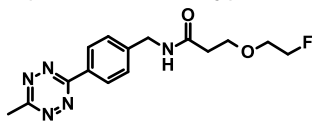
[4-(6-Methyl-1,2,4,5-tetrazin-3-yl)phenyl]methyl *N*-[2-(2-fluoroethoxy)ethyl]carbamate (**3**)



14 (50 mg, 247 μmol) was dissolved in 2 mL tetrahydrofuran to give a pink solution. Carbonyldiimidazole (48.1 mg, 297 μmol) was added at 22 °C and the reaction solution was stirred for 3 h. A solution of 2-(2-fluoroethoxy)ethanamine hydrochloride (35.5 mg, 247 μmol) in 1 mL tetrahydrofuran and Hünigs base (63.9 mg, 86.4 μL , 495 μmol) were added to allow the solution to stir at 22 °C for 16 h. The solution was concentrated and purified by flash chromatography to give 61 mg (yield: 74%) of the desired product as a pink solid with a purity of 98%.

^1H NMR (300 MHz, $\text{DMSO-}d_6$) δ 8.47 (d, J = 8.28 Hz, 2H), 7.62 (d, J = 8.28 Hz, 2H), 7.44 (br t, J = 5.25, 1H), 5.16 (s, 2H), 4.60-4.46 (m, 2H), 3.69-3.59 (m, 2H), 3.47 (t, J = 5.85 Hz, 2H), 3.19 (m, 2H), 3.00 (s, 3H). LC-MS (ESI) m/z : 336.4 ($[\text{M}+\text{H}]^+$).

3-(2-Fluoroethoxy)-*N*-[[4-(6-methyl-1,2,4,5-tetrazin-3-yl)phenyl]methyl]propanamide (**4**)

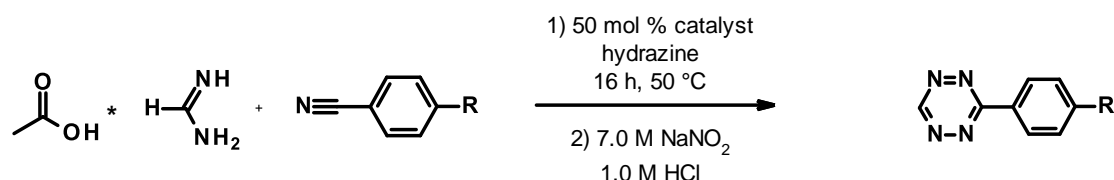


15 (120 mg, 398 μmol) was dissolved in 1.5 mL dichloromethane to give a pink solution. Trifluoroacetic acid (454 mg, 307 μl , 3.98 mmol) was added and the solution was stirred at 22 °C for 30 min. In presence of toluene, the solution was concentrated in vacuo and the residue dissolved in 6 mL *N,N*-dimethylformamide. 3-(2-fluoroethoxy)propionic acid

(81.3 mg, 478 μmol), *N,N,N',N'*-tetramethyl-*O*-(benzotriazol-1-yl)uronium tetrafluoroborate (192 mg, 597 μmol) and Hünigs base (257 mg, 348 μL , 1.99 mmol) were added and the reaction solution was stirred at 22 °C for 3 h. The reaction mixture was diluted with water and extracted with dichloromethane. The organic layers were combined, dried over sodium sulfate, concentrated in vacuo, and the crude product was purified by flash chromatography to give 76 mg (yield: 60%) of the desired product as a pink solid in a purity of 98%.

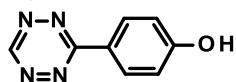
^1H NMR (300 MHz, CDCl_3) δ 8.55 (d, $J = 8.48$ Hz, 2H), 7.51 (d, $J = 8.48$ Hz, 2H), 6.67 (br s, 1H), 4.64-4.45 (m, 4H), 3.82-3.69 (m, 4H), 3.10 (s, 3H), 2.58 (t, $J = 5.65$ Hz, 2H). LC-MS (ESI) m/z : 320.4 ($[\text{M}+\text{H}]^+$).

General procedure for 3-*H*-6-aryl-tetrazine (H-Tz)-based intermediates



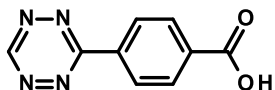
In a 25 mL sealable tube, equipped with a stir bar, 4.2 mmol of 4-cyano aryl derivative, 42.0 mmol formamidine acetate, 2.1 mmol catalyst (Ni(OTf)₂ or Zn(OTf)₂), 210 mmol hydrazine monohydrate were dissolved in 2.5 mL *N,N*-dimethylformamide to give a yellow colored solution. The tube was sealed and the reaction solution was stirred for 16 h at 50 °C. The reaction solution was cooled to 22 °C and transferred into 250 mL three-neck round-bottom flask. 7 M sodium nitrite solution (12 mL) was added with ice bath cooling, followed by dropwise addition of 1 M hydrogen chloride (75 mL) until no gas evolution was observed and a pH of 3-4 was reached. The mixture was extracted 3x with ethyl acetate, the organic phases were separated, dried over sodium sulfate, and concentrated in vacuo. The crude residue was purified using flash chromatography to yield 14 – 17% of the desired product.

4-(1,2,4,5-Tetrazin-3-yl)phenol (**16**)



Starting from 500 mg 4-hydroxybenzonitrile (4.2 mmol) and Zn(OTf)₂, 122 mg of the title compound was isolated by basic alumina-based flash chromatography (2% to 10% methanol in dichloromethane) as a pink solid. Yield: 17%, purity: 98%. ^1H NMR (300 MHz, DMSO-*d*₆) δ 10.45 (s, 1H), 8.37 (d, $J = 7.87$ Hz, 2H), 7.03 (d, $J = 7.87$ Hz, 2H). LC-MS (ESI) m/z : 173.1 ($[\text{M}-\text{H}]^-$).

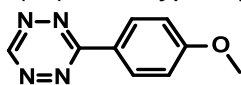
4-(1,2,4,5-Tetrazin-3-yl)benzoic acid (**17**)



Starting from 4-cyanobenzoic acid and Ni(OTf)₂, the title compound was isolated by silica-based flash chromatography (2% to 10% ethyl acetate in dichloromethane) as a pink solid. Yield: 14%, purity: 99%. ¹H NMR (300 MHz, DMSO-*d*₆) δ 13.47 (b, 1H), 10.66 (s, 1H), 8.61 (d, *J* = 8.48 Hz, 2H), 8.22 (d, *J* = 8.48 Hz, 2H). LC-MS (ESI) *m/z*: 201.3 ([M+H]⁺).

Synthesis of 3-H-6-aryl-tetrazines (H-Tzs)

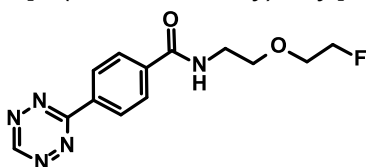
3-(4-(Methoxyphenyl)-1,2,4,5-tetrazine (**5**)



In a 25 mL two-necked flask, 195 mg (1.12 mmol) **16** was dissolved in 8 mL acetone to give a pink solution. 730 mg (2.24 mmol) cesium carbonate and iodomethane (159 mg, 69.9 μL, 1.12 mmol) were added. After stirring for 1 h at 22 °C, the reaction mixture was poured into 10 mL water and extracted with ethyl acetate (2 x 20 mL). The organic layers were combined, washed with brine, dried over sodium sulfate and concentrated in vacuo. The crude material was purified by flash chromatography to give 20 mg (yield: 10%) of the desired compound **5** as a pink oil with a purity of 99%.

¹H NMR (300 MHz, CDCl₃) δ 10.50 (s, 1H), 8.48 (m, 2H), 7.23 (m, 2H), 3.93 (s, 3H). LC-MS (ESI) *m/z*: 187.1 ([M-H]⁻).

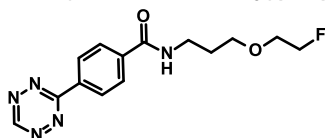
N-[2-(2-Fluoroethoxy)ethyl]-4-(1,2,4,5-tetrazin-3-yl)benzamide (**6**)



In a 10 mL round-bottomed flask, **17** (45 mg, 223 μmol) was dissolved in 4 mL *N,N*-dimethylformamide. 2-(2-Fluoroethoxy)ethanamine hydrochloride (38.4 mg, 267 μmol), Hünigs base (144 mg, 194 μL, 1.11 mmol), and 1-propanephosphonic acid cyclic anhydride 50% in *N,N*-dimethylformamide (354 mg, 328 μL, 556 μmol) were added. The reaction solution was stirred at 22 °C for 2 h. The reaction solution was poured into 5 mL saturated sodium hydrogen carbonate solution and extracted with ethyl acetate (2 x 30 mL). The combined organic layers were washed with brine, dried over sodium sulfate and concentrated dryness. The crude material was purified using flash chromatography to give 21 mg (yield: 32%) of the title compound **6** as a pink solid with a purity of 99%.

$^1\text{H NMR}$ (300 MHz, CDCl_3) δ 10.27 (s, 1H), 8.72 (d, $J = 8.88$ Hz, 2H), 8.02 (d, $J = 8.88$ Hz, 2H), 6.71 (br s, 1H), 4.69-4.53 (m, 2H), 3.83-3.75 (m, 6H). LC-MS m/z : 292.4 ($[\text{M}+\text{H}]^+$).

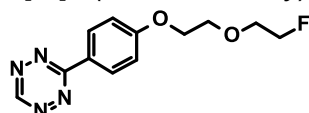
N-[3-(2-Fluoroethoxy)propyl]-4-(1,2,4,5-tetrazin-3-yl)benzamide (**7**)



This compound was prepared following the synthesis procedure of **6** from **17** (45 mg, 223 μmol) and 3-(2-fluoro-ethoxy)-propionic acid (41 mg, 334 μmol). 13 mg (yield: 19%) of the title compound was isolated as a pink solid with a purity of 99%.

$^1\text{H NMR}$ (300 MHz, CDCl_3) δ 10.26 (s, 1H), 8.70 (d, $J = 8.88$ Hz, 2H), 8.03 (d, $J = 8.88$ Hz, 2H), 7.23 (br s, 1H), 4.69-4.54 (m, 2H), 3.74 (m, 6H), 1.97 (dt, $J = 11.45, 5.68$ Hz, 2H). LC-MS (ESI) m/z : 306.2 ($[\text{M}+\text{H}]^+$).

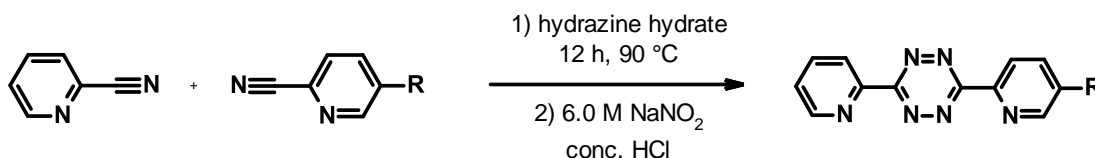
3-[4-[2-(2-Fluoroethoxy)ethoxy]phenyl]-1,2,4,5-tetrazine (**8**)



This compound was prepared following the synthesis procedure of **5** from **16** (91 mg, 530 μmol) and 2-(2-fluoroethoxy)ethyl 4-methylbenzene-1-sulfonate (289 mg, 1.06 mmol). 34 mg (yield: 24%) of the title compound was isolated as a pink solid with a purity of 99%.

$^1\text{H NMR}$ (300 MHz, CDCl_3) δ 10.12 (s, 1H), 8.57 (d, $J = 8.88$ Hz, 2H), 7.11 (d, $J = 8.88$ Hz, 2H), 4.67-4.55 (m, 2H), 4.27 (m, 2H), 3.95 (m, 2H), 3.88-3.80 (m, 2H). LC-MS (ESI) m/z : 265.2 ($[\text{M}+\text{H}]^+$).

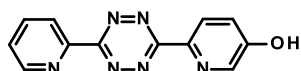
General procedure for 3,6-bis(2-pyridyl)-tetrazine (Py-Tz)-based intermediates



A suspension of 2-cyanopyridine (8.33 mmol) and 2-cyano-5-hydroxypyridine or 2-cyano-5-aminopyridine in hydrazine hydrate (33.33 mmol) was heated at 90 °C for 12 h. The reaction mixture was cooled to 22 °C. The resulting precipitate was separated from the solution, washed with cold water, and freeze-dried. The intermediate was purified using flash chromatography over silica gel, deactivated with 7% triethylamine/hexane. In the next step, the purified intermediate was dissolved in tetrahydrofuran. A stream of nitrous acid gases, generated by adding 6 M sodium nitrite solution (6 mL) to

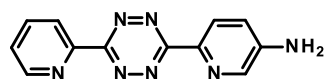
concentrated hydrogen chloride (5 mL) was bubbled through the solution over 1 h. The color of the mixture changed from orange to red and a solid formed. Solvent and excess nitrous gases were evaporated to give a red powder, which was dissolved in dichloromethane and extracted with saturated sodium hydrogen carbonate solution. The layers were separated and the aqueous layer was extracted with dichloromethane. The combined organic layers were washed with brine, dried over sodium sulfate, filtered, and evaporated to give a colored solid.

6-[6-(2-Pyridyl)-1,2,4,5-tetrazin-3-yl]pyridin-3-ol (**18**)



Starting from 2-cyano-5-hydroxypyridine, the title compound **18** was isolated as a yellow solid. Yield: 12%, purity: 99%. ¹H NMR (300 MHz, DMSO-*d*₆) δ 10.93 (br s, 1 H), 8.93 (d, *J* = 4.67 Hz, 1H), 8.58 (dt, *J* = 7.87, 1.01 Hz, 1H), 8.53 (d, *J* = 8.68 Hz, 1H), 8.47 (d, *J* = 2.42 Hz, 1H), 8.16 (dt, *J* = 7.77, 1.82 Hz, 1H), 7.73 (ddd, *J* = 7.62, 4.79, 1.11 Hz, 1H), 7.48 (dd, *J* = 8.68, 2.83 Hz, 1H). LC-MS (ESI) *m/z*: 253.2 ([M+H]⁺).

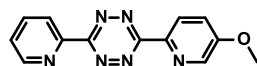
6-[6-(2-Pyridyl)-1,2,4,5-tetrazin-3-yl]pyridin-3-amine (**19**)



Starting from 2-cyano-5-aminopyridine, the title compound **19** was isolated as a red solid. Yield: 20%, purity: 99%. ¹H NMR (300 MHz, DMSO-*d*₆) δ 8.91-8.89 (m, 1H), 8.55-8.52 (m, 1H), 8.36 (d, *J* = 8.66 Hz, 1H), 8.24 (d, *J* = 2.82 Hz, 1H), 8.13 (dt, *J* = 7.70, 1.81 Hz, 1H), 7.69 (ddd, *J* = 7.70, 4.68, 1.21 Hz, 1H), 7.13 (dd, *J* = 8.66, 2.82 Hz, 1H), 6.80-5.90 (b, 2H) LC-MS (ESI) *m/z*: 252.2 ([M+H]⁺).

Synthesis of 3,6-bis(2-pyridyl)-tetrazines (Py-Tzs)

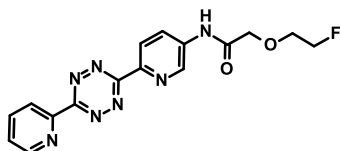
3-(5-Methoxy-2-pyridyl)-6-(2-pyridyl)-1,2,4,5-tetrazine (**9**)



In a 10 mL pear-shaped flask, **18** (10 mg, 39.6 μmol) was dissolved in 100 μL toluene and 100 μL acetone to give a pink solution. Cesium carbonate (25.8 mg, 79.3 μmol) and methyl-4-nitrobenzenesulfonate (**22**) (8.61 mg, 39.6 μmol) were added. The reaction mixture was stirred at 22 °C for 2 h. The crude material was concentrated and purified using flash chromatography to give 8.6 mg (yield: 81%) of the title compound **9** as a pink solid with a purity of 99%.

¹H NMR (300 MHz, DMSO-*d*₆) δ 8.93 (d, *J* = 4.46 Hz, 1H), 8.62 (m, 3H), 8.15 (dt, *J* = 7.77, 1.61 Hz, 1H), 7.73 (m, 2H), 4.00 (s, 3H). LC-MS (ESI) *m/z*: 267.1 ([M+H]⁺).

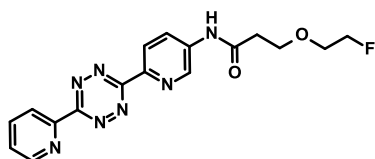
2-(2-Fluoroethoxy)-N-[6-[6-(2-pyridyl)-1,2,4,5-tetrazin-3-yl]-3-pyridyl]acetamide (10)



To a solution of **19** (300 mg, 1.2 mmol) in 20 mL dry tetrahydrofuran was added fluoroacetic acid sodium salt (120 mg, 1.2 mmol) followed by Hünigs base (0.79 mL, 4.78 mmol) and 1-propanephosphonic acid cyclic anhydride (50% solution in ethyl acetate, 2 mL, 3.0 mmol) at 25 °C. The reaction mixture was refluxed for 16 h. Volatiles were removed under reduced pressure. Resultant crude material was purified using flash chromatography over silica gel, deactivated with 7% triethylamine/hexane. 115 mg (yield: 31%) of the title compound **10** was isolated as a red solid with a purity of 99%.

¹H NMR (300 MHz, CDCl₃) δ 8.99 (ddd, *J* = 4.71, 1.74, 0.91 Hz, 1H), 8.96 (d, *J* = 2.42 Hz, 1H), 8.79-8.74 (m, 3H), 8.61 (dd, *J* = 8.66, 2.62 Hz, 1H), 8.01 (dt, *J* = 7.70, 1.71 Hz, 1H), 7.58 (ddd, *J* = 7.70, 4.73, 1.16 Hz, 1H), 4.76-4.68 (m, 2H), 4.25 (s, 2H), 3.97-3.92 (m, 2H). LC-MS (ESI) *m/z*: 356.1 ([M+H]⁺).

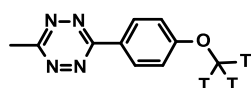
3-(2-Fluoroethoxy)-N-[6-[6-(2-pyridyl)-1,2,4,5-tetrazin-3-yl]-3-pyridyl]propanamide (11)



This compound was prepared following the synthesis procedure of **10** from **19** (250 mg, 1 mmol) and 3-(2-fluoro-ethoxy)-propionic acid (135 mg, 1 mmol). 135 mg (yield: 37%) of the title compound **11** was isolated as a red solid with a purity of 91%. ¹H NMR (300 MHz, DMSO-*d*₆) δ 10.63 (s, 1H), 9.06 (d, *J* = 2.30 Hz, 1H), 8.94 (d, *J* = 4.28 Hz, 1H), 8.63 (d, *J* = 8.70 Hz, 1H), 8.59 (d, *J* = 7.80 Hz, 1H), 8.44 (dd, *J* = 8.70, 2.30 Hz, 1H), 8.16 (dt, *J* = 7.80, 1.44 Hz, 1H), 7.73 (m, 1 H), 4.59-4.47 (m, 2H), 3.79 (t, *J* = 6.12 Hz, 2H), 3.72-3.64 (m, 2H), 2.71 (t, *J* = 6.12 Hz, 2H). LC-MS (ESI) *m/z*: 370.2 ([M+H]⁺).

Tritium-labeled compounds

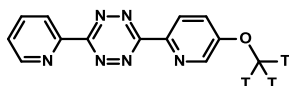
[³H]3-(4-Methoxyphenyl)-6-methyl-1,2,4,5-tetrazine ([³H]1)



[³H]Methyl nosylate ([³H]**22**) (1.85 GBq, 50 mCi, 132 μg, 0.591 μmol), cesium carbonate (481 μg, 1.48 μmol), and the phenol-precursor **12** (333 μg, 1.77 μmol) were dissolved in 400 μL tetrahydrofuran. The solution was stirred at 50 °C for 5 h. The reaction mixture was diluted with 1 mL dichloromethane and passed through a strong anion exchange (SAX) solid phase extraction (SPE) cartridge to remove the sulfonic acid by-product. The

solvent was removed and the residue dissolved in acetonitrile/water to purify the compound using preparative-HPLC to yield 278 MBq (7.5 mCi, yield: 15%) of [³H]**1** in a radiochemical purity of 98%. The specific activity was 3.3 TBq/mmol (88 Ci/mmol). The specific activity was taken from the starting compound [³H]**22**, as [³H]**1** did not ionize in mass spectrometric analysis and therefore no isotope pattern was determined.

*[³H]3-(5-Methoxy-2-pyridyl)-6-(2-pyridyl)-1,2,4,5-tetrazine ([³H]**9**)*

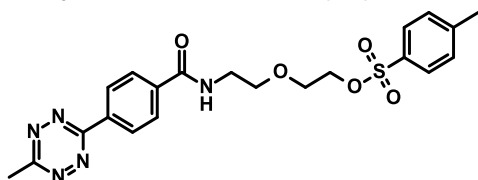


[³H]-**9** was synthesis in analogy to the procedure described for [³H]**1**. Starting with **18** and [³H]**22**, 33.3 MBq (0.9 mCi) was isolated, which corresponds to a radiochemical yield of 2%, in a radiochemical purity of 97%. Since the same batch of [³H]methyl nosylate was used for the synthesis, the achieved specific activity was 3.3 TBq/mmol (88 Ci/mmol). The specific activity was taken from the starting compound [³H]**22**, since [³H]**9** did not ionize in mass spectrometric analysis and therefore no isotope pattern was determined.

Fluorine-18-labeled compounds

Precursors for ¹⁸F-compounds

*2-(2-((4-(6-Methyl-1,2,4,5-tetrazin-3-yl)benzyloxy)carbonylamino)ethoxy)ethyl 4-methylbenzenesulfonate (**23**)*

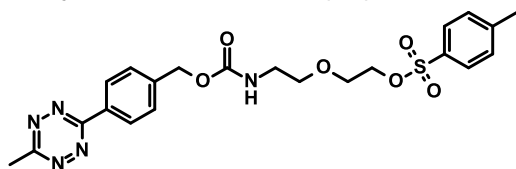


In a 25 mL round-bottomed flask, **13** (230 mg, 1.06 mmol) was dissolved in 8 mL *N,N*-dimethylformamide to give a pink solution. After the addition of 2-(2-aminoethoxy)ethanol (134 mg, 128 μ L, 1.28 mmol), Hünigs base (550 mg, 742 μ L, 4.26 mmol), and 1-propanephosphonic acid cyclic anhydride (50% solution in ethyl acetate, 1.6 g, 1.57 mL, 3.0 mmol), the reaction solution was stirred for 1 h at 22 °C. The reaction solution was poured into 10 mL saturated sodium hydrogen carbonate solution, extracted with ethyl acetate (2 x 30 mL) and brine (2x 20 mL). The combined organic phases were dried with sodium sulfate, transferred into a 25 mL round-bottomed flask, and concentrated in vacuo to dryness. The residue (195 mg) was dissolved in 10 mL chloroform. Pyridine (200 mg, 205 μ L, 2.53 mmol) and 4-methylbenzene-1-sulfonyl chloride (362 mg, 1.9 mmol) were added and the reaction solution was stirred for 20 h and 22 °C. After extraction with 10 mL water, the organic phase was washed with 10 mL

brine, dried with sodium sulfate, and purified by silica based chromatography to give 211 mg (yield: 44%) of the title compound **20** in a purity of 99%.

¹H NMR (300 MHz, CDCl₃) δ 8.67 (d, *J* = 8.48 Hz, 2H), 8.03 (d, *J* = 8.48 Hz, 2H), 7.78 (d, *J* = 8.20 Hz, 2H), 7.33 (d, *J* = 8.20 Hz, 2H), 6.82 (br s, 1H), 4.25 (m 2H), 3.74 (m, 2H), 3.68 (m, 4H), 3.12 (s, 3H), 2.42 (s, 3H). LC-MS (ESI) *m/z*: 458.4 ([M+H]⁺).

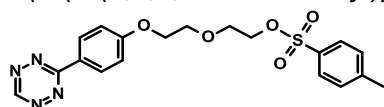
2-(2-((4-(6-Methyl-1,2,4,5-tetrazin-3-yl)benzyloxy)carbonylamino)ethoxy)ethyl 4-methylbenzenesulfonate (24)



14 (71 mg, 351 μmol) and carbonyldiimidazole (62.6 mg, 386 μmol) were dissolved in 3 mL tetrahydrofuran and stirred at 22 °C for 2 h. 2-(2-Aminoethoxy)ethanol (44.3 mg, 42.3 μL, 421 μmol) was added and the reaction solution was stirred at 22 °C for 4 h. The solvent was removed by evaporation and the residue purified by silica-based chromatography (50-100% ethyl acetate in heptane) to give 98 mg (yield: 84%) of the hydroxy-intermediate, which was dissolved in 3 mL dichloromethane and pyridine (140 mg, 143 μL, 1.76 mmol) to give a pink solution. 4-Methylbenzene-1-sulfonyl chloride (112 mg, 588 μmol) was added and the solution was stirred at 22 °C for 48 h. The reaction mixture was poured into 10 mL water and extracted with dichloromethane (2 x 25 mL). The organic layers were washed with brine, dried over sodium sulfate, and concentrated in vacuo to purify the crude product by silica-based chromatography (40-100% ethyl acetate in heptane). 130 mg (overall yield: 76%) of the title compound was isolated in a purity of 98%.

¹H NMR (300 MHz, CDCl₃) δ 8.59 (d, *J* = 8.28 Hz, 2H), 7.80 (d, *J* = 8.28 Hz, 2H), 7.58 (d, *J* = 8.28 Hz, 2H), 7.33 (d, *J* = 8.28 Hz, 2H), 5.22 (s, 2H), 5.16 (br s, 1H), 4.18 (m, 2H), 3.66 (m, 2H), 3.51 (t, *J* = 5.10, 2H), 3.36 (q, *J* = 5.10, 2H), 3.10 (s, 3H), 2.43 (s, 3H). LC-MS (ESI) *m/z*: 488.4 ([M+H]⁺).

2-(2-(4-(1,2,4,5-Tetrazin-3-yl)phenoxy)ethoxy)ethyl 4-methylbenzenesulfonate (25)

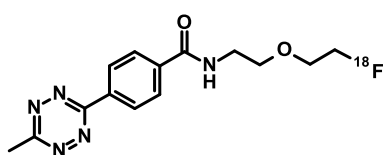


The intermediate 2-(2-(4-(1,2,4,5-tetrazin-3-yl)phenoxy)ethoxy)ethanol was synthesized according to the general procedure for 3-H-6-aryl-tetrazine (H-Tz)-based intermediates, starting with 4-(2-(2-hydroxyethoxy)ethoxy)benzotrile (500 mg, 2.41 mmol) and Zn(OTf)₂. 170 mg (yield: 24%) of the intermediate was isolated after silica-based chromatography as a pink solid. 126 mg (480 μmol) of the crude intermediate and 4-methylbenzene-1-sulfonyl chloride (550 mg, 2.9 mmol) were dissolved in 2 mL

dichloromethane. After the addition of pyridine (456 mg, 465 μ L, 5.77 mmol) at 0 °C, the reaction solution was stirred for 1 h at 0 °C. The solution was diluted with 10 mL dichloromethane and poured into 10 mL water and extracted with dichloromethane (3 x 10 mL). The combined organic phases were washed with 10 mL brine, dried with magnesium sulfate, and purified by silica-based chromatography to give 176 mg (overall yield: 17%) of the title compound **21** as a pink solid in a purity of 98%.

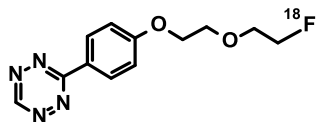
^1H NMR (300 MHz, CDCl_3) δ 10.14 (s, 1H), 8.58 (m, 2H), 7.80 (d, J = 8.48 Hz, 2H), 7.32 (d, J = 8.07 Hz, 2H), 7.08 (m, 2H), 4.22 (m 2H), 4.18 (m, 2H), 3.86 (m, 2H), 3.80 (m, 2H), 2.42 (s, 3H). LC-MS (ESI) m/z : 417.2 ($[\text{M}+\text{H}]^+$).

N-[2-(2- ^{18}F)Fluoranyloxy]ethyl]-4-(6-methyl-1,2,4,5-tetrazin-3-yl)benzamide (^{18}F **2**)



Precursor **23** (5 mg) was dissolved in 200 μ L dimethylsulfoxide and 300 μ L tert-butyl alcohol prior to the end of bombardment (EOB). At EOB, the aqueous ^{18}F -fluoride ion, produced by proton bombardment of ^{18}O -enriched water (57 μ A for 43 minutes), was trapped on an ion exchange column. The ion exchange column was eluted with 150 μ L of a stock solution, consist of 6.6 mg Kryptofix 2.2.2 and 26.0 mg potassium oxalate in 1 mL of ethanol:water 1:1, into the reaction vial, followed by 250 μ L ethanol. The fluoride solution was evaporated to dryness at 110 °C *via* nitrogen flow and further dried azeotopically by 2x 250 μ L ethanol. The reaction vial was cooled with compressed air for 2 minutes. The precursor was added and then heated in a thermal heating block at 110 °C for 9 minutes, after which the vial was cooled and the solution was quenched with 2 mL of 10 mM ammonium formate. The reaction mixture was injected onto semi-preparative HPLC column (XBridge C18, 10x150 mm, 10 μ m) eluted with 30:70 methanol/ 10mM ammonium formate at 10 mL/min. The HPLC effluent was monitored at 254 nm and an in-line radioactivity detector. ^{18}F **2** was collected in 50 mL water. The product solution was eluted through a Waters Oasis HLB Light cartridge, washed with 10 mL Milli-Q water, then SPE was manually eluted with 0.4 mL absolute ethanol and followed by 4 mL normal saline into the final product vial. Aliquots were removed from the final product vial for qualitative control analysis using analytical HPLC (column: XBridge C18, 100 x 4.6 mm, 3.5 μ m) eluted with 20:80 acetonitrile/0.1M ammonium formate at 2 mL/min (RT = 4.2 minutes) and monitored at 318 nm to determine radiochemical and chemical purity and chemical identity. 4,329 MBq (11.7 mCi) of the title compound ^{18}F **2** was isolated with a radiochemical purity of 86%.

3-[4-[2-(2-[¹⁸F]Fluoroethoxy)ethoxy]phenyl]-1,2,4,5-tetrazine ([¹⁸F]**8**)



Precursor **25** (5.5 mg) was dissolved in 400 μ L dimethylsulfoxide prior to the end of bombardment (EOB). At EOB, the aqueous ¹⁸F-fluoride ion, produced by proton bombardment of ¹⁸O-enriched water (60 μ A for 30 minutes), was trapped on an ion exchange column. The ion exchange column was eluted with 150 μ L of a stock solution, consist of 38 mg Kryptofix 2.2.2 and 9 mg potassium bicarbonate in 1 mL of acetonitrile:water 1:3, into the reaction vial, followed by 250 μ L acetonitrile. The fluoride solution was evaporated to dryness at 110 °C *via* nitrogen flow and further dried azeotopically by 2x 250 μ L acetonitrile. The reaction vial was remotely transferred to the microwave cavity (Resonance Instruments). And cooled with compressed air for 2 minutes. The precursor was added and then microwaved for 30 seconds at 50 W after which the solution was cooled, then quenched with 3 mL of water. The reaction mixture was injected onto semi-preparative HPLC column (XBridge C18, 10x150 mm, 10 μ m) eluted with 20/80 acetonitrile/0.1M ammonium formate at 15 mL/min. The HPLC effluent was monitored at 254 nm and an in-line radioactivity detector. [¹⁸F]**8** (RT 18 minutes) was collected in 50 mL water, containing 400 mg ascorbic acid. The product solution was eluted through a Waters C18 Sep Pak Plus cartridge, washed with 10 mL Milli-Q water, then eluted with 1 mL absolute ethanol and followed by 10 mL normal saline into the final product vial *via* a 0.22 μ m Millipore FG sterilizing filter. Aliquots were removed from the final product vial for qualitative control analysis using analytical HPLC (column: XBridge C18, 100 x 4.6 mm, 3.5 μ m) eluted with 30/70 acetonitrile/0.1M ammonium formate at 2 mL/min (RT = 5.5 minutes) and monitored at 318 nm to determine radiochemical and chemical purity, specific activity and chemical identity. [¹⁸F]**8** (2523 MBq; 68.3 mCi) was isolated with a specific activity of 1.5 GBq/ μ mol (40 Ci/ μ mol) and a radiochemical purity of 95%.

Physicochemical Properties of Tetrazine Derivatives

CNS-PET-MPO scores were calculated based on the chemical structures in analogy to a previous report.³⁸ ClogD calculations were replaced by an in house ML model (mlLogD). ALogP was used instead of CLogP. pKa was calculated with the program MOKA. All the properties were weighted equally with a desirability score ranging from 0.0 to 1.0, and the summation of scores from these parameters yielded the final MPO score of each individual structure.

Standardized Aqueous Stability Assay

Tetrazine derivatives were dissolved in the pH corresponding buffer at 37 °C for 2 h. pH 1: 2 mM glycine; 120 mM hydrochloric acid; 3 mM sodium chloride; pH 4: 56 mM citric acid; 44 mM hydrochloric acid; 110 mM sodium hydroxide; pH 6.5: 0.05 M phosphoric acid; pH 8: 110 mM boric acid; 56 mM sodium hydroxide; 44 mM hydrochloric acid; pH 10: 50 mM boric acid; 44 mM sodium hydroxide; 50 mM hydrochloric acid. To determine the pH-depending stability of the tetrazine derivatives, the area under the curve at T_0 was compared to the area under the curve after T_{2h} by means of analytical HPLC combined with mass spectrometry.

Passive membrane permeability (PAMPA)

The PAMPA assay was carried out as a high throughput experiment in 96-deep well plate (Thermo Fisher Scientific, Waltham, MA; volume well: 2200 μ L). The compound was dissolved in DMSO at a concentration of 10 mM. The drug solution (15 μ L) was added to the plate containing donor buffer (985 μ L, 50 mM 3-morpholino-2-hydroxypropanesulfonic acid with 0.5% glycocholic acid, pH = 6.0) in each well. The mixture was later filtered through a filter plate coated with a phospholipid-containing solution (\varnothing 0.45 μ m, MultiScreen Deep Well Solvinert, Merck Millipore, Darmstadt, Germany), and analyzed using a Spectramax plus 384 UV reader (Molecular Devices, Sunnyvale, CA) at a wavelength of 246–650 nm as previously reported to determine the permeability.³¹

Microsomal Clearance

Liver microsomes (human BD UltraPool HLM 150 or C57BL/6J mice) were purchased from Corning Incorporated (Woburn) and used for microsomal clearance assays according to a previous report.³⁹ 96-deep well plates were applied for the microsome incubations, which were incubated at 37 °C on a TECAN (Tecan Group Ltd, Switzerland) equipped with Te-Shake shakers and a heating device (Tecan Group Ltd, Switzerland). A phosphate buffer (0.1 M) at pH 7.4 was used for the experiments. The NADPH regenerating system consisted of 30 mM glucose-6-phosphate disodium salt hydrate, 10 mM NADP, 30 mM $MgCl_2 \times 6 H_2O$, and 5 mg/mL glucose-6-phosphate dehydrogenase (Roche Diagnostics, Penzberg, Germany) in the phosphate buffer. Test compounds were incubated at 1 μ M with microsome concentrations of 0.5 mg/mL plus the cofactor NADPH in 96-well plates at 37 °C. Incubation solutions were transferred and quenched with 3:1 (v/v) acetonitrile containing internal standards. Samples were then cooled and centrifuged before analysis by LC–MS/MS. Log peak area ratios (test

compound peak area / internal standard peak area) were plotted against incubation time and a linear fit made to the data with emphasis upon the initial rate of compound disappearance. The slope of the fit was then used to calculate the intrinsic clearance:

$$\text{Cl}_{\text{int}} (\mu\text{L}/\text{min}/\text{mg protein}) = -\text{slope} (\text{min}^{-1}) * 1000 / [\text{protein concentration (mg/mL)}]$$

In vitro transport assay for identification of mouse and human P-Glycoprotein substrates

Active transport by P-glycoprotein (permeability-glycoprotein, abbreviated as “P-gp”, also known as multidrug resistance protein 1 (MDR1) was assessed using the recently described unidirectional apical efflux ratio (AP-ER) assay.³⁰

Bimolecular Reaction Rate Determination

Reaction kinetics were performed on a BioLogic (Seyssinet-Pariset, France) SFM-3000 instrument, coupled with fluorescence detection mode at a wavelength excitation of 294 nm and a cut-on filter of 550 nm for Tzs **1-4** and **8**. Tzs **9-11** were detected *via* UV absorbance at 325 nm. All Tzs and TCO-OH were dissolved in 10% DMSO in phosphate-buffered saline (v/v). To characterize the reaction rates for **21** with tetrazines, stopped-flow kinetic measurements were carried out in principle as described by Yang et al.³² and Blackman et al.³³ Given values are averages \pm standard error of the fit to data of five technical replicantes.

Single-Dose Pharmacokinetic and brain/CSF uptake Studies in Rats (SD PK)

All rodent studies for compound (**1**, **2**, **3**, **11**) were conducted with the approval of the local veterinary authority in strict adherence to the Swiss federal regulations on animal protection and to the rules of the Association for Assessment and Accreditation of Laboratory Animal Care International (AAALAC). The used methodology is already detailed described.⁴⁰ In brief, adult male Wistar rats weighing circa 250 g were obtained from Harlan Laboratories (Horst, Netherlands) and housed with access to food and water ad libitum. To rats (n=2 per compound) were administered the test compounds (**1**, **2**, **3**, **11**) intravenously (bolus) at 1, 0.7, 1, and 0.4 mg/kg, respectively. Blood samples, brain, and CSF were collected under deep anesthesia with 5% isoflurane in pure oxygen. Brain and CSF collection was performed at 1 h post-dose. Multiple blood samples starting immediately after the intravenous administration were collected until 1 h post dose by heart puncture into K₂EDTA coated polypropylene tubes and placed on ice. Plasma was prepared within 30 min and frozen immediately. Between 50 and 100 μL of CSF were

collected by cisternal puncture of the atlanto-occipital membrane with a 22-gauge needle through silastic tubing in a 96-well plate. At the terminal point, the full rat brain was removed and the right half hemisphere was weighted homogenized (Precellys Lysing kit, LabForce AG, CH). All samples were stored at $-20\text{ }^{\circ}\text{C}$. Compound concentrations in plasma, brain homogenate, and CSF were determined by LC–MS/MS. Basic PK parameters such as systemic CL, Vss, and $T_{1/2}$ were calculated by standard non-compartmental analysis. Compound concentration ratio in CSF/plasma, and brain/plasma at 1 h post dose were also derived.

Biodistribution Study

Distributions of activity were determined in male C57BL6 mice ($n = 3/\text{group}$, weight = 24-27 g) after injection of [^{18}F]**2** and [^{18}F]**8**. Standards were prepared using 0.1 mL of injected ^{18}F -Tzs + 4.9 mL saline (1:100) for a final volume of 5 mL standard solution. Aliquots of 100 μL was then distributed into each of three counting tubes, and counted before and after every three sets of organ samples. Samples were assayed using a conventional gamma counter set to 511 \pm 100 keV. The counter automatically corrected for decay, beginning at the start of counting. Once counts were obtained, the percent dose per organ was calculated for all organs dissected. The experimental protocol was approved by the Animal Care and Use Committee of Johns Hopkins University.

Click-Chemistry

Antibody construct for proof-of-concept was produced in-house and consists of an IgG subtype 1 against β -amyloid and a fused Brain Shuttle (8D3) to the C-terminus of the heavy chain. In addition, the A β -mAb (4 mg/mL in PBS, pH 8.4) was functionalized with a TCO-unit by conjugation of **23** (10 eq, 10 mM in DMSO) to the A β -mAb Brain Shuttle construct. The solution was gently shaken orbitally for 2 h at $22\text{ }^{\circ}\text{C}$ and purified using Slide-A-Lyzer Dialysis Cassettes (10,000 MWCO, Thermo Fisher Scientific) against Dulbeccos PBS, pH 7.4. The buffer was changed after 30 min for 4 times and stored over night at $4\text{ }^{\circ}\text{C}$.

The TCO-functionalized A β -mAb (4 mg/mL in PBS, pH 7.4) and [^3H]**1** (3.3 TBq/mmol, 88 Ci/mmol, in 25 μL DMSO) were mixed in a 1:1 molar ratio (2-10 μM) and incubated for 1 h at $22\text{ }^{\circ}\text{C}$, purified by dialysis (Slide-A-Lyzer Dialysis, 10,000 MWCO, Thermo Scientific) against PBS, pH 7.4 to obtain A β -mAb-TCO- ^3H -Tetrazine in a radiochemical purity of $>95\%$.

Electrophoresis and Autoradiography of ³H-labeled mAb

SDS-PAGE was performed using the XCell SureLock™ Mini-Cell Electrophoresis System (Invitrogen, Thermo Fisher Scientific) and stained with Coomassie blue. Samples were diluted in NuPAGE lithium dodecyl sulfate (LDS) sample buffer (4x, Thermo Fisher Scientific) and NuPAGE Sample Reducing Agent (10x, Thermo Fisher Scientific), heated at 70 ° for 10 min, and 2 µg protein in 20 µL were separated using a Novex NuPAGE 4-12% Bis-Tris Gel (Thermo Fisher Scientific) with a NuPAGE MOPS-SDS running buffer (Thermo Fisher Scientific).

After separation gels were disassembled, rinsed 3x5 min in dH₂O and stained for 2 h at 22 °C under gentle orbital shaking using SimpleBlue SafeStain Coomassie solution (Thermo Fisher Scientific). Gel was destained for 3 h at 22 °C under gentle shaking. A second destaining step for 1 h with dH₂O for was performed to achieve maximum sensitivity and a clear background.

Coomassie stained gel were dried using a gel drying system (Life Technologies, now ThermoFisher Scientific). Briefly, gel was washed 3x5 min in water at 22 °C, incubated in gel drying solution (max. 5 min) and placed centrally on, in drying solution wetted, cellophane sheet. A second wet cellophane sheet was carefully placed on the gel, installed into a drying frame and dried over night at 22 °C.

After pressing the dry gel, it was scanned using conventional scanner. Gel samples were placed next to the phosphor screen in the exposure cassette for 5 days on tritium-sensitive phosphorimaging plates (BAS-IP TR2025, Fujifilm). Plates were scanned using the Fujifilm BAS-5000 phosphorimager and analyzed using MCID Analysis software (Imaging Research Inc, part of GE Healthcare).

References


- (1) Aluicio-Sarduy, E., Ellison, P. A., Barnhart, T. E., Cai, W., Nickles, R. J., and Engle, J. W. (2018) PET radiometals for antibody labeling. *J. Label. Compds. Radiopharm.* 61, 636-651.
- (2) Kaplon, H., Chenoweth, A., Crescioli, S., and Reichert, J. M. (2022) Antibodies to watch in 2022. *MAbs* 14, #2014296.
- (3) Van Dongen, G. A., Visser, G. W., Lub-de Hooge, M. N., De Vries, E. G., and Perk, L. R. (2007) Immuno-PET: A Navigator in Monoclonal Antibody Development and Applications. *Oncologist* 12, 1379-1389.
- (4) Edelmann, M. R., and Hauri, S. (2021) Functional in vitro assessment of modified antibodies: Impact of label on protein properties. *PLoS One* 16, e0257342.
- (5) Sehlin, D., Fang, X. T., Cato, L., Antoni, G., Lannfelt, L., and Syvänen, S. (2016) Antibody-based PET imaging of amyloid beta in mouse models of Alzheimer's disease. *Nat. Commun.* 7, 1-11.
- (6) Eigenmann, M. J., Fronton, L., Grimm, H. P., Otteneder, M. B., and Krippendorff, B.-F. (2017) Quantification of IgG monoclonal antibody clearance in tissues. *MAbs* 9, 1007-1015.
- (7) Stéen, E. J. L., Edem, P. E., Nørregaard, K., Jørgensen, J. T., Shalgunov, V., Kjaer, A., and Herth, M. M. (2018) Pretargeting in nuclear imaging and

- radionuclide therapy: Improving efficacy of theranostics and nanomedicines. *Biomaterials* 179, 209-245.
- (8) Liu, G. (2018) A revisit to the pretargeting concept - A target conversion. *Front. Pharmacol.* 9, Article 1476.
- (9) Huisgen, R. (1961) Centenary Lecture: 1,3-Dipolar Cycloadditions. *Proc. Chem. Soc.*, 357-396.
- (10) Stöckmann, H., Neves, A. A., Stairs, S., Brindle, K. M., and Leeper, F. J. (2011) Exploring isonitrile-based click chemistry for ligation with biomolecules. *Org. Biomol. Chem.* 9, 7303-7305.
- (11) Karver, M. R., Weissleder, R., and Hilderbrand, S. A. (2011) Synthesis and evaluation of a series of 1, 2, 4, 5-tetrazines for bioorthogonal conjugation. *Bioconjug. Chem.* 22, 2263-2270.
- (12) Liu, F., Liang, Y., and Houk, K. (2017) Bioorthogonal cycloadditions: computational analysis with the distortion/interaction model and predictions of reactivities. *Acc. Chem. Res.* 50, 2297-2308.
- (13) Rondon, A., Schmitt, S., Briat, A., Ty, N., Maigne, L., Quintana, M., Membreno, R., Zeglis, B. M., Navarro-Teulon, I., and Pouget, J.-P. (2019) Pretargeted radioimmunotherapy and SPECT imaging of peritoneal carcinomatosis using bioorthogonal click chemistry: probe selection and first proof-of-concept. *Theranostics* 9, 6706.
- (14) Shi, X., Gao, K., Huang, H., and Gao, R. (2018) Pretargeted immuno-PET based on bioorthogonal chemistry for imaging EGFR positive colorectal cancer. *Bioconjug. Chem.* 29, 250-254.
- (15) Sun, L., Li, Z., Ma, Y., Ludwig, J., Kim, H. S., and Zeng, D. (2021) PET Imaging of CD8 via SMART for Monitoring the Immunotherapy Response. *Biomed. Res. Int.* 2021.
- (16) Kissel, K., Hamm, S., Schulz, M., Vecchi, A., Garlanda, C., and Engelhardt, B. (1998) Immunohistochemical localization of the murine transferrin receptor (TfR) on blood-tissue barriers using a novel anti-TfR monoclonal antibody. *Histochem. Cell Biol.* 110, 63-72.
- (17) Poduslo, J. F., Curran, G. L., and Berg, C. T. (1994) Macromolecular permeability across the blood-nerve and blood-brain barriers. *Proc. Natl. Acad. Sci. (USA)* 91, 5705-5709.
- (18) Yu, Y. J., Zhang, Y., Kenrick, M., Hoyte, K., Luk, W., Lu, Y., Atwal, J., Elliott, J. M., Prabhu, S., and Watts, R. J. (2011) Boosting brain uptake of a therapeutic antibody by reducing its affinity for a transcytosis target. *Sci. Transl. Med.* 3, 84ra44.
- (19) Yu, Y. J., Atwal, J. K., Zhang, Y., Tong, R. K., Wildsmith, K. R., Tan, C., Bien-Ly, N., Hersom, M., Maloney, J. A., and Meilandt, W. J. (2014) Therapeutic bispecific antibodies cross the blood-brain barrier in nonhuman primates. *Sci. Transl. Med.* 6, 261ra154.
- (20) Niewoehner, J., Bohrmann, B., Collin, L., Urich, E., Sade, H., Maier, P., Rueger, P., Stracke, J. O., Lau, W., and Tissot, A. C. (2014) Increased brain penetration and potency of a therapeutic antibody using a monovalent molecular shuttle. *Neuron* 81, 49-60.
- (21) Row, R. D., and Prescher, J. A. (2018) Constructing new bioorthogonal reagents and reactions. *Acc. Chem. Res.* 51, 1073-1081.
- (22) Thalhammer, F., Wallfahrer, U., and Sauer, J. (1990) Reaktivität einfacher offenkettiger und cyclischer Dienophile bei Diels-Alder-Reaktionen mit inversem Elektronenbedarf. *Tetrahedron Lett.* 31, 6851-6854.
- (23) Darko, A., Wallace, S., Dmitrenko, O., Machovina, M. M., Mehl, R. A., Chin, J. W., and Fox, J. M. (2014) Conformationally strained trans-cyclooctene with improved stability and excellent reactivity in tetrazine ligation. *Chem. Sci.* 5, 3770-3776.
- (24) Hoff, L. V., Schnell, S. D., Tomio, A., Linden, A., and Gademann, K. (2021) Cross-coupling reactions of monosubstituted tetrazines. *Org. Lett.* 23, 5689-5692.

- (25) Curtius, T., and Hess, A. (1930) Einwirkung von Hydrazin auf m-Cyanbenzoesäure. *J. Prakt. Chem.* **125**, 40-53.
- (26) Yang, J., Karver, M. R., Li, W., Sahu, S., and Devaraj, N. K. (2012) Metal-catalyzed one-pot synthesis of tetrazines directly from aliphatic nitriles and hydrazine. *Angew. Chem. Int. Ed.* **51**, 5222-5225.
- (27) Rossin, R., Van Den Bosch, S. M., Ten Hoeve, W., Carvelli, M., Versteegen, R. M., Lub, J., and Robillard, M. S. (2013) Highly reactive trans-cyclooctene tags with improved stability for Diels–Alder chemistry in living systems. *Bioconjug. Chem.* **24**, 1210-1217.
- (28) Trifonov, R., Zubarev, V. Y., Malin, A., and Ostrovskii, V. (1998) Basicity of 3, 6-diphenyl-1, 2, 4, 5-tetrazine. *Chem. Heterocycl. Compd.* **34**, 111-114.
- (29) Spanget-Larsen, J. (1985) A structure–reactivity relationship for the basicity of aza-arenes. *J. Chem. Soc., Perkin Trans.*, 417-419.
- (30) Fischer, H., Senn, C., Ullah, M., Cantrill, C., Schuler, F., and Yu, L. (2021) Calculation of an apical efflux ratio from P-glycoprotein (P-gp) in vitro transport experiments shows an improved correlation with in vivo cerebrospinal fluid measurements in rats: impact on P-gp screening and compound optimization. *J. Pharmacol. Exp. Ther.* **376**, 322-329.
- (31) Kansy, M., Senner, F., and Gubernator, K. (1998) Physicochemical high throughput screening: parallel artificial membrane permeation assay in the description of passive absorption processes. *J. Med. Chem.* **41**, 1007-1010.
- (32) Yang, J., Šečutě, J., Cole, C. M., and Devaraj, N. K. (2012) Live-cell imaging of cyclopropene tags with fluorogenic tetrazine cycloadditions. *Angew. Chem.* **124**, 7594-7597.
- (33) Blackman, M. L., Royzen, M., and Fox, J. M. (2008) Tetrazine ligation: fast bioconjugation based on inverse-electron-demand Diels–Alder reactivity. *J. Am. Chem. Soc.* **130**, 13518-13519.
- (34) Pounds, S. (2004) Synthesis and Applications of Isotopically Labelled Compounds, (Dean, D. C., Filer, C. N., and MacCarthy, K. E., Eds.) pp 63-66, John Wiley & Sons Ltd.
- (35) Edelmann, M. R., and Muser, T. (2021) Tritium O-Methylation of N-Alkoxy Maleimide Derivatives as Labeling Reagents for Biomolecules. *Bioconjug. Chem.* **32**, 1027-1033.
- (36) Muri, D., and Edelmann, M. R. (2018) Tools for work-up and prepurification of tritium-labeled small molecules. *J. Label. Compds. Radiopharm.* **61**, 912-915.
- (37) Holt, D. P., Ravert, H. T., and Dannals, R. F. (2016) Synthesis and quality control of [¹⁸F] T807 for tau PET imaging. *J. Label. Compds. Radiopharm.* **59**, 411-415.
- (38) Zhang, L., Villalobos, A., Beck, E. M., Bocan, T., Chappie, T. A., Chen, L., Grimwood, S., Heck, S. D., Helal, C. J., and Hou, X. (2013) Design and selection parameters to accelerate the discovery of novel central nervous system positron emission tomography (PET) ligands and their application in the development of a novel phosphodiesterase 2A PET ligand. *J. Med. Chem.* **56**, 4568-4579.
- (39) Di, L., Keefer, C., Scott, D. O., Strelevitz, T. J., Chang, G., Bi, Y.-A., Lai, Y., Duckworth, J., Fenner, K., Troutman, M. D., and Obach, S. R. (2012) Mechanistic insights from comparing intrinsic clearance values between human liver microsomes and hepatocytes to guide drug design. *Eur. J. Med. Chem.* **57**, 441-448.
- (40) Caruso, A., Alvarez-Sánchez, R., Hillebrecht, A., Poirier, A., Schuler, F., Lavé, T., Funk, C., and Belli, S. (2013) PK/PD assessment in CNS drug discovery: Prediction of CSF concentration in rodents for P-glycoprotein substrates and application to in vivo potency estimation. *Biochem. Pharmacol.* **85**, 1684-1699.

Chapter Nine

Antibody-based *in vivo* imaging of central nervous system targets – Evaluation of a pretargeting approach utilizing a TCO-conjugated BrainShuttle antibody and radiolabeled tetrazines

This declaration concerns the article entitled:			
Antibody-based <i>in vivo</i> imaging of central nervous system targets – Evaluation of a pretargeting approach utilizing a TCO-conjugated BrainShuttle antibody and radiolabeled tetrazines			
Publication status (tick one)			
Draft manuscript	<input type="checkbox"/>	Submitted	<input type="checkbox"/>
In review	<input type="checkbox"/>	Accepted	<input type="checkbox"/>
		Published	<input checked="" type="checkbox"/>
Publication details (reference)	Bredack C*, Edelmann MR, Boroni E, Gobbi LC, Honer M*. (2022) <i>Pharmaceuticals</i> . 15(12):1445		
Copyright status (tick the appropriate statement)			
I hold the copyright for this material	<input checked="" type="checkbox"/>	Copyright is retained by the publisher, but I have been given permission to replicate the material here	<input type="checkbox"/>
Candidate's contribution to the paper (provide details, and also indicate as a percentage)	<p>The candidate contributed to / considerably contributed to / predominantly executed the...</p> <p>Formulation of ideas: 40%</p> <p>Design of methodology: 40%</p> <p>Experimental work: 50%</p> <p>Presentation of data in journal format: 80%</p>		
Statement from Candidate	This paper reports on original research I conducted during the period of my Higher Degree by Research candidature.		
Signed		Date	17.10.22

Introduction

Many antibodies are characterized by exquisite specificity and affinity towards their targets. This feature makes them ideal tracers for molecular imaging techniques, such as positron emission tomography (PET), particularly for targets for which a specific small molecule PET tracer does not exist. Antibodies are particularly stable molecules with long-lasting exposure in the bloodstream. Their long biological half-life does not match with the physical half-life of the typically used short-lived PET radioisotopes, such as ^{11}C ($t_{1/2}$: 20.4 min) or ^{18}F ($t_{1/2}$: 109.7 min). The rapid decay of the label along with the slow pharmacokinetics of the antibody will not allow the selection of an appropriate imaging time point yielding a sufficient signal in brain tissue over a background signal in the bloodstream. Consequently, antibodies would need to be labeled with longer-lived radionuclide such as ^{89}Zr ($t_{1/2}$: 3.27 d).^{1,2} However, this would lead to an increased and possibly intolerable radiation exposure to patients.³⁻⁶

Most of the challenges related to imaging strategies with directly radiolabeled antibodies can be addressed by a pretargeting approach where antibody and radiotracer administration are temporally uncoupled and the *in situ* labeling of a pretargeted antibody occurs at a time point when the modified antibody is still bound to the target antigen but already cleared from non-target tissues and the bloodstream.

Various pretargeting concepts have been reported, including the use of bispecific antibodies binding to the antigen and a radiolabeled hapten based on the high streptavidin-biotin affinity^{7,8} or oligonucleotide modified antibodies combined with radioactively labeled complementary nucleic acid strands.⁹ The bioorthogonal click chemistry reactions, another modality used for a pretargeting approach, have been extensively investigated, especially in preclinical oncology models.^{4,10-15} The inverse-electron-demand Diels-Alder (IEDDA) reaction of a 1,2,4,5-tetrazine group and a *trans*-cyclooctene (TCO) derivative is of particular interest.¹⁶⁻¹⁸ With reaction constants of up to $3.3 \times 10^6 \text{ M}^{-1} \text{ s}^{-1}$,¹⁹ this reaction is rapid and biological processes are not influenced due to the selectivity and bioorthogonality under physiological conditions.²⁰⁻²³ This click-reaction has been reported for fluorescent labeling of nanoparticles,^{24,25} antibodies,^{26,27} oligonucleotides,^{28,29} or the synthesis of radiopharmaceuticals.^{15,30-32}

The use of antibodies, such as immunoglobulin G (IgG), for pretargeted *in vivo* PET imaging of central nervous system (CNS) targets is severely limited by their large size, hydrophilicity, and the associated poor penetration of the blood-brain barrier (BBB)³³ Usually only around 0.1% of the injected dose is able to enter the CNS by passive transport mechanisms.^{33,34} Concepts have been developed to transport large molecules across the BBB more efficiently. One concept is the use of the transferrin receptor (TfR), which enables the active transport of molecules across the BBB *via*

receptor-mediated transcytosis³⁵⁻³⁹ due to its expression in endothelial cells of the BBB⁴⁰ and on neurons.⁴¹ A Roche developed brain-shuttle module was shown to have up to 55-fold increased uptake of an antibody-based cargo across the BBB into the brain.^{42,43}

This study aimed to establish an antibody-based pretargeting approach in combination with the IEDDA cycloaddition for *in vivo* imaging of targets expressed in the CNS. The amyloid-beta (A β) binding antibody mAb31 in its brain shuttle version (mAb31-BrainShuttle) along with the PS2APP Alzheimer's disease mouse model was used as a tracer-target pair for this proof-of-concept study.⁴⁴ This animal model shows a very pronounced amyloidosis in broad parts of the brain, with only a small extent of pathology in the cerebellum, which can be used as a reference region for *in vivo* experiments. Furthermore, mAb31-BrainShuttle is a well-established antibody with specificity for A β plaques and with increased brain uptake compared to a classical IgG.^{42,43} A tritiated version of a tetrazine derivative known from the literature⁴⁵ was synthesized in-house and was used in this study as a tool compound for *in vitro*, *ex vivo*, and *in vivo* experiments.

Results

TCO Modification and Radiolabeling of the Antibody Construct

The mAb was conjugated with TCO-NHS reagent to obtain mAb-TCO for subsequent click chemistry experiments (**Figure 1**). In order to determine the degree of labeling, the TCO-modified antibody was deglycosylated and the intact protein was analyzed using LC-MS. The MS data revealed an average of 2.5 TCO moieties per antibody molecule (data not shown).

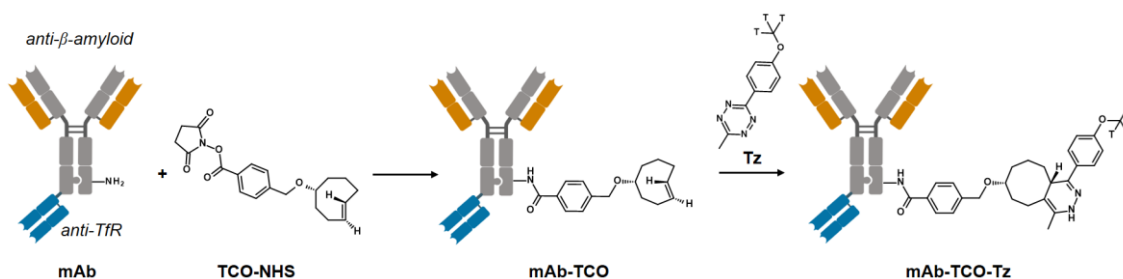


Figure 1: Nomenclature of compounds used in this study. Conjugation of **NHS-TCO** to **mAb** and the inverse electron-demand Diels-Alder cycloaddition between the modified antibody **mAb-TCO** and a ³H-labeled tetrazine derivative **Tz** to form **mAb-TCO-Tz**.

The click chemistry reactivity of mAb-TCO was tested with Tetrazine-biotin (Tz-biotin). SDS-PAGE under reducing conditions, followed by a Western Blot analysis of mAb, mAb-TCO, and mAb-TCO-Tz-biotin showed that the overall structure was not affected after modifications, no proteolytic fragments were detected. Three distinct bands

of the antibody construct were detected, corresponding to the light (~25 kDa), heavy (~50 kDa), and heavy + BrainShuttle (~100 kDa) chains. The click reaction with the Tz-biotin confirmed that all three chains were labeled with TCO (**Figure 2**).

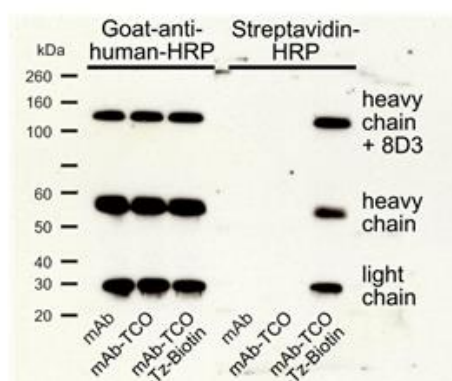


Figure 2: Western-Blot analysis of the mAb, mAb-TCO and mAb-TCO-Tz-biotin, generating three distinct bands, did not reveal a difference in the overall biochemical composition (Goat-anti-human-HRP detection). A TCO labeling of all three antibody chains was detected (Streptavidin-HRP detection).

In this study, a tritiated tetrazine (Tz) was used in various radio click chemistry experiments: 1) For tritium labeling of mAb-TCO to receive mAb-TCO-Tz (**Figure 1**); 2) *in vitro* radio click reaction on mouse brain sections with pre-incubated mAb-TCO; 3) for *ex vivo* (mAb-TCO injected *in vivo*, Tz incubation *ex vivo* on brain sections), and 4) *in vivo* pretargeting (mAb-TCO injected *in vivo*, Tz applied *in vivo*) experiments.

mAb-TCO was clicked in a 1:1 molar ratio with the Tz *in vitro* in order to receive the radiolabeled antibody construct mAb-TCO-Tz. An estimated average radiochemical yield of $51 \pm 13\%$ was achieved over 5 labeling experiments. Furthermore, a specific activity of 8 ± 2 kBq/ μ g, which is equal to a molar activity of 1.7 ± 0.4 TBq/mmol, was achieved.

Retained Antibody Binding to A β Plaques after TCO-Modification

The introduction of TCO groups and subsequent click reaction may influence the binding characteristics of the antibody towards its A β plaque epitope. To assess a potential impact by the modification, the TCO-modified mAb was clicked *in vitro* with the Tz, yielding mAb-TCO-Tz. Incubation of brain sections using the tritium-labeled mAb-TCO-Tz revealed a clear difference in binding pattern between transgenic (PS2APP) animals and wild-type (WT) controls (**Figure 3A**). The radiolabeled antibody specifically visualized A β plaques on brain sections from transgenic animals in reported brain regions, such as cortex, hippocampus, or thalamus.⁴⁴ No specific signals on WT brain sections were observed. The binding ratios in the target region of interest (transgenic vs

wild-type) were above 2 in all cases, which confirms the preserved specificity of the antibody against A β plaques.

In order to mimic a pretargeting experiment, PS2APP brain sections were first incubated *in vitro* with mAb-TCO, followed by an on slide click reaction with Tz. Autoradiographic analysis of the brain slices revealed clear imaging of A β plaques (**Figure 3B**). As a negative control, brain sections incubated with TCO-unconjugated mAb, did not show any significant radioactive signal with very low background. Binding ratios in the cerebellum, cortex, and hippocampus of mAb-TCO treated vs mAb treated brain sections were 3.90, 6.66, and 4.56, respectively. This result confirms that TCO-modification of mAb does not affect the specificity towards A β plaques, but also highlights the exquisite specificity of the click reaction between TCO and Tz *in vitro* on a brain section.

Further *in vitro* assays were performed to confirm the retained functionality of the modified mAb. The binding affinity of mAb-TCO towards A β was tested by ELISA. With an EC₅₀ of 1.4 nM for mAb-TCO compared to an EC₅₀ of 0.8 nM for the non-conjugated mAb (**Figure 3C**), no pronounced impact on binding affinity were observed in a single experiment.

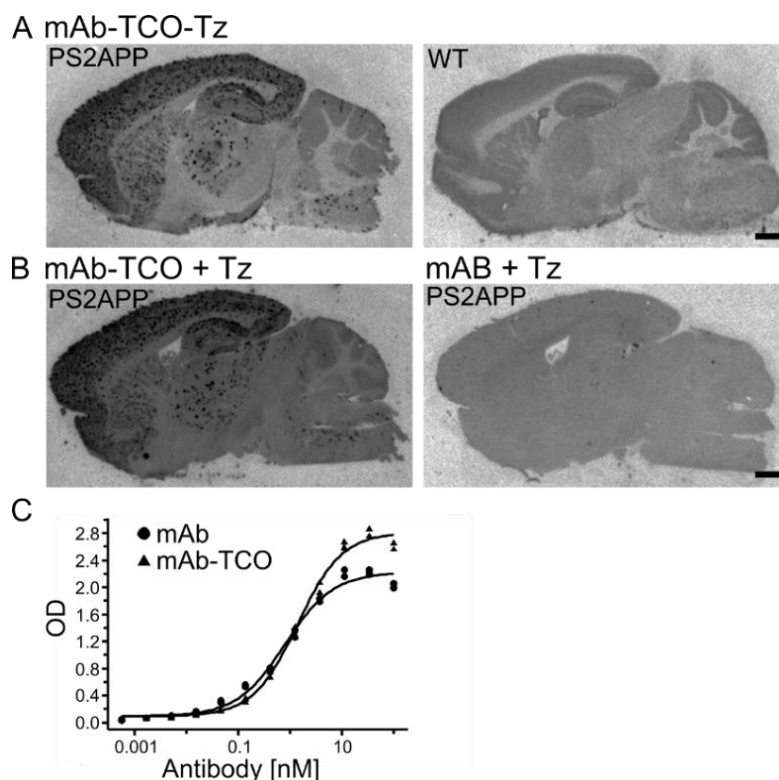


Figure 3: Maintained mAb affinity towards A β plaques after TCO-conjugation. (A) *In vitro* autoradiography of mAb-TCO-Tz (clicked *in vitro* in a vial before incubation) showing binding to A β plaques in PS2APP mouse brain sections in comparison to WT brain sections. Scale = 1 mm. (B) *In vitro* autoradiography of mAb-TCO after *in vitro*, on slide click reaction with Tz showing a clear signal of A β plaque binding in PS2APP mouse brain sections. Incubation of mAb (lacking the TCO) followed by *in vitro*, on slide click reaction using Tz on transgenic mouse brain sections (as a control) did not yield a specific A β plaque related signal, revealing the high selectivity and specificity of the click reaction. Scale = 1 mm. (C) Comparison of mAb vs mAb-TCO binding to A β . The applied ELISA assay did not reveal a change in the binding affinity towards the antigen.

TCO Modified Antibody Retains Binding to Transferrin Receptor and Enters the Brain

The binding of the antibody to the transferrin receptor (TfR) is crucial for a sufficient brain uptake of the modified brain shuttle antibody. *In vivo* experiments were conducted to assess TfR binding and the ability of the antibody construct to enter the brain after TCO modification. Upon *i. v.* injection of mAb-TCO-Tz ($19.1 \pm 1.3 \mu\text{g/g}$, $125.8 \pm 40.9 \text{ kBq/g}$, $3.4 \pm 1.1 \text{ MBq}$) in PS2APP mice, brain uptake and target binding was analyzed using autoradiography and immunofluorescent staining. In A β -deposit-containing brain regions, a radioactive signal was detected and co-localized with the presence of the antibody, as determined by immunofluorescent staining against the injected modified mAb-TCO-Tz (**Figure 4A**). Plaque-free brain regions did not show a signal in both analysis modalities. High brain uptake of mAb-TCO-Tz was corroborated by a quantitative tissue sampling and counting analysis yielding %ID/g values of 0.51 in the cortex vs 0.33 in the cerebellum (low plaque density) after 3 days. Uptake values decreased to 0.21 %ID/g in the cortex and 0.09 %ID/g in the cerebellum 12 days post-injection of the antibody.

The binding affinity of mAb-TCO towards TfR was assessed *in vitro* using Fluorescence-Activated Cell Sorting (FACS) flow cytometry analysis. A strong influence of TCO-conjugation on the binding characteristics towards TfR was not detected. The EC₅₀ for mAb-TCO was 3.19 ng/mL whereas the EC₅₀ of the conjugated mAb was 10.16 ng/mL (**Figure 4B**).

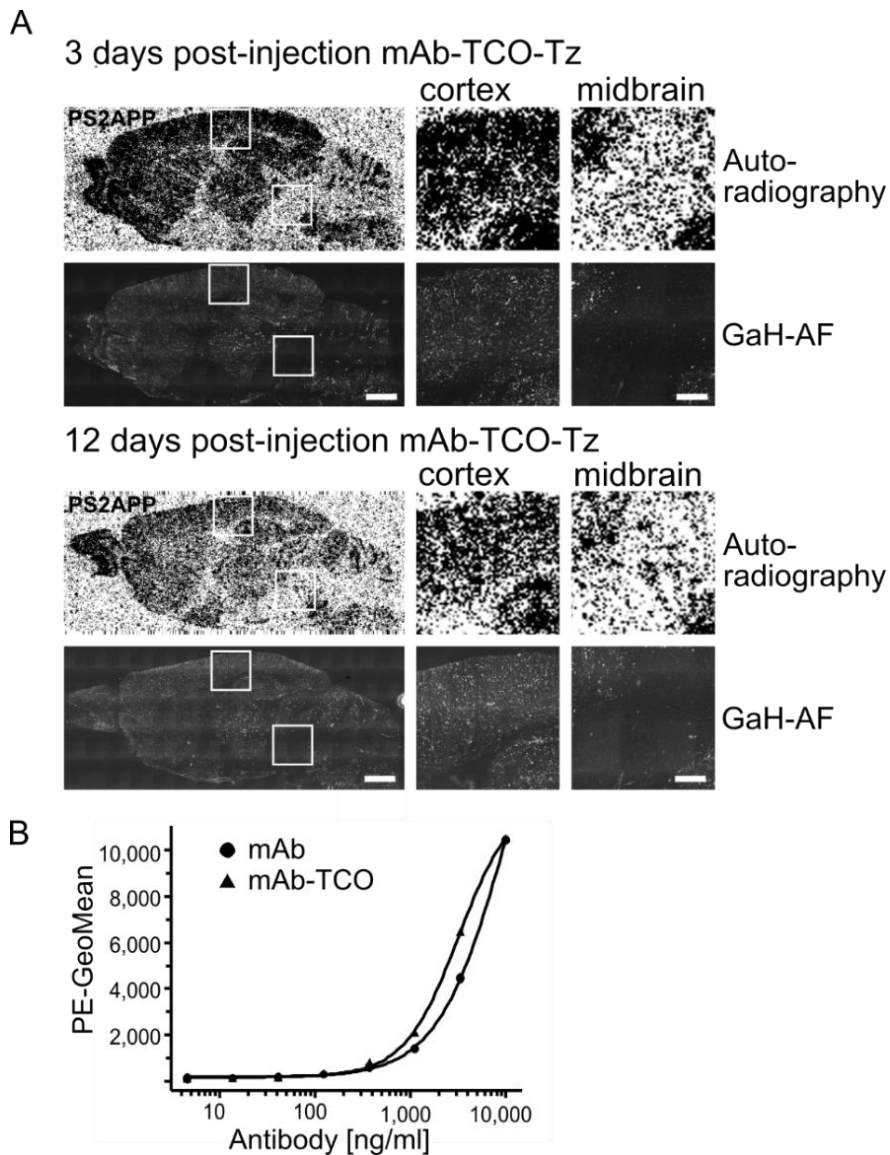


Figure 4: Maintained TfR binding and brain uptake of mAb-TCO-Tz. (A) Autoradiography of brain sections from PS2APP animals, 3-days and 12-days post-injection of mAb-TCO-Tz *in vivo*, showed a clear signal in A β plaques containing regions. Colocalization between the radioactive signal (autoradiography) and the mAb (GaH-AF) was visualized, using immunohistochemistry stainings, in the cortex, hippocampus, thalamus, and other A β containing brain regions. Scale = 1mm, magnification scale = 200 μ m. (B) For completeness, a FACS analysis proved a slight influence of the TCO coupling on the mAb-binding (mAb-TCO, triangle) to the TfR as compared to the non-modified mAb (circle).

Conjugated TCO Remains Reactive Towards Tz after In Vivo Injection

After confirming the remaining affinities of mAb-TCO in *in vitro* and *in vivo* experiments, the interval between antibody injection and radiotracer application, i. e., the optimal pretargeting interval, and the persistence of TCO functionality over time were analyzed. Upon treatment of PS2APP and WT control animals with 20 mg/kg mAb-TCO, animals were sacrificed after four different time points (1, 3, 6, 12 days post-injection), and their brains dissected. As anticipated, the TCO-modified antibody passed the blood-brain barrier and bound to A β plaques in the expected brain regions (including cortex,

hippocampus, thalamus), as demonstrated by immunofluorescent detection of the mAb-TCO antibody (**Figure 5**). Brain sections were incubated with the Tz in order to test the reactivity of the TCO moiety by an *ex vivo*, on slide click reaction. Six- and twelve-days post-injection, no specific difference between the transgenic and the WT animals was detected (data not shown). In contrast, the earlier time points 1 day and 3 days post-injection of mAb-TCO revealed a specific signal in the autoradiographic detection on brain sections of the transgenic animals. A β plaques were clearly visualized on PS2APP mouse brain sections in the areas like the cortex, hippocampus, thalamus, pons, and colliculi while brains sections of WT control animals did not show the characteristic dotted binding pattern (**Figure 5**). Radioactive signals on wild-type mouse brain sections only represented non-specific background binding (**Table 1**). Consequently, the reactivity of the TCO moiety of the injected mAb is limited to a pretargeting time interval of 3 days to ensure a successful *in vivo* click reaction and a sufficient radioactive signal.

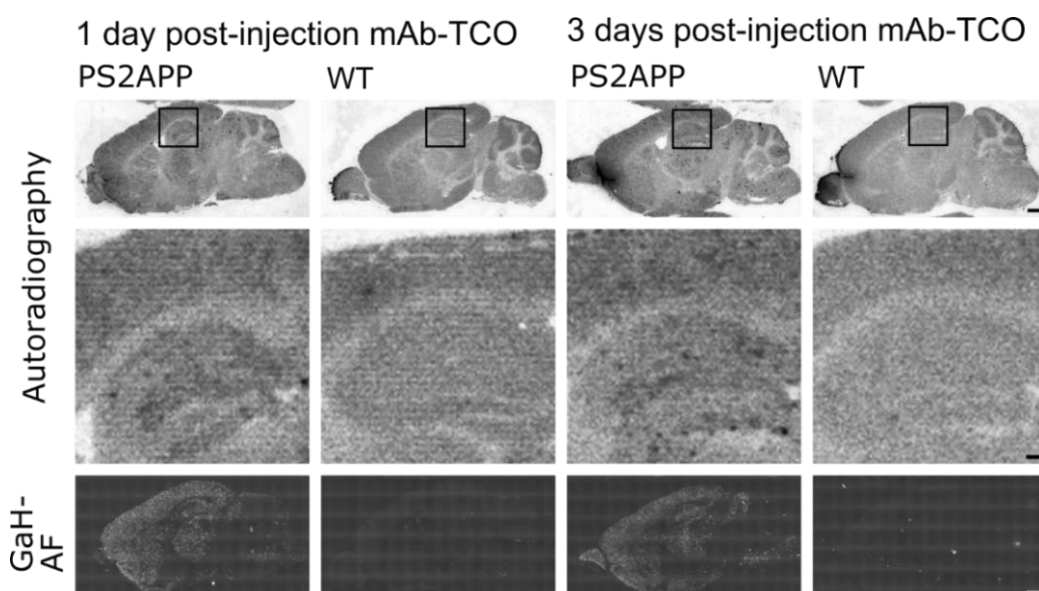


Figure 5: Maintained reactivity of the TCO moiety *in vivo*. Autoradiography results of mouse brain sections from PS2APP and WT controls following *ex vivo* click-reaction using the Tz, 1-day and 3-days post-injection of mAb-TCO (Scale = 1 mm). The magnification shows a clear, autoradiographic signal in brain sections of the transgenic animal and not the wildtype (Scale = 200 μ m). Immunohistochemical staining (GaH-AF) proofs mAb-TCO enters the brain and is responsible for the detected signal.

Table 1: Number of plaques detected by autoradiography after *ex vivo* click reaction. Data expressed as spots/ mm^2 (plaque density).

Plaque Density	1-day post-injection		3 days post-injection	
	PS2APP	WT	PS2APP	WT
Cortex	12.40 \pm 2.13	3.63 \pm 0.95	14.55 \pm 3.27	3.30 \pm 0.49
Hippocampus	12.12 \pm 1.42	1.85 \pm 0.47	11.84 \pm 3.00	1.77 \pm 0.44
Thalamus	9.45 \pm 0.96	1.26 \pm 0.4	9.15 \pm 1.34	0.66 \pm 0.18

In Vivo Click Reaction did not Reveal a Specific Radioactive Signal in the Brain

Finally, an *in vivo* click reaction between injected TCO-mAb and Tz was attempted in PS2APP and WT animals. Animals were injected with 20 mg/kg mAb-TCO *i. v. via* the tail vein. Based on previous results described above, animals were injected with the Tz (123.5 ± 24.5 ng; 1.8 ± 0.4 MBq; 55.1 ± 4.8 kBq/g) 1 day and 3 days post-injection of mAb-TCO. Tz entered the brain and the radioactive signal reached $1.4 \pm 0.2\%$ ID/g in the cortex 1 day after injection and $1.2 \pm 0.4\%$ ID/g in the cerebral cortex of the transgenic animals 3 days after injection. However, no difference in binding pattern and signal intensity was observed by autoradiography in PS2APP animals compared to WT control animals. In particular, no A β plaque imaging was detected by autoradiography (**Figure 6**). Image analysis showed similar uptake ratios in all regions of interest in transgenic animals compared to control animals. The presence of mAb-TCO on the brain sections was confirmed by immunofluorescent staining (**Figure 6**), but the *in vivo* click reaction of mAb-TCO with the radioactive Tz only occurred to an insufficient degree.

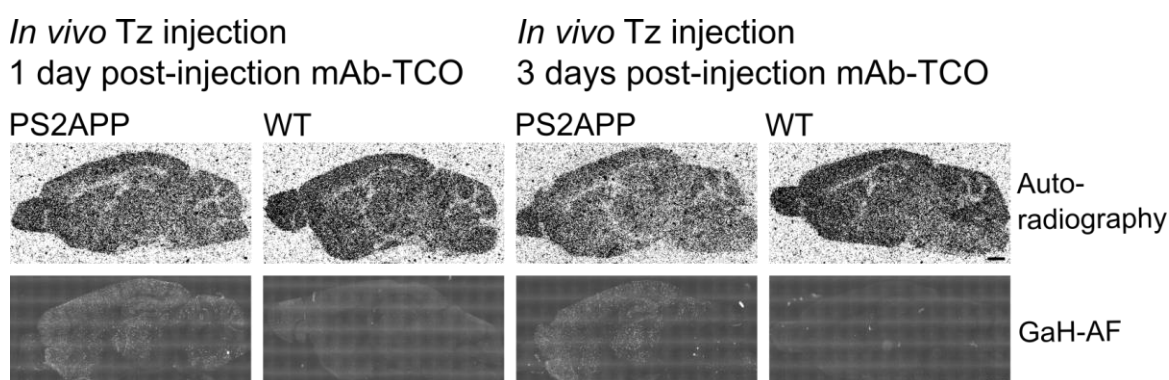


Figure 6: *In vivo* click reaction did not reveal a specific A β plaque signal. Tz was applied *in vivo* 1-day and 3-days post-injection of the mAb-TCO in PS2APP animals and WT controls at day 0. The *in vivo* click reaction between the Tz and the bound mAb-TCO did not show a specific signal which could be detected by autoradiography in neither the transgenic animal nor the control wildtype. The mAb enters the brain and binds to A β plaques as revealed by the GaH-AF staining. Scale = 1 mm.

Discussion

The described study combines an antibody-based pretargeting approach with the bioorthogonal click reaction between a strained *trans*-cyclooctene and an electron-deficient tetrazine by IEDDA. This concept has been extensively studied for the imaging of peripheral targets, for example targets overexpressed in xenograft-based oncology mouse model.^{4,10,12,46,47} It was demonstrated that *in vivo* PET imaging is possible with high tracer uptake in tumor, a high tumor to non-target tissue ratio, and a significantly decreased radioactive burden to non-tumor tissues. However, all reported studies about

pretargeted imaging were limited to peripheral targets. The presented work is among the first studies applying the antibody based pretargeting approach to a target in the CNS.

TCO-modified mAb (mAb-TCO) was successfully clicked *in vitro* with tritium-labeled tetrazine (Tz) yielding mAb-TCO-Tz. Brain sections, incubated *in vitro* with mAb-TCO-Tz, showed clear plaque imaging in PS2APP transgenic mouse brain sections, whereas no specific signal could be detected in wild-type controls. Furthermore, an *in vitro* click reaction on brain sections with pretargeted mAb-TCO and Tz as the secondary agent confirmed the reactivity on transgenic PS2APP brain tissue. In contrast, the same brain sections incubated with mAb (without TCO) and subsequent Tz treatment did not show any specific radioactive signal. This finding confirmed that the binding of the modified mAb at the A β plaques and the accessibility of the TCO moieties on the antibody for Tz is maintained *in vitro*.

Based on the results, *in vivo* experiments demonstrated the brain shuttling capability of *in vitro* prepared mAb-TCO-Tz in PS2APP transgenic mice by autoradiography imaging and fluorescent staining. Co-localized signals of both autoradiographical imaging and immunofluorescent staining were detected in typical A β -containing brain regions. In a next step, the optimized pretargeting interval, the time between antibody injection and injection of Tz, was determined in PS2APP and wild-type control mice treated with mAb-TCO. After 1, 3, 6, and 12 days, the animals were sacrificed, the brain dissected, and the sections incubated with tritiated Tz for an *ex vivo* click reaction. After 1-day and 3-days post-injection, a clear signal could be detected that distinguishes PS2APP transgenic from wild-type animals. A β deposits were visualized by autoradiography on transgenic animal brain sections only. The signal detected on wild-type sections represented background binding. This finding clearly demonstrated that a sufficient amount of antibody enters the brain for proper visualization of the target. Furthermore, the conjugated TCO-group remained chemically reactive to click with the applied tritiated tetrazine derivative. Longer pretargeting intervals (6 days and 12 days), however, did not result in autoradiography signals, although mAb-TCO entered the brain, which could be visualized by fluorescent detection using a secondary antibody. No signals by *ex vivo* click Tz treatment was observed after 6 days suggesting that the TCO moiety does not remain reactive too long for an efficient click reaction. The TCO is likely to be inactivated by copper catalyzed *trans-cis* isomerization. The *cis* isomer of TCO is orders of magnitude less reactive than the *trans*-isomer,⁴⁸ which might explain the lack of signal 6 days and later after injection of the antibody. All *in vitro* and *ex vivo* click experiments suggested that the mAb-TCO passed the blood-brain barrier, binds to A β targets and TCO remains reactive towards the Tz up to 3 days.

In the next step, an *in vivo* click-experiment was carried out using PS2APP transgenic and wild-type mice. First, a dose of 20 mg/kg mAb-TCO was injected followed

by Tz injection 1-day and 3-days later. Two hours after the application of Tz, the animals were sacrificed and analyzed for the presence of a genotype specific brain signal. Even though the antibody entered the brain as expected, no clear signal of target visualization in PS2APP transgenic mice was detected. Transgenic and wild-type brain sections looked similar revealing a homogenous background for both time points analyzed. This finding indicated that the tracer entered the brain, but no *in vivo* click reaction took place or was detectable due to the high background signal. It remains to be analyzed why the click reaction did not occur *in vivo* after 1 day and 3 days, even though the previous experiments indicated 1 day and 3 days to be an optimal pretargeting time point. Several reasons can be considered. It has been reported that the strained ring of *trans*-cyclooctene may undergo *cis-trans* isomerization, thereby reducing its reactivity towards tetrazines dramatically.^{12,48} Regarding the degree of labeling of the antibody with the TCO, “the more the better” could be considered. However, there is a tradeoff of potentially disturbed antibody functionality or pharmacokinetic characteristics when the conjugation degree with TCOs is too high.⁴⁹ The more TCO groups attached to the antibody, the more likely the functionality of binding to its target and the brain shuttling *via* the TfR are affected. An approach to increase the modification rate of the antibody, and minimizing the effect on the antibody functionality, is to introduce PEG linkers between the antibody and the TCO moiety. The further away the TCO from the antibody molecule, the lesser the influence of potential hydrophobic interactions between TCO and the mAb, which can influence the binding behavior. Furthermore, steric hindrances are reduced, that could influence the access of the TCO to the lysine residues during the modification. However, the further a TCO protrudes from the antibody, the more exposure to the surrounding, which can increase *trans-cis* isomerization.⁵⁰ Further approaches to increase the TCO loading of a mAb are the use of multi-functionalized moieties, that can be attached to an antibody (like branched, dendric scaffolds containing higher numbers of TCO molecules).^{51,52}

In addition, it has not yet been demonstrated whether the tetrazine derivative reaches the brain in sufficient quantities. Although the tracer was shown to penetrate into the brain, the concentration may have been too low. The ratio between available Tz and functional TCO might not be optimal for a detectable click reaction to occur. Another reason for the failure of the *in vivo* click reaction could be the instability of the tritiated tetrazine derivative. Tetrazines are highly reactive molecules and might degrade faster than expected in an *in vivo* animal system.⁵³ The metabolism of the tracer could be responsible for the biotransformation to an inactive species lacking a reactive tetrazine group. Recently, it was attempted to reverse the approach, i. e., functionalizing the antibody with tetrazine and applying a radioactive TCO as a secondary agent for bioorthogonal click reaction.^{53,54} However, this approach seemed to be

counterproductive in the case of a bioorthogonal click reaction of brain targets, as the Tz is a highly reactive and unstable molecule. The longer the Tz remains bound to the target, the higher the risk for a decomposition of the Tz. Furthermore, the LogD values (as a parameter of lipophilicity), which are crucial for brain penetration, are higher for the TCO derivatives than for the Tz derivatives. A higher lipophilicity suggests an increased unspecific binding to plasma protein and a faster oxidative metabolism and clearance of the compound, which may lead to a decreased brain uptake.^{55,56}

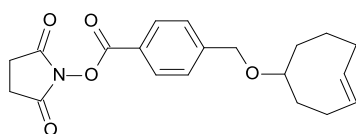
Despite the failed *in vivo* click reaction, the used approach represents a promising avenue for *in vivo* imaging of CNS targets *via* PET. The pretargeting approach is versatile and modular to be broadly applied to a number of antibodies and CNS targets, which currently cannot be approached by small molecule PET tracers. The latest generation of bifunctional antibodies allows an increased uptake of the pretargeting compound in the brain for a reliable detection.^{57,58} Further experimental work needs to be performed to identify a TCO/tetrazine combination with increased stability paired with high reactivity. An increased stability of both components, possibly combined with a blood-brain barrier non-penetrable clearing agent,^{46,59} might lead to a successful pretargeting-based *in vivo* imaging of brain targets.

Nonetheless, this study demonstrates the promising approach of using antibody-based click chemistry for *in vivo* brain imaging and may extend the application to targets currently considered undruggable and not approachable by a traditional small molecule PET tracer.

Materials and Methods

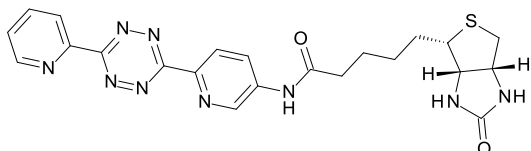
The antibody construct mAb31-BrainShuttle was produced in-house and consists of an immunoglobulin G subclass 1 monoclonal antibody (mAb31) directed against A β ⁶⁰ and a brain shuttle construct fused to the C terminus of the heavy chain as described previously.^{42,43} The brain shuttle construct is a single-chain single Fab fragment of an anti-mouse Transferrin monoclonal antibody.⁴² Hereinafter the mAb31-BrainShuttle construct is referred to as mAb. Solvents and reagents were obtained from commercial sources (as indicated) and were used without further purification.

(2,5-Dioxopyrrolidin-1-yl) 4-[[[(4E)-cyclooct-4-en-1-yl]oxymethyl]benzoate (TCO-NHS) was synthesized and prepared in-house following the method reported by Rossin et al.¹⁰



A colorless solid was isolated in a yield of 21% and purity of 99%. ^1H NMR (300 MHz, CDCl_3) δ 8.12 (d, $J = 8.28$ Hz, 2H), 7.51 (d, $J = 8.28$ Hz, 2H), 5.68 (m, 1H), 5.53 (m, 1H), 4.57 (m, 2H), 3.69 (m, 1H), 2.91 (br, s, 4H), 2.38 (m, 2H), 2.24 (m, 2H), 2.07 (m, 1H), 1.84 (m, 3H), 1.54 (m, 1H), 1.23 (m, 1H), LC-MS (ESI) m/z $\text{C}_{20}\text{H}_{23}\text{NO}_5$ requires: 358.2 ($[\text{M}+\text{H}]^+$).

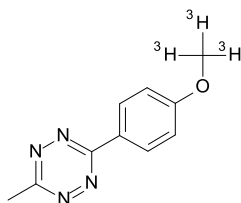
5-((3a*S*,4*S*,6a*R*)-2-Oxohexahydro-1*H*-thieno[3,4-*d*]imidazol-4-yl)-*N*-(6-(6-(pyridin-2-yl)-1,2,4,5-tetrazin-3-yl)pyridin-3-yl)pentanamide (Tz-biotin)



Biotin (217 mg, 870 μmol), 1-hydroxy-7-azabenzotriazole (148 mg, 1.04 mmol), and 1-ethyl-3-(3'-dimethylaminopropyl)carbodiimide hydrochloride (204 mg, 1.04 mmol) were dissolved in dry DMF (6 mL) under an argon atmosphere to give a colorless solution. Triethylamine (176 mg, 242 μL , 1.74 mmol) was added and the mixture was stirred at 22 $^\circ\text{C}$ for 1 h. Then, 6-(6-(pyridin-2-yl)-1,2,4,5-tetrazin-3-yl)pyridin-3-amine (230 mg, 870 μmol) was added and stirring was continued for 47 h at 50 $^\circ\text{C}$. All volatiles were evaporated and the crude material was purified by flash chromatography (silica gel pretreated with 7% Et_3N in heptane, 40 g column, 0% to 100% acetone in heptane in 20 min to yield 86 mg (19%) of the desired compound Tz-biotin.

^1H NMR (600 MHz, $\text{DMSO}-d_6$) δ 10.56 (s, 1H), 9.05 (d, $J = 2.52$ Hz, 1H), 8.94 (d, $J = 4.69$ Hz, 1H), 8.62 (d, $J = 8.76$ Hz, 1H), 8.59 (d, $J = 7.76$ Hz, 1H), 8.44 (dd, $J = 2.52$, 8.76 Hz, 1H), 8.16 (ddd, $J = 1.81$, 7.76, 7.76 Hz, 1H), 7.73 (ddd, $J = 1.21$, 4.69, 7.76 Hz, 1H), 6.45 (s, 1H), 6.37 (s, 1H), 4.29-4.34 (m, 1H), 4.12-4.17 (m, 1H), 3.07-3.20 (m, 1H), 3.05 (br s, 1H), 2.84 (dd, $J = 5.14$, 12.49, 1H), 2.52-2.61 (m, 1H), 2.39-2.48 (m, 1H), 1.35-1.71 (m, 6H). LC-MS m/z $\text{C}_{22}\text{H}_{23}\text{N}_9\text{O}_2\text{S}$ requires: 478.1 ($[\text{M}+\text{H}]^+$), 500.3 ($[\text{M}+\text{Na}]^+$).

^3H]3-(4-Methoxyphenyl)-6-methyl-1,2,4,5-tetrazine (Tz)



To a 25 mL sealable tube, equipped with a stir bar, 452 mg (3.8 mmol) of 4-hydroxybenzonitrile, 1.9 mmol $\text{Zn}(\text{OTf})_2$, 188 mmol hydrazine monohydrate, and 2 mL (38 mmol) acetonitrile was added to give a purple colored solution. The tube was sealed, and the reaction solution was stirred for 16 h at 80 $^\circ\text{C}$. The reaction solution was cooled to 22 $^\circ\text{C}$ and transferred into a 250 mL three-neck round bottom flask. 25 mL of a 3.5 M

sodium nitrate solution was added slowly with ice bath cooling, followed by dropwise addition of 1 M hydrogen chloride (75 mL) until no gas evolution was observed and a pH of 3-4 was reached. The mixture was extracted 3x with ethyl acetate, the combined organic phase was separated, dried over sodium sulfate, and concentrated in vacuo. The crude residue was purified using silica-based flash chromatography to yield 38% (271 mg, 1.44 mmol) of the desired phenol-precursor as an orange solid in a purity of 98%.

^1H NMR (300 MHz, CDCl_3) δ 8.52 (d, $J = 8.98$ Hz, 2H), 7.03 (d, $J = 8.98$ Hz, 2H), 5.21 (s, 1H), 3.07 (s, 3H). LC-MS (ESI) m/z $\text{C}_{10}\text{H}_8\text{N}_4\text{O}$ requires: 189.4 ($[\text{M}+\text{H}]^+$).

$[\text{}^3\text{H}]$ Methyl nosylate (1.85 GBq, 132 μg , 0.591 μmol), cesium carbonate (481 μg , 1.48 μmol), and 333 μg (1.77 μmol) of the phenol-precursor were dissolved in 400 μL tetrahydrofuran. The solution was stirred at 50 $^\circ\text{C}$ for 5 h. The reaction mixture was diluted with 1 mL dichloromethane and passed through a strong anion exchange (SAX) solid phase extraction (SPE) cartridge to remove the sulfonic acid by-product.⁶¹ The solvent was removed and the residue dissolved in acetonitrile/water to purify the compound using preparative-HPLC to yield 278 MBq (15%) of Tz in a radiochemical purity of 98%. The specific activity of 3.3 TBq/mmol was taken from the starting compound $[\text{}^3\text{H}]$ methyl nosylate, since Tz did not ionize in mass spectrometric analysis and therefore no isotope pattern could be determined.

Antibody TCO-conjugation

Ten-fold molar excess of TCO-NHS (10 mM in DMSO) was added to the mAb (4-5 mg/mL in PBS, pH 7.4). The solution was shaken orbitally for 2 h at 22 $^\circ\text{C}$ and purified using Slide-A-Lyzer Dialysis Cassettes (10,000 MWCO, Thermo Fisher Scientific) against PBS, pH 7.4. The buffer was changed after 30 min for 4 times in total to generate mAb-TCO in a yield of $83 \pm 11\%$ ($n=9$) with a degree of label of 2.5 on average.

In Vitro Click Reaction

mAb-TCO (5 mg/mL in PBS, pH 7.4) and Tz (3.26 TBq/mmol, 185 MBq/mL in ethanol) were mixed in a 1:1 molar ratio (2-10 μM) and incubated for 1 h at 22 $^\circ\text{C}$, purified by dialysis (Slide-A-Lyzer Dialysis, 10,000 MWCO, Thermo Scientific) against PBS pH 7.4 to obtain mAb-TCO-Tz in a radiochemical purity of $> 95\%$.

In analogy, mAb-TCO was coupled with a biotinylated Tz derivative. For this click reaction, a 10-fold excess of Tz-biotin (5 mM in DMSO) was used to ensure complete conversion to mAb-TCO-Tz-biotin.

Intact Protein Mass Spectrometry (MS) Analysis

For protein MS analysis of mAb-TCO, the protein concentration was adjusted to 0.5 mg/mL with 0.1 M Tris pH 7.8. The samples were chromatographed on a Waters nanoAcquity system using an Agilent, Poroshell column (SB-C8, 0.5 mm x 75 mm, 5 µm, 300 Å, injection volume of 10 µL) heated to 65 °C. Eluent A was 0.1% trifluoroacetic acid in water, eluent B was 0.1% trifluoroacetic acid in acetonitrile. The following gradient for the separation was applied; initial: 10% B, 0.2 min: 10% B, 1 min: 20% B, 11 min: 60% B, 15 min: 90% B, 16 min: 90% B, 17 min: 10% B, 20 min: 10% B with a flow rate of 70 µL/min. The eluent was analyzed with the Waters LCT Premier XE mass spectrometer using the electrospray method for ionization of the sample (ESI, positive, V mode; with a capillary voltage of 2.8 kV and a cone voltage of 200 V). The raw data were deconvoluted with the MaxEnt1 software (Waters Corporation) and displayed using standard software.

SDS-PAGE and Western Blot Analysis

Modified antibody constructs were subjected to SDS-PAGE and Western Blot analysis. SDS-PAGE was performed using the XCell SureLock™ Mini-Cell Electrophoresis System (Invitrogen, Thermo Fisher Scientific) under reducing conditions. Samples were diluted in NuPAGE LDS Sample buffer (4x, Thermo Fisher Scientific) and NuPAGE Sample Reducing Agent (10x, Thermo Fisher Scientific), heated at 70 °C for 10 min, and 1 - 2 µg in 20 µL were separated using a Novex NuPAGE 4-12% Bis-Tris Gel (Thermo Fisher Scientific) with a 1x NuPAGE MOPS-SDS running buffer (Thermo Fisher Scientific). Separated proteins were transferred to a nitrocellulose membrane using the iBlot Gel Transfer System (Thermo Fisher Scientific, 7 min, 23 V) in conjunction with Novex Mini iBlot Gel Transfer Stacks (Thermo Fisher Scientific). The membrane was blocked for 1 h at 22 °C with 5% TopBlock (LubioScience, Lucerne, Switzerland), 0.1% Tween-20 in 1x PBS pH 7.6. mAb-TCO was detected using a goat-anti-human-horseradish peroxidase (HAP) coupled antibody (1:250,000, 1 h at 22 °C in 1% TopBlock/TBS/T, Thermo Fisher Scientific Pierce) and mAb-TCO-Tz-biotin was detected using a Streptavidin-HPA (1:200,000, 20 min, 22 °C in 5% TopBlock/TBS/T, Thermo Fisher Scientific). Membrane was rinsed twice in blocking buffer, washed 1x15 min followed by 2x5 min in blocking buffer, 1x5 min in TBS-T (1xTBS pH 7.6, 0.1% Tween-20) and 1x5 min in TBS pH 7.6. The modified proteins were detected using the Amersham ECL Western Blotting Detection Reagents and developed by applying standard procedures using the Amersham Hyperfilm high performance chemiluminescence film.

A β ELISA Affinity Assay

Binding of fusion constructs to fibrillary A β was measured by an ELISA assay. Briefly, the 40 amino acid residue peptide A β (1-40) (Roche, Germany) was coated at 7 μ g/mL in PBS onto Maxisorp plates (Nunc, ThermoFisher Scientific) for 3 days at 37 °C to produce fibrillary A β then dried for 3 h at 22 °C. The plate was blocked with 1% Casein and 0.1% BSA in PBS (blocking buffer) for 1 h at 22 °C, then washed once with wash buffer. Fusion polypeptides or controls were added at concentrations up to 100 nM in blocking buffer and incubated at 4°C for 16 h. After 4 wash steps, constructs were detected by addition of anti-human-IgG-HRP (Jackson ImmunoResearch) at 1:10,000 dilution in blocking buffer (1 h, 22 °C), followed by 6 washes and incubation in TMB (Sigma). Absorbance was read out at 450 nm after stopping color development with 1 M HCl.

Fluorescence-Activated Cell Sorting (FACS) Flow Cytometry Analysis

Binding of fusion constructs to murine transferrin receptor was tested by FACS analysis on mouse BA/F3 pro-B cells. Cells were harvested by centrifugation, washed once with PBS and 5 x 10⁴ cells incubated with a 1.5 pM to 10 nM dilution series of the antibody fusions in 100 μ L RPMI/10% FCS for 1.5 h on ice. After 2 washes with RPMI/10% FCS, cells were incubated with goat-anti-human IgG coupled to Phycoerythrin (Jackson ImmunoResearch) at a dilution of 1:600 in RPMI/10% FCS for 1.5 h on ice. Cells were washed again, re-suspended in RPMI/10% FCS and Phycoerythrin fluorescence measured on a FACS-Canto instrument (Becton-Dickinson).

In Vivo Mouse Experiments

All animal experiments were performed according to the Swiss federal regulations on animal protection and to the rules of the Association for Assessment and Accreditation of Laboratory Animal Care International (AAALAC).

Adult male or female APP751 swedish x PS2N141I transgenic (PS2APP)⁴⁴ mice on a homozygous C57BL/6 genetic background and C57BL/6 wild-type (WT) control animals at an age of 12-18 months, used for the experiments, were bred at the animal facility of Roche, Basel. The mice were group housed in open cages and maintained on a 12:12-h light:dark cycle, with constant temperature (21–24 °C) and humidity (40–80%). Each cage was provided with unrestricted access to municipal water and sterilized food (Provimi Kliba 3436). All cages were supplied with autoclaved sawdust bedding and environmental enrichments, which were applied to best practice animals' welfare

standards and rotated weekly. The mice were acclimated for at least 1 week before the start of the study. The study design is described in **Table 2**.

Table 2: Study design and overview of *in vivo* experiments, used animals, injected compounds.

Experiment	Animals used		Antibody injected <i>in vivo</i>	Time [d] *	Tz administered
	WT	PS2APP			
Brain Uptake		1x	mAb-TCO-Tz	3	<i>in vitro</i> , in vial
		2x	mAb-TCO-Tz	12	<i>in vitro</i> , in vial
<i>In vivo</i> Stability of mAb-TCO	1x	1x	mAb-TCO	1	<i>ex vivo</i> , on slide
	1x	1x	mAb-TCO	3	<i>ex vivo</i> , on slide
	1x	1x	mAb-TCO	6	<i>ex vivo</i> , on slide
	1x	1x	mAb-TCO	12	<i>ex vivo</i> , on slide
<i>In vivo</i> Click Reaction	2x	3x	mAb-TCO	1	<i>in vivo</i> , intravenous
	3x	3x	mAb-TCO	3	<i>in vivo</i> , intravenous

* Time interval post-injection of antibody to sacrifice animal or inject Tz.

In Vivo Target Engagement

Animals were injected intravenously (*i. v.*) with 20 mg/kg mAb-TCO-Tz in PBS (injection volume 5 mL/kg, protein concentration 3-5 mg/mL) and sacrificed 3-days and 12-days post-injection. The brain was dissected and hemisected along the midline. One hemisphere was used for cryosections and immediately frozen on powdered dry ice. The other hemisphere was dissected to obtain brain regions including the cerebellum, hippocampus, cortex, and the rest brain, used for beta scintillation counting. The brain tissue was stored at -80 °C.

mAb-TCO Administration for Ex Vivo Click Reaction

Animals were injected intravenously (*i. v.*) with 20 mg/kg mAb-TCO in PBS (injection volume 5 mL/kg, protein concentration 3-5 mg/mL). After 1, 3, 6, 12 d post-injection, animals were sacrificed by decapitation. The brain was hemisected and frozen in powdered dry ice. The brain tissue was stored at -80 °C.

In Vivo Click Reaction

Animals were injected *i. v.* with a single dose of 20 mg/kg mAb-TCO. 24 h and 72 h post-injection of the antibody, the animals received a single dose *i. v.* injection of 55.5 MBq/kg Tz in PBS, pH 7.4 (2.96 TBq/mmol, 9.25 MBq/mL, 5 mL/kg injection volume). 2 h after the Tz injection the animals were sacrificed by decapitation and plasma samples were

collected. The brain was hemisected. One hemisphere was frozen on powdered dry ice, the other one was dissected and brain regions including cerebellum, cortex, hippocampus, and rest brain were frozen on dry ice. The brain tissue was stored at -80 °C.

Immunohistochemistry, Radio-Immunohistochemistry

Animals were deeply anaesthetized using 3-5% (vol %) isoflurane in an anesthesia box with the support gas, oxygen/air (2:1). Animals were sacrificed by decapitation. The brains were removed, rinsed in 0.9% NaCl solution, blotted dry, hemisected along the midsagittal plane, and immediately frozen on powdered dry ice for histology and/or autoradiography.

Brains were cut sagittally on a cryostat (Leica CM 3050). Sections (10 µm thickness) were thaw-mounted on HistoBond plus glass slides (Marienfeld, Lauda-Königshofen, Germany), air dried for at least 2 h, and stored at -80°C until further use.

Slides were defrosted, rehydrated with PBS (Thermo Fisher Scientific), fixed with acetone (Sigma-Aldrich, 3 min, -20 °C) and blocked for 20 min at 22 °C (1% bovine serum albumin + 1% ovalbumin + 1% normal goat serum in PBS).

The mAb constructs, either applied *in vitro* or injected *in vivo*, were detected using a fluorescently labeled secondary antibody (goat-anti-human Alexa Fluor (AF) 488, AF 555, or AF 647, 15 µg/mL in 1% normal goat serum in PBS, 1 h, 22 °C, Thermo Fisher Scientific). The sections were counterstained with 1 µg/mL 4',6-diamidino-2-phenylindole (DAPI, Roche) in PBS for 3 min. Sections were thoroughly washed with PBS between each incubation step. Standard SudanBlack B (0.3% in 70% ethanol, 3 min, Merck KGaA, Darmstadt, Germany) staining was used to quench lipofuscin autofluorescence. Microscopic, whole slice images were acquired using the Metafer 4 slide scanner (MetaSystems, Altussheim, Germany).

Fixed and blocked brain sections from transgenic and wild-type animals were incubated with 1 µg/mL mAb-TCO-Tz antibody solution in 1% normal goat serum in PBS for 1 h at 22 °C or 4 °C for 16 h. After intensive washing with PBS, the sections were air dried at 4 °C and used for autoradiography.

For the *in vitro* and *ex vivo* on-slide click reaction, the brain sections of transgenic animals were defrosted, re-hydrated and blocked (no blocking step for *ex vivo* on-slide click reaction) as described above. *In vitro* staining with 1 µg/mL mAb-TCO or mAb as control in 1% normal goat serum in PBS, 4 °C for 16 h, was carried out. Slides were washed for 3x5 min with PBS followed by 3x5 min with a Ringer solution (146.5 mM NaCl, 2.7 mM KCl, 0.85 mM MgCl₂, 1.2 mM CaCl₂, 1.2 mM Na₂HPO₄, 0.27 mM NaH₂PO₄, pH 7.4; Merck KGaA, Fluka).

On slide click-reaction was carried out for 2 h at 22 °C using 100 µL to 200 µL of 100 nM Tz (2.96 TBq/mmol, 34.4 MBq/mL in ethanol) in Ringer solution. Sections were washed 3x15 min with a Ringer solution and dipped briefly in distilled water at 4 °C. The slides were air dried at 4 °C and used for autoradiography.

Radioactive Assays, Autoradiography, and Analysis

Air-dried brain sections were exposed for 5 - 10 days on tritium-sensitive phosphor imaging plates (BAS-IP TR2025, Fujifilm). Plates were scanned using the Fujifilm BAS-5000 phosphorimager and analyzed using MCID Analysis software (Imaging Research Inc, part of GE Healthcare). Regions of interest were selected, and bound radioactivity was analyzed based on a standard (American Radiolabeled Chemicals, ART0123) co-exposed with the brain sections. Bound radioactivity was expressed as ratios between the regions of interest in the transgenic animal divided by the bound radioactivity of the same regions in the wild-type control animal.

Dissected brain regions were weighted and homogenized in ice-cold homogenization buffer (1% NP-40, cOmplete Ultra Proteinase Inhibitor tablets (Roche, according to manufactures instructions) in 50 mM Tris/HCl, pH 7.4) using a Polytron PT1200 (Kinematica AG, Lucerne, Switzerland) and/or ultrasound (Branson Sonifier 250). A 100 µL aliquot was mixed with 3 mL UltimaGold scintillation cocktail (Perkin Elmer) and incubated over night before beta counting in the TriCarb 2500 Beta Counter (Perkin Elmer Packard). Disintegrations per minute (DPM) were used to calculate concentrations of the radioactive tracer (fmol/mg) and %ID/g (percentage of injected dose per gram tissue weight).

Conclusions

This study explored the suitability of an antibody-based pretargeting approach for *in vivo* imaging of targets in the central nervous system. As a first step, the A β -specific, brain shuttle version of mAb31 (mAb31-BrainShuttle, short mAb) was successfully radiolabeled *in vitro* using the inverse-electron-demand Diels-Alder reaction of a tritiated 1,2,4,5-tetrazine (Tz) group and a *trans*-cyclooctene modified mAb (mAb-TCO). The mAb-TCO-Tz antibody retained its functionality and specificities as demonstrated by *in vitro* experiments using PS2APP mouse brain sections, ELISA, FACS assays, radio-immunohistochemistry, and *in vivo* approaches. The radiolabeled A β specific antibody crossed the blood-brain barrier and bound its target. One- to three-day post-injection of mAb-TCO proofed to be a suitable time window for *in vivo* pretargeting. The TCO groups remained reactive towards the tetrazine reactant since a specific radioactive labeling of A β plaques was evident in brain sections of PS2APP mice, using an *ex vivo* click

reaction. However, the *in vivo* click reaction with intravenously injected Tz one- and three-days after injection of the TCO-modified antibody did not reveal a specific difference in binding intensity between the transgenic and wildtype animals. A radioactive signal was detected in brain tissue, but no click reaction was revealed by autoradiography. Further experiments are needed to optimize the multi-component pretargeting system, such as the TCO degree of labeling of the mAb, mode of conjugation of the TCO, concentration of Tz, type of Tz. The right balance between stability and reactivity of both components can thus be observed for a successful *in vivo* pretargeting reaction. The presented study suggests that the application of PET imaging in drug development and for clinical diagnostics may be extended to targets currently considered undruggable and not approachable by a traditional small molecule PET tracer.

References

- (1) Deri, M. A., Zeglis, B. M., Francesconi, L. C., and Lewis, J. S. (2013) PET imaging with ⁸⁹Zr: from radiochemistry to the clinic. *Nucl. Med. Biol.* **40**, 3-14.
- (2) Zeglis, B. M., Houghton, J. L., Evans, M. J., Viola-Villegas, N., and Lewis, J. S. (2014) Underscoring the influence of inorganic chemistry on nuclear imaging with radiometals. *Inorg. Chem.* **53**, 1880-1899.
- (3) Sharkey, R. M., and Goldenberg, D. M. (2011) Cancer radioimmunotherapy. *Immunotherapy* **3**, 349-370.
- (4) Zeglis, B. M., Sevak, K. K., Reiner, T., Mohindra, P., Carlin, S. D., Zanzonico, P., Weissleder, R., and Lewis, J. S. (2013) A pretargeted PET imaging strategy based on bioorthogonal Diels–Alder click chemistry. *J. Nucl. Med.* **54**, 1389-1396.
- (5) Zeglis, B. M., Brand, C., Abdel-Atti, D., Carnazza, K. E., Cook, B. E., Carlin, S., Reiner, T., and Lewis, J. S. (2015) Optimization of a pretargeted strategy for the PET imaging of colorectal carcinoma via the modulation of radioligand pharmacokinetics. *Mol. Pharm.* **12**, 3575-3587.
- (6) Zeglis, B. M., and Lewis, J. S. (2011) A practical guide to the construction of radiometallated bioconjugates for positron emission tomography. *Dalton Trans.* **40**, 6168-6195.
- (7) Moro, M., Pelagi, M., Fulci, G., Paganelli, G., Dellabona, P., Casorati, G., Siccardi, A. G., and Corti, A. (1997) Tumor cell targeting with antibody-avidin complexes and biotinylated tumor necrosis factor α . *Cancer Res.* **57**, 1922-1928.
- (8) Yao, Z., Zhang, M., Kobayashi, H., Sakahara, H., Nakada, H., Yamashina, I., and Konishi, J. (1995) Improved targeting of radiolabeled streptavidin in tumors pretargeted with biotinylated monoclonal antibodies through an avidin chase. *J. Nucl. Med.* **36**, 837-841.
- (9) Liu, G., Dou, S., Liu, Y., Wang, Y., Rusckowski, M., and Hnatowich, D. J. (2011) ⁹⁰Y labeled phosphorodiamidate morpholino oligomer for pretargeting radiotherapy. *Bioconjug. Chem.* **22**, 2539-2545.
- (10) Rossin, R., Renart Verkerk, P., van den Bosch, S. M., Vuldere, R. C., Verel, I., Lub, J., and Robillard, M. S. (2010) In vivo chemistry for pretargeted tumor imaging in live mice. *Angew. Chem. Int. Ed.* **49**, 3375-3378.
- (11) Houghton, J. L., Zeglis, B. M., Abdel-Atti, D., Sawada, R., Scholz, W. W., and Lewis, J. S. (2016) Pretargeted immuno-PET of pancreatic cancer: overcoming circulating antigen and internalized antibody to reduce radiation doses. *J. Nucl. Med.* **57**, 453-459.

- (12) Rossin, R., van Duijnhoven, S. M., Läppchen, T., van den Bosch, S. M., and Robillard, M. S. (2014) Trans-cyclooctene tag with improved properties for tumor pretargeting with the Diels–Alder reaction. *Mol. Pharm.* *11*, 3090-3096.
- (13) Cook, B. E., Adumeau, P., Membreno, R., Carnazza, K. E., Brand, C., Reiner, T., Agnew, B. J., Lewis, J. S., and Zeglis, B. M. (2016) Pretargeted PET imaging using a site-specifically labeled immunoconjugate. *Bioconjug. Chem.* *27*, 1789-1795.
- (14) Mandikian, D., Rafidi, H., Adhikari, P., Venkatraman, P., Nazarova, L., Fung, G., Figueroa, I., Ferl, G. Z., Ulufatu, S., and Ho, J. (2018) Site-specific conjugation allows modulation of click reaction stoichiometry for pretargeted SPECT imaging. *MAbs* *10*, 1269-1280.
- (15) Sarrett, S. M., Keinänen, O., Dayts, E. J., Roi, D.-L., Rodriguez, C., Carnazza, K. E., and Zeglis, B. M. (2021) Inverse electron demand Diels–Alder click chemistry for pretargeted PET imaging and radioimmunotherapy. *Nat. Protoc.* *16*, 3348-3381.
- (16) Rossin, R., Versteegen, R. M., Wu, J., Khasanov, A., Wessels, H. J., Steenbergen, E. J., Ten Hoeve, W., Janssen, H. M., van Onzen, A. H., and Hudson, P. J. (2018) Chemically triggered drug release from an antibody-drug conjugate leads to potent antitumour activity in mice. *Nat. Commun.* *9*, 1-11.
- (17) Li, H., Conde, J., Guerreiro, A., and Bernardes, G. J. (2020) Tetrazine Carbon Nanotubes for Pretargeted In Vivo “Click-to-Release” Bioorthogonal Tumour Imaging. *Angew. Chem. Int. Ed.* *59*, 16023-16032.
- (18) Handula, M., Chen, K.-T., and Seimille, Y. (2021) IEDDA: An Attractive Bioorthogonal Reaction for Biomedical Applications. *Molecules* *26*, 4640.
- (19) Darko, A., Wallace, S., Dmitrenko, O., Machovina, M. M., Mehl, R. A., Chin, J. W., and Fox, J. M. (2014) Conformationally strained trans-cyclooctene with improved stability and excellent reactivity in tetrazine ligation. *Chem. Sci.* *5*, 3770-3776.
- (20) Debets, M. F., Van Berkel, S. S., Dommerholt, J., Dirks, A. J., Rutjes, F. P., and Van Delft, F. L. (2011) Bioconjugation with strained alkenes and alkynes. *Acc. Chem. Res.* *44*, 805-815.
- (21) Sletten, E. M., and Bertozzi, C. R. (2009) Bioorthogonal chemistry: fishing for selectivity in a sea of functionality. *Angew. Chem. Int. Ed.* *48*, 6974-6998.
- (22) Blackman, M. L., Royzen, M., and Fox, J. M. (2008) Tetrazine ligation: fast bioconjugation based on inverse-electron-demand Diels–Alder reactivity. *J. Am. Chem. Soc.* *130*, 13518-13519.
- (23) Wu, H., and Devaraj, N. K. (2016) Inverse Electron-Demand Diels–Alder Bioorthogonal Reactions, in *Cycloadditions in Bioorthogonal Chemistry. Topics in Current Chemistry Collections.* (Vrabel, M., and Carell, T., Eds.) pp 109-130, Springer Nature, Switzerland.
- (24) Han, H.-S., Devaraj, N. K., Lee, J., Hilderbrand, S. A., Weissleder, R., and Bawendi, M. G. (2010) Development of a bioorthogonal and highly efficient conjugation method for quantum dots using tetrazine–norbornene cycloaddition. *J. Am. Chem. Soc.* *132*, 7838-7839.
- (25) Devaraj, N. K., Hilderbrand, S., Upadhyay, R., Mazitschek, R., and Weissleder, R. (2010) Bioorthogonal turn-on probes for imaging small molecules inside living cells. *Angew. Chem.* *122*, 2931-2934.
- (26) Haun, J. B., Devaraj, N. K., Hilderbrand, S. A., Lee, H., and Weissleder, R. (2010) Bioorthogonal chemistry amplifies nanoparticle binding and enhances the sensitivity of cell detection. *Nat. Nanotechnol.* *5*, 660-665.
- (27) Zeglis, B. M., Mohindra, P., Weissmann, G. I., Divilov, V., Hilderbrand, S. A., Weissleder, R., and Lewis, J. S. (2011) Modular strategy for the construction of radiometalated antibodies for positron emission tomography based on inverse electron demand diels–alder click chemistry. *Bioconjug. Chem.* *22*, 2048-2059.
- (28) Schoch, J., Staudt, M., Samanta, A., Wiessler, M., and Jäschke, A. (2012) Site-specific one-pot dual labeling of DNA by orthogonal cycloaddition chemistry. *Bioconjug. Chem.* *23*, 1382-1386.

- (29) Asare-Okai, P., Agustin, E., Fabris, D., and Royzen, M. (2014) Site-specific fluorescence labelling of RNA using bio-orthogonal reaction of trans-cyclooctene and tetrazine. *Chem. Commun.* 50, 7844-7847.
- (30) Reiner, T., Lacy, J., Keliher, E. J., Yang, K. S., Ullal, A., Kohler, R. H., Vinegoni, C., and Weissleder, R. (2012) Imaging therapeutic PARP inhibition in vivo through bioorthogonally developed companion imaging agents. *Neoplasia* 14, 169-77.
- (31) Li, Z., Cai, H., Hassink, M., Blackman, M. L., Brown, R. C., Conti, P. S., and Fox, J. M. (2010) Tetrazine–trans-cyclooctene ligation for the rapid construction of 18F labeled probes. *Chem. Commun.* 46, 8043-8045.
- (32) Syvanen, S., Fang, X. T., Faresjo, R., Rokka, J., Lannfelt, L., Olberg, D. E., Eriksson, J., and Sehlin, D. (2020) Fluorine-18-labeled antibody ligands for PET imaging of amyloid- β in brain. *ACS Chem. Neurosci.* 11, 4460-4468.
- (33) Poduslo, J. F., Curran, G. L., and Berg, C. T. (1994) Macromolecular permeability across the blood-nerve and blood-brain barriers. *Proc. Natl. Acad. Sci. (USA)* 91, 5705-5709.
- (34) Bard, F., Cannon, C., Barbour, R., Burke, R.-L., Games, D., Grajeda, H., Guido, T., Hu, K., Huang, J., and Johnson-Wood, K. (2000) Peripherally administered antibodies against amyloid β -peptide enter the central nervous system and reduce pathology in a mouse model of Alzheimer disease. *Nat. Med.* 6, 916-919.
- (35) Pardridge, W. M. (2012) Drug transport across the blood–brain barrier. *J. Cereb. Blood Flow Metab.* 32, 1959-1972.
- (36) Yu, Y. J., Zhang, Y., Kenrick, M., Hoyte, K., Luk, W., Lu, Y., Atwal, J., Elliott, J. M., Prabhu, S., and Watts, R. J. (2011) Boosting brain uptake of a therapeutic antibody by reducing its affinity for a transcytosis target. *Sci. Transl. Med.* 3, 84ra44.
- (37) Yu, Y. J., Atwal, J. K., Zhang, Y., Tong, R. K., Wildsmith, K. R., Tan, C., Bien-Ly, N., Hersom, M., Maloney, J. A., and Meilandt, W. J. (2014) Therapeutic bispecific antibodies cross the blood-brain barrier in nonhuman primates. *Sci. Transl. Med.* 6, 261ra154.
- (38) Syvänen, S., Fang, X. T., Hultqvist, G., Meier, S. R., Lannfelt, L., and Sehlin, D. (2017) A bispecific Tribody PET radioligand for visualization of amyloid-beta protofibrils—a new concept for neuroimaging. *Neuroimage* 148, 55-63.
- (39) Gustavsson, T., Syvänen, S., O’Callaghan, P., and Sehlin, D. (2020) SPECT imaging of distribution and retention of a brain-penetrating bispecific amyloid- β antibody in a mouse model of Alzheimer’s disease. *Transl. Neurodegener.* 9, 1-11.
- (40) Hersom, M., Helms, H. C., Pretzer, N., Goldeman, C., Jensen, A. I., Severin, G., Nielsen, M. S., Holm, R., and Brodin, B. (2016) Transferrin receptor expression and role in transendothelial transport of transferrin in cultured brain endothelial monolayers. *Mol. Cell. Neurosci.* 76, 59-67.
- (41) Moos, T. (1996) Immunohistochemical localization of intraneuronal transferrin receptor immunoreactivity in the adult mouse central nervous system. *J. Comp. Neurol.* 375, 675-692.
- (42) Niewoehner, J., Bohrmann, B., Collin, L., Urich, E., Sade, H., Maier, P., Rueger, P., Stracke, J. O., Lau, W., and Tissot, A. C. (2014) Increased brain penetration and potency of a therapeutic antibody using a monovalent molecular shuttle. *Neuron* 81, 49-60.
- (43) Weber, F., Bohrmann, B., Niewoehner, J., Fischer, J. A., Rueger, P., Tiefenthaler, G., Moelleken, J., Bujotzek, A., Brady, K., and Singer, T. (2018) Brain shuttle antibody for Alzheimer’s disease with attenuated peripheral effector function due to an inverted binding mode. *Cell Rep.* 22, 149-162.
- (44) Richards, J. G., Higgins, G. A., Ouagazzal, A.-M., Ozmen, L., Kew, J. N., Bohrmann, B., Malherbe, P., Brockhaus, M., Loetscher, H., and Czech, C. (2003) PS2APP transgenic mice, coexpressing hPS2mut and hAPPswe, show age-related cognitive deficits associated with discrete brain amyloid deposition and inflammation. *J. Neurosci.* 23, 8989-9003.

- (45) Kjaer, A., Petersen, I. N., Herth, M. M., and Kristensen, J. L., Novel tetrazine compounds for in vivo imaging, WO2020/108720 A1.
- (46) Rossin, R., Läppchen, T., Van Den Bosch, S. M., Laforest, R., and Robillard, M. S. (2013) Diels–Alder reaction for tumor pretargeting: in vivo chemistry can boost tumor radiation dose compared with directly labeled antibody. *J. Nucl. Med.* *54*, 1989-1995.
- (47) Billaud, E. M., Belderbos, S., Cleeren, F., Maes, W., Van de Wouwer, M., Koole, M., Verbruggen, A., Himmelreich, U., Geukens, N., and Bormans, G. (2017) Pretargeted PET imaging using a bioorthogonal ¹⁸F-labeled trans-cyclooctene in an ovarian carcinoma model. *Bioconjug. Chem.* *28*, 2915-2920.
- (48) Rossin, R., Van Den Bosch, S. M., Ten Hoeve, W., Carvelli, M., Versteegen, R. M., Lub, J., and Robillard, M. S. (2013) Highly reactive trans-cyclooctene tags with improved stability for Diels–Alder chemistry in living systems. *Bioconjug. Chem.* *24*, 1210-1217.
- (49) Edelmann, M. R., and Hauri, S. (2021) Functional in vitro assessment of modified antibodies: Impact of label on protein properties. *PLoS One* *16*, e0257342.
- (50) Rondon, A., Ty, N., Bequignat, J.-B., Quintana, M., Briat, A., Witkowski, T., Bouchon, B., Boucheix, C., Miot-Noirault, E., and Pouget, J.-P. (2017) Antibody PEGylation in bioorthogonal pretargeting with trans-cyclooctene/tetrazine cycloaddition: in vitro and in vivo evaluation in colorectal cancer models. *Sci. Rep.* *7*, 1-11.
- (51) Cook, B. E., Membreno, R., and Zeglis, B. M. (2018) Dendrimer scaffold for the amplification of in vivo pretargeting ligations. *Bioconjug. Chem.* *29*, 2734-2740.
- (52) Membreno, R., Keinänen, O. M., Cook, B. E., Tully, K. M., Fung, K. C., Lewis, J. S., and Zeglis, B. M. (2019) Toward the optimization of click-mediated pretargeted radioimmunotherapy. *Mol. Pharm.* *16*, 2259-2263.
- (53) Maggi, A., Ruivo, E., Fissers, J., Vangestel, C., Chatterjee, S., Joossens, J., Sobott, F., Staelens, S., Stroobants, S., and Van Der Veken, P. (2016) Development of a novel antibody–tetrazine conjugate for bioorthogonal pretargeting. *Org. Biomol. Chem.* *14*, 7544-7551.
- (54) Billaud, E. M., Shahbazali, E., Ahamed, M., Cleeren, F., Noël, T., Koole, M., Verbruggen, A., Hessel, V., and Bormans, G. (2017) Micro-flow photosynthesis of new dienophiles for inverse-electron-demand Diels–Alder reactions. Potential applications for pretargeted in vivo PET imaging. *Chem. Sci.* *8*, 1251-1258.
- (55) Stéen, E. J. L., Jørgensen, J. T., Denk, C., Battisti, U. M., Nørregaard, K., Edem, P. E., Bratteby, K., Shalgunov, V., Wilkovitsch, M., and Svatunek, D. (2021) Lipophilicity and click reactivity determine the performance of bioorthogonal tetrazine tools in pretargeted in vivo chemistry. *ACS Pharmacol. Trans. Sci.* *4*, 824-833.
- (56) Waterhouse, R. N. (2003) Determination of lipophilicity and its use as a predictor of blood–brain barrier penetration of molecular imaging agents. *Mol. Imaging Biol.* *5*, 376-389.
- (57) Freskgård, P.-O., and Urich, E. (2017) Antibody therapies in CNS diseases. *Neuropharmacol.* *120*, 38-55.
- (58) van den Broek, S. L., Shalgunov, V., Sehlin, D., Syvanen, S., and Herth, M. (2020) Development of trans-cyclooctene modified antibodies for pretargeted imaging within the central nervous system. *J. Nucl. Med.* *61*, 196-196.
- (59) Meyer, J.-P., Tully, K. M., Jackson, J., Dilling, T. R., Reiner, T., and Lewis, J. S. (2018) Bioorthogonal masking of circulating antibody–TCO groups using tetrazine-functionalized dextran polymers. *Bioconjug. Chem.* *29*, 538-545.
- (60) Bohrmann, B., Baumann, K., Benz, J., Gerber, F., Huber, W., Knoflach, F., Messer, J., Oroszlan, K., Rauchenberger, R., and Richter, W. F. (2012) Gantenerumab: a novel human anti-A β antibody demonstrates sustained cerebral amyloid- β binding and elicits cell-mediated removal of human amyloid- β . *J. Alzheimers Dis.* *28*, 49-69.
- (61) Muri, D., and Edelmann, M. R. (2018) Tools for work-up and prepurification of tritium-labeled small molecules. *J. Label. Compds. Radiopharm.* *61*, 912-915.

Chapter Ten

Conclusions

In recent decades, small molecules have dominated the pipeline of the pharmaceutical industry. Now, molecules from other modalities such as nucleic acid-based drugs, peptides, or antibodies are appearing on the market. These molecules are usually larger (significantly >1 kDa), usually multi-charged, and often poorly soluble in organic solvents. A major challenge with molecules of the new modalities is the prediction of drug targeting, which, together with solubility, contributes to the overall exposure of drugs and drug candidates in the systemic circulation or their ability to enter the brain. It is not just the molecules that are getting more complex, but also the biochemical assays and the radiolabelling methods.

Radiolabelling of small molecules with beta emitters like carbon-14 ($t_{1/2}$: 5,730 y; molar activity: 2.3 GBq/mmol; 62.4 mCi/mmol) or tritium ($t_{1/2}$: 12.3 y; molar activity: 984.2 GBq/mmol; 26.6 Ci/mmol) has been intensively investigated over the last decades and new concepts for the introduction of radionuclides continue to be regularly reported. New catalysts that cause carbon/hydrogen activation are capable of incorporating isotopes such as deuterium or tritium into small molecules. These established labelling methods are of limited applicability to nucleic acid-based drugs, therapeutic antibodies, or peptides typical of the molecules currently being investigated as new therapeutic modalities. However, in preclinical research, radiolabelling is often required to track and monitor drug candidates in metabolism, biotransformation, or pharmacokinetic studies.

Radiolabelling of nucleic acid-based drugs with a beta emitter is a major challenge. The use of carbon-14 for radiolabelling oligonucleotides is usually not practical because the molar activity is too low. Tritium, on the other hand, has over a 400-fold higher molar activity and is suitable for larger molecules (> 1 kDa) in a variety of biochemical assays or in imaging studies. By now the most commonly used approach to tritium-labelled oligonucleotides consisting of a phosphorothioate backbone is based on a methodology that dates back to 1995 and is still state-of-the-art. The chemical approach requires a complex, multi-step pre-synthesis of the ^3H -nucleoside phosphoramidite monomer for subsequent solid-phase synthesis to the desired ^3H -oligonucleotide. In addition, high specific activity cannot be achieved because the tritium-labelled nucleoside phosphoramidite must be diluted with non-radioactive monomer to avoid strong radiolysis. These issues lead to a high expenditure of time, a high proportion of radioactive waste, and thus high costs. A novel labelling concept was developed by conjugating a tritium-labelled *N*-ethylmaleimide ($[^3\text{H}]\text{NEM}$) to a thiol linker attached to either the 5'-end or the 3'-end of an oligonucleotide. However, this modification also poses a risk of altering molecular properties, in terms of stability or

target engagement. To address these concerns, *in vitro* binding studies and *in vivo* biodistribution studies were performed and the results compared to the corresponding unmodified compound. It was demonstrated that the modification has no impact on biological behaviour and is therefore a fast, safe, and cost-effective access to tritium-labelled oligonucleotides.

However, sample preparation of [³H]NEM for conjugation to a thiol-linker from an oligonucleotide proved to be very difficult, as NEM arrived in the laboratory in a pentane solution. The pentane had to be removed for a solvent change to a water-miscible solvent. The high volatility of NEM does not allow the a removal of the pentane by distillation or by using a gentle argon stream. This issue was addressed by transferring the pentane solution to a short silica gel-based cartridge and eluting the NEM from the matrix using DMSO. This high amount of DMSO in the subsequent conjugation to the thiol-linker induced a sulfur/oxygen exchange in the phosphorothioate backbone. For this reason, a synthetic route to tritium-labelled maleimide derivatives was developed, which provides maleimides that are easily accessible, non-volatile, and available in high molar activity.

Starting from *N*-substituted maleimides with exocyclic hydroxy functionality, base-stable intermediates were obtained by a Diels-Alder [4+2] cycloaddition in 2,5-dimethylfuran as solvent. Protected maleimides enable methylation of primary alcohols under basic conditions and prevent nucleophilic attack from Michael-type donors. The final products were obtained by deprotection *via* a retro-Diels-Alder reaction by heating the protected tritiated maleimides at 110 °C. The special feature is not only that these maleimides are less volatile than NEM, but the purified radioactive maleimides can be used directly from the preparative HPLC fractions for subsequent bioconjugations without solvent exchange. This enables quantitative use without loss of radioactivity and allows for safe handling. The reactivity of the novel tritium-labelled maleimide derivatives was demonstrated by a bioconjugation step on thiol-functionalized oligonucleotides. This concept opens up new possibilities for a safe, fast, and inexpensive access to tritium-labelled maleimide derivatives for the radiolabelling of thiol-functionalized biomolecules.

Inserting a tritium atom into a peptide can be challenging. Insertion of a tritiated amino acid into a peptide sequence is theoretically possible, but in practice it is difficult and time-consuming when larger peptides are to be labelled. Late-stage catalytic titration is often complicated by the presence of interfering functional groups in the peptide sequence, which can deactivate the catalyst during a reduction or exchange reaction. Two approaches were investigated for the incorporation of tritium into the human peptide neuromedin S (NMS): halogenation of NMS followed by metal-catalysed halogen-tritium exchange. Derivatisation of the primary amine residues with [³H]*N*-succinimidyl propionate ([³H]NSP).

Halogenation was achieved with sodium iodide and chloramine-T on the histidine residue (0%, I₀, 35% I₁ and 65% I₂). However, subsequent exchange of iodine for deuterium was not successful. In a non-radioactive preliminary experiment, NSP was conjugated with primary amines present at the following amino acids of the peptide sequence: Ile-1, Lys-15, and Lys-16. In a functional *in vitro* Fluorometric Imaging Plate Reader (FLIPR) assay, the binding behaviour between the modified NMS derivatives and the protein NMUR₂ proved to be comparable to that of the unlabelled NMS, irrespective of the degree of labelling and the position of the label. With these encouraging results, a conjugation with radioactive NSP to NMS was performed, resulting in several peptide products with different degrees of labelling and labelling positions. After preparative HPLC, two main fractions containing radioactive peptide derivatives were isolated. The first fraction consisted of a mixture of a single conjugation at Lys-15 and another product labelled at Lys-16 (total yield: 13 %), which could not be separated due to their almost identical retention times. The second major fraction consisted of the conjugation product with a single label at *N*-terminal Ile-1 (yield: 7 %) in high purity (>95 %) and a molar activity of 3.3 TBq/mmol (90 Ci/mmol). To the best of our knowledge, this study is the first approach to tritiated NMS and opens the door for further studies to characterise the behaviour of NMS or corresponding ligands.

When labelling an antibody with a fluorescent tag or radioisotope, there is a risk that the modification will alter the physicochemical properties or the pharmacokinetic (PK) behaviour of the protein. Therefore, there is a need for an *in vitro* assessment workflow to predict a change in the physiological properties of antibodies after label incorporation. The combination of multiple analytical methods reveal changes after label conjugation that would otherwise have gone undetected. In addition to classic size-exclusion chromatography (SEC), the core element of the developed analysis package consists of the correlation of relative retention times for FcRn and heparin affinity chromatography of labelled mAbs with the unlabelled variant.

Direct iodination has been shown to damage mAbs, as demonstrated by FcRn affinity chromatography. An alternative to direct iodination is indirect iodination using the Bolton-Hunter reagent. The quality assessment after protein modification by conjugation of the iodinated Bolton-Hunter reagent shows a less pronounced change in protein properties compared to direct iodination. Protein modifications with maleimide-based tags that require prior partial reduction of the protein can lead to disruption of the quaternary protein structure. SEC analysis under denatured sample preparation conditions indicated free heavy and light chains after maleimide-based labeling. During the reduction step, cystine disulfide bonds are reduced to allow free Cys to conjugate with the labelling reagent. After successful labelling at cysteine residues, no intramolecular disulfide bridges can be reformed. The quaternary structure of the

antibody is maintained by only intermolecular forces, e.g. ionic or hydrogen bonds. Under denaturing conditions caused by low pH and organic solvent, these bonds are broken and since there are no covalent disulfide bonds left, the antibody breaks down into heavy and light chains. This could be important in an *in vivo* setting if, during FcRn recycling, the endosomal pH drops and the antibody is degraded instead of being recycled into the circulation. Both the type and degree of labeling of modified IgGs can lead to changes in the physicochemical protein properties. In addition, harsh labelling conditions can also affect the behaviour of labelled mAbs. Finally, it was shown that identical labels on different constructs of IgG1 lead to different affinities for FcRn and heparin. This result highlights the importance of assessing the implications of labelling for each new antibody construct individually, and unfortunately the results of this study cannot be taken as a general guide as to which labelling strategy is most appropriate in all cases. Considering the assessment data, only 6 of the 11 modified mAbs in this study can be recommended for use in *in vitro* or *in vivo* experiments.

The advantages of the developed quality assessment prior to mechanistic studies are manifold. Obviously, time and resources can be saved by minimizing the risk of using inappropriate or even unstable test molecules that generate questionable data. Another key benefit is the reduction in animal testing avoiding proteins that have been compromised in the labelling process. From an ethical point of view, this analytical workflow is a contribution to the 3Rs principles, so that no animal testing is performed that could lead to wrong results or conclusions, related to human data or clinical studies.

Applications of antibodies labelled with [³H]NSP are in tracking and quantification in biodistribution studies. Animal studies in mice confirmed that drug/anti-drug antibody (ADA) immune complexes (IC) are cleared from the circulation faster than the therapeutic drug. It was not previously known exactly where and when these ICs were distributed or excreted in the body. An important finding of these biodistribution studies with radiolabelled proteins (tritium drug versus tritium ICs) is that high levels of radioactivity from ICs accumulate in the pancreas in female Wistar rats. Furthermore, the finding that in the first 24 h a high amount of radioactivity was found in the urine from the group that received the pre-complexed dose. So far it has not been possible to identify the main degradation product. An estimation was only possible by a molecular weight marker by SEC, which showed a peptide with a size of ~1.2 kDa. More research needs to be done to gain more insight into IC degradation.

For drug discovery programmes targeting the central nervous system (CNS), early development of new small molecule drugs requires a translational approach to provide evidence of distribution, exposure, and function in specific brain regions. Positron emission tomography (PET) provides a means of assessing the distribution of drug candidates in the brain and their binding to the target of interest *in vivo*, provided

radiolabelling of the drug is possible or a suitable radioligand is available. PET is an important tool from diagnostic imaging to the early stages of drug discovery programmes.

The endocannabinoid system (ECS) is a versatile system that plays an important role in physiological and pathological conditions. Among other things, it consists of the endogenous ligand 2-arachidonoyl-glycerol (2-AG). 2-AG is mainly degraded by monoacylglycerol lipase (MAGL) into fatty acid and glycerol. Consequently, pharmacological inhibition of MAGL, a serine hydrolase in the brain, leads to an increase in 2-AG levels in the CNS and decreases prostaglandin (PG) production, resulting in cytokine-lowering effects. Therefore, MAGL has gained a great attention as a promising therapeutic target for neurological diseases such as Alzheimer's, Parkinson's, or multiple sclerosis.

Recently, a morpholin-3-one derivative was discovered as a novel scaffold for imaging MAGL by PET. However, its slow kinetics *in vivo* hindered its application. In this study, structural optimisation was performed. Eleven new MAGL inhibitors were designed and synthesised. Based on the results of MAGL inhibition potency, *in vitro* metabolic stability and surface plasmon resonance assay results, one compound was identified as a potential MAGL PET tracer candidate. The corresponding ^{11}C -labelled compound was synthesised by direct $^{11}\text{CO}_2$ fixation and successfully mapped MAGL distribution patterns in rodent brains by *in vitro* autoradiography. PET studies in mice using the ^{11}C -tracer demonstrated its improved kinetic profile compared to previously reported MAGL-PET tracers. Its high specificity *in vivo* was demonstrated by using MAGL-KO mice. Although further studies confirmed that the novel ^{11}C -tracer is a P-glycoprotein (P-gp) substrate in mice, the low P-gp efflux rate on cells transfected with human protein suggests that this should not be an issue for clinical implementation as a novel reversible MAGL-PET tracer in humans. Overall, the developed PET tracer ($[^{11}\text{C}]\text{RO7284390}$) showed promising results that warrant further clinical evaluation.

The bioorthogonal approach decouples the biological half-life of an antibody from the physical half-life of a short-lived radioisotope. This opens up the possibility of using modified antibodies as PET tracers for targets in the brain that cannot be reached with a classical small molecule PET tracer. Tetrazine (Tz) derivatives undergoing inverse electron demand-Diels-Alder (IEDDA) reactions with an antibody carrying *trans*-cyclooctene (TCO) moieties were investigated. Eleven tetrazines were evaluated and classified for their properties as potential CNS radiotracers and click partners for bioorthogonal PET imaging based on several *in vitro* and *in vivo* experiments. These experiments included evaluation of pH-dependent stability, *in vitro* membrane permeability, P-gp efflux, and microsomal clearance. The biodistribution using fluorine-18-labelled Tzs and the cerebrospinal fluid (CSF)/plasma ratio of selected non-radioactive tetrazines was determined in *in vivo* experiments. Two Tzs out of the eleven

can be proposed as the most promising candidates that showed the best properties in terms of brain penetration and a balance between stability and reaction rate with a TCO unit. In the next step, the selected Tzs will be evaluated for their suitability as bioorthogonal click partners for PET imaging of misfolded proteins in the CNS on brain tissue *in vivo* and *ex vivo*.

Initially, the A β -specific BrainShuttle version of mAb31 (mAb31-BrainShuttle, mAb for short) was successfully radiolabelled *in vitro* by conjugating a tritiated 1,2,4,5-Tz and a *trans*-cyclooctene modified mAb (mAb-TCO) in an IEDDA reaction. The mAb-TCO-Tz antibody retained its functionality and specificity as demonstrated in several *in vitro* experiments using PS2APP mouse brain slices, ELISA, FACS assays, radio-immunohistochemistry, and *in vivo* approaches. The radiolabelled A β -specific antibody crossed the blood-brain barrier (BBB) and bound its target. One to three days after mAb-TCO injection proved to be a suitable time window for *in vivo* pretargeting. The TCO groups remained reactive to the Tz reagent as specific radiolabelling of A β -plaques was detected in brain slices from PS2APP mice using an *ex vivo* click reaction. However, the *in vivo* click reaction with intravenously injected Tz one and three days after injection of the TCO-modified antibody revealed no specific difference in binding intensity between the transgenic and wild-type animals. A radioactive signal was detected in the brain tissue, but no click response was detected by autoradiography. Further experiments are needed to optimise the multicomponent pretargeting system, e.g. the TCO labelling level of the mAb, the administered Tz concentration, and the molecular structure of the Tz, to ensure the right balance between stability and reactivity of both components for a successful *in vivo* pretargeting response. The study described suggests that the application of PET imaging in drug development and for clinical diagnostics can be extended to targets that are currently considered untreatable and for which a conventional small molecule PET tracer is not suitable.

In this thesis, in 9 chapters including 8 peer-reviewed journal articles, radiolabelling small and biomolecules for tracking and monitoring has been achieved.

APPENDIX

Abstracts of Invited Talks and Poster Presentations

Oral presentations at:

- TIDES, Brussels, Belgium (November 15th, 2021)
- Biologics UK, London, UK (March, 21st, 2022)

Title

A Novel Access to Tritium Labelled Oligonucleotides

Bullet Points summarizing the content of the presentation

- Thiol modifiers were positioned at the 3'-end of ASOs, conjugated with [³H]ethyl maleimide, and compared with their untagged counterparts.
- Conjugates were metabolically stable *in vitro* for at least up to 72 h.
- Radiolabelled ASOs showed similar *in vivo* behaviour in liver, kidney, and spleen compared to the untagged ASO.

Biography

Martin studied Biological Chemistry at the University of Applied Science Mannheim, Germany in 2003 and completed his diploma thesis at Novartis in Switzerland in 2006. After 4 years of research in medicinal chemistry at the Novartis Institutes for BioMedical Research, Martin moved to Roche's isotope synthesis laboratory at the end of 2010. His responsibilities include labelling small molecules, oligonucleotides, and proteins with carbon-14 and tritium. At the beginning of 2020, Martin started his PhD studies at the University of Bath, UK in the Department of Pharmacy and Pharmacology under supervision of Dr Ian S. Blagbrough and Prof Stephen M. Husbands as well as Dr Michael B. Otteneder and Dr Filippo Sladojevich (Roche). The aim of his PhD thesis is to investigate new ways of radiolabelling nucleic acid-based medicines and biomolecules for tracking and monitoring. The talk describes a part of Martin's PhD on a novel method to label oligonucleotides.

A Novel Access to Tritium-Labelled Oligonucleotides

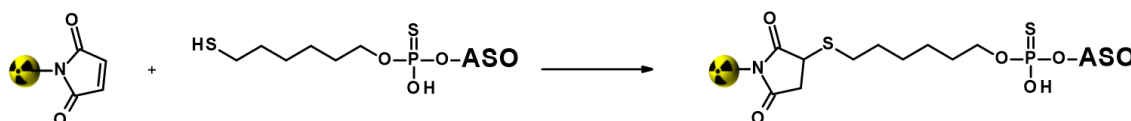
Martin R. Edelman^{a,b}

^a*Department of Pharmacy and Pharmacology, University of Bath, Bath BA2 7AY, U.K.*

^b*Roche Innovation Center Basel, F. Hoffmann-La Roche, 4070 Basel, CH*

E-mail: martin.edelmann@roche.com

Antisense oligonucleotide (ASO) based therapies are a fast growing field in drug discovery, targeting modulation of mRNA translation. The labelling of ASO with ³H for biodistribution and imaging studies in preclinical research is a major challenge. A novel synthetic approach¹ has been established for fast, efficient, and inexpensive access to tritium-labelled oligonucleotides. A thiol reactive group was inserted at the 5'- or 3'-end with a standard C₆ spacer arm on an ASO. Tritium-labelled maleimides react specifically with the terminal sulfhydryl group at pH 7 (**Scheme 1**). Radiochemical yields in the range of 70 - 99% and molar activities of 8 - 21 Ci/mmol were achieved in several labelling experiments.



Scheme 1: General synthetic route to oligonucleotides containing tritium-labelled maleimides on C₆-thiol linker.

In order to compare potential differences in PK behaviours between untagged and modified ASOs, mice received a single subcutaneous dose of 1 mg/kg of untagged ASOs, whereas their counterparts were dosed with ASOs tagged with [³H]*N*-ethylmaleimide (NEM). The concentration in liver, spleen, and kidney of untagged and tritium-labelled ASOs were determined at different time points. For all tissues, the results obtained for the labelled and unlabelled counterparts were comparable, which indicates a similar distribution in the tissues examined. In a further step, improved tritium-*O*-methylated *N*-alkoxy-maleimide derivatives were synthesized in a 3-step route, including: 1) Diels-Alder protection of the maleimide core, 2) *O*-methylation using of commercially available [³H]methyl nosylate, 3) deprotection by retro-Diels Alder reaction.² The major advantage of *N*-alkoxy maleimides in comparison to *N*-alkylated maleimides such as NEM is their lower volatility, which enables safer handling with respect to radiation-safety protection.

Reference

- [1] Edelman MR *et al.* *AAPS Open*, 2021, **7**: 4(2021).
- [2] Edelman MR, Muser T. *Bioconjugate Chem.* 2021 **32**: 1027-1033.

A Novel Access to Tritium-Labelled Oligonucleotides

Martin R. Edelmann^{1,2}

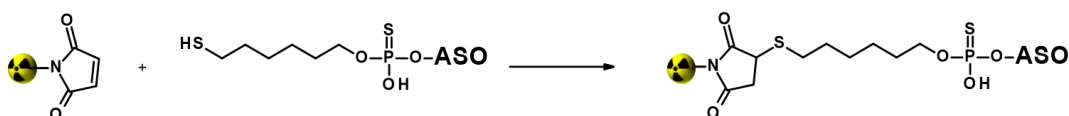
¹ Department of Pharmacy and Pharmacology, University of Bath, Bath BA2 7AY, UK

² Roche Innovation Center Basel, F. Hoffmann-La Roche, 4070 Basel, CH

martin.edelmann@roche.com

Objectives

Antisense oligonucleotide (ASO) based therapies are a fast growing field in drug discovery, targeting modulation of mRNA translation. The labelling of ASO with ³H for biodistribution and imaging studies in preclinical research is a major challenge. A thiol reactive group can be inserted at the 5'- or 3'-end with a standard C₆ spacer arm on an ASO, allowing tritium-labelled maleimides to react specifically with the terminal sulfhydryl group (**Scheme 1**).



Scheme 1: General synthetic route to oligonucleotides containing tritium-labelled maleimides on C₆-thiol linker.

Materials and methods

In order to compare potential differences in PK behaviours between untagged and modified ASOs, mice received a single subcutaneous dose of 1 mg/kg of untagged ASOs, whereas their counterparts were dosed with ASOs tagged with [³H]*N*-ethylmaleimide (NEM). The concentration in liver, spleen, and kidney of untagged and tritium-labelled ASOs were determined at different time points.

Results

For all tissues, the results obtained for the labelled and unlabelled counterparts were comparable, which indicates a similar distribution in the tissues examined. In a further step, improved tritium-*O*-methylated *N*-alkoxy-maleimide derivatives were synthesized in a 3-step route, including: 1) Diels-Alder protection of the maleimide core, 2) *O*-methylation using of commercially available [³H]methyl nosylate, 3) deprotection by retro-Diels Alder reaction [1]. Radiochemical yields in the range of 70 - 99% and molar activities of 8 - 21 Ci/mmol were achieved in several labelling experiments.

Conclusions

A novel synthetic approach [2] has been established for fast, efficient, and inexpensive access to tritium-labelled oligonucleotides. The major advantage of *N*-alkoxy maleimides in comparison to *N*-alkylated maleimides such as NEM is their lower volatility, which enables safer handling with respect to radiation-safety protection.

References

- [1] Edelmann M.R., Muser T., 2021. Tritium *O*-Methylation of *N*-Alkoxy Maleimide Derivatives as Labeling Reagents for Biomolecules. *Bioconjug. Chem.* 32, 1027-1033.
- [2] Edelmann M.R. *et al.*, 2021. Tritium labeling of antisense oligonucleotides *via* different conjugation agents. *AAPS Open*, 7, 4(2021).